



Testing the chemical tagging technique with open clusters

Sergi Blanco-Cuaresma

► **To cite this version:**

Sergi Blanco-Cuaresma. Testing the chemical tagging technique with open clusters. Astrophysics [astro-ph]. Université de Bordeaux, 2014. English. <NNT : 2014BORD0079>. <tel-01104201v2>

HAL Id: tel-01104201

<https://tel.archives-ouvertes.fr/tel-01104201v2>

Submitted on 18 Jun 2015

HAL is a multi-disciplinary open access archive for the deposit and dissemination of scientific research documents, whether they are published or not. The documents may come from teaching and research institutions in France or abroad, or from public or private research centers.

L'archive ouverte pluridisciplinaire **HAL**, est destinée au dépôt et à la diffusion de documents scientifiques de niveau recherche, publiés ou non, émanant des établissements d'enseignement et de recherche français ou étrangers, des laboratoires publics ou privés.

THÈSE PRÉSENTÉE
POUR OBTENIR LE GRADE DE
DOCTEUR DE
L'UNIVERSITÉ DE BORDEAUX

ÉCOLE DOCTORALE DES SCIENCES PHYSIQUES ET DE L'INGENIEUR
SPÉCIALITÉ : Astrophysique, Plasmas, Nucléaire

Par Sergi Blanco-Cuaresma

**Test de la technique de marquage chimique avec
des amas ouverts**

Sous la direction de : Caroline Soubiran

Soutenue le 30 septembre 2014

Membres du jury :

Jonathan Braine	Astronome, Université de Bordeaux, France	Président du jury
David Montes	Prof. titular, Univ. Complutense de Madrid, Spain	rapporteur
Philippe Prugniel	Astronome, Observatoire de Lyon, France	rapporteur
Alejandra Recio-Blanco	Astronome Adjointe, Nice, France	Examineur
Ulrike Heiter,	Chercheur, Uppsala University, Suède	Examineur
Caroline Soubiran	Directrice de recherche, CNRS, Bordeaux, France	Directrice de thèse

Titre : Test de la technique de marquage chimique avec des amas ouverts

Résumé :

Contexte. Les étoiles naissent ensemble dans des nuages moléculaires géants. Si nous faisons l'hypothèse qu'ils étaient à l'origine chimiquement homogènes et bien mélangés, nous nous attendrions à ce que les étoiles issues d'un même nuage aient la même composition chimique. La plupart des groupes d'étoiles sont perturbés lors de leur évolution dans la galaxie et l'information dynamique est perdue. Ainsi la seule possibilité que nous ayons de reconstruire l'histoire de la formation stellaire est d'analyser les abondances chimiques que l'on observe aujourd'hui.

But. La technique de marquage chimique a pour but de retrouver les amas d'étoiles dissociés en se basant uniquement sur leur composition chimique. Nous évaluons la viabilité de cette technique pour retrouver les étoiles qui sont nées dans un même amas mais qui ne sont plus gravitationnellement liées.

Méthodes. Nous avons créé une librairie de spectres stellaires de haute qualité afin de faciliter l'évaluation des analyses spectrales. Nous avons développé notre propre outil d'analyse spectrale, nommée iSpec, capable d'homogénéiser les spectres stellaires venant de tous types d'instruments et de dériver les paramètres atmosphériques et les abondances chimiques. Finalement, nous avons compilé des spectres stellaires d'étoiles de 32 amas ouverts, nous avons dérivé de façon homogène les paramètres atmosphériques et les abondances de 17 espèces, et nous avons utilisé des algorithmes d'apprentissage automatique pour grouper les étoiles en se basant sur leur composition chimique.

Résultats. Nous avons trouvé que les étoiles à des étapes d'évolution différentes ont des motifs chimiques distincts qui peuvent être dus à des effets NLTE, de diffusion atomique, de mélange et de corrélation à partir des déterminations de paramètres atmosphériques. Quand nous séparons les étoiles suivant leur stade d'évolution, nous observons qu'il y a un important degré de recouvrement dans la détermination des signatures chimiques des amas ouverts. Ceci rend difficile de retrouver les groupes d'étoiles nées ensemble en utilisant la technique de marquage chimique.

Mots clés : spectroscopie, amas ouverts, abondances chimiques, étoiles, Galaxie

Title : Testing the chemical tagging technique with Open Clusters

Abstract :

Context. Stars are born together from giant molecular clouds and, if we assume that they were chemically homogeneous and well-mixed, we expect them to share the same chemical composition.

Most of the stellar aggregates are disrupted while orbiting the Galaxy and the dynamic information is lost, thus the only possibility to reconstruct the stellar formation history is to analyze the chemical abundances that we observe today.

Aims. The chemical tagging technique aims to recover disrupted stellar clusters based merely on their chemical composition. We evaluate the viability of this technique to recover conatal stars that are not gravitationally bound anymore.

Methods. We built a high-quality stellar spectra library to facilitate the assessment of spectral analyses. We developed our own spectral analysis framework, named iSpec, capable of homogeneizing stellar spectra and deriving atmospheric parameters/chemical abundances. Finally, we compiled stellar spectra from 32 Open Clusters, homogeneously derived atmospheric parameters and 17 abundance species, and applied machine learning algorithms to group the stars based on their chemical composition. This approach allows us to evaluate the viability of the chemical tagging technique.

Results. We found that stars in different evolutionary stages have distinguished chemical patterns may be due to NLTE effects, atomic diffusion, mixing and correlations from atmospheric parameter determinations. When separating stars per evolutionary stage, we observed a high degree of overlapping among Open Cluster's chemical signatures, making it difficult to recover conatal aggregates by applying the chemical tagging technique.

Keywords : spectroscopy, open clusters, chemical abundances, stars, Galaxy

Unité de recherche

Laboratoire d'Astrophysique de Bordeaux
Observatoire Aquitain des Sciences de l'Univers (OASU, UMR 5804-LAB)
2, rue de l'observatoire - 33 271 Floirac CEDEX



Thèse préparée au
Laboratoire d'Astrophysique de Bordeaux
Observatoire Aquitain des Sciences de l'Univers (OASU, UMR 5804-LAB)
2, rue de l'observatoire
33 271 FLOIRAC CEDEX

Acknowledgements

Thanks to my family, friends and colleagues for all the support received.

Contents

Contents	9
List of Figures	15
List of Tables	21
1 Introduction	25
1.1 The universe	26
1.2 The Galaxy	27
1.2.1 Structure	28
1.2.2 Formation	28
1.2.3 Chemical evolution	29
1.3 Stars	30
1.3.1 Formation	30
1.3.2 Evolution	31
1.3.3 Clusters	31
1.4 Chemical tagging	33
1.4.1 Calibration tools	34
1.4.2 Spectroscopic analysis	35
1.4.3 Testing the chemical tagging technique	36
2 The Gaia FGK Benchmark Stars library	37
2.1 Introduction	39
2.2 Observational data	40
2.2.1 NARVAL spectra	40

2.2.2	HARPS spectra	43
2.2.3	UVES spectra	43
2.2.4	UVES-POP spectra	43
2.2.5	Atlas spectra	46
2.3	Data handling and processing	46
2.3.1	Cleaning and cosmic rays removal	46
2.3.2	Co-addition	48
2.3.3	Telluric lines	48
2.3.4	Gaps	49
2.3.5	Normalization	49
2.3.6	Resolution degradation	49
2.3.7	Merge	51
2.3.8	Radial velocity	51
2.3.9	Re-sampling	52
2.3.10	Errors	52
2.4	Validation	53
2.4.1	Normalization	53
2.4.2	Resolution	53
2.4.3	Radial velocity	57
2.4.4	Equivalent widths	57
2.5	Resulting library	63
2.5.1	Spectra	63
2.5.2	Telluric lines	63
2.6	Conclusions	64
3	Determining stellar atmospheric parameters and chemical abundances with iSpec	65
3.1	Introduction	67
3.2	Spectroscopic software framework	68
3.2.1	Data treatment	68
3.2.2	Line selection	69
3.2.3	Spectral synthesis and abundances from equivalent widths	69
3.2.4	Atmospheric parameter determination	73

3.2.5	Error estimation	75
3.3	Pipeline description and validation	76
3.3.1	Line selection	76
3.3.2	Atmospheric parameters determination	77
3.3.3	Chemical abundances	83
3.4	Additional validations	84
3.4.1	Model atmosphere interpolation	84
3.4.2	Minimization process	87
3.4.3	Signal-to-noise ratios and spectral resolutions	89
3.5	Conclusions	91
4	Testing the chemical tagging technique with Open Clusters	93
4.1	Introduction	94
4.2	Sample selection and observations	95
4.2.1	NARVAL spectra	95
4.2.2	HARPS spectra	96
4.2.3	UVES spectra	96
4.2.4	Data homogenization	96
4.3	Spectral analysis	97
4.3.1	Atmospheric parameters	97
4.3.2	Chemical abundances	98
4.3.3	Chemical outliers	100
4.4	Chemical tagging	102
4.4.1	Continuum normalization effects	102
4.4.2	Abundance and astrophysical parameter correlations	102
4.4.3	Clusters homogeneity	110
4.4.4	The role of different elements	117
4.5	Conclusions	117
5	Conclusions and perspectives	125
5.1	Conclusions	126
5.1.1	The spectral library	127
5.1.2	The spectroscopic framework	127

5.1.3	The chemical tagging technique	128
5.2	Perspectives	129
6	Conclusions et perspectives (version en français)	131
6.1	Conclusions	132
6.1.1	La librairie spectrale	133
6.1.2	L'analyse spectroscopique	133
6.1.3	La technique de marquage chimique	135
6.2	Perspectives	136
	Bibliography	139
A	iSpec User's manual	153
A.1	Introduction	154
A.2	Installation	154
A.2.1	Virtual Machine	154
A.2.2	GNU/Linux systems	158
A.2.3	MacOSX systems	160
A.3	Interactive usage	162
A.3.1	Input and output files	162
A.3.2	Execution	164
A.3.3	Basic interaction	165
A.3.4	Regions	166
A.3.5	Continuum fitting	167
A.3.6	Line fitting	169
A.3.7	Automatic continuum regions	170
A.3.8	Automatic line masks	171
A.3.9	Adjust line masks	172
A.3.10	Create segments around line masks	172
A.3.11	Barycentric velocity calculation	172
A.3.12	Velocity determination and correction	173
A.3.13	Spectroscopic binaries identification	176
A.3.14	Signal-to-Noise Ratio (SNR) estimation	177
A.3.15	Errors estimation	178

A.3.16	Add noise	178
A.3.17	Resolving power estimation	178
A.3.18	Resolution degradation	179
A.3.19	Continuum normalization	179
A.3.20	Wavelength range reduction	180
A.3.21	Apply mathematical expression	180
A.3.22	Fluxes and errors cleaning	181
A.3.23	Clean telluric regions	182
A.3.24	Spectrum resampling	183
A.3.25	Spectra combination	183
A.3.26	Interoperability with other SAMP applications	184
A.3.27	Spectral synthesis and parameter determination	186
A.4	Automatic usage	191
A.5	Bug reporting	192

List of Figures

1.1	Chemical enrichment cycle. Inspired by a presentation of Nikos Prantzos in the “GREAT ITN School: Galaxy modelling”, Besançon (France) 2012. . . .	27
1.2	Structure of the Galaxy (not to scale).	29
1.3	Chemical evolution of the Galaxy.	30
1.4	In the Hertzsprung-Russell diagram the temperatures of stars are plotted against their luminosities. The position of a star in the diagram provides information about its present stage and its mass. Stars that burn hydrogen into helium lie on the main sequence. When a star exhausts all the hydrogen, it leaves the main sequence and becomes a red giant or a super-giant, depending on its mass. Stars with the mass of the Sun which have burnt all their fuel evolve finally into a white dwarf (left low corner). Source (image and caption text): ESO (http://www.eso.org/public/images/).	32
1.5	Mean metallicity of Open Clusters per publication, as shown in Heiter et al. [2014]. A number is assigned to each open cluster (X-axis) and the measured abundances found in the literature are shown in the Y-axis.	34
2.1	Flowchart of the automatic computational process developed to build the library.	47
2.2	Normalization comparison for δ Eri (upper part) and the Sun (lower part). The spectra of reference are in black and the flux differences with the remaining observation are in blue. The regions compared correspond to the magnesium triplet (left) and H- α (right). Regions affected by tellurics were removed. . . .	55
2.3	Relative difference in FWHM (upper part) and equivalent widths (lower part) for the δ Eri spectrum, with the moving average overplotted (red) for visual guidance. The numeric details of the HARPS against NARVAL (left plot) and HARPS against UVES-POP (right plot) comparisons can be found in Table 2.10.	57
2.4	Relative differences in the equivalent width measured for the Sun by Ramírez and Allende Prieto [2011].	58

2.5	Normalized fluxes (black) and fitted Gaussians (red) for the lines with the highest relative difference in EW compared to Ramírez and Allende Prieto [2011]. The fluxes correspond to the co-added spectra of the Sun observed by NARVAL.	59
2.6	Relative differences in the equivalent width measured for Arcturus by Ramírez and Allende Prieto [2011].	60
2.7	Normalized fluxes (black) and fitted Gaussians (red) for the lines with the highest relative difference in EW compared to Ramírez and Allende Prieto [2011]. The fluxes correspond to the Arcturus spectrum observed by NARVAL.	61
3.1	Original pre-computed MARCS model atmospheres for solar metallicity (upper), complete grid with interpolated and extrapolated atmospheres (middle), and homogeneously sampled grid (lower). The color scale represents the temperature for the first model atmosphere layer.	72
3.2	Iron abundances as a function of the excitation potential with a fitted linear model (green) and outlier values (red).	75
3.3	Differences in effective temperature between the reference (the Gaia FGK benchmark stars) and the derived value by iSpec (synthetic spectral fitting method). Stars are sorted by temperature; the color represents the metallicity, and larger symbols represent lower surface gravity.	79
3.4	Differences in surface gravity between the reference (the Gaia FGK benchmark stars) and the derived value by iSpec (synthetic spectral fitting method). Stars are sorted by surface gravity; the color represents the metallicity, and larger symbols represent lower surface gravity.	80
3.5	Differences in neutral iron abundances between the reference (the Gaia FGK benchmark stars) and the derived value by iSpec, synthetic spectral fitting method (left) and equivalent width method (right) when using the atmospheric parameters found (top) and the reference values (bottom). Stars are sorted by metallicity; the color represents the temperature, and the size is linked to the surface gravity.	85
3.6	Temperature (K) as a function of mass depth (g cm^{-1}) for a computed (dotted black) and an interpolated atmosphere (solid black) from upper and lower effective temperature models (dashed red and blue) and upper and lower surface gravity models (solid red and blue).	86
3.7	Synthetic spectra using a computed (black) and interpolated (red) model atmosphere.	87
3.8	Impact on the effective temperatures and metallicity derived from synthetic spectral fitting (left) and equivalent width method (right) when fixing the surface gravity to the reference value. A linear model was fitted (red line) and the differences correspond to the constrained minus unconstrained values.	88

4.1	Dwarf (left) and giant stars (right) from all clusters represented using the first two components of the PCA with the central cluster location subtracted. Stars chemically identified as outliers are shown in red.	101
4.2	Abundances (top) and mean number of lines used (bottom) in function of species (element code at top, atomic number and ionization state in Kurucz format at bottom where '0' is neutral and '1' is ionized) for M67 dwarfs showing all the analyzed stars (left) and after filtering outliers (right). All the abundance ratios are referenced to iron except iron itself, which is relative to hydrogen. Each color represents a star with an identification name shown in the legend.	103
4.3	Hertzsprung–Russell diagram for M67 with Yonsai-Yale isochrones [3 different ages; Demarque et al., 2004], color scale corresponding to the neutral iron abundance and size represents abundance dispersion.	105
4.4	Hertzsprung–Russell diagram for M67 with Yonsai-Yale isochrones [3 different ages; Demarque et al., 2004], color scale corresponding to the silicon abundance and size represents abundance dispersion.	106
4.5	Average chemical abundances (top), dispersion (middle) and mean number of lines (bottom) used for M67 stars (left) and divided in four stellar type groups (right). All the abundance ratios are referenced to iron except iron itself, which is relative to hydrogen.	108
4.6	Abundances represented by the two first principal components. The surface gravity of each star is encoded in a color scale bar.	109
4.7	Dwarfs represented using the first two components of PCA. Background colors correspond to the clusters found by the K-Means algorithm. Centroids are marked with white crosses.	112
4.8	Giants represented using the first two components of PCA. Background colors correspond to the clusters found by the K-Means algorithm. Centroids are marked with white crosses.	113
4.9	Stellar abundances and mean number of lines used in function of species (element code at top, atomic number and ionization state in Kurucz format at bottom where '0' is neutral and '1' is ionized) for M67 and IC4651 giants. The number of neutral iron lines are not included because they outnumber significantly the rest. All the abundance ratios are referenced to iron except iron itself, which is relative to hydrogen.	114
4.10	Stellar abundances and mean number of lines used in function of species for NGC6494 and IC2714 giants. The figure format is described in the caption of the Fig. 4.9.	115
4.11	Stars represented in the PCA space using the two first principal components. The stellar ages are encoded in a color scale bar.	116
4.12	Elements' PCA weights per stellar subgroup.	118
A.1	Oracle VirtualBox website, download section (2014/03/31).	155

A.2	Open “iSpec_Xubuntu.vbox” with VirtualBox to add it to the list of virtual machines.	155
A.3	Start the virtual machine.	156
A.4	Virtual machine running iSpec with a solar spectrum.	156
A.5	Access to the virtual machine settings.	157
A.6	Add a shared folder between the real and virtual machine.	157
A.7	Access to a shared folder from the virtual machine.	157
A.8	Test execution script which allows to view 5 different stars.	159
A.9	iSpec showing several spectra.	159
A.10	MacPorts installation	161
A.11	Empty editor.	164
A.12	Multiple spectra: the active one is marked with an “[A]” in the legend.	165
A.13	Show errors in plot.	165
A.14	From left to right: Home button, back/forward arrows, Pan mode and Zoom mode.	166
A.15	Actions and elements.	167
A.16	Properties for the fitting of the continuum.	168
A.17	Continuum fitting algorithm.	169
A.18	Properties for fitting lines.	169
A.19	Continuum and lines fitted.	170
A.20	Properties for the automatic mechanism of finding continuum regions.	171
A.21	Properties for the automatic mechanism of finding line masks.	171
A.22	Properties for the automatic mechanism of finding line masks.	172
A.23	Properties for the automatic mechanism of finding line masks.	172
A.24	Barycentric velocity determination and correction.	172
A.25	Velocity determination by using atomic/telluric lines or a template.	173
A.26	Mask for cross-correlation. iSpec permits to choose the mask size in velocity and the minimum depth.	175
A.27	Velocity profile.	176
A.28	Cross-match correlation determined by ELODIE and iSpec for HD005516A spectroscopic binary	177
A.29	Properties for the global SNR estimation.	178
A.30	Properties for the global SNR estimation.	178
A.31	Add Poisson noise given a SNR.	178

A.32 Resolution degradation properties	179
A.33 Wavelength range reduction properties	180
A.34 Apply a mathematical expression to the active spectrum	181
A.35 Filter out all the measurements that are not in these range limits.	182
A.36 Filter out all the measurements potentially affected by telluric lines.	182
A.37 Properties for spectrum resampling. Some basic statistics of the active spectrum are printed next to the wavelength step field in order to have a point of reference.	183
A.38 Spectra combination properties	183
A.39 TOPCAT SAMP hub with different programs already connected	184
A.40 iSpec “Send spectrum to...” option	184
A.41 TOPCAT with data sent from iSpec	185
A.42 Splat with data sent from iSpec	185
A.43 VOSpec with data sent from iSpec	186
A.44 Properties for synthetic spectrum generation	188
A.45 Properties for determining astrophysical parameters	189
A.46 Output with the determined astrophysical parameters.	189
A.47 Properties for the chemical abundance determination	190
A.48 Chemical abundance determination	190

List of Tables

2.1	List of the high-resolution spectra available per benchmark star and instrument.	41
2.2	Spectra observed with the NARVAL spectrograph (average resolving power of $\sim 81,000$).	42
2.3	Spectra observed with the HARPS instrument (average resolving power of $\sim 115,000$).	44
2.4	Spectra observed with the UVES instrument.	45
2.5	Spectra observed with the UVES instrument and processed by the UVES-POP pipeline (average resolving power of 80,000).	45
2.6	Parameters used for the spectral synthesis in the normalization process.	50
2.7	Average RMS difference in flux for the normalized spectra of the same star but observed by different instruments.	54
2.8	Mean RMS differences in flux for atlas spectra and our normalized spectra observed by different instruments.	54
2.9	Mean difference between expected and measured FWHM in km/s (see Eq. 2.10) and mean estimated original resolving power with their corresponding standard deviation.	56
2.10	Difference in FWHM and equivalent widths between HARPS observations and the other instruments.	56
2.11	Relative EW differences with external measurements [Ramírez and Allende Prieto, 2011, Luck and Heiter, 2006, 2007].	62
3.1	Standard abundance composition for pre-computed MARCS model atmospheres.	71
3.2	Synthetic spectral grid for determining the initial parameters. The rotation ($v \sin(i)$) was fixed to 2 km s^{-1} and the micro/macroturbulence was calculated by using the same empirical relation as in Blanco-Cuaresma et al. [2014b].	77

3.3	Average difference and standard deviation (left) between the synthetic spectral fitting technique and the reference values. Average dispersion (right) for stars with multiple observed spectra.	81
3.4	Difference between the parameters derived from the two methods and the reference values (neutral iron abundance is used as a proxy for metallicity). For stars with several observed spectra, the difference corresponds to the average, and the standard deviation is also reported.	82
3.5	Average difference and standard deviation (left) between the equivalent width method and the reference values. Average dispersion (right) for stars with multiple observed spectra.	83
3.6	Average difference and standard deviation (left) between the derived parameters and the reference values. Average dispersion (right) for stars with multiple observed spectra.	84
3.7	Average differences and standard deviation between the iron abundances derived from the two methods and the reference values (LTE and NLTE).	84
3.8	Difference between the parameters derived from the two methods and the reference values on each iteration of the least-squares minimization process. The number of converged spectra per iteration is also included (78 in total).	89
3.9	Linear model parameters ($y = mx + c$) fitted using the differences on the effective temperatures/metallicity and free or fixed surface gravity shown in Fig. 3.8. The Pearson correlation coefficients are also included.	89
3.10	Difference between the parameters derived from the two methods (using degraded synthetic spectra instead of observations) and the reference values for different levels of signal-to-noise ratio (S/N). The synthetic spectra had a resolution of 70,000.	90
3.11	Difference between the parameters derived from the two methods (using synthetic spectra) and the reference values for different resolution levels. The synthetic spectra had a signal-to-noise ratio of 100. From lower to higher resolution, they approximately correspond to the surveys SDSS DR7 (R=1800-2200), Rave, Gaia RVS, GES Giraffe HR21, APOGEE, HERMES/GALAH, GES UVES and the standard resolution of the Gaia FGK benchmark stars library.	90
4.1	List of analyzed clusters with the number of co-added spectra per instrument and other known cluster properties from the literature.	99
4.2	Iron abundances from neutral lines when using two slightly different normalization processes and comparison to literature metallicities.	104
4.3	Chemical differences for M67 and IC4651 stars in different evolutionary stages.	107
4.4	Clustering metrics for different stellar groups and dimensions.	111
4.5	Clusters found for dwarf stars and their real open clusters.	117
4.6	Clusters found for giant stars and their real open clusters.	120

4.7	Weighted mean abundances and dispersion per cluster and stellar subgroup.	121
4.7	Continued.	122
4.8	Weighted mean abundances and dispersion per cluster.	123
A.1	Astrophysical paramters for the 5 very well-known stars included	160
A.2	Combination of actions and elements	167
A.3	MARCS Standard abundance composition	187

Chapter 1

Introduction

Contents

1.1	The universe	26
1.2	The Galaxy	27
1.2.1	Structure	28
1.2.2	Formation	28
1.2.3	Chemical evolution	29
1.3	Stars	30
1.3.1	Formation	30
1.3.2	Evolution	31
1.3.3	Clusters	31
1.4	Chemical tagging	33
1.4.1	Calibration tools	34
1.4.2	Spectroscopic analysis	35
1.4.3	Testing the chemical tagging technique	36

1.1 The universe

We can consider galaxies as the major building blocks of the universe. Charles Messier created the first catalogue in 1781 but, at that time, they were named nebulae objects since they were considered to belong to our own Galaxy. In 1845, Lord Rosse constructed a new telescope and was able to distinguish a range of morphologies, from elliptical to spiral nebulae. The latter were considered small proto-planetary disks located in the Galaxy by some astronomers, while others claimed they really were distant objects outside our Galaxy. The controversy existed as late as 1920, when Edwin Hubble showed that the Andromeda Nebula must reside well outside our Galaxy by measuring its distance thanks to the characteristic variation in the brightness of Cepheid variable stars.

In 1936, Hubble produced a classification system for galaxies based on their morphology. It is mainly composed by ellipticals (E), lenticulars (S0) and spirals (S) galaxy types. Today we know that galaxies are massive gravitationally-bound systems composed of stars, interstellar medium and dark matter. Spiral and irregular late-type galaxies have younger stellar populations (less than 10 Gyr¹), and they present active star formation in a rotating disk of gas and dust. Elliptical and lenticular galaxies contain old (more than 10 Gyr) stellar population and very little interstellar material.

There are probably more than 170 billion galaxies in the observable universe and they can range from dwarfs with as few as ten million stars (10^7) to giants with more than one hundred trillion stars (10^{14}). The galaxies that conform all this cosmic structure were born thanks to the small quantum fluctuations in the early hot and dense universe, about 13.8 billion years ago. These fluctuations were magnified into bigger over-density regions during the inflationary stage, as proposed in 1980 by the physicist Alan Guth, where the universe suffered an exponential expansion of space in a very short time scale between the 10^{-36} and 10^{-32} seconds after the Big Bang. The over-density regions and the force of gravity allowed the gas (mainly composed by hydrogen, helium and traces of lithium created by the primordial nucleosynthesis²) to coalesce into large clumps, forming the first generation of stars that were also gravitationally attracted into larger groups.

The first stars synthesized heavier elements³ through the nuclear fusion processes that take place in their interior. When the stars reached the final phase of its evolution, the internal processed material was ejected via stellar wind or through supernovae depending on their stellar mass, enriching the interstellar medium (ISM). The subsequent generations of stars were born from enriched clouds and continued to produce heavier elements. The full cycle is still an ongoing process, where new stars are still born nowadays (see Fig. 1.1).

1. 1 Gyr (gigayears) equals a billion years (10^9 years).

2. Also named Big Bang nucleosynthesis or BBN

3. The terms metals and heavy elements refers to all elements heavier than helium.

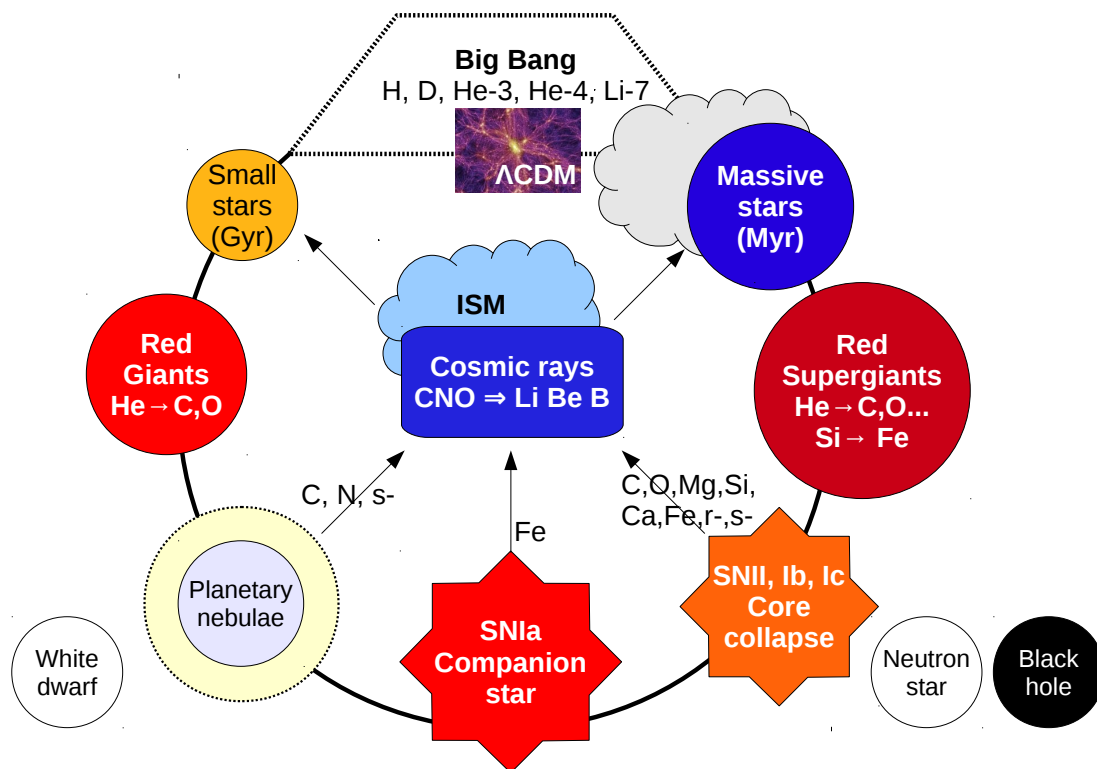


Figure 1.1 – Chemical enrichment cycle. Inspired by a presentation of Nikos Prantzos in the “GREAT ITN School: Galaxy modelling”, Besançon (France) 2012.

The simplest model that is in general agreement with the observed cosmic structure is the Λ Cold Dark Matter cosmology (Λ CDM), where the main driver for the formation of the galaxies is gravity and dark matter (which represents 23% of the current content of the universe). Under this model, dark matter halos envelop galaxies dominating the total mass and extending beyond the edge of the visible matter [Navarro et al., 1996]. Nevertheless, since they consist of dark matter, halos cannot be observed directly but their existence is inferred through, for instance, their effects on the motions of stars and gas in galaxies (i.e. rotation curve of spiral galaxies).

The rest of the content of the universe is made up of dark energy (72%) and baryonic matter (4.6%). The former is an hypothetical form of energy for which there is no direct observational evidences (as for dark matter) but it is necessary to explain phenomena such as the accelerated expansion of the universe. The latter is mainly found in the intergalactic medium, interstellar clouds, stars, and planets. For instance, the human body is made up of 65% of oxygen, 18% of carbon, 10% of hydrogen, and other heavier elements that were produced in the interior of the stars.

1.2 The Galaxy

Our Galaxy, the Milky Way, appears as a band in the night sky because we observe its disk-shaped structure from within the same Galaxy. It represents an unique laboratory where different lines of research converge (such as dynamics, astrometry, star formation and evolution,

chemical evolution, and interstellar medium) and theories can be tested (e.g. structure formation at galactic and cosmic levels).

1.2.1 Structure

Today we know that the Milky Way is a spiral galaxy and it has several structural components that appeared at different stages in the formation process (see Fig. 1.2): the bulge, the thin and thick disk and the stellar halo [Carollo et al., 2007, Feltzing and Chiba, 2013].

The bulge is located in the inner part of the Galaxy. It is a dense concentration of mostly old stars in a roughly spheroidal shape around the super-massive central black hole [Minniti and Zoccali, 2008]. It probably formed in a series of starbursts about 12 Gyr ago [Zoccali et al., 2006, Lee, 2007]. The stellar population is metal poor, although enough gas and dust are still being drawn in from outlying regions by gravitational attraction towards the massive galactic core and new stars can still be born. Hence, there is also a population of metal-rich globular clusters around the galactic center [Minniti, 1996].

The stellar halo (spheroid) surrounds the whole Galaxy and it is composed by very old and very metal poor stars, stellar remnants (e.g., white dwarfs), globular clusters and satellite galaxies that were captured gravitationally.

Stellar formation is still occurring in the thin disk where its oldest stars are about 10 Gyr old [Wyse, 2009] and the more metal rich stars reside in the inner part. Freeman and Bland-Hawthorn [2002] present the thin disk as the end product of the quiescent dissipation of most of the baryons and contains almost all of the baryonic angular momentum. The stellar density follows an exponential with a vertical scale height of about 300 pc [Chang et al., 2011].

The thick disc was discovered by Gilmore and Hewett [1983] and it is formed by stars older than 10 Gyr. In terms of metallicity⁴, stars are at an intermediate level between the thin disc and the stellar halo. Its scale height is about 900 pc [Jurić et al., 2008] and its origin is still an open question.

In the disk, there are higher densities regions of interstellar gas, dust and stars that correspond to the spiral arms. Due to the difficulty of studying our own Galaxy from within it, it is still not completely clear if there are 4 or 2 arms present [Englmaier et al., 2011] although more studies support the former option.

1.2.2 Formation

The age of our galaxy is approximately 13.6 Gyr and its formation is traditionally explained by two different scenarios:

1. Top-down model: A rapid monolithic collapse of a proto-galactic gas cloud to form the halo, followed by a galactic disk formation as the residual gas dissipationally collapsed

4. Proportion of matter made up of chemical elements other than hydrogen and helium compared to the Sun. The iron abundance is used a proxy for the metallicity and the most common representation is: $[Fe/H] = \log_{10} \left(\frac{N_{Fe}}{N_H} \right)_{star} - \log_{10} \left(\frac{N_{Fe}}{N_H} \right)_{sun}$ where N_{Fe} and N_H are the number of iron and hydrogen atoms per unit of volume respectively. The unit frequently used for metallicity is the "dex" (decimal exponent).

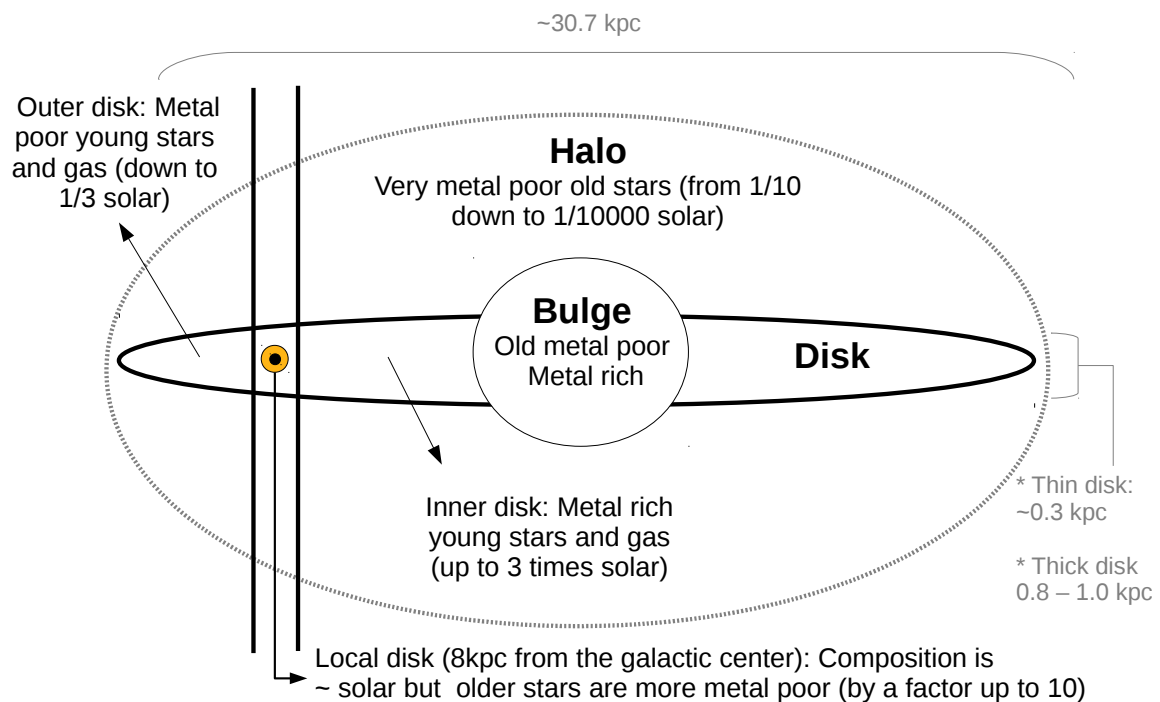


Figure 1.2 – Structure of the Galaxy (not to scale).

[[Eggen et al., 1962](#)]. This would explain an old metal poor stellar population in the halo and a younger metal rich in the galactic plane.

2. Bottom-up model: Small cloud fragments, where stars were already formed, are merged together creating bigger hierarchical structures [[Searle and Zinn, 1978](#)]. This would explain the higher number of small sized galaxies in our universe. We also observe galaxies that are gravitationally bounded in clusters and, in some cases, there are ongoing merging processes. For instance, our Galaxy will be merged in about 5-6 Gyr with the Andromeda galaxy [[van der Marel et al., 2012](#)].

Other plausible scenarios might be somewhere in between both scenarios. The stellar chemical composition is a key component that can help us unravel the history of our Galaxy.

1.2.3 Chemical evolution

The chemical composition of the galaxy is enriched with time depending on the star formation rate, the chemical yields, the efficiency of recycling, gas infall and outflow from/to the intergalactic medium, and the amount of mixing in the gas (see Fig. 1.3). Thus, it is generally expected that old stars are more metal poor than younger ones.

Understanding the chemical abundance distribution in the Galaxy and establishing a link with stellar ages can lead to a better understanding of the formation history of the Galaxy. However, age and accurate chemical abundance determinations are not trivial tasks since high-quality observations and sophisticated models for stellar physics are required.

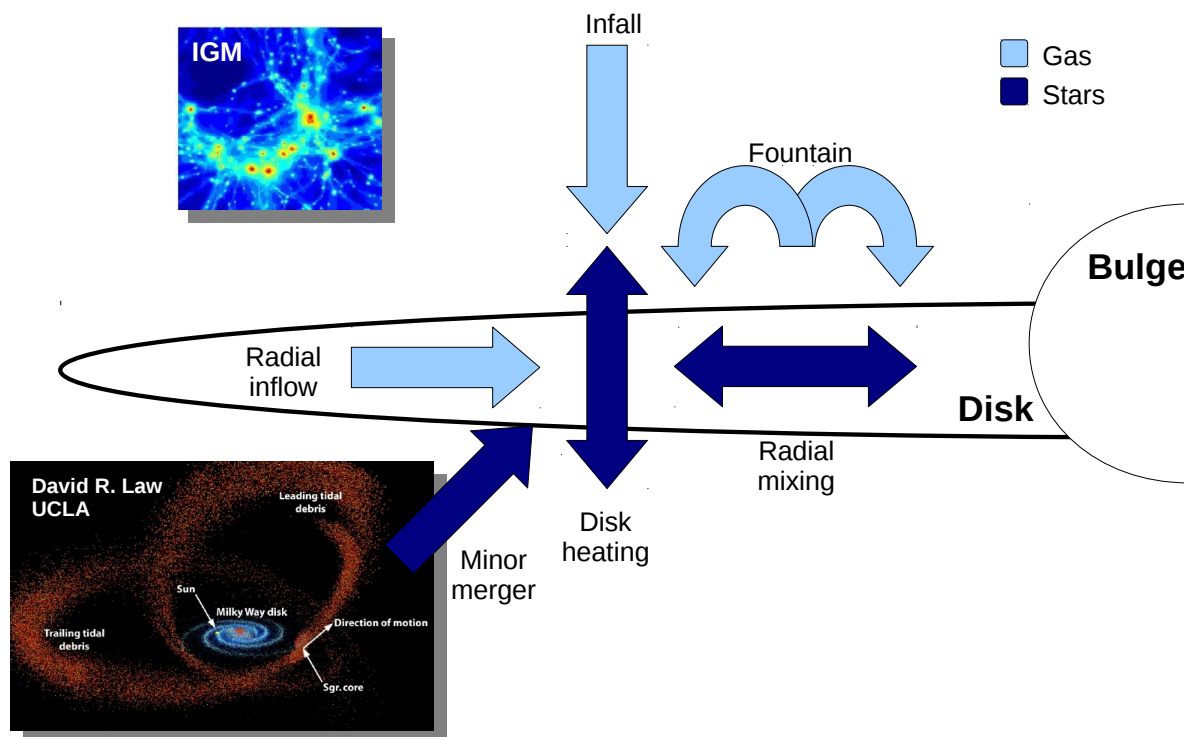


Figure 1.3 – Chemical evolution of the Galaxy.

1.3 Stars

If galaxies are the major building blocks of the universe, the stars are the building block of the galaxies and the key to understand the galactic history.

1.3.1 Formation

Stars are born in aggregates from molecular clouds as supported by many studies [Shu et al., 1987, Meyer et al., 2000, Lada and Lada, 2003, McKee and Ostriker, 2007]. Theoretical hydrodynamical simulations indicate that the progenitor cloud undergoes fragmentation preventing contraction onto a single star [Jappsen et al., 2005, Tilley and Pudritz, 2004, Larson, 1995]. Hundreds to thousands of stars can be formed from one single cloud.

Over time, most of the stellar aggregates will be disrupted by, for instance, the gravitational influence of giant molecular clouds, spiral arms or even external events as they move through the galaxy. We can still observe some gravitationally unbound group of stars that clearly share the same direction through space, these stellar associations are usually referred as moving groups and they probably are former clusters in process of disruption. Fortunately, some of the clusters managed to overcome the disruption process and today we observe them still gravitationally bound.

1.3.2 Evolution

In 1910, Ejnar Hertzsprung and Henry Norris Russell created the Hertzsprung–Russell diagram (or HR diagram, see Fig. 1.4) where stars are represented in function of their absolute magnitude (or luminosity) and the spectral type (or color indices). It represented a major step forward in the understanding of stellar evolution since it showed that only certain areas of the diagram were populated with stars (e.g. the main sequence, red giant branch, super-giants, white dwarfs).

Stars born with masses between 1 - 8 M_{\odot} spent most of their lifetime on the main sequence where they irradiate energy due to reactions that convert hydrogen into helium by nuclear fusion. Depending on the initial mass of the star, this process happens through the p-p chain or the CNO cycle.

While the star is in the pre-main sequence phase, it is still chemically homogeneous because of the internal convection. But when the star reaches the main sequence phase (i.e. the nuclear engine is ignited), it starts developing a chemical gradient with increasing helium abundance in the centre.

With time, a helium core is slowly formed and, since it still does not produce nuclear reactions to compensate the gravity pull, the inner layers initiate its contraction to maintain the hydrostatic equilibrium. Hydrogen fusion is then accelerated provoking the expansion of the outer envelope of the star, increasing its radius and reducing its effective temperature. At this stage, the star evolves towards the red giant branch (RGB) in a relatively fast timescale.

The core of red-giant-branch stars slow down the collapse when it is dense enough to be supported by the electron degeneracy pressure, leaving a helium core, a buffer convective shell and an outer shell burning hydrogen. During this phase, the outer convective shell can dredge up freshly processed material (i.e. mixing process) and original material that was sunk by gravity during the main sequence phase (i.e. atomic diffusion). As a result, the chemical composition of the atmosphere is restored with the original abundances from the progenitor molecular cloud and enriched with the products of the H-burning.

While hydrogen continues to be consumed in a shell, the helium core contracts until it reaches the critical temperature to start the helium burning. If the helium core is in a complete degenerate state (typically $M < 2.3 M_{\odot}$), the core may experience a fast and explosive ignition named “the helium flash”. The next phase is the horizontal branch (HB) where the star burns helium in the core via the triple- α process and hydrogen in a shell separated from the core by a convective buffer. The star slowly ascends the asymptotic giant branch (AGB) and when it reaches the top, it goes through a super-wind phase where the material of outer layers leaves the star.

Eventually, the ejected material is ionized by the stellar radiation giving birth to a planetary nebula. When all the fuel is consumed, the star enters the white dwarf stage and it slowly cools down losing all the energy gain in the last evolutionary stages.

1.3.3 Clusters

Clusters may contain from few dozens to thousands of stars and they generally classified in two types: Globular clusters are larger and denser, they are generally old and are mainly found

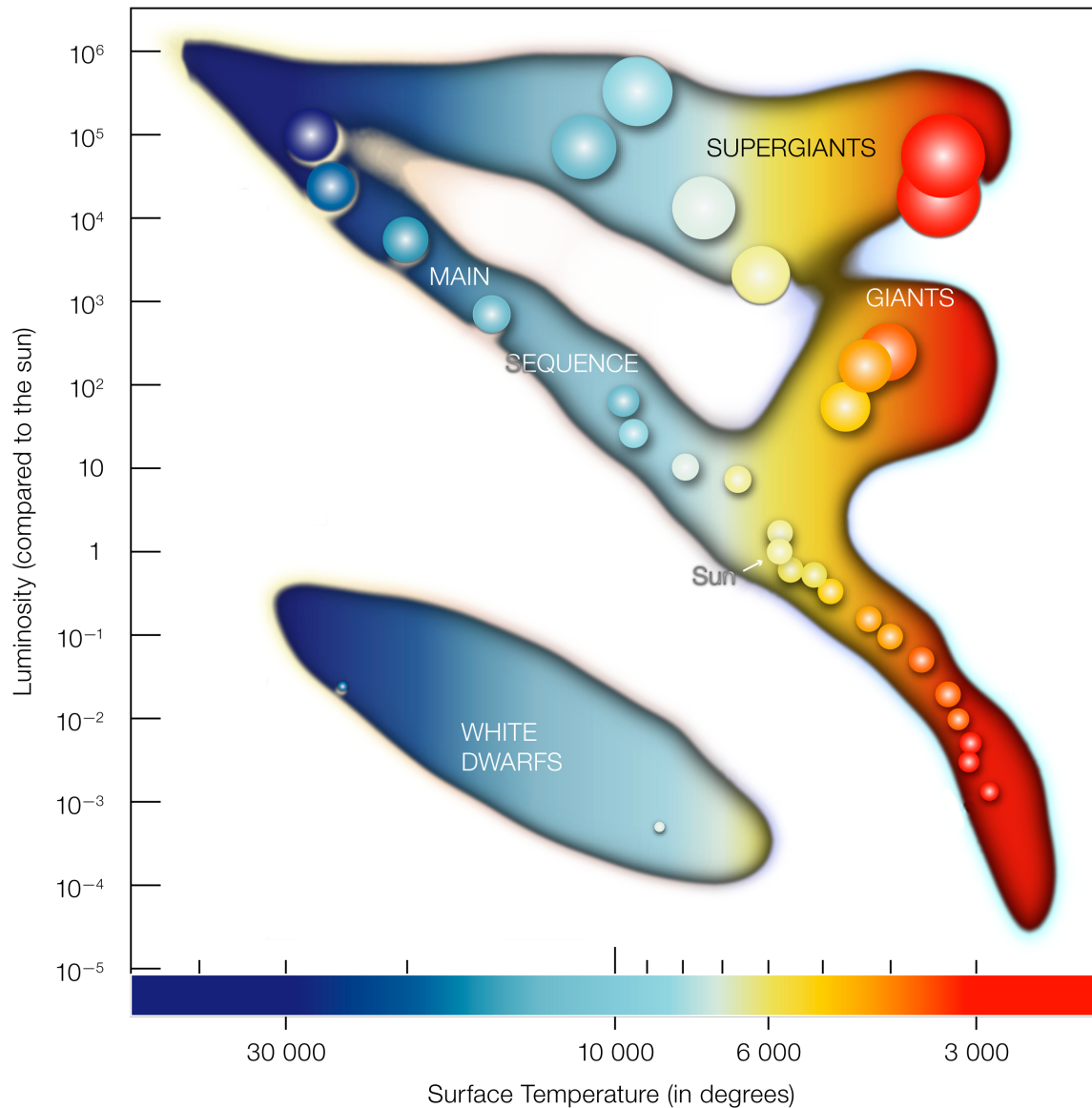


Figure 1.4 – In the Hertzsprung-Russell diagram the temperatures of stars are plotted against their luminosities. The position of a star in the diagram provides information about its present stage and its mass. Stars that burn hydrogen into helium lie on the main sequence. When a star exhausts all the hydrogen, it leaves the main sequence and becomes a red giant or a super-giant, depending on its mass. Stars with the mass of the Sun which have burnt all their fuel evolve finally into a white dwarf (left low corner). Source (image and caption text): ESO (<http://www.eso.org/public/images/>).

in the halo; Open clusters contain typically $\sim 10^2$ to 10^4 members, they are young with ages ranging from a few Myr to several Gyr [Friel, 1995] and they are located mainly in the galactic disk.

Since open clusters have much lower densities, it is easier to resolve individual stars and study their properties. They are also believed to be a good tracers of the Galactic disk, where most of the stellar formation takes place [Bonatto et al., 2006]. We know more than a thousand open clusters [Brown, 2001, Dias et al., 2002] in our Galaxy, but it is estimated that the total number should go up to 10^5 [Piskunov et al., 2006].

Old clusters are primarily found at higher vertical distances and large galactic radii. These regions further from the plane offer an advantageous position to survive the disruption process. However, a selection effect might be also present since it is much easier to detect them in those areas. On the other hand, young clusters are expected to be near spiral arms since most of the star formation in our Galaxy takes place in those denser regions [Dias and Lépine, 2005].

1.4 Chemical tagging

Understanding the formation and evolution of galaxies and their structure (e.g. disks) is an outstanding problem in near-field cosmology. One approach to tackle this problem is to study our own Galaxy by unravelling the sequence of events that took place in the formation of the Galactic disk (where most star formation occurs).

Unfortunately, as seen in Section 1.2, most of the dynamical information is already lost since the disk was formed in a dissipative process and it evolved dynamically. Nevertheless, the chemical composition of the stars can potentially help us to recover the history of our Galaxy.

Since stars are born in groups from giant molecular clouds (see Section 1.3), if we assume that they are chemically well-mixed, then we expect them to have a homogeneous chemical composition. With this information, we could use the method of chemical tagging to track individual stars back to their common formation sites as proposed by Freeman and Bland-Hawthorn [2002].

The viability of this approach depends on two critical issues: Do stars born together have a unique chemical signature? And, are the chemical signatures different enough among stars formed from different molecular clouds? The final goal of this work is to give an answer to those questions.

We can derive the chemical composition of stars (among other properties such as effective temperature or surface gravity) by studying their stellar spectrum of electromagnetic radiation. Previous spectroscopic studies have tried to answer those questions but they were based on a limited amount of observations [e.g. De Silva et al., 2006] or on non-homogeneous determined abundances found in the literature [e.g. De Silva et al., 2009]. The use of different spectral analysis methods (e.g. equivalent width or synthetic spectral fitting), atomic data, model atmospheres and continuum normalization processes can lead to systematic errors. For instance, Heiter et al. [2014] showed the dispersion found in the literature for the iron abundance of different open clusters (see Fig. 1.5).

To reduce differences among studies, it is important to have tools that help us to assess

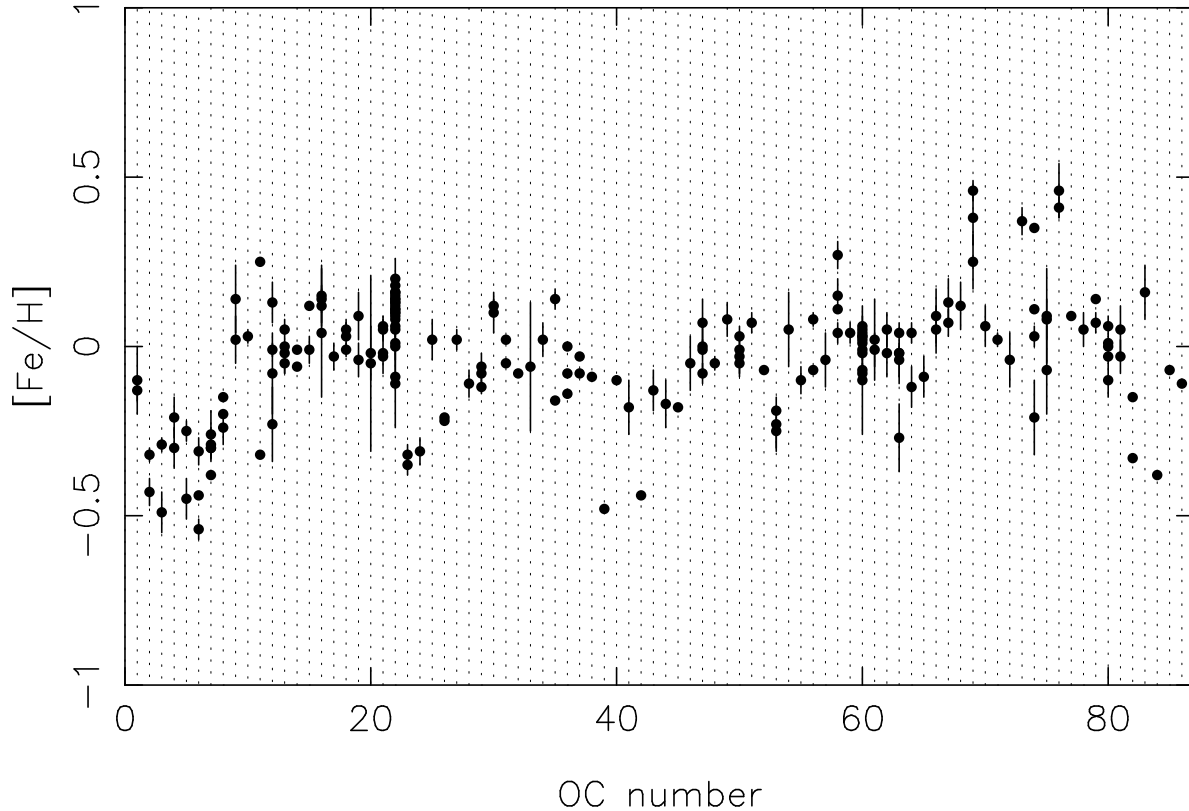


Figure 1.5 – Mean metallicity of Open Clusters per publication, as shown in Heiter et al. [2014]. A number is assigned to each open cluster (X-axis) and the measured abundances found in the literature are shown in the Y-axis.

the results and limit systematic errors. We developed those tools for this work by: creating a high-resolution spectral library for calibration and assessment purposes; and an automatic code to derive atmospheric parameters and chemical abundances.

1.4.1 Calibration tools

There are several stellar spectral libraries available in the community that are used for calibration in some sense [see, e.g., Munari and Sordo, 2005, for a compilation], providing a large sample of good spectra of stars covering a large part of the HR diagram and metallicities. Examples of them are ELODIE [Prugniel and Soubiran, 2001], Indo-US [Valdes et al., 2004], MILES [Sánchez-Blázquez et al., 2006], StarCAT [Ayres, 2010], and UVES-POP [Bagnulo et al., 2003]. These libraries contain a large number of stars (usually above 1,000) and they differ from each other in terms of resolution and wavelength coverage. They are frequently used for stellar population synthesis models and galactic studies [e.g., Vazdekis et al., 2012, Percival et al., 2009, Zhang et al., 2005, and references therein] and for calibration or validation of methods that determine stellar parameters from stellar spectra [e.g. Allende Prieto et al., 2008b, Koleva et al., 2009, Wu et al., 2011]. Nevertheless, the Sun is frequently the only calibration star in common between different methods/surveys and, depending on the survey, its observation is not always possible.

It was necessary to define a common set of very well-known calibration stars beyond the Sun, covering different regions of the HR diagram and spanning a wide range in metallicity.

We selected 34 very well-known stars and we named the sample as the Gaia FGK benchmark stars since they will be used as pillars for the calibration of the parameters that will be derived for one billion stars by Gaia [Perryman et al., 2001].

Gaia will implement a two-level procedure to estimate stellar effective temperatures, surface gravities and metallicities where the 34 Gaia benchmark stars are at the first level [Bailer-Jones et al., 2013]. For this first group of stars, their Hipparcos parallaxes, angular diameters and bolometric fluxes are known, and their masses have been determined in a homogeneous way, so their effective temperatures and surface gravities can be derived independently of spectroscopy (Heiter et al., in prep.). The reference metallicities needed to be determined from ground-based spectra, thus we compiled a homogeneous library of high-resolution and signal-to-noise spectra and derived the reference metallicity as explained in Jofré et al. [2014]. At the second level, Gaia will use a much larger sample of several hundred reference stars with parameters derived from spectra and calibrated with the stars of the first level (i.e. the Gaia benchmark stars).

The Gaia FGK Benchmark Star library is also a very valuable tool to assess and optimize spectroscopic pipelines. In Chapter 2 we describe the creation process of the library and the verification tests that we performed to ensure its quality.

1.4.2 Spectroscopic analysis

If we want to be ready to analyze the vast amount of spectra being observed by massive surveys such as the Gaia ESO survey [GES, Gilmore et al., 2012, Randich et al., 2013] and the future HERMES/GALAH [Freeman, 2010], we need to almost eliminate human interventions in the analysis chain (e.g. manual continuum and/or line fitting), reducing dependence on subjective criteria and facilitating the execution of homogeneous analysis. We developed a code capable of analyzing high-resolution and high signal-to-noise spectra in a complete automatic fashion. Some of its features include:

1. Homogenize observations from different instruments:
 - (a) **Cosmic rays removal:** Spectra may contain residuals from cosmic rays which are automatically detected by using a median filter to smooth out single flux deviations.
 - (b) **Continuum normalization:** The continuum points of a spectrum are found by applying a median and maximum filter with different window sizes. Afterwards, a polynomial or group of splines can be used to model the continuum and finally normalize the spectrum by dividing all the fluxes by the model.
 - (c) **Resolution degradation:** The spectral resolution can be degraded by convolving the fluxes with a Gaussian of a given FWHM (km/s).
 - (d) **Radial velocity:** By cross-correlating [Allende Prieto, 2007] the spectrum with a mask or template (e.g. observed or synthetic), the radial velocity of the star can be derived and corrected.
 - (e) **Telluric lines identification:** Telluric lines from Earth's atmosphere contaminate ground-observed spectra and it can affect the parameter determination. Their position in the spectra can be determined by cross-correlating with a telluric mask build from a synthetic spectrum (thanks to TAPAS Bertaux et al. 2013).

- (f) **Resampling:** Spectra can be re-sampled by using linear (2 points) or Bessel (4 points) interpolation [Katz et al., 1998].
2. Derive atmospheric parameters and individual chemical abundances using two different techniques:
- (a) **Synthetic spectral fitting technique:** iSpec compares an observed spectrum with synthetic ones generated on the fly, in a similar way as Spectroscopy Made Easy (SME) tool does [Valenti and Piskunov, 1996]. A least-squares algorithm (Levenberg-Marquardt implementation) minimizes the difference between the synthetic and the observed spectra in order to converge towards the closest synthetic spectrum. In each iteration, the algorithm will vary each one of the free parameters at a time and prognosticate in what direction it should move to find the solution. Specific regions of the spectrum can be selected to minimize the computation time and focus onto the most relevant parts to better identify stars (i.e. wings of H- α /MgI triplet, Fe I/II lines).
- (b) **Equivalent widths method:** Gaussian models are fitted for a given list of Fe I/II lines, from their integrated area we can derive their respective equivalent width and thus their abundances. The algorithm for determining the atmospheric parameters is a least-squares technique (as explained above) based on the assumption of excitation and ionization equilibrium, similar to GALA [Mucciarelli et al., 2013] and FAMA [Magrini et al., 2013].

In Chapter 2 we describe the homogenization features that were used in the creation of the Gaia benchmark star library. The functionalities linked to the atmospheric parameter and chemical abundances determination are detailed in Chapter 3, where we also take advantage of the Gaia benchmark stars library to verify and improve our code. A methodologically comparison of different popular spectral analysis techniques, model atmospheres and atomic line lists is presented.

1.4.3 Testing the chemical tagging technique

We recall that the goal of this work is to test the chemical tagging technique by answering this two critical issues: Do stars born together have an unique chemical signature? And, are the chemical signatures different enough among stars formed from different molecular clouds?

As seen in Section 1.3, open clusters are the leftovers of star forming aggregates in the Galactic disk that have managed to survive until the present day. We can be certain that their birth took place from the same molecular cloud at roughly the same period. Thus we can use our developed tools to automatically and homogeneously derive chemical abundances for a extensive group of open clusters' stars. We tested the limits of the chemical tagging technique by applying machine learning algorithms that try to blindly reconstruct the original clusters from only the chemical information. The results are presented in Chapter 4.

The Gaia FGK Benchmark Stars library

Paper published in Astronomy & Astrophysics [Blanco-Cuaresma et al., 2014b]. The co-authors contribution was mainly linked to the selection of Benchmark Stars, the determination of the reference parameters, the compilation of spectra from public archives, and they also proposed and carried out dedicated observing programs. I developed the tools needed to homogenize the spectra, designed the automatic transformation pipeline and the different quality verification tests.

Contents

2.1	Introduction	39
2.2	Observational data	40
2.2.1	NARVAL spectra	40
2.2.2	HARPS spectra	43
2.2.3	UVES spectra	43
2.2.4	UVES-POP spectra	43
2.2.5	Atlas spectra	46
2.3	Data handling and processing	46
2.3.1	Cleaning and cosmic rays removal	46
2.3.2	Co-addition	48
2.3.3	Telluric lines	48
2.3.4	Gaps	49
2.3.5	Normalization	49
2.3.6	Resolution degradation	49
2.3.7	Merge	51
2.3.8	Radial velocity	51
	Zero point template	51
	Cross-correlation	51
2.3.9	Re-sampling	52
2.3.10	Errors	52
2.4	Validation	53
2.4.1	Normalization	53

2.4.2	Resolution	53
2.4.3	Radial velocity	57
2.4.4	Equivalent widths	57
	External consistency	58
	Internal consistency	63
2.5	Resulting library	63
2.5.1	Spectra	63
2.5.2	Telluric lines	63
	Gap regions	63
2.6	Conclusions	64

2.1 Introduction

Investigations into how the Milky Way is formed and its evolution are being revolutionized thanks to the many ongoing stellar spectroscopic surveys such as SDSS [York et al., 2000], LAMOST [Zhao et al., 2006], RAVE [Steinmetz et al., 2006], Gaia [Perryman et al., 2001], Gaia-ESO [GES, Gilmore et al., 2012], HERMES/GALAH [Freeman, 2010] and APOGEE [Allende Prieto et al., 2008a]. Tracing the chemical and dynamical signatures of large samples of stars helps us to distinguish the different Galactic components and thus understand when and how the different Galactic formation scenarios took place. The quantity of spectroscopic data available today requires the development of automatic spectral analysis. Numerous methods have been developed over the past years [e.g., Valenti and Piskunov, 1996, Katz et al., 1998, Recio-Blanco et al., 2006, Lee et al., 2008, Koleva et al., 2009, Jofré et al., 2010, Posbic et al., 2012, Mucciarelli et al., 2013, Magrini et al., 2013, to name a few] to assess large datasets, where each of them have different approaches to calibrate and evaluate their results.

However, each survey has its own setup (e.g., spectral range, resolution) and each spectral analysis code has its own particularities (i.e., continuum normalization, atomic line lists). The consequence is that the resulting parameters cannot be directly combined and used for galactic and stellar studies. Thus, spectroscopic calibration with a common reference set of stars is required.

There are several stellar spectral libraries available in the community that are used for calibration in some sense [see, e.g., Munari and Sordo, 2005, for a compilation], providing a large sample of good spectra of stars covering a large part of the Hertzsprung-Russel (HR) diagram and metallicities. Examples of them are ELODIE [Prugniel and Soubiran, 2001], Indo-US [Valdes et al., 2004], MILES [Sánchez-Blázquez et al., 2006], StarCAT [Ayres, 2010], and UVES-POP [Bagnulo et al., 2003]. These libraries contain a large number of stars (usually above 1,000) and they differ from each other in terms of resolution and wavelength coverage. They are frequently used for stellar population synthesis models and galactic studies [e.g., Vazdekis et al., 2012, Percival et al., 2009, Zhang et al., 2005, and references therein] and for calibration or validation of methods that determine stellar parameters from stellar spectra [e.g. Allende Prieto et al., 2008b, Koleva et al., 2009, Wu et al., 2011]. Nevertheless, the Sun is frequently the only calibration star in common between different methods/surveys and, depending on the survey, its observation is not always possible.

Our motivation for defining the Gaia FGK benchmark stars is to provide a common set of calibration stars beyond the Sun, covering different regions of the HR diagram and spanning a wide range in metallicity. They will be used as pillars for the calibration of the parameters that will be derived for one billion stars by Gaia [Perryman et al., 2001]. The defining property of these stars is that we know their radius and bolometric flux, which allows us to estimate their effective temperature and surface gravity *fundamentally*, namely, independent of the spectra. In Heiter et al (in prep, Paper I), we provide the main properties of our sample of the Gaia FGK benchmark stars and describe the determination of temperature and gravity. In this article (Paper II), we introduce the spectral library of the Gaia FGK benchmark stars. In Jofré et al. [2013, Paper III], we analyse our library with the aim to provide a homogeneous scale for the metallicity.

The current sample of Gaia benchmark stars is composed of bright, well-known FGK dwarfs, subgiants, and giants with metallicities between solar and -2.7 dex. We selected stars for which angular diameter and bolometric flux measurements are available or possible. They have accurate parallax measurements, mostly from the HIPPARCOS mission. The sample contains several visual binary stars. In particular, both the A and B components are included for the α Cen and the 61 Cyg systems. The star η Boo is a single-lined spectroscopic binary [Thévenin et al., 2005].

The fastest rotators in the sample are η Boo and HD 49933, with $v \sin i \gtrsim 10$ km s $^{-1}$. The metal-poor dwarf Gmb 1830 has the highest proper motion (4.0 and -5.8 arcsec/yr in right ascension and declination, respectively). Most of the other stars have proper motions less than 1 arcsec/yr.

Our library provides a homogeneous set of high-resolution and high signal-to-noise ratio (S/N) spectra for the 34 benchmark stars. Moreover, the stellar parameters of these benchmark stars were determined consistently and homogeneously, making them perfect for being used as reference. This library of 34 benchmark stars is therefore a powerful tool to cross-calibrate methods and stellar surveys, which is crucial for having a better understanding of the structure and evolution of the Milky Way.

The observed spectra of the benchmark stars were obtained from different telescopes with different instruments and specifications (i.e., resolution and sampling). We developed an automatic process to transform the spectra into one final homogeneous dataset. This allows us to easily generate new versions of the library adapted to the needs of specific surveys (i.e., downgrading the resolution or selecting a different spectral region). Additionally, since reproducibility is one of the main pillars of science, our code will be provided under an open source license to any third party wishes to reproduce the results [Blanco-Cuaresma et al., 2013].

This article is structured as follows. In Sect. 2.2, we describe the original observed spectra and its sources, while in Sect. 2.3 we introduce the computer process that was developed to create the library. Section 2.4 presents the different tests that were performed to validate the correctness of processing and the consistency of the library. In Sect. 2.5, we describe the resulting library's elements that we provide, and finally, we conclude the paper in Sect. 2.6

2.2 Observational data

The original observed spectra come mainly from the archives of three different instruments (NARVAL, HARPS, and UVES). In some cases, observations of the same star were obtained by different telescopes, which gives us the possibility to evaluate instrumental effects (see Table 2.1 for a general overview).

2.2.1 NARVAL spectra

The NARVAL spectropolarimeter is mounted on the 2m Telescope Bernard Lyot [Aurière, 2003] located at Pic du Midi (France). The data from NARVAL were reduced with the Libre-ESPRIT pipeline [Donati et al., 1997]. Most of these spectra were taken within a large programme proposed as part of the "Ground-based observations for Gaia" (P.I: C. Soubiran). The benchmark stars observed with this instrument are listed in Table 2.2, where we indicate the S/N and the radial velocity.

Note that one of the solar spectra was created by co-adding 11 spectra of asteroids with the aim to have higher S/N. The asteroids were observed on different nights, therefore there is no observation date in Table 2.2. Another solar spectrum corresponding to one single asteroid observation (Metis) with low S/N is included in our sample, which can be used to study S/N effects in spectral analysis.

NARVAL spectra cover a large wavelength range ($\sim 300 - 1100$ nm), with a resolving power¹ that varies for different observation dates and along the wavelength range, typically from 75,000 around 400 nm to 85,000 around 800 nm. However, it is acceptable to initially assume a constant resolving power of $R \approx 81,000$ as we prove in Sect. 2.4.2.

1. The terms "resolving power" and "resolution" refer to the relation $R = \frac{\lambda}{\Delta\lambda}$, although we prefer to use the former when talking about instrumental capabilities and the latter for already observed spectra

Table 2.1 – List of the high-resolution spectra available per benchmark star and instrument.

Star	NARVAL	HARPS	UVES	UVES-POP
α Cen A		✓	✓	
α Cen B		✓		
α Cet	✓	✓	✓	
α Tau	✓	✓		
β Ara		✓		
β Gem		✓		
β Hyi		✓	✓	✓
β Vir	✓	✓		
δ Eri	✓	✓	✓	✓
ϵ Eri		✓	✓	✓
ϵ For		✓		
ϵ Vir	✓	✓		
η Boo	✓	✓		
γ Sge	✓			
μ Ara		✓	✓	
μ Cas	✓			
μ Leo	✓			
ψ Phe		✓		
τ Cet	✓	✓		
ξ Hya		✓		
18 Sco	✓	✓		
61 Cyg A	✓			
61 Cyg B	✓			
Arcturus	✓	✓	✓	✓
Gmb 1830	✓			
HD 107328	✓	✓		
HD 122563	✓	✓	✓	✓
HD 140283	✓	✓	✓	✓
HD 220009	✓	✓		
HD 22879	✓	✓		
HD 49933		✓		
HD 84937	✓	✓	✓	✓
Procyon	✓	✓	✓	✓
Sun	✓	✓	✓	

Table 2.2 – Spectra observed with the NARVAL spectrograph (average resolving power of $\sim 81,000$).

Star	S/N	RV	Date
18 Sco	310 / 393 / 429	11.62 ± 0.05	2012-03-10
61 Cyg A	248 / 375 / 429	-65.84 ± 0.04	2009-10-16
61 Cyg B	290 / 464 / 548	-64.71 ± 0.05	2009-10-13
α Cet	192 / 296 / 367	-26.12 ± 0.04	2009-12-09
α Tau	209 / 319 / 382	54.31 ± 0.04	2009-10-26
Arcturus	283 / 388 / 443	-5.31 ± 0.04	2009-12-11
β Vir	349 / 414 / 437	4.39 ± 0.06	2012-01-09
δ Eri	277 / 356 / 393	-6.27 ± 0.03	2009-10-26
ϵ Vir	309 / 388 / 425	-14.37 ± 0.04	2009-11-27
η Boo	366 / 433 / 452	-6.04 ± 0.12	2009-12-11
γ Sge	301 / 467 / 565	-34.53 ± 0.03	2011-09-30
Gmb 1830	334 / 420 / 458	-98.22 ± 0.07	2012-01-09
HD 107328	278 / 384 / 439	36.41 ± 0.04	2009-11-26
HD 122563	274 / 352 / 398	-26.09 ± 0.18	2009-11-27
HD 140283	265 / 317 / 345	-170.56 ± 0.44	2012-01-09
HD 220009	278 / 384 / 441	40.36 ± 0.04	2009-10-16
HD 22879	256 / 306 / 326	120.37 ± 0.09	2009-11-27
HD 84937	189 / 220 / 231	-14.89 ± 0.51	2012-01-08
μ Cas	220 / 278 / 302	-96.48 ± 0.06	2009-11-26
μ Leo	307 / 415 / 465	13.53 ± 0.03	2011-12-10
Procyon	676 / 790 / 824	-5.75 ± 0.08	2012-03-16
Sun (Metis)	36 / 47 / 52	2.87 ± 0.05	2010-04-25
Sun (co-added)	584 / 723 / 778	5.41 ± 0.05	-
τ Cet	296 / 368 / 399	-16.65 ± 0.05	2009-12-08

Notes. The S/N ratio is reported for three different segments: 480 - 540 / 540 - 610 / 610 - 680 nm. The measured radial velocities are in km/s. The last column corresponds to the observation date.

2.2.2 HARPS spectra

HARPS is the ESO facility for the measurement of radial velocities with very high accuracy. It is fibre-fed by the Cassegrain focus of the 3.6m telescope in La Silla [Mayor et al., 2003]. The spectra were reduced by the HARPS Data Reduction Software (version 3.1). Most of the data for benchmark stars were obtained within the programme for critical tests on stellar atmosphere models within the Gaia-SAM collaboration (P.I: U. Heiter). The remaining HARPS data were taken from the public archives.

The list of HARPS spectra can be found in Table 2.3. The solar spectra correspond to two observations of asteroids (Ceres and Vesta) and one observation of one of Jupiter’s moons (Ganymede). We could obtain them directly from the public archive thanks to Molaro and Monai [2012], who presented a detailed analysis of absorption lines of the those spectra. Additionally, we co-added those spectra to have a solar spectrum with higher S/N.

The spectra for the stars HD84937 and HD140283 are the result of the co-addition of four and two individual observed spectra, respectively. The reason for combining these spectra is to increase the S/N. The spectra of each star were taken on the same night, with the date indicated in Table 2.3.

The spectral range covered is 378 – 691 nm, but as the detector consists of a mosaic of two CCDs, one spectral order (from 530 nm to 533 nm) is lost in the gap between the two chips.

2.2.3 UVES spectra

The UVES spectrograph is hosted by unit telescope 2 of ESO’s VLT [Dekker et al., 2000]. We took the spectra of benchmark stars available the Advanced Data Products collection of the ESO Science Archive Facility² (reduced by the standard UVES pipeline version 3.2, Ballester et al., 2000) by selecting only the most convenient³ spectrum for each star based on visual inspection.

The setup used for each observation (CD#3, centered around 580 nm) provides a spectrum with two different parts which approximately cover the ranges from 476 to 580 nm (lower part) and from 582 to 683 nm (upper part). The resolution of each spectrum and lower/upper parts might be different depending on the slit width used during the observation. There is a relation between the slit width (or the seeing if it is considerable smaller than the slit width) and the resolution, which depends on the date of observation⁴. We went through those relations for each spectrum and estimated its resolution which can be found in Table 2.4.

2.2.4 UVES-POP spectra

The UVES Paranal Observatory Project UVES-POP library [Bagnulo et al., 2003, processed with data reduction tools specifically developed for that project] contains stellar spectra along the complete UVES wavelength range (300-1000 nm with two gaps around 580 nm and 860 nm). The benchmark stars that are included in this library are listed in Table 2.5.

2. http://archive.eso.org/eso/eso_archive_adp.html

3. Those spectra with high S/N and smooth continuum, given that sometimes the merging of the orders did not produce a smooth spectrum along the wavelength range

4. http://www.eso.org/observing/dfo/quality/UVES/reports/HEALTH/\trend_report_ECH_RESOLUTION_DHC_HC.html

Table 2.3 – Spectra observed with the HARPS instrument (average resolving power of $\sim 115,000$).

Star	S/N	RV	Δ RV	Date
18 Sco	146 / 168 / 173	11.82 ± 0.04	-0.02	2009-05-20
α Cen A	381 / 442 / 487	-22.6 ± 0.04	-0.02	2005-04-08
α Cen A	433 / 495 / 540	-22.6 ± 0.04	-0.02	2005-04-19
α Cen B	393 / 467 / 507	-21.86 ± 0.03	-0.05	2005-04-08
Arcturus	368 / 470 / 554	-5.19 ± 0.03	-0.01	2004-07-08
β Hyi	381 / 424 / 465	23.16 ± 0.05	0.01	2005-11-13
β Vir	272 / 313 / 329	4.55 ± 0.05	0.03	2009-04-10
δ Eri	436 / 521 / 576	-6.21 ± 0.03	-0.04	2005-10-23
ϵ Eri	383 / 474 / 537	16.4 ± 0.04	-0.05	2005-12-28
HD 49933	293 / 323 / 329	-12.06 ± 0.19	0.06	2011-01-05
μ Ara	207 / 250 / 275	-9.35 ± 0.04	-0.02	2004-06-08
Sun-1 (Ceres)	227 / 253 / 267	3.99 ± 0.04	0.07	2006-07-16
Sun-2 (Gan.)	312 / 362 / 389	6.02 ± 0.04	-0.02	2007-04-13
Sun-3 (Vesta)	174 / 194 / 201	3.77 ± 0.04	0.0	2009-12-25
Sun (co-added)	421 / 483 / 514	3.97 ± 0.04	-	-
τ Cet	219 / 260 / 282	-16.57 ± 0.04	-0.04	2008-09-09
α Cet	165 / 228 / 284	-25.66 ± 0.04	-0.16	2007-10-22
α Tau	47 / 69 / 86	54.21 ± 0.03	-0.06	2007-10-22
β Ara	285 / 408 / 488	0.22 ± 0.04	0.25	2007-09-29
β Gem	287 / 359 / 416	3.42 ± 0.03	-0.04	2007-11-06
ϵ For	281 / 330 / 358	40.8 ± 0.04	-0.01	2007-10-22
ϵ Vir	319 / 386 / 421	-14.28 ± 0.03	-0.02	2008-02-24
η Boo	358 / 410 / 439	-2.23 ± 0.12	0.06	2008-02-24
HD 107328	343 / 452 / 524	36.66 ± 0.03	-0.02	2008-02-24
HD 122563	353 / 430 / 492	-26.24 ± 0.17	0.07	2008-02-24
HD 140283	441 / 497 / 535	-170.46 ± 0.42	0.05	2008-02-24
HD 220009	262 / 342 / 398	40.18 ± 0.04	0.01	2007-10-22
HD 22879	296 / 322 / 336	120.38 ± 0.08	-0.03	2007-10-22
HD 84937	444 / 484 / 513	-14.76 ± 0.49	0.24	2007-12-03
ξ Hya	318 / 386 / 422	-4.53 ± 0.04	-0.01	2008-02-24
Procyon	352 / 373 / 377	-3.11 ± 0.08	0.0	2007-11-06
ψ Phe	274 / 352 / 460	3.07 ± 0.06	-0.31	2007-09-30

Notes. The S/N ratio is reported for three different segments: 480 - 540 / 540 - 610 / 610 - 680 nm. The measured radial velocities are in km/s and Δ RV is the difference from the reported velocity by HARPS pipeline. The last column corresponds to the observation date.

Table 2.4 – Spectra observed with the UVES instrument.

Star	S/N	RV	R	Date
α Cen A	287 / 328 / 324	-23.13 ± 0.04	90000 85000	2000-04-11
α Cet	157 / 209 / 227	-25.53 ± 0.04	115000 90000	2003-08-11
Arcturus	213 / 291 / 306	-5.18 ± 0.03	115000 95000	2004-08-03
β Hyi	407 / 447 / 411	22.96 ± 0.05	85000 78000	2001-07-27
δ Eri	176 / 208 / 217	-5.87 ± 0.03	85000 75000	2001-11-29
ϵ Eri	204 / 231 / 222	15.99 ± 0.04	115000 90000	2001-10-02
HD 122563	288 / 326 / 327	-26.66 ± 0.17	82000 72000	2002-02-19
HD 140283	279 / 305 / 298	-170.79 ± 0.41	85000 78000	2001-07-09
HD 84937	215 / 229 / 228	-15.19 ± 0.48	80000 72000	2002-11-28
μ Ara	292 / 327 / 309	-9.25 ± 0.04	115000 95000	2003-09-05
Procyon	349 / 379 / 356	-2.35 ± 0.08	82000 75000	2002-10-08
Sun (Vesta)	337 / 383 / 418	-5.52 ± 0.04	78000 78000	2000-10-18

Notes. The S/N ratio is reported for three different segments: 480 - 540 / 540 - 610 / 610 - 680 nm. The measured radial velocities are in km/s. The reported resolving power correspond to the lower and upper parts of each spectrum. The last column corresponds to the observation date.

Table 2.5 – Spectra observed with the UVES instrument and processed by the UVES-POP pipeline (average resolving power of 80,000).

Star	S/N	RV	Date
Arcturus	1123 / 1312 / 1235	-5.48 ± 0.03	2003-02-16
β Hyi	596 / 690 / 717	22.99 ± 0.06	2001-07-25
δ Eri	421 / 547 / 606	-5.94 ± 0.03	2001-11-28
ϵ Eri	1468 / 1625 / 1808	16.09 ± 0.04	2002-10-11
HD 122563	846 / 934 / 624	-26.73 ± 0.18	2002-08-18
HD 140283	807 / 901 / 864	-170.75 ± 0.43	2001-07-08
HD 84937	511 / 537 / 567	-15.13 ± 0.48	2002-11-28
Procyon	1297 / 1449 / 948	-2.25 ± 0.08	2002-10-07

Notes. The S/N ratio is reported for three different segments: 480 - 540 / 540 - 610 / 610 - 680 nm. The measured radial velocities are in km/s. The last column corresponds to the observation date.

2.2.5 Atlas spectra

We included the already normalized atlas spectra from [Hinkle et al. \[2000\]](#) for the Sun and Arcturus. The observations were made with the Coude Feed Telescope on Kitt Peak with the spectrograph in the Echelle mode, reaching a resolving power of 150,000 and a high S/N. The authors of that work also removed the telluric lines from the provided spectra.

The inclusion of this observations in the library is only for normalization validation purposes (see Sect. 2.4.1); they were not treated by the same homogeneous normalization process as the other spectra.

2.3 Data handling and processing

An automatic computational process was developed to transform the observed spectra presented in Sect. 2.2 into a homogeneous library of the benchmark stars. Since the wavelength range varies from one set of observations to another, we chose to limit the current library to the range between 480 and 680 nm, where all the spectra provide their best S/N. Additionally, the range matches the interests of the Gaia-ESO Survey [GES, [Gilmore et al., 2012](#)] given their UVES setup on the ESO-VLT telescope.

In this section, we describe how the data are treated to determine and correct the radial velocity of the star, fit the continuum and normalize, convolve the spectra to a common desired resolution, and re-sample the spectra to finally obtain a homogeneous library (see Fig. 2.1 for a general overview).

2.3.1 Cleaning and cosmic rays removal

The spectra obtained by different instruments have different conventions to indicate errors in the observation. For instance, bad pixels can be marked with negative fluxes. These values should not be considered as good data, therefore we automatically ignore them.

On the other hand, spectra may contain residuals from cosmic rays which can affect the normalization process and future analyses. We implemented an algorithm that detects them automatically using a median filter to smooth out single-measurement deviations. The process is as follows:

1. Re-sample the spectrum to have a homogeneous sampling of 0.001 nm steps (small enough to respect the original resolution).
2. Obtain a smoothed spectrum by applying a median filter with a window of 15 points, which equals to 0.015 nm.
3. Re-sample the smoothed spectrum to the original wavelength grid again.
4. Subtract the smoothed spectrum from the original one.
5. Mark all the points with differences higher than 0.01 (1% of total flux) which are located above the continuum as cosmic rays (determined by a preliminary execution of the steps described in Sect. 2.3.5).

Cosmic rays may also appear under the continuum, but if we attempt to remove them, we might also affect the upper parts of sharply blended lines. Therefore, we preferred to limit ourselves to cosmic rays above the continuum.

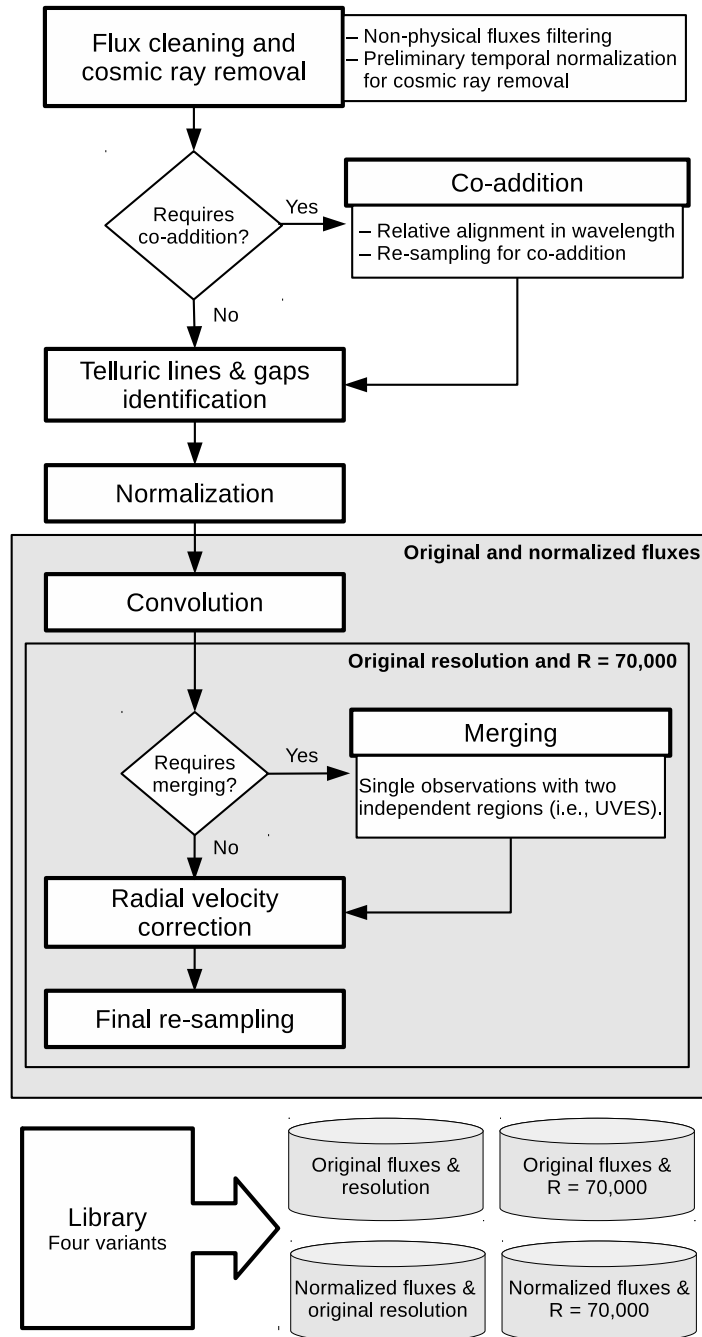


Figure 2.1 – Flowchart of the automatic computational process developed to build the library.

2.3.2 Co-addition

As specified in Sect. 2.2.2, several spectra observed by HARPS were co-added for the stars HD140283 and HD84937. Additionally, three solar spectra observed by HARPS and 11 asteroids observed by NARVAL were co-added into two single spectra (one per instrument).

For each co-addition, we selected one spectrum as reference, we removed those regions that are potentially affected by telluric lines (see Sect. 2.3.3) and we executed a cross-correlation process (see Sect. 2.3.8) against the other spectra of the same star. Finally, we aligned all the spectra (zero differential velocity), re-sampled them (see Sect. 2.3.9), and summed up their fluxes.

2.3.3 Telluric lines

Telluric lines from Earth's atmosphere contaminate ground-observed spectra and might affect stellar analyses. We identified automatically those potentially affected regions which allows the users to easily ignore or remove them.

In this process, a synthetic spectrum from TAPAS [Bertaux et al., 2013] was used. TAPAS is an on-line service that provides simulated atmospheric transmission spectra for specific observing conditions.

We do not need to recover the exact telluric spectrum for the day and place of observation since our goal is not to correct them but to identify the potentially affected regions. Therefore, we obtained a synthetic spectrum as if all the observations were done at ESO observatory (La Silla, Chile) pointing to the zenith (angle of zero degrees).

Once the non-convolved synthetic spectrum was obtained and normalized (as described in Sect. 2.3.5), an automatic process for absorption line detection was applied. The process performs the following steps:

1. Search local minimum (representing absorption peaks) and maximum points (corresponding to the limits of the absorption line).
2. Discard lines found that are false positive or noise by ignoring:
 - (a) peaks that have a smaller depth than its nearby maximums (false positives),
 - (b) peaks too close (2 or less bins away) to the next and previous maximums (noise);
3. Discard those line candidates that do not have a minimum depth (1.0% of depth with respect to the continuum).
4. Fit a Gaussian model to the line candidates.
5. Discard lines with bad fits.

The process provides us with the position of the telluric lines peaks and the full-width at half-maximum (FWHM) of the fitted Gaussian. In order to delimit where the lines start and end, we searched for local maximums $4 \times \text{FWHM}$ around each telluric line's peak or we directly used $2 \times \text{FWHM}$ if no local maximum was found.

The resulting telluric line list was used as a mask for locating the telluric lines in each observed spectra by using cross-correlation (as the one described in Sect. 2.3.8). The identified regions affected by telluric lines were ignored in the normalization process (Sect. 2.3.5).

2.3.4 Gaps

Depending on the instrument, some spectra contain gaps (regions without fluxes or all fluxes set to zero). We identified them automatically to be able to easily ignore those regions.

2.3.5 Normalization

The spectra were normalized automatically, reducing biases and inhomogeneities due to subjective criteria. For each observed star, the process uses a synthetic spectrum generated with the MARCS model atmospheres [Gustafsson et al., 2008], an atomic line list from VALD [Kupka et al., 2011], the SPECTRUM code [Gray and Corbally, 1994] and the atmospheric parameters listed in Table 2.6. The fitting algorithm is as follows:

1. Ignore all the fluxes that have a value below 0.98 in their respective synthetic spectra (computed with the reference atmospheric parameters). This way, we reduce the effect of strong lines in the normalization process.
2. Ignore gaps and regions affected by telluric lines.
3. Reduce the noise effects by applying a median filter with a window of 0.01nm (window sizes were selected after several validation and optimization tests).
4. Apply a maximum filter with a window of 1.0nm to select those fluxes that have more probabilities belonging to the continuum.
5. Fit second degree splines every 1.0nm to the filtered points and divide the original observed spectrum by the fitted model.

After several tests, we found this was the most robust strategy to homogeneously normalize the library's spectra.

2.3.6 Resolution degradation

The resulting final library was homogenized to the highest minimum resolving power, which corresponds to 70,000. The process convolves the spectra by performing the following steps for each flux value:

1. Define a window with size $FWHM_\lambda$ which depends on the original and final desired resolution:

$$FWHM_\lambda = \sqrt{\left(\frac{\lambda}{R_{\text{final}}}\right)^2 - \left(\frac{\lambda}{R_{\text{initial}}}\right)^2}. \quad (2.1)$$

2. Build a Gaussian profile $g(\lambda_x)$ using the sigma corresponding to $FWHM_\lambda$ and the wavelength values of a spectral window around the wavelength λ that it is going to be convolved:

$$g(\lambda_x) = \frac{1}{\sqrt{2\pi\sigma_\lambda^2}} e^{-\frac{(\lambda_x - \lambda)^2}{2\sigma_\lambda^2}}, \quad (2.2)$$

where $\sigma_\lambda = \frac{FWHM_\lambda}{2\sqrt{2\log 2}}$.

Table 2.6 – Parameters used for the spectral synthesis in the normalization process.

Star	Teff	log(g)	[M/H]	Vmic	Vmac	v sin(i)
ψ Phe	3472	0.51	-1.23	1.54	6.26	3.00
α Cet	3796	0.68	-0.45	1.36	5.68	3.00
γ Sge	3807	1.05	-0.16	1.43	5.01	6.00
α Tau	3927	1.11	-0.37	1.36	5.23	5.00
61 Cyg B	4044	4.67	-0.38	0.85	5.00	1.70
β Ara	4173	1.04	-0.05	1.24	5.09	5.40
HD 220009	4275	1.47	-0.75	1.23	5.39	1.00
Arcturus	4286	1.64	-0.53	1.25	5.05	3.80
61 Cyg A	4374	4.63	-0.33	0.86	4.19	0.00
μ Leo	4474	2.51	0.26	1.28	3.63	5.10
HD 107328	4496	2.09	-0.34	1.23	4.60	1.90
HD 122563	4587	1.61	-2.74	1.13	6.13	5.00
Gmb 1830	4827	4.60	-1.46	0.82	3.49	0.50
β Gem	4858	2.90	0.12	1.22	3.68	2.00
δ Eri	4954	3.75	0.06	1.00	3.60	0.70
ϵ Vir	4983	2.77	0.13	1.23	3.78	2.00
ξ Hya	5044	2.87	0.14	1.23	3.72	2.40
ϵ Eri	5076	4.60	-0.10	0.88	3.22	2.40
ϵ For	5123	3.52	-0.62	1.02	4.05	4.20
α Cen B	5231	4.53	0.22	0.93	2.79	1.00
μ Cas	5308	4.41	-0.82	0.91	3.85	0.00
τ Cet	5414	4.49	-0.50	0.94	3.70	0.40
HD 140283	5514	3.57	-2.43	1.05	5.18	5.00
Sun	5777	4.44	0.02	1.07	4.19	1.60
α Cen A	5792	4.30	0.24	1.11	4.01	1.90
18 Sco	5810	4.44	0.01	1.08	4.34	2.20
HD 22879	5868	4.27	-0.88	1.09	5.45	4.40
β Hyi	5873	3.98	-0.07	1.16	4.82	3.30
μ Ara	5902	4.30	0.33	1.15	4.40	2.20
β Vir	6083	4.10	0.21	1.24	5.62	2.00
η Boo	6099	3.80	0.30	1.30	5.74	12.70
HD 84937	6356	4.15	-2.09	1.29	9.24	5.20
Procyon	6554	3.99	-0.04	1.48	9.71	2.80
HD 49933	6635	4.20	-0.46	1.48	10.87	10.00

Notes. The effective temperature (K) and surface gravity (dex) were obtained from Paper I, the metallicity corresponds to the Fe I LTE abundances (dex) from Paper III (SPECTRUM code assumes Local Thermodynamic Equilibrium, LTE), the micro/macroturbulence (km/s) is derived from an empirical relation calibrated by the Gaia ESO Survey working groups (M. Bergemann and V. Hill, private communication) and the rotation (km/s) found in the literature (see Papers I/III).

3. Normalize the Gaussian profile and multiply it by the original fluxes in the spectral window. The sum of that operation will be the new convolved value for the wavelength λ :

$$\text{flux}(\lambda) = \sum_{\text{window}}^x \text{flux}(\lambda_x) \left(\frac{g(\lambda_x)}{\sum_{\text{window}}^x g(\lambda_x)} \right). \quad (2.3)$$

2.3.7 Merge

The spectra from the UVES instrument were observed with a setup that provides a separate lower and upper spectral part (see Sect. 2.2.3). In these cases, we performed the cleaning, normalization and convolution separately and, afterwards, the resulting spectra were merged.

2.3.8 Radial velocity

Zero point template

As a zero point we could use, for instance, the solar HARPS spectrum since this instrument provides high precision radial velocity measurements. We preferred to use the co-added solar NARVAL spectrum because it does not contain any gap, however, in order to transform the NARVAL solar spectrum into a reliable zero point template, we removed the regions affected by telluric lines and we cross-correlated it with a solar HARPS spectrum, which was corrected by using the radial velocity reported by HARPS pipeline. Finally, we corrected the NARVAL spectrum with the relative velocity shift found.

Cross-correlation

The first stage in the radial velocity determination process is the generation of the velocity profile by the cross-match correlation algorithm [Pepe et al., 2002], which sums the spectrum's fluxes multiplied by a mask/template function 'p':

$$C(v) = \sum_{\lambda} p(\lambda, v) \cdot \text{flux}(\lambda), \quad (2.4)$$

where v is the velocity.

1. Create a wavelength grid uniformly spaced in terms of velocity. This means that an increment in position ($x \rightarrow x + 1$) supposes a constant velocity increment (velocity step) but a variable wavelength increment. The following formula is used for determining the wavelength ranges (relativistic Doppler effect):

$$\lambda_{x+1} = \lambda_x + \lambda_x \left(1 - \sqrt{\frac{1 - \frac{v}{c}}{1 + \frac{v}{c}}} \right), \quad (2.5)$$

where c is the speed of light in vacuum and λ the original wavelengths.

2. Calculate the cross-correlation function [Baranne et al., 1996, Allende Prieto, 2007] between the spectrum and the specified template by shifting the template from limits (see below).

Once the velocity profile was constructed from the cross-correlation process, the mean velocity is calculated by fitting a second order polynomial near the peak. Additionally, a Gaussian model is fitted (with fixed mean velocity) to determine other complementary parameters such as the FWHM.

The whole process is repeated two times: Firstly a general estimation is obtained by using a velocity step of 5.0 km/s (1.0 km/s if we are cross-correlating with a telluric line mask) with lower and upper limits of ± 200 km/s; Secondly, a more precise value is determined by using a step of 0.25 km/s with lower and upper limits of $\pm 4 \times \text{FWHM}$ around the first velocity estimation.

The error in the radial velocity determination is calculated by following [Zucker \[2003\]](#):

$$\sigma_v^2 = - \left[N \frac{C''(v)}{C(v)} \frac{C^2(v)}{1 - C^2(v)} \right]^{-1}, \quad (2.6)$$

where N is the number of bins in the spectrum, C is the cross-correlation function, and C'' is its second derivative.

Finally, the correction is performed by applying the following formula:

$$\lambda_{corrected} = \lambda \sqrt{\frac{1 - \frac{v}{c}}{1 + \frac{v}{c}}}. \quad (2.7)$$

2.3.9 Re-sampling

The final step in the homogenization process is to sample all the spectra by establishing a constant increment in wavelength (0.001 nm) from 480 to 680 nm. To do so, we implemented a Bessel's Central-Difference interpolation similar to that used in TGMET [[Katz et al., 1998](#)].

A quadratic Bessel's interpolation formula was employed. It makes use of two points before and two points after the value to be interpolated (except where there are not enough, such as at the beginning and end of the spectrum, where a linear interpolation is performed). The formula is as follows:

$$f(\lambda) = f(\lambda_0) + p(f(\lambda_1) - f(\lambda_0)) + \left[\frac{p(p-1)}{4} \right] (f(\lambda_2) - f(\lambda_1) - f(\lambda_0) + f(\lambda_{-1})), \quad (2.8)$$

where $p = \frac{\lambda - \lambda_0}{\lambda_1 - \lambda_0}$, $f(\lambda)$ is the flux, λ is the target wavelength, and $\lambda_{-1} < \lambda_0 < \lambda < \lambda_1 < \lambda_2$. The zero and first order terms correspond to a linear interpolation, while the second order term is a correction factor to that linear interpolation.

2.3.10 Errors

All the observed spectra have individual errors associated with each measured flux except the atlas spectra. For the latter, we estimated the errors dividing the fluxes by the S/N, which was obtained by calculating the ratio between the mean flux and the standard deviation for groups of ten measurements around each wavelength point and selecting the mean value.

For the operations that implied flux modification (e.g., convolution, continuum normalization), the errors were taken into account and appropriately propagated.

2.4 Validation

The resulting library was evaluated to guarantee that the data were properly treated and that the spectra present a high level of quality.

2.4.1 Normalization

The normalization process should produce similar spectra for the same stars independent of the instrument used for the observation. To validate that statement and therefore the internal coherence, we compared spectra from different instruments by calculating their root mean square (RMS) difference in flux as:

$$\text{RMS} = \sqrt{\frac{\sum (\text{flux}_{\text{reference}} - \text{flux})^2}{\text{num_fluxes}}}, \quad (2.9)$$

where $\text{flux}_{\text{reference}}$ is the flux from a given spectrum (i.e., the first in the treatment chain).

The test was performed using the whole wavelength range and three individual regions: H- α (653 - 660 nm), H- β (483 - 489 nm), and Mg triplet (515 - 520 nm). Regions affected by telluric lines or gaps were not considered in the comparison.

No general trends as a function of wavelength or systematic effects were found even in difficult regions with strong lines such as H- α and the Mg triplet (see Fig. 2.2). The mean relative difference⁵ is 0.001 ± 0.002 (0.1%) and the average RMS is 0.009 ± 0.004 , which as expected depends on the type of the star (see Table 2.7) since colder stars have more absorption lines and the continuum fitting process becomes more difficult.

Additionally, we compared our normalized spectra with the atlas spectra (Sun and Arcturus), which were normalized by an independent external procedure. The mean relative difference is -0.001 ± 0.002 (-0.1%) for the Sun and $-0.003\% \pm 0.002\%$ (-0.3%) for Arcturus. The average RMS is smaller than 0.02 (see Table 2.8) and no systematic effects were found. The normalization in strong line regions is also consistent (see Fig. 2.2).

2.4.2 Resolution

In order to assess the quality of a spectrum, it is important to validate that the assumed initial resolving power is correct and that the convolution process works correctly.

We assumed that the final resulting library has a resolution of 70,000, which corresponds to a FWHM of 4.28 km/s ($\text{FWHM} = \frac{c}{R}$). By using only the regions affected by the telluric lines, we cross-correlated the original and convolved normalized spectrum with the telluric mask and we obtained the FWHM in both cases (FWHM_1 and FWHM_2 respectively). Therefore, we can quantify how much the FWHM was changed as a result of the convolution process and validate that the difference is consistent with the expected initial resolution, that is,

$$\Delta \text{FWHM}_{\text{cross}} = (4.28 + (\text{FWHM}_1 - \text{FWHM}_2)) - (c/R_{\text{initial}}), \quad (2.10)$$

5. The mean relative difference is defined by $\Delta \text{flux} = \frac{\text{flux}_{\text{reference}} - \text{flux}}{\text{flux}_{\text{reference}}}$

Table 2.7 – Average RMS difference in flux for the normalized spectra of the same star but observed by different instruments.

Star	All	H-α	H-β	MgTriplet
α Cen A	0.012	0.009	0.008	0.004
α Cet	0.021	0.015	0.026	0.018
α Tau	0.014	0.010	0.015	0.013
β Hyi	0.009	0.009	0.008	0.003
β Vir	0.007	0.007	0.006	0.005
δ Eri	0.008	0.006	0.010	0.007
ϵ Eri	0.015	0.015	0.008	0.007
ϵ Vir	0.006	0.005	0.006	0.006
η Boo	0.005	0.005	0.005	0.004
μ Ara	0.012	0.014	0.011	0.008
τ Cet	0.007	0.008	0.007	0.005
18 Sco	0.007	0.009	0.007	0.007
Arcturus	0.010	0.010	0.012	0.015
HD 107328	0.006	0.008	0.008	0.009
HD 122563	0.008	0.007	0.007	0.004
HD 140283	0.009	0.006	0.006	0.004
HD 220009	0.006	0.005	0.007	0.007
HD 22879	0.007	0.006	0.007	0.005
HD 84937	0.007	0.005	0.009	0.005
Procyon	0.013	0.008	0.008	0.005
Sun	0.008	0.004	0.008	0.005
Mean	0.009	0.008	0.009	0.007
StdDev	0.004	0.003	0.004	0.004

Notes. Apart from the whole wavelength range (All), three individual regions are also reported: H- α (653 - 660 nm), H- β (483 - 489 nm), and Mg triplet (515 - 520 nm).

Table 2.8 – Mean RMS differences in flux for atlas spectra and our normalized spectra observed by different instruments.

Star	All	H-α	H-β	MgTriplet
Arcturus	0.015	0.023	0.022	0.018
Sun	0.009	0.009	0.018	0.007

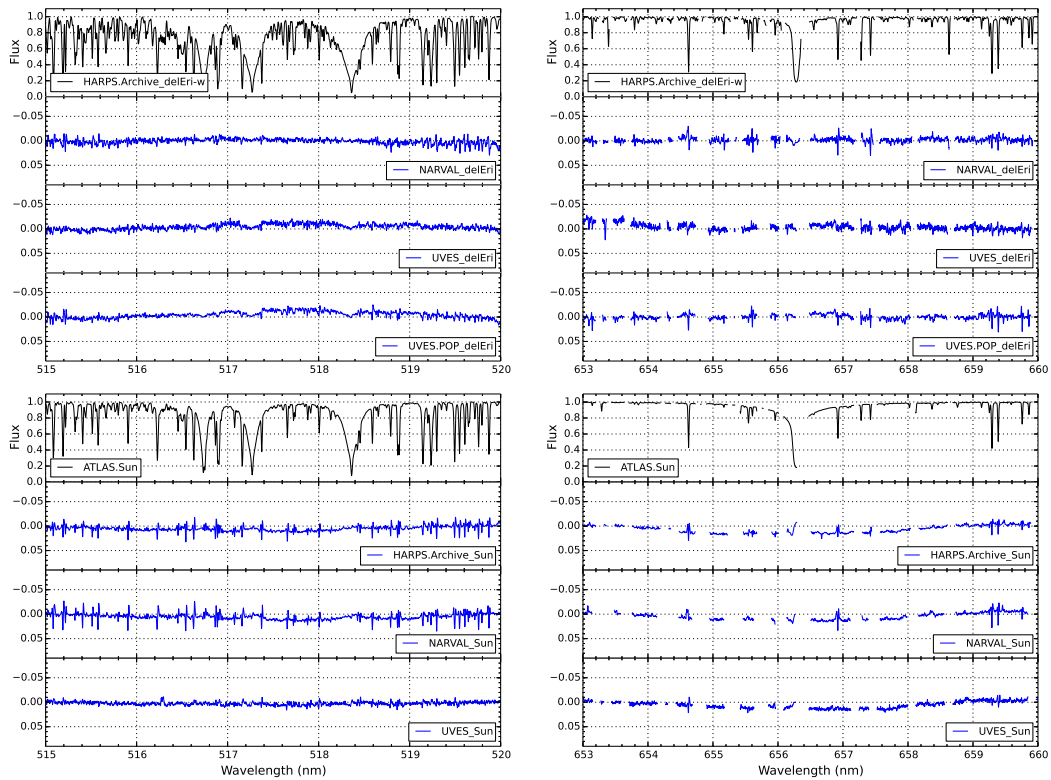


Figure 2.2 – Normalization comparison for δ Eri (upper part) and the Sun (lower part). The spectra of reference are in black and the flux differences with the remaining observation are in blue. The regions compared correspond to the magnesium triplet (left) and H- α (right). Regions affected by tellurics were removed.

Table 2.9 – Mean difference between expected and measured FWHM in km/s (see Eq. 2.10) and mean estimated original resolving power with their corresponding standard deviation.

Instrument	$\Delta\text{FWHM}_{\text{cross}}$	Estimated R_{initial}
	$\mu \pm \sigma$	$\mu \pm \sigma$
HARPS	-0.07 ± 0.21	118825 ± 9655
NARVAL	0.10 ± 0.13	79050 ± 2999
UVES	0.19 ± 0.14	83200 ± 10397
UVES.POP	-0.01 ± 0.15	80932 ± 3942

Table 2.10 – Difference in FWHM and equivalent widths between HARPS observations and the other instruments.

Star	Instrument	ΔFWHM	ΔEW
		$\mu \pm \sigma$	$\mu \pm \sigma$
Sun	NARVAL	-0.08 ± 0.05	-0.00 ± 0.03
Sun	UVES	-0.05 ± 0.04	-0.02 ± 0.06
Arcturus	NARVAL	-0.06 ± 0.03	0.02 ± 0.02
Arcturus	UVES	0.00 ± 0.03	0.03 ± 0.03
Arcturus	UVES.POP	-0.05 ± 0.03	0.02 ± 0.03
18 Sco	NARVAL	-0.00 ± 0.07	0.02 ± 0.07
δ Eri	NARVAL	-0.02 ± 0.05	-0.01 ± 0.05
δ Eri	UVES	0.01 ± 0.05	0.00 ± 0.06
δ Eri	UVES.POP	-0.02 ± 0.05	0.00 ± 0.05
η Boo	NARVAL	0.00 ± 0.04	0.00 ± 0.05
HD 220009	NARVAL	-0.02 ± 0.05	-0.01 ± 0.06
Procyon	NARVAL	-0.01 ± 0.05	-0.00 ± 0.06
Procyon	UVES	0.03 ± 0.07	0.01 ± 0.09
Procyon	UVES.POP	0.02 ± 0.05	0.02 ± 0.11
Mean		-0.02 ± 0.03	0.01 ± 0.01

where c is the speed of light and R_{initial} the expected initial resolution (see Tables 2.2, 2.3, 2.4, and 2.5), should be close to zero.

The results⁶ presented in Table 2.9 are in general agreement with the expected original resolving power. UVES spectra show the biggest dispersion in measured original resolving power, which is natural since not all the original spectra share the exact same resolving power (it can even vary between the lower and higher parts of the spectrum).

We recall that NARVAL resolving power is not constant along the entire wavelength range. To show that this is not problematic, we measured the individual FWHM of a group of stellar lines (see Sect. 2.4.4) for each spectra. For those stars with more than one spectrum, we calculated the relative difference in FWHM for the lines in common (see Table 2.10):

$$\Delta\text{FWHM} = \frac{\text{FWHM}_{\text{other}} - \text{FWHM}_{\text{HARPS}}}{\text{FWHM}_{\text{HARPS}}}. \quad (2.11)$$

6. Atlas spectra were not considered since the telluric lines are not present in the original spectra.

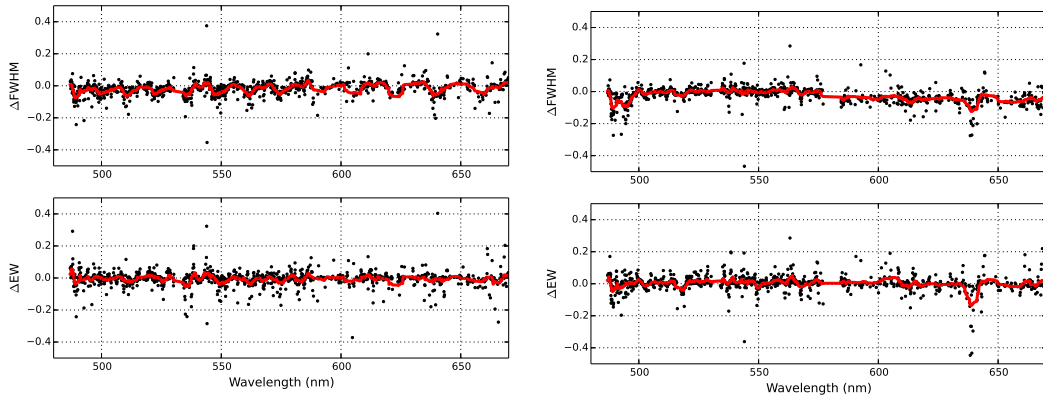


Figure 2.3 – Relative difference in FWHM (upper part) and equivalent widths (lower part) for the δ Eri spectrum, with the moving average overplotted (red) for visual guidance. The numeric details of the HARPS against NARVAL (left plot) and HARPS against UVES-POP (right plot) comparisons can be found in Table 2.10.

The relative difference in FWHM for a spectrum observed by HARPS and NARVAL compared to the same spectrum observed by HARPS and UVES is not significant as we show in Fig. 2.3. The variable resolving power of NARVAL is small enough to be neglected and it does not have a relevant impact in spectroscopic analyses, such as the one performed in Paper III.

2.4.3 Radial velocity

The HARPS pipeline provides high precision radial velocity measurements for each observed spectrum. We used those measurements to test our radial velocity determination method and we obtained a zero mean difference with a standard deviation of 0.08. The individual differences can be found in Table 2.3.

2.4.4 Equivalent widths

Different observations of the same Benchmark Star with the same resolution should have the same equivalent widths (EW). Thus, measuring and comparing EW provides us a different perspective to validate the normalization and convolution processes.

In that sense, we used the lines from Ramírez and Allende Prieto [2011] for the Sun and Arcturus, which are good representatives for the dwarf and giant stellar types. The authors derived the EWs from high resolution spectra ($R > 300,000$ ⁷ for the Sun, Kurucz et al. [1984], $R \sim 100,000$ for Arcturus [Hinkle and Wallace, 2005]), therefore we used the original non-convolved observations of the Benchmark Stars for the comparison.

The analysis was complemented with the inclusion of lines measured by Luck and Heiter [2006] and Luck and Heiter [2007] for 11 additional stars (seven dwarfs, four giants). In this case, the authors measured the EWs from spectra with a resolving power of 60,000. In consequence, we downgraded the resolution of the corresponding stars to match the same value and thereby equalize the conditions (i.e., same degree of blends).

Our EWs are determined by fitting a Gaussian profile in each absorption line and integrating its

7. <http://kurucz.harvard.edu/sun/fluxatlas/fluxatlastext.tab>

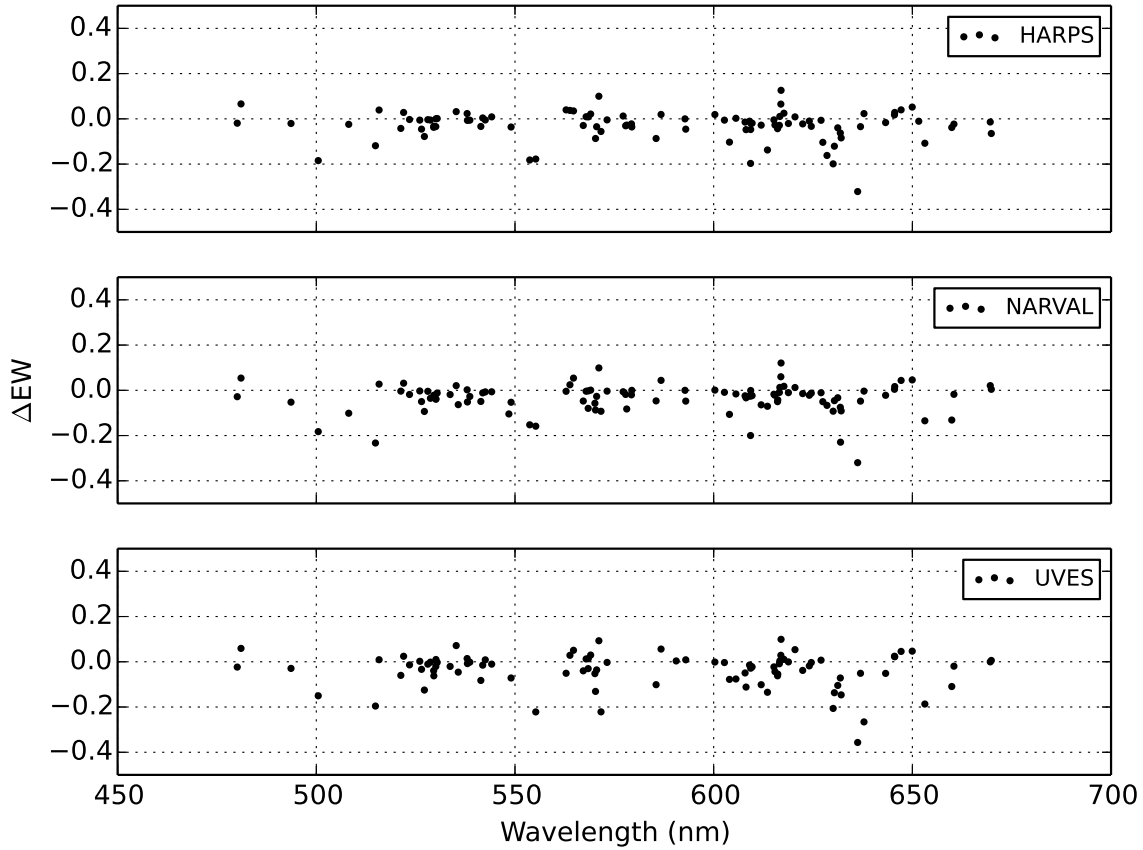


Figure 2.4 – Relative differences in the equivalent width measured for the Sun by [Ramírez and Allende Prieto \[2011\]](#).

area. In the process, we discarded those lines that do not present a good fit (i.e., $RMS > 0.05$). The relative EW difference is calculated as:

$$\Delta EW = \frac{EW_{external} - EW}{EW}. \quad (2.12)$$

External consistency

We obtained a high level of consistency with the independently measured EWs (see Fig. 2.4 and Fig. 2.6), the mean relative EW difference is around -0.03 ± 0.07 for the Sun and -0.03 ± 0.12 for Arcturus. The dispersion is logically higher for the latter since the continuum in giants is less trivial to fit.

The visual inspection of lines with higher relative EW differences (see Fig. 2.5 and Fig. 2.7) shows that our fit is consistent. The cause of the differences seems to be related to the continuum placement, which is specially amplified for weak absorption lines.

The additional stars present the same high level of agreement with a mean relative difference of -0.01 ± 0.04 (1%), all the detailed results can be found in Table 2.11.

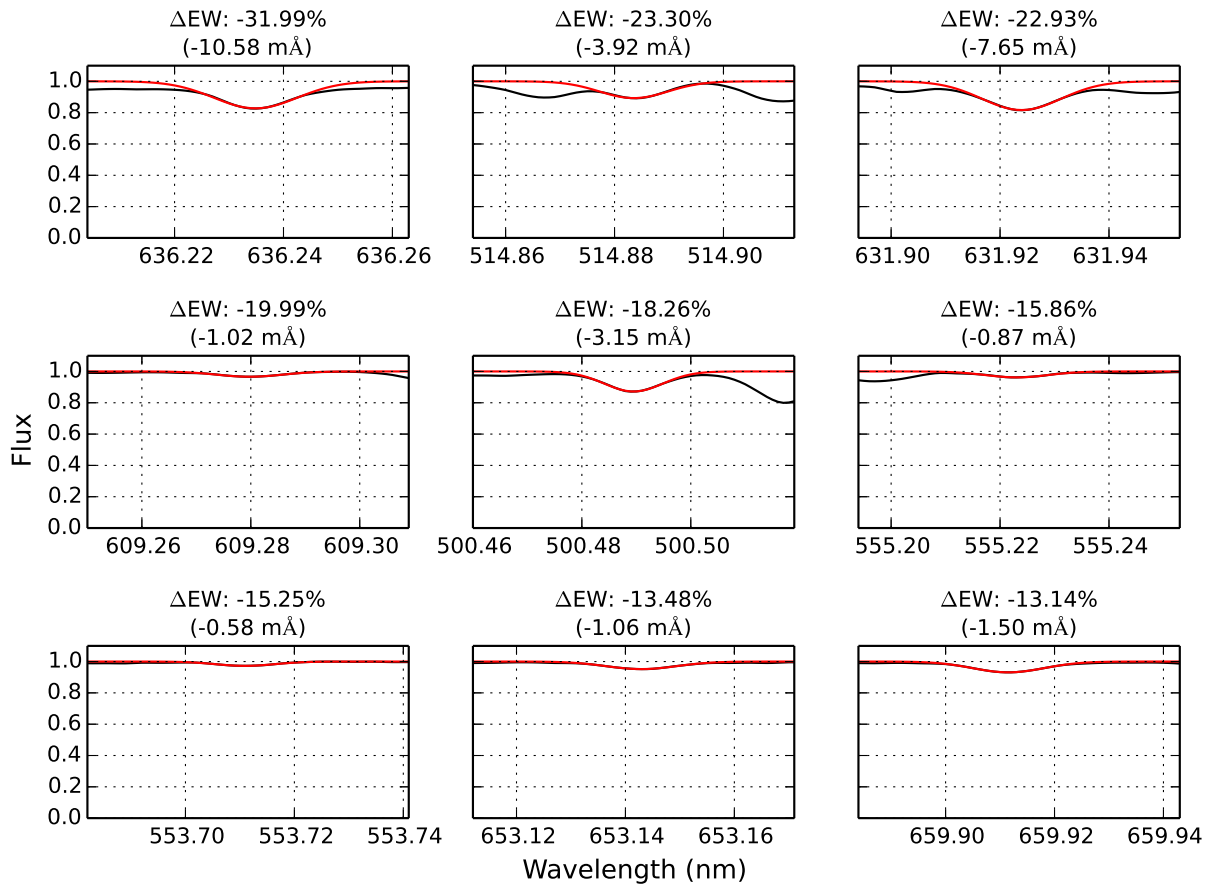


Figure 2.5 – Normalized fluxes (black) and fitted Gaussians (red) for the lines with the highest relative difference in EW compared to [Ramírez and Allende Prieto \[2011\]](#). The fluxes correspond to the co-added spectra of the Sun observed by NARVAL.

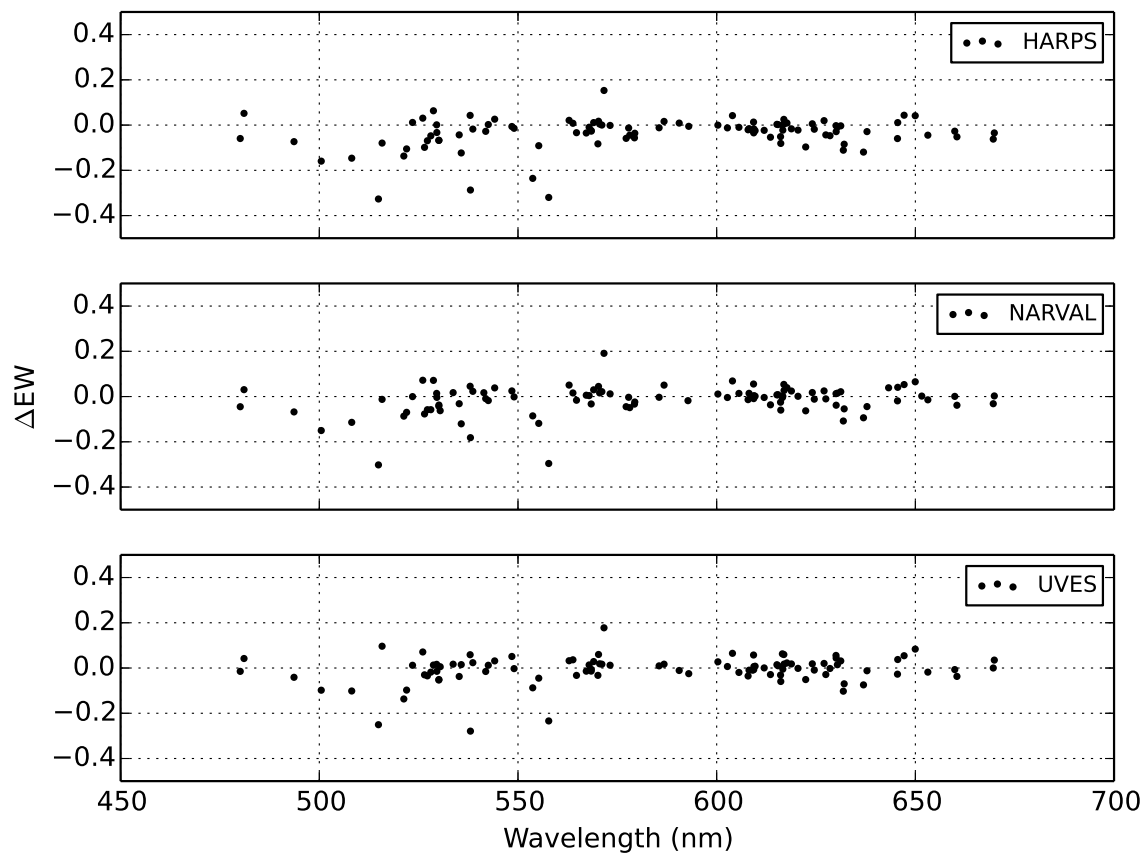


Figure 2.6 – Relative differences in the equivalent width measured for Arcturus by [Ramírez and Allende Prieto \[2011\]](#).

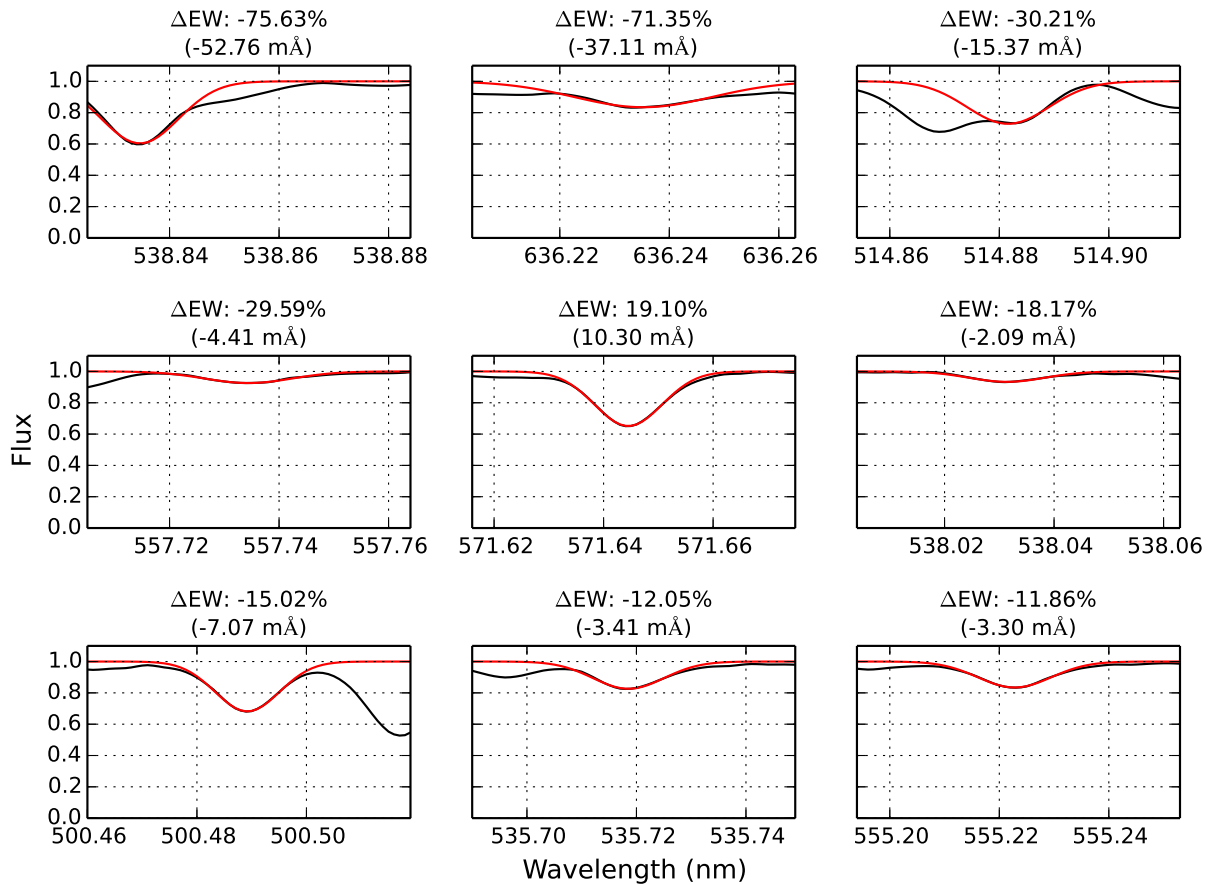


Figure 2.7 – Normalized fluxes (black) and fitted Gaussians (red) for the lines with the highest relative difference in EW compared to [Ramírez and Allende Prieto \[2011\]](#). The fluxes correspond to the Arcturus spectrum observed by NARVAL.

Table 2.11 – Relative EW differences with external measurements [Ramírez and Allende Prieto, 2011, Luck and Heiter, 2006, 2007].

Star	Instrument	ΔEW $\mu \pm \sigma$	Num. of lines
Sun	Atlas	0.01±0.07	107
Sun	HARPS	-0.03±0.07	101
Sun	NARVAL	-0.04±0.06	106
Sun	UVES	-0.04±0.08	94
Arcturus	Atlas	-0.02±0.12	109
Arcturus	HARPS	-0.05±0.12	104
Arcturus	NARVAL	-0.03±0.12	105
Arcturus	UVES	-0.02±0.12	101
Arcturus	UVES.POP	-0.03±0.12	100
18 Sco	HARPS	-0.02±0.15	866
18 Sco	NARVAL	0.00±0.15	885
δ Eri	HARPS	0.01±0.15	1071
δ Eri	NARVAL	0.01±0.15	1109
δ Eri	UVES	0.02±0.16	1055
δ Eri	UVES.POP	0.02±0.15	1072
β Gem	HARPS	0.02±0.16	1176
η Boo	HARPS	-0.04±0.14	562
η Boo	NARVAL	-0.04±0.14	564
HD 220009	HARPS	0.00±0.15	1048
HD 220009	NARVAL	-0.00±0.14	1075
Procyon	HARPS	-0.07±0.12	530
Procyon	NARVAL	-0.07±0.11	548
Procyon	UVES	-0.06±0.13	524
Procyon	UVES.POP	-0.05±0.12	526
61 Cyg A	NARVAL	0.04±0.23	717
61 Cyg B	NARVAL	0.12±0.31	764
Gmb 1830	NARVAL	0.06±0.21	414
μ Cas	NARVAL	-0.00±0.15	675
μ Leo	NARVAL	0.03±0.20	1041
Mean		-0.01±0.04	

Internal consistency

We compared the measured EWs from those stars observed by different instruments. The level of internal consistency is very high (see Fig. 2.3) and the mean relative EW difference is 0.01 ± 0.01 (1%) as shown in Table 2.10. We estimated that abundance analysis based on EW methods show a very small variation of the order of ± 0.007 dex in metallicity when EWs are changed by 1% (based on the analysis of a solar spectrum).

2.5 Resulting library

The latest version of the library can be downloaded from <http://www.blancocuaresma.com/s/>. In this section we describe the contained data and their file formats.

2.5.1 Spectra

The library contains 78 spectra corresponding to the 34 benchmark stars. They cover the spectral range from 480 to 680 nm, homogeneously sampled with wavelength step of 0.001 nm (equivalent to 190,000 bins).

We provide four library variants: convolved/not convolved original non-normalized fluxes and convolved/not convolved normalized spectra.

The spectra are saved in two different formats:

1. FITS format, following the standards of the IAU⁸ [Greisen and Calabretta, 2002, Greisen et al., 2006], where the spectral coordinates (wavelengths) are specified in the header via CRVAL1 and CDELTA1 keywords. The FITS headers also contain metadata for each spectrum, such as their observation date, instrument, celestial coordinates, and history log. The fluxes and errors are stored, respectively, in the primary data unit and in an image extension [Grosbol et al., 1988] as 1D arrays.
2. Compressed plain text files with three columns delimited by tabulations: wavelength (nm), flux, and error.

2.5.2 Telluric lines

As described in Sect. 2.3.3, regions potentially affected by telluric lines were identified, thus the user can discard them easily. For each spectrum, we provide a plain text file with three columns (delimited by tabulations) which correspond to the telluric line peak, beginning, and end of the affected region (in nanometers).

Gap regions

As described in Sect. 2.3.4, some spectra contain gaps (regions without valid fluxes). We provide those regions in individual plain text files (one per spectrum) with two columns (delimited by tabulations), which correspond to the beginning and end of the gap (in nanometers).

8. International Astronomical Union

2.6 Conclusions

We created a homogeneous library of high resolution and high S/N spectra corresponding to 34 benchmark stars with four different variants (convolved/not convolved original non-normalized fluxes, convolved/not convolved normalized spectra). The library provides a powerful tool to assess spectral analysis methods and calibrate spectroscopic surveys.

We validated the consistency of the library by carefully checking the normalization and convolution treatments. The radial velocity corrections was certified by comparing the results with the high precision measurements of HARPS pipeline. We verified the coherence of the treated spectra by comparing them with EW measurements completely independent from our process. These strict tests proved the high quality level of the spectral library.

The whole creation and verification process was automatized, minimizing human subjectivity and ensuring reproducibility. It also allows us to create new versions of the library adapted to particular needs (i.e., different resolutions and spectral ranges) of specific spectroscopic surveys or spectral analyses.

The Gaia FGK benchmark stars library provides an opportunity to homogenize spectroscopic results (from single observations to massive surveys), reducing their dispersion and making them more comparable. This higher level of homogeneity can lead to a better and more robust understanding of the Galaxy such as its formation, evolution, and current structure.

Determining stellar atmospheric parameters and chemical abundances with iSpec

Paper accepted for publication in Astronomy & Astrophysics [Blanco-Cuaresma et al., 2014a]. The co-authors contribution was mainly focused on helping with the interpretation of the verification tests' results. I developed the iSpec framework integrating different external elements such as model atmospheres, atomic line lists and the spectral synthesizer. I also designed and executed the verification tests that are presented on the paper.

Contents

3.1	Introduction	67
3.2	Spectroscopic software framework	68
3.2.1	Data treatment	68
3.2.2	Line selection	69
3.2.3	Spectral synthesis and abundances from equivalent widths	69
	Atomic line-lists	69
	Abundances	70
	Pre-computed model atmospheres grid	70
	Interpolation of model atmospheres	71
3.2.4	Atmospheric parameter determination	73
	Initial parameters	73
	Synthetic spectral fitting	74
	Equivalent width method	74
3.2.5	Error estimation	75
3.3	Pipeline description and validation	76
3.3.1	Line selection	76
	Atomic data verification	76
	Observation verification	76
3.3.2	Atmospheric parameters determination	77
	Initial parameters	77

Synthetic spectral fitting method	77
Equivalent width method	78
Method comparison	82
3.3.3 Chemical abundances	83
3.4 Additional validations	84
3.4.1 Model atmosphere interpolation	84
3.4.2 Minimization process	87
Iterations	87
Correlations	87
3.4.3 Signal-to-noise ratios and spectral resolutions	89
3.5 Conclusions	91

3.1 Introduction

Ongoing high-resolution spectroscopic surveys such as the Gaia ESO survey [GES, [Gilmore et al., 2012](#), [Randich et al., 2013](#)] and the future HERMES/GALAH [[Freeman, 2010](#)] provide an enormous amount of high-quality spectra, increasing the data already available in observatory’s archives [[Moultaka et al., 2004](#), [Delmotte et al., 2006](#), [Petit et al., 2014](#)]. This represents a unique opportunity to unravel the history of our Galaxy by studying the chemical signatures of large star samples.

This huge amount of spectroscopic data challenges us to develop automatic processes to perform the required analysis. Numerous automatic methods have been developed over the past years [e.g., [Valenti and Piskunov, 1996](#), [Katz et al., 1998](#), [Recio-Blanco et al., 2006](#), [Koleva et al., 2009](#), [Jofré et al., 2010](#), [Mucciarelli et al., 2013](#), [Magrini et al., 2013](#), to name a few] to treat the spectra and derive atmospheric parameters from large datasets.

The two most common approaches are the direct comparison of observed and synthetic spectra, and the use of equivalent width technique based on excitation equilibrium and ionization balance. Nevertheless, typically the implementations of those methods use different ingredients (e.g., atomic data, model atmospheres) and continuum normalization strategies, which hinders direct comparisons.

We developed a software framework, named iSpec, to easily treat spectral observations and derive atmospheric parameters by applying the two most popular strategies: the synthetic spectral fitting technique and the equivalent width method. The code provides a wide variety of options, which facilitates executing homogeneous analysis using the same continuum normalization strategy, model atmospheres, atomic information, and radiative transfer code (SPECTRUM from [Gray and Corbally 1994](#)).

For the synthetic spectral fitting technique, iSpec compares an observed spectrum with synthetic ones generated on-the-fly, in a similar way as the tool Spectroscopy Made Easy (SME) does [[Valenti and Piskunov, 1996](#)]. A least-squares algorithm minimizes the difference between the synthetic and observed spectra. In each iteration, the algorithm varies one free parameter at a time and prognosticates in which direction it should move. Specific regions of the spectrum can be selected to minimize the computation time, focusing on the most relevant regions to better identify stars (i.e., wings of H- α /MgI triplet, Fe I/II lines).

Regarding the equivalent widths method, iSpec fits Gaussian models to a given list of Fe I/II lines, and from their integrated area derives their respective equivalent width and thus their abundances. The algorithm for determining the atmospheric parameters is based on the same least-squares technique mentioned above, but the minimization criterion is linked to the assumption of excitation equilibrium and ionization balance, similar to GALA [[Mucciarelli et al., 2013](#)], FAMA [[Magrini et al., 2013](#)] and StePar [[Taberner et al., 2012](#)].

iSpec was previously used to create a high-resolution spectral library of the Gaia FGK benchmark stars [[Blanco-Cuaresma et al., 2014b](#)], which are a common set of calibration stars in different regions of the HR diagram and span a wide range in metallicity. The defining property of these stars is that we know their radius and bolometric flux, which allows us to obtain their effective temperature and surface gravity *fundamentally*, namely, independently of the spectra.

For 34 FGK stars and M giants, angular diameters θ_{LD} , bolometric fluxes F_{bol} and parallaxes π were extracted from the literature. Stellar masses were determined from the comparison of effective temperature and luminosity to the output of stellar evolution models. We used two sets of models for most stars, provided by the Padova [[Bertelli et al., 2008, 2009](#)] and Yonsei-Yale [[Yi et al., 2003](#), [Demarque et al., 2004](#)] groups, which cover a wide range of masses and metallicities. With these input data, T_{eff} and $\log g$ were derived from fundamental relations, independently of spectroscopy¹.

1. $T_{eff} = (F_{bol}/\sigma)^{0.25}(0.5\theta_{LD})^{-0.5}$ and $g = (GM)^2(0.5\theta_{LD}/\pi)^{-2}$, where σ is the Stefan-Boltzmann constant

The reference iron abundances were also derived by [Jofré et al. \[2014\]](#). A brief description of the Gaia FGK benchmark stars and their reference parameters is given in [Jofré et al. \[2013\]](#). A detailed discussion of their fundamental T_{eff} and $\log g$ values and comparison to T_{eff} and $\log g$ values derived from high-resolution spectroscopy will be given in Heiter et al. (in prep.).

In this paper, we show how the library of the Gaia FGK benchmark stars can be used to assess and improve spectroscopic pipelines (in our case, based on iSpec) by comparing the derived atmospheric parameters and chemical abundances with the reference values.

The framework was designed to be flexible enough to be adapted to the needs of individual studies or extensive stellar surveys. iSpec can be used in automatic massive analysis through Python scripts, but it also includes a user-friendly visual interface that can easily interoperate with other astronomical applications such as TOPCAT², VOSpec³ and splat⁴, facilitating an indirect way to access the Virtual Observatory⁵

We describe the iSpec software framework in Sect. 3.2. The particularities of the pipelines developed for the current work, together with the tests and validations using the Gaia FGK benchmark star library are presented in Sect. 3.3. Additional general validations are reported in Sect. 3.4 and, finally, the conclusions can be found in Sect. 4.5.

3.2 Spectroscopic software framework

3.2.1 Data treatment

The main functionalities for spectra treatment integrated into iSpec cover the following fundamental aspects:

1. Continuum normalization: the continuum points of a spectrum are found by applying a median and maximum filter with different window sizes. The former smooths out noisy and the later ignores deeper fluxes that belong to absorption lines (the continuum will be placed in slightly upper or lower locations depending on the values of those parameters). Afterwards, a polynomial or group of splines (to be chosen by the user) can be used to model the continuum, and finally the spectrum is normalized by dividing all the fluxes by the model.
2. Resolution degradation: the spectral resolution can be degraded by convolving the fluxes with a Gaussian of a given full width at half maximum (km s^{-1}).
3. Radial velocity: iSpec includes several observed and synthetic masks and templates for different spectral types that can be used to derive the radial velocity of the star by applying the cross-correlation technique [[Allende Prieto, 2007](#)].
4. Telluric lines identification: telluric lines from Earth's atmosphere contaminate ground-observed spectra, and this can affect the parameter determination. Their position in the spectra can be determined by cross-correlating with a telluric mask built from a synthetic spectrum (from the TAPAS database, [Bertaux et al. 2014](#)).

and G the Newtonian constant of gravitation

2. <http://www.star.bris.ac.uk/~mbt/topcat/>
3. <http://www.sciops.esa.int/index.php?project=ESAV0&page=vospec>
4. <http://star-www.dur.ac.uk/~pdraper/splat/splat.html>
5. <http://www.ivoa.net/>

5. Re-sampling: spectra can be re-sampled by using linear (two points) or Bessel (four points) interpolation [Katz et al., 1998].
6. Equivalent width (EW) measurement: EWs are determined by fitting a Gaussian profile (a Voigt profile can also be chosen) in each absorption line and integrating its area.

To analyze observed stellar spectra, it is commonly necessary to apply some of these operations to the reduced spectra. Nevertheless, it is possible to use third-party software (e.g., ARES from Sousa et al. 2007, DAOSPEC from Stetson and Pancino 2008, or DOOp from Cantat-Gaudin et al. 2014) for these steps in combination with iSpec for the subsequent analysis.

The Gaia FGK benchmark stars library was created integrally with iSpec and is a good example of the data treatment capabilities of the framework. An extensive description and exhaustive validation of these operations can be found in Blanco-Cuaresma et al. [2014b].

3.2.2 Line selection

To determinate atmospheric parameters and individual abundances, it is necessary to chose which absorption lines are going to be used. This selection will definitively affect the results, thus it is important to consider the level of reliability of the atomic data (i.e., oscillator strengths). iSpec provides the user with all the functionalities needed to perform a custom selection (e.g., line synthesis, theoretical equivalent width calculation, user interface for easy visual comparison). For instance, an effective approach to identify the lines with the best atomic data is described in Sousa et al. [2014].

In a second stage, iSpec also facilitates the quality assessment of the spectral regions that are going to be used in the analyses (see Sect. 3.3.1). For instance, spectra might be affected by different levels of noise, cosmic rays, and telluric lines.

3.2.3 Spectral synthesis and abundances from equivalent widths

iSpec uses SPECTRUM to generate synthetic spectra and determinate abundances from equivalent widths. The framework includes all the basic ingredients needed for these purposes.

Atomic line-lists

Several atomic line-lists are included in iSpec. They were previously transformed to the format that SPECTRUM requires:

1. Central wavelength (\AA) of the absorption line.
2. Species description formed by a combination of the atomic number and the ionization state (e.g., “26.0” and “26.1” refers to a neutral and ionized iron line, respectively).
3. Lower and upper excitation energies (cm^{-1}).
4. Logarithm of the product of the statistical weight of the lower level and the oscillator strength for the transition (i.e., $\log(gf)$).
5. Fudge factor (parameter to adjust the line broadening due to poorly understood physical factors).

6. Transition type indicating whether the σ and α parameters used in the Anstee and O'Mara broadening theory are provided (coded as AO type) or the van der Waals broadening should be used (GA type). The individual broadening half-widths for Natural broadening and Stark broadening may also be specified.

Some original line-lists provide the lower excitation energies in electron volts (eV), thus they were transformed to cm^{-1} by multiplying by a conversion factor ($1 \text{ eV} = 8065.544 \text{ cm}^{-1}$). When the upper excitation state was not provided, it was obtained by applying the following relation:

$$E^{\text{upper}} = E_{\text{lower}} + \frac{hc}{\lambda} 6.24150974 \times 10^{18}, \quad (3.1)$$

where the upper and lower excitation energies are in cm^{-1} , h is the Planck constant ($h = 6.62606957 \times 10^{-34} \text{ m}^2 \text{ kg s}^{-1}$), c the speed of light in vacuum ($c = 299792458.0 \text{ m s}^{-1}$), λ is the line wavelength position in meters and the final change in energy is converted to eV with a conversion factor ($1 \text{ J} = 6.24150974 \times 10^{18} \text{ eV}$). Physical constants and conversion factors were taken from [Mohr et al. \[2012\]](#). The fudge factor was disabled for all the lines (i.e., set to 1).

iSpec provides several ready-to-use atomic line-lists with wide wavelength coverage (from 300 to 1100 nm), such as the original SPECTRUM line-list, which contains atomic and molecular lines obtained mainly from the NIST Atomic Spectra Database [[Ralchenko, 2005](#)] and Kurucz line-lists [[Kurucz and Bell, 1995](#)], and the default line-list extracted from the VALD database [[Kupka et al., 2011](#)] in February 2012.

Abundances

iSpec provides a collection of ready-to-use solar abundances from [Anders and Grevesse \[1989\]](#), [Grevesse and Sauval \[1998\]](#), [Asplund et al. \[2005\]](#), [Grevesse et al. \[2007\]](#), and [Asplund et al. \[2009\]](#). SPECTRUM requires these abundances for the process of spectral synthesis, where the values will be scaled based on the target metallicity ($[M/H]$). Nevertheless, individual abundances can be fixed to a given unscaled value if required. iSpec's synthetic spectral fitting technique takes advantage of this functionality to derive individual chemical abundances from a given list of absorption lines. The related accuracy can be considerably improved when using a line-by-line differential approach [[Ramírez et al., 2009](#)] because part of the biases in data treatment and errors in the atomic information will cancel out (specially if all the stars are of the same type).

Pre-computed model atmospheres grid

iSpec incorporates different ATLAS⁶ [[Kurucz, 2005](#)] and MARCS⁷ [[Gustafsson et al., 2008](#)] model atmospheres properly transformed to the format that SPECTRUM requires:

1. $\int \rho dx$: mass depth (g cm^{-2})
2. T : temperature (K)
3. P_{gas} : gas pressure (dyn cm^{-2})
4. n_e : electron density (cm^{-3})
5. κ_R : Rosseland mean absorption coefficient ($\text{cm}^2 \text{ g}^{-1}$)

6. <http://kurucz.harvard.edu/grids.html>

7. <http://marcs.astro.uu.se/>

Table 3.1 – Standard abundance composition for pre-computed MARCS model atmospheres.

[Fe/H]	[α /Fe]	[C/Fe]	[N/Fe]	[O/Fe]
+1.00 to 0.00	0.00	0.00	0.00	0.00
-0.25	+0.10	0.00	0.00	+0.10
-0.50	+0.20	0.00	0.00	+0.20
-0.75	+0.30	0.00	0.00	+0.30
-1.00 to -5.00	+0.40	0.00	0.00	+0.40

6. P_{rad} : radiation pressure (dyn cm^{-2})

7. V_{mic} : microturbulent velocity (m s^{-1})

The original MARCS models do not provide the electron densities, thus they were derived with the following relation:

$$n_e = \frac{P_e}{k T}, \quad (3.2)$$

where P_e is the electron pressure (dyn cm^{-2}) present in the MARCS model atmospheres, and k is the Boltzmann constant ($1.3806488 \times 10^{-16} \text{ erg K}^{-1}$).

It is worth noting that the MARCS grid is formed by a combination of plane-parallel and spherical models (ATLAS is plane-parallel only). The first is adequate for modeling the atmosphere of dwarf stars, while the second is more appropriate for giant stars. However, SPECTRUM will interpret the spherical models as plane-parallel. The differences that may be introduced are not important for the F, G, and K giants, as shown by Heiter and Eriksson [2006].

The included MARCS model atmospheres cover the 2500 to 8000 K range in effective temperature, 0.00 to 5.00 dex in surface gravity, and -5.00 to 1.00 dex in metallicity with standard abundance composition (Table 3.1). The original ATLAS by Kurucz [2005] and subsequent versions computed by Kirby [2011] and Mészáros et al. [2012] for APOGEE [Allende Prieto et al., 2008a], cover the 4500 to 8750 K range in effective temperature, 0.00 to 5.00 dex in surface gravity and -5.00 to 1.00 dex in metallicity.

Interpolation of model atmospheres

The pre-computed model atmosphere grids presented in Sect. 3.2.3 offer a reasonable coverage for the synthesis of typical FGK stars, but they do not provide a model for every single combination of effective temperature, surface gravity, and metallicity (e.g., white gaps in the upper plot from Fig. 3.1 represent missing model atmospheres). On the other hand, the steps on effective temperature (typically ~ 250 K), surface gravity (~ 0.5 dex) and metallicity (~ 0.50 dex) are not fine enough to optimally explore the parameter space.

We completed the model atmospheres grid as shown in the middle plot in Fig. 3.1 by using interpolation and extrapolation. For the temperature-gravity combinations for which there is no pre-computed atmosphere, the procedure is as follows:

1. First stage: linearly interpolate each value of each model atmosphere's layer from the existing pre-computed ones. In the best cases, two interpolated atmospheres are obtained and averaged:
 - (a) fixed gravity, and temperatures above and below the target parameters,

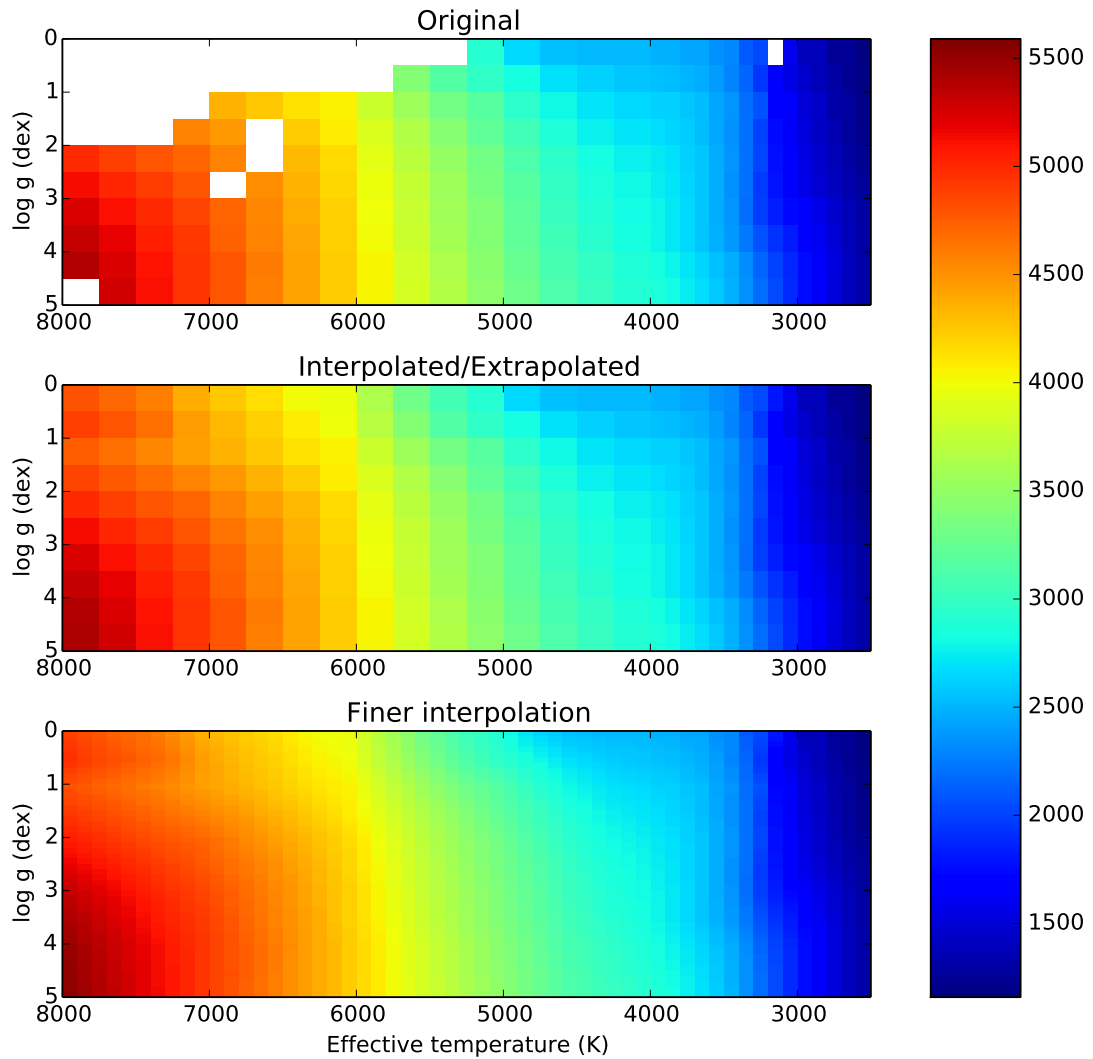


Figure 3.1 – Original pre-computed MARCS model atmospheres for solar metallicity (upper), complete grid with interpolated and extrapolated atmospheres (middle), and homogeneously sampled grid (lower). The color scale represents the temperature for the first model atmosphere layer.

- (b) fixed temperature, and gravities above and below the target parameters.
2. Second stage: linearly extrapolate. Again, in the best cases, two extrapolated atmospheres are obtained and combined with a weighted average that depends on their distance to the target atmosphere:
 - (a) fixed gravity, and two atmospheres with the closest temperature,
 - (b) fixed temperature, and two atmospheres with the closest gravity.

Extrapolated values were limited by the highest and lowest values found in all the real atmospheres to try to avoid unphysical results.

All the quantities in the atmosphere (e.g., temperature, gas pressure, electron density) are re-sampled on a common optical depth scale as described in [Mészáros and Allende Prieto \[2013\]](#). After the complete grid without gaps is constructed, it is easy to linearly interpolate any atmosphere that lies between any of the parameter combinations (i.e., effective temperature, surface gravity, and metallicity), as shown by the finer grid presented in the lower plot in [Fig. 3.1](#). iSpec includes the complete interpolated version of the model atmosphere grids, only the in-between interpolation is made on-the-fly when requested by the user.

3.2.4 Atmospheric parameter determination

iSpec is capable of determining atmospheric parameters and individual chemical abundances by using the synthetic spectral fitting technique and the equivalent width method.

In both cases, a χ^2 minimization is performed by executing a nonlinear least-squares (Levenberg–Marquardt) fitting algorithm [[Markwardt, 2009](#)]. The code starts from a given point in the parameter space and performs several iterations until convergence (i.e., the current/predicted χ^2 is lower than a given threshold or the maximum number of iterations has been reached). In each iteration, the Jacobian is calculated via finite differences, linearizing the problem around the trial parameter set and changing each of the free parameters by a pre-established amount:

$$p_i = p_i^0 + \Delta p_i, \quad (3.3)$$

where p_i is a given free parameter, p_i^0 the current value, and Δp_i the evaluation step.

Initial parameters

It is always recommended to provide initial parameters as close as possible to the expected final result, thus the computation time can be significantly reduced. Prior information such as photometry could be used for this purpose, but other approaches can be applied. For instance, iSpec provides the functionalities needed for computing a grid of synthetic spectra that can be used for deriving initial guesses via fast comparisons.

By default, iSpec does not include any pre-computed synthetic spectral grid since it strongly depends on the user requirements (i.e., wavelength ranges, atomic line-lists, model atmospheres). Therefore the user can employ the framework to build any custom grid and perform the initial parameter estimation.

Synthetic spectral fitting

The synthetic spectral fitting technique tries to minimize the difference between the observed and synthetic spectrum by directly comparing the whole observation or some delimited regions.

While exploring the parameter space, iSpec computes (via SPECTRUM) the synthetic spectra on-the-fly, which can be quite time-consuming depending on the extension of the chosen regions to be calculated and compared. Some codes prefer to approach this problem by executing the more time-consuming processes (i.e., pre-computing a huge grid of synthetic spectra) before starting the analysis, thus afterward the comparison time per star can be significantly faster. On the other hand, the on-the-fly approach is more flexible (e.g., it is very easy to adapt the analysis to different spectral resolutions).

The parameters that can be determined by using this method are the effective temperature, surface gravity, metallicity, microturbulence, macroturbulence, rotation, limb-darkening coefficient, and resolution. An efficient strategy is to let the first five parameters free and fix the rotation to 2 km s^{-1} (since it degenerates with macroturbulence), limb-darkening coefficient to 0.6 and resolution to the one corresponding to the observation. After the atmospheric parameters are determined, individual chemical abundances can also be derived by the same method.

After several tests, we determined that the optimal step size for fastest convergence with the least-squares algorithm (Eq. 3.3) is 100 K for the effective temperature, 0.10 dex for surface gravity, 0.05 dex for metallicity, 0.50 km s^{-1} for microturbulence, 2.0 km s^{-1} for macroturbulence, 2.0 km s^{-1} for rotation, 0.2 for the limb darkening coefficient, and 100 for the resolution.

Equivalent width method

The equivalent width method does not use all the information contained in the shape of the absorption-line profiles, but only their area. Therefore, broadening parameters such as rotation or macroturbulence are not considered.

iSpec derives (via SPECTRUM) individual abundances from the atomic data, the measured equivalent width, and a given effective temperature, surface gravity and microturbulence. The last three parameters are unknown and an initial guess is needed. iSpec gradually adjusts the atmospheric parameters by using neutral and ionized iron lines to enforce excitation equilibrium and ionization balance, which means that:

1. Abundances as a function of the excitation potential should have no trends. If the trend is positive, the effective temperature is underestimated.
2. Abundances as a function of the reduced equivalent width ($\text{EWR} = \log_{10} \frac{\text{EW}}{\lambda}$) should have no trends. If the trend is negative, the microturbulence is overestimated.
3. The abundances of neutral iron (Fe 1) should be equal to the abundance of ionized iron (Fe 2). If the difference (Fe 1 - Fe 2) is positive, the surface gravity is underestimated.

At the first iteration, iSpec identifies abundance outliers (see Fig. 3.2) by robustly fitting a linear model using an M-estimator⁸. If r_i is the residual between the i^{th} observation and its fitted value, a standard least-squares method would minimize $\sum_i r_i^2$, which is strongly affected by outliers present in the data and distorts the estimation. The M-estimators try to reduce the effect of outliers by solving the following iterated re-weighted least-squares problem:

8. “M” for “maximum-likelihood-type”

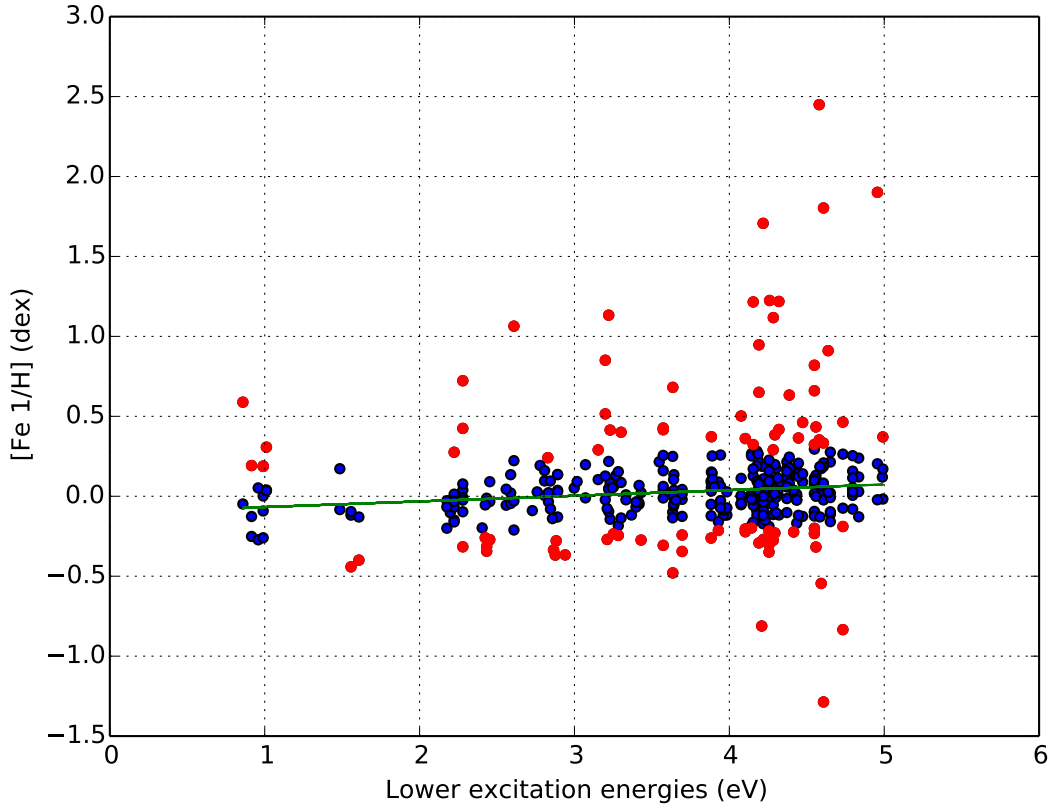


Figure 3.2 – Iron abundances as a function of the excitation potential with a fitted linear model (green) and outlier values (red).

$$\min \sum_i w(r_i^{k-1}) r_i^2, \quad (3.4)$$

where k indicates the iteration number, and the weights $w(r_i^{k-1})$ are recomputed after each iteration. After several tests, we determined that it is safe to discard abundances with assigned weights smaller than 0.90 (the weight scale ranges from zero to one). Robust regression estimators are shown to be more reliable than sigma clipping [Hekimoglu et al., 2009].

After the initial abundance outliers are discarded, the least-squares algorithm minimizes three values: the two slopes of the linear models fitted as a function of the excitation potential and the reduced equivalent width and the difference in abundances from neutral and ionized iron lines.

The step size for the least square algorithm (Eq. 3.3) differs from the ones used in the synthetic spectral fitting technique. Based on different tests, we found that the optimal steps for fastest convergence are 500 K for the effective temperature, 0.50 dex for surface gravity, 0.05 dex for metallicity, and 0.50 km s⁻¹ for microturbulence.

3.2.5 Error estimation

The atmospheric parameter errors are calculated from the covariance matrix constructed by the non-linear least-squares fitting algorithm. Nevertheless, they highly depend on the good estimation of the spectral flux errors. If they are underestimated, consequently, the atmospheric parameters errors will

present unrealistically low values. The minimization process can be executed ignoring flux errors, but then the errors of the atmospheric parameters will be generally overestimated.

For the chemical abundance errors estimation, when possible (i.e., there is enough lines to measure), it is preferred to derive abundances for each line individually and consider the standard deviation as the internal error.

3.3 Pipeline description and validation

We developed two different pipelines based on the synthetic spectral fitting technique and the equivalent width method. In this section we describe some of their particularities and present results for different configurations (e.g., different model atmospheres).

3.3.1 Line selection

Atomic data verification

For the current work, in addition to the atomic line lists included in iSpec by default, we also used the atomic data (without hyperfine structures and molecules) kindly provided by the GES line-list subworking group prior to publication (Heiter et al., in prep.). The line-list covers the optical range (i.e., 475 – 685 nm) and provides a selection of medium and high-quality lines (based on the reliability of the oscillator strength and the blend level) for iron and other elements (e.g., Na, Mg, Al, Si, Ca, Sc, Ti, V, Cr, Mn, Co, Ni, Cu, Zn, Sr, Y, Zr, Ba, Nd, and Sm).

Observation verification

The line selection is not only based on the quality of the atomic data, but also on the observed spectra to be analyzed. Using the iSpec framework, we fitted Gaussian profiles for all the selected absorption lines in each spectra. We automatically discarded lines that fall into one of these cases:

1. Fitted Gaussian peak is too far away from the expected position (more than 0.0005 nm). Convection could produce shifts, but it is also possible that a strong close-by absorption line dominates the region and considerably blends the original targeted line. The analysis would require manual inspection, thus we reject those lines.
2. Poor fits with extremely big root mean square difference (e.g., due to a cosmic ray)
3. Potentially affected by telluric lines.
4. Invalid fluxes (i.e., negative or nonexistent because of gaps in the observation).

Additionally, only for the pipeline based on the equivalent width method and inspired by the GALA code, we filtered weak and strong lines based on their reduced equivalent widths. Weak lines are more sensitive to noise and errors in the continuum placement, while strong lines are usually significantly blended and may be severely affected by incorrect broadening parameters.

This verification process allowed us to adapt the analysis to the peculiarities of each observation, ensuring that only the best-quality regions were used for the final parameter determination.

Table 3.2 – Synthetic spectral grid for determining the initial parameters. The rotation ($v \sin(i)$) was fixed to 2 km s^{-1} and the micro/macroturbulence was calculated by using the same empirical relation as in Blanco-Cuaresma et al. [2014b].

Class	T_{eff}	$\log(g)$	[M/H]
Giant	3500	1.00, 1.50	-2.00, -1.00, 0.00
Giant/Dwarf	4500	1.50, 4.50	-2.00, -1.00, 0.00
Dwarf	5500	4.50	-2.00, -1.00, 0.00
Dwarf	6500	4.50	-2.00, -1.00, 0.00

Notes. The micro/macroturbulence relation is based on GES UVES data release 1, the benchmark stars [Jofré et al., 2014], and globular cluster data from external literature sources.

3.3.2 Atmospheric parameters determination

The Gaia FGK benchmark stars library is a powerful tool for assessing the derived atmospheric parameters from different spectroscopic methods. We used the library to fine-tune our pipelines. The goal is to have results as similar as possible to the Gaia FGK benchmark stars reference values (accuracy) and with the lowest possible dispersion (precision).

Initial parameters

To determinate the initial parameters (effective temperature, surface gravity, metallicity, micro/macroturbulence), we built a basic grid of synthetic spectra with iSpec for a selection of key parameters that allows us to easily separate giants from dwarfs and metal-rich from metal-poor stars (Table 3.2).

We compared the observed spectrum with all the spectra contained in the grid considering a selection of lines (see Sect. 3.3.1) and the wings of H- α , H- β , and the magnesium triplet (around 515-520 nm). Finally, we adopted the parameters of the synthetic spectrum with the lowest χ^2 .

Synthetic spectral fitting method

In Table 3.3, we present the results for different configurations. In the interpretation, we consider a result as good when its differences are close to zero and its dispersion is low, but we prioritized lower dispersion over well centered values since it is easier to correct for a systematic shift than for a high dispersion. Among the different parameters, we also prioritized the surface gravity (even if that represents a slightly poorer result for the others) because it is the most difficult to derive when using only spectra.

1. Line selection: the best results are obtained when combining lines from several elements (see Sect. 3.3.1) with the wings of the H- α , H- β , and the magnesium triplet.
2. Reduced equivalent width (EWR) filter: we evaluated the results obtained without a filter (unlimited) and two levels of restriction. The strong filter discards lines with an EWR lower than -5.8 and higher than -4.65, which means that lines with an equivalent width lower than $8 \text{ m}\text{\AA}$ and higher than $111 \text{ m}\text{\AA}$ at 500 nm were discarded. The relaxed filter discards lines with EWR lower than -6.0 and higher than -4.3. At 500 nm, this equals discarding all the lines with an equivalent width lower than $5 \text{ m}\text{\AA}$ and higher than $250 \text{ m}\text{\AA}$. The results clearly do not

show a better strategy, thus we chose the relaxed filter to match the same configuration as for the equivalent width pipeline (see Sect. 3.3.2).

3. Atomic line list: the Gaia ESO Survey line-list (without hyper-fine structure and molecules) was compared with a line list extracted from VALD with the default options (2012) and with the SPECTRUM line-list, which includes molecules (see Sect. 3.2.3). For the SPECTRUM line-list, we obtained poorer surface gravity and metallicities precisions. On the other hand, the GES and VALD line-lists are similar. Again, we chose the GES line-list to match the equivalent width pipeline configuration (see Sect. 3.3.2).
4. Model atmospheres and solar abundances: ATLAS models, independent of the chosen solar abundance, are not as precise in all three atmospheric parameters, although they show a lower dispersion for stars with multiple spectra. We obtained better precisions with MARCS models when we combined them with the solar abundances from [Grevesse et al. \[2007\]](#), thus we opted for these models.
5. Initial atmospheric parameters: we performed one analysis starting systematically from the same point in the parameter space for all the stars (effective temperature of 5000 K, 2.5 dex in surface gravity, and solar metallicity) and one starting from an initial guess per spectrum (see Sect. 3.3.2). The results are very similar, showing that the minimization process works well with independence of the starting point. On the other hand, it is preferred to always perform the initial guess because the computation time is considerably reduced (from an average of 50 minutes to 36 minutes per spectrum, see Sect. 3.4.2).
6. Resolution: we downgraded the resolution of the library to match the resolving power of Giraffe ESO/VLT (HR21 setup used in GES), which corresponds to 16200, and re-adjusted the continuum by renormalizing with a linear model. The results show that the pipeline could be used effectively for high and medium-resolution spectra.

The results per star with the best configuration can be found in the Table 3.4 and Figs. 3.3 and 3.4. The average error (estimated by the least-square algorithm) is 19 K for effective temperature, 0.05 dex for surface gravity, and 0.02 dex for metallicity. These estimations have the same order of magnitude as the average dispersion obtained for the stars with several observed spectra: 15 K in effective temperature, 0.06 dex in surface gravity, and 0.01 dex in metallicity.

Equivalent width method

In the Table 3.5, we present the results for different configurations (the criteria for the interpretation are the same as in section 3.3.2):

1. Iron line selection: a medium and high-quality selection of lines (495/286 neutral and 42/25 ionized iron lines) were tested, where the later is a subgroup of the former (see Sect. 3.3.1). The results show that the medium-quality group is preferred; a larger line sample seems to provide a higher statistical advantage for the equivalent width method.
2. Reduced equivalent width filter: a filter based on different levels of the reduced equivalent width (as described in Sect. 3.3.2) was applied. The highest effective temperature and surface gravity precision is achieved when using a relaxed limit, while strong limits show a better metallicity precision. We chose the former because we preferred to prioritize the surface gravity precision.
3. Outliers filtering: the process of identifying outlier lines based on the derived abundance (see Sect. 3.2.4) was disabled to test its efficiency. The results clearly show that outlier filtering improves the accuracy and precision for all the parameters.

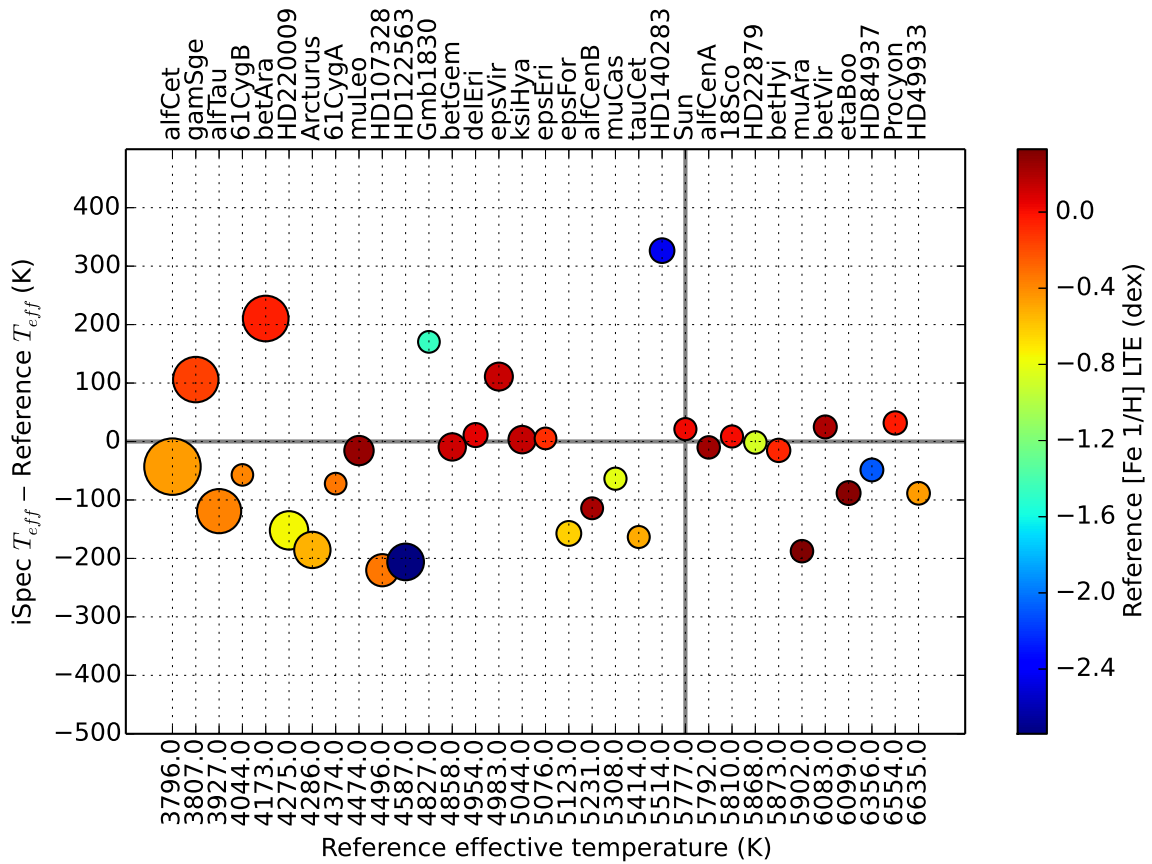


Figure 3.3 – Differences in effective temperature between the reference (the Gaia FGK benchmark stars) and the derived value by iSpec (synthetic spectral fitting method). Stars are sorted by temperature; the color represents the metallicity, and larger symbols represent lower surface gravity.

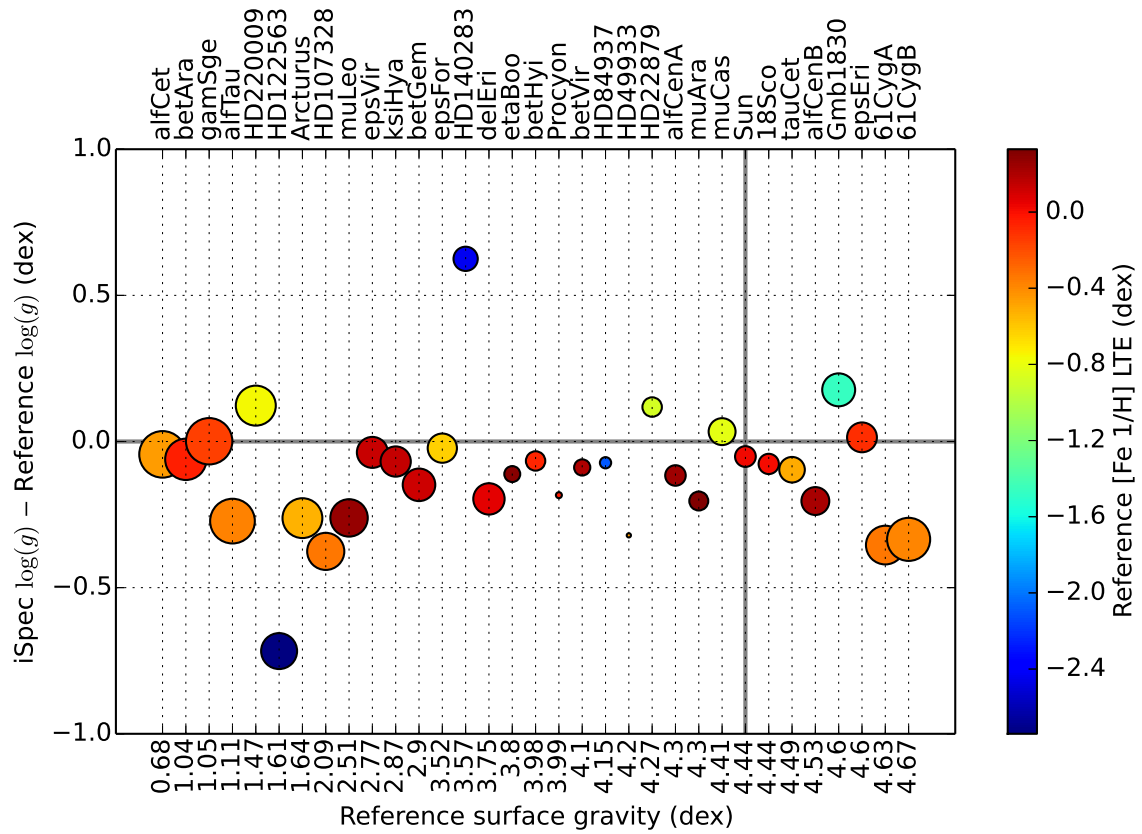


Figure 3.4 – Differences in surface gravity between the reference (the Gaia FGK benchmark stars) and the derived value by iSpec (synthetic spectral fitting method). Stars are sorted by surface gravity; the color represents the metallicity, and larger symbols represent lower surface gravity.

Table 3.3 – Average difference and standard deviation (left) between the synthetic spectral fitting technique and the reference values. Average dispersion (right) for stars with multiple observed spectra.

Case	Differences						Dispersion		
	ΔT_{eff}		$\Delta \log(g)$		$\Delta[M/H]$		ΔT_{eff}	$\Delta \log(g)$	$\Delta[M/H]$
	μ	σ	μ	σ	μ	σ			
All elements + wings	-24	124	-0.11	0.21	0.01	0.14	15	0.06	0.01
Only iron + wings	-2	110	-0.13	0.34	0.00	0.18	18	0.05	0.02
Only iron	-2	129	-0.29	0.35	-0.04	0.16	19	0.05	0.02
Relaxed EWR limit	-24	124	-0.11	0.21	0.01	0.14	15	0.06	0.01
Strong EWR limit	-14	122	-0.10	0.19	0.05	0.16	20	0.05	0.02
Unlimited EWR	-11	119	-0.07	0.21	0.02	0.14	16	0.04	0.01
GES	-24	124	-0.11	0.21	0.01	0.14	15	0.06	0.01
VALD	4	119	-0.09	0.18	0.06	0.14	15	0.06	0.01
SPECTRUM	6	158	-0.17	0.25	0.07	0.16	19	0.05	0.02
MARCS/Grevesse 2007	-24	124	-0.11	0.21	0.01	0.14	15	0.06	0.01
MARCS/Asplund 2005	-28	125	-0.17	0.25	0.01	0.14	13	0.05	0.02
ATLAS/Grevesse 2007	-47	244	-0.12	0.27	0.00	0.22	15	0.04	0.01
ATLAS/Asplund 2005	-50	243	-0.16	0.26	0.00	0.22	16	0.04	0.01
Estimate initial AP	-24	124	-0.11	0.21	0.01	0.14	15	0.06	0.01
Fixed initial AP	-27	122	-0.12	0.22	0.02	0.15	12	0.05	0.01
R = 70000	-24	124	-0.11	0.21	0.01	0.14	15	0.06	0.01
R = 16200	-31	139	-0.15	0.20	0.06	0.22	18	0.06	0.03
R = 16200/re-norm	-58	137	-0.10	0.16	-0.07	0.14	17	0.06	0.02

- Atomic line list: the results are better centered with the SPECTRUM line-list, but a lower dispersion is generally found for the GES line-list. Since we prioritize a low dispersion, we chose the GES line-list.
- Model atmospheres: the precision is very similar independently of the model atmosphere used, but MARCS produces slightly more accurate results.
- Initial atmospheric parameters: as described in Sect. 3.3.2, we executed the analysis starting from a single point in the parameter space and compared this with starting from an initial guess (see Sect. 3.3.2). The equivalent width method seems to be much more sensitive to the starting point, and it is highly recommended to start the analysis from a good initial guess.
- Resolution: absorption lines are more blended for lower spectral resolution. Consequently, the equivalent width method has more difficulties with low-resolution spectra, for which it overestimates abundances and provides poorer results.
- Line profile: using Gaussian profiles to fit lines and derive equivalent widths seems to provide slightly better results than Voigt profiles.

The results per star with the best configuration can be found in the Table 3.4. The average error (estimated by the least-squares algorithm) is 67 K for effective temperature, 0.13 dex for surface gravity, and 0.09 dex for metallicity. These estimates have the same order of magnitude as the average dispersion obtained for the stars with several observed spectra: 38 K in effective temperature, 0.12 dex in surface gravity, and 0.03 dex in metallicity.

Table 3.4 – Difference between the parameters derived from the two methods and the reference values (neutral iron abundance is used as a proxy for metallicity). For stars with several observed spectra, the difference corresponds to the average, and the standard deviation is also reported.

Star	Reference			Synthetic spectral fitting						Equivalent width					
	T_{eff}	$\log(g)$	[Fe 1/H]	ΔT_{eff}		$\Delta \log(g)$		$\Delta [M/H]$		ΔT_{eff}		$\Delta \log(g)$		$\Delta [M/H]$	
			<i>LTE</i>	μ	σ	μ	σ	μ	σ	μ	σ	μ	σ	μ	σ
18 Sco	5810	4.44	0.01	19	15	-0.06	0.03	0.03	0.01	-19	4	-0.04	0.03	0.03	0.01
Arcturus	4286	1.64	-0.53	-179	8	-0.19	0.10	-0.11	0.02	-126	50	0.07	0.14	-0.13	0.04
HD 107328	4496	2.09	-0.34	-218	3	-0.37	0.01	-0.18	0.01	-253	10	-0.28	0.01	-0.24	0.01
HD 122563	4587	1.61	-2.74	-163	77	-0.61	0.32	0.00	0.05	434	30	0.61	0.13	0.57	0.04
HD 140283	5514	3.57	-2.43	329	22	0.33	0.32	0.08	0.03	664	37	0.79	0.11	0.53	0.02
HD 220009	4275	1.47	-0.75	-147	7	0.14	0.03	0.01	0.00	-10	41	0.56	0.13	0.04	0.03
HD 22879	5868	4.27	-0.88	-1	1	0.13	0.02	0.16	0.00	-69	38	0.20	0.09	0.09	0.02
HD 84937	6356	4.15	-2.09	-23	33	-0.05	0.06	0.17	0.04	291	76	0.55	0.09	0.46	0.08
Procyon	6554	3.99	-0.04	22	18	-0.20	0.02	-0.06	0.01	-35	75	0.24	0.17	0.00	0.01
Sun	5777	4.44	0.02	23	15	-0.06	0.02	-0.02	0.05	-4	25	-0.03	0.04	-0.01	0.03
α Cen A	5792	4.30	0.24	-24	13	-0.13	0.01	-0.05	0.01	6	10	0.02	0.01	-0.04	0.00
α Cen	3796	0.68	-0.45	-50	11	-0.01	0.04	0.22	0.01	317	36	1.02	0.25	0.24	0.02
α Tau	3927	1.11	-0.37	-120	2	-0.20	0.10	0.10	0.00	347	75	0.70	0.71	0.23	0.21
β Hyi	5873	3.98	-0.07	-25	9	-0.08	0.01	-0.06	0.01	26	9	0.13	0.01	0.00	0.01
β Vir	6083	4.10	0.21	32	10	-0.08	0.01	-0.11	0.01	113	25	0.13	0.07	-0.02	0.01
δ Eri	4954	3.75	0.06	16	9	-0.18	0.02	-0.01	0.01	284	30	0.20	0.12	0.08	0.04
ϵ Eri	5076	4.60	-0.10	-13	16	-0.01	0.02	0.00	0.00	292	170	-0.29	0.18	0.02	0.00
ϵ Vir	4983	2.77	0.13	111	0	-0.02	0.02	-0.05	0.00	262	21	0.69	0.07	0.04	0.02
η Boo	6099	3.80	0.30	-103	20	-0.12	0.02	-0.15	0.00	54	7	0.31	0.04	0.10	0.01
μ Ara	5902	4.30	0.33	-196	11	-0.21	0.01	-0.09	0.00	-170	14	-0.10	0.03	-0.08	0.01
τ Cet	5414	4.49	-0.50	-156	10	-0.08	0.03	0.05	0.01	-95	8	-0.28	0.03	0.04	0.02
61 Cyg A	4374	4.63	-0.33	-72		-0.35		0.11		344		0.00		0.09	
61 Cyg B	4044	4.67	-0.38	-57		-0.33		0.17		135		-1.28		-0.36	
Gmb 1830	4827	4.60	-1.46	170		0.18		0.22		383		0.40		0.36	
HD 49933	6635	4.20	-0.46	-89		-0.32		-0.05		-39		0.24		0.14	
α Cen B	5231	4.53	0.22	-114		-0.20		-0.03		-64		-0.24		-0.06	
β Ara	4173	1.04	-0.05	210		-0.06		-0.06		51		-1.04		1.37	
β Gem	4858	2.90	0.12	-9		-0.15		-0.09		-57		-0.24		-0.14	
ϵ For	5123	3.52	-0.62	-157		-0.02		0.07		-43		0.04		0.09	
γ Sge	3807	1.05	-0.16	106		0.00		0.04		233		1.08		0.36	
ξ Hya	5044	2.87	0.14	3		-0.07		-0.11		156		0.50		-0.01	
μ Cas	5308	4.41	-0.82	-64		0.03		0.09		173		0.04		0.16	
μ Leo	4474	2.51	0.26	-16		-0.26		-0.03		157		-0.49		-0.26	
ψ Phe	3472	0.51	-1.23	83		-0.35		0.92		941		0.30		0.65	

Method comparison

To our knowledge, this is the first time that these two methods were compared by covering such a wide range of parameters and using exactly the same normalization process, atomic data, model atmospheres, and radiative transfer code (i.e., SPECTRUM). The tests show that our pipeline based on the synthetic spectral fitting technique provides more accurate and precise atmospheric parameters (Table 3.6), thus it is our preferred strategy when using iSpec.

On the other hand, it is worth noting that one of the advantages of other implementations of the equivalent width method (i.e., those based on the MOOG code [Snedden et al. 2012](#), such as GALA, FAMA and StePar) is their execution speed. SPECTRUM derives abundances from equivalent widths by completely synthesizing the lines, which makes the execution significantly slower (see Sect. 3.4.2).

Table 3.5 – Average difference and standard deviation (left) between the equivalent width method and the reference values. Average dispersion (right) for stars with multiple observed spectra.

Case	Differences						Dispersion		
	ΔT_{eff}		$\Delta \log(g)$		$\Delta [M/H]$		ΔT_{eff}	$\Delta \log(g)$	$\Delta [M/H]$
	μ	σ	μ	σ	μ	σ			
Medium-quality lines	135	241	0.20	0.44	0.12	0.27	38	0.12	0.03
High-quality lines	129	311	0.14	0.47	0.09	0.30	39	0.09	0.06
Relaxed EWR limit	135	241	0.20	0.44	0.12	0.27	38	0.12	0.03
Strong EWR limit	134	259	0.30	0.50	0.13	0.23	41	0.09	0.02
Unlimited EWR	173	371	0.20	0.53	0.21	0.45	58	0.14	0.06
Outlier filter	135	241	0.20	0.44	0.12	0.27	38	0.12	0.03
With outliers	178	374	0.41	0.67	0.13	0.31	80	0.18	0.06
GES	135	241	0.20	0.44	0.12	0.27	38	0.12	0.03
VALD	118	313	0.20	0.58	0.19	0.24	57	0.12	0.06
SPECTRUM	-1	326	-0.06	0.45	0.10	0.29	67	0.12	0.05
MARCS	135	241	0.20	0.44	0.12	0.27	38	0.12	0.03
ATLAS	157	221	0.22	0.44	0.13	0.26	37	0.12	0.03
Estimate initial AP	135	241	0.20	0.44	0.12	0.27	38	0.12	0.03
Fixed initial AP	152	359	-0.23	0.81	0.08	0.26	49	0.18	0.04
R = 70000	135	241	0.20	0.44	0.12	0.27	38	0.12	0.03
R = 16200	419	598	0.62	0.99	0.53	0.57	118	0.25	0.11
R = 16200/re-norm	475	520	0.86	0.89	0.21	0.79	62	0.17	0.05
Gaussian profiles	135	241	0.20	0.44	0.12	0.27	38	0.12	0.03
Voigt profiles	131	286	0.30	0.52	0.14	0.24	97	0.19	0.06

3.3.3 Chemical abundances

It is important to clarify that the metallicity parameter derived by iSpec is a global scale factor that is applied to all the elements (taking the solar abundance as the reference point) and it is not a direct measurement of the iron abundance (although it is a close approximation). Nevertheless, when the atmospheric parameters are known, iSpec can also determine individual chemical abundances for any element.

We limited our analysis to the determination of neutral and ionized iron since, up to now, it is the only element for which a reference value exists.

Our pipeline implements a line-by-line differential analysis (see 3.2.3) that follows these steps:

1. Derive the solar absolute abundances for each of the selected lines (see Sect. 3.3.1) using the reference atmospheric parameters. Seven out of the eight solar spectra included in the Gaia FGK benchmark stars library were used; we discarded one with a very low signal-to-noise ratio.
2. Discard lines with a high dispersion among the seven solar spectra (interquartile range higher than 0.025).
3. Derive the absolute abundances for each of the selected lines using the spectrum to be analyzed.
4. Calculate the relative abundances by subtracting the solar absolute abundances to the absolute abundances of the spectrum being analyzed.

Table 3.6 – Average difference and standard deviation (left) between the derived parameters and the reference values. Average dispersion (right) for stars with multiple observed spectra.

	Differences						Dispersion		
	ΔT_{eff}		$\Delta \log(g)$		$\Delta [M/H]$		ΔT_{eff}	$\Delta \log(g)$	$\Delta [M/H]$
	μ	σ	μ	σ	μ	σ			
SSF	-24	124	-0.11	0.21	0.01	0.14	15	0.06	0.01
EW	135	241	0.20	0.44	0.12	0.27	38	0.12	0.03

Notes. SSF stands for synthetic spectral fitting technique and EW for equivalent width method.

Table 3.7 – Average differences and standard deviation between the iron abundances derived from the two methods and the reference values (LTE and NLTE).

	Element	$\Delta [X/H]_{\text{LTE}}$		$\Delta [X/H]_{\text{NLTE}}$	
		μ	σ	μ	σ
		Synthetic spectral fitting	Fe 1	0.04	0.14
	Fe 2	0.09	0.18	0.07	0.16
Equivalent width	Fe 1	0.09	0.19	0.06	0.19
	Fe 2	0.12	0.27	0.11	0.17

- Derive the final abundance for the spectrum by calculating the median value and consider the dispersion as the internal error.

The results are presented in Table 3.7, where the derived iron abundances from both methods are compared with the LTE and NLTE reference values. Thanks to the differential approach, part of the NLTE effects seems to cancel out (specially for solar-type stars), and the derived results agree better with these reference values. A trend depending on the reference iron abundances is observed in the top plots from Fig. 3.5. Both methods overestimate iron abundances for metal-poor stars.

Since errors in the atmospheric parameters propagate into the abundance determination, we repeated the analysis by fixing the effective temperature, surface gravity, and metallicity to the reference values (bottom plots in Fig. 3.5). The trend is still present although it is less steep. The remaining effect could still be caused by NLTE effects, which become more important at low $[Fe/H]$, and the normalization process where the continuum placement is strongly influenced by the stellar type and metallicity (e.g., the most discrepant stars are those with the coolest and lowest surface gravity ones). For instance, if we re-normalize the spectra by forcing the continuum to be placed 1% lower, the overall metallicity decreases by ~ 0.07 dex when analyzed with the synthetic spectral fitting pipeline.

3.4 Additional validations

3.4.1 Model atmosphere interpolation

The model atmosphere interpolation processes were tested by removing a list of existing pre-computed models from the original MARCS grid and forcing their interpolation. This way, we compared the interpolated version calculated by iSpec with the original pre-computed models.

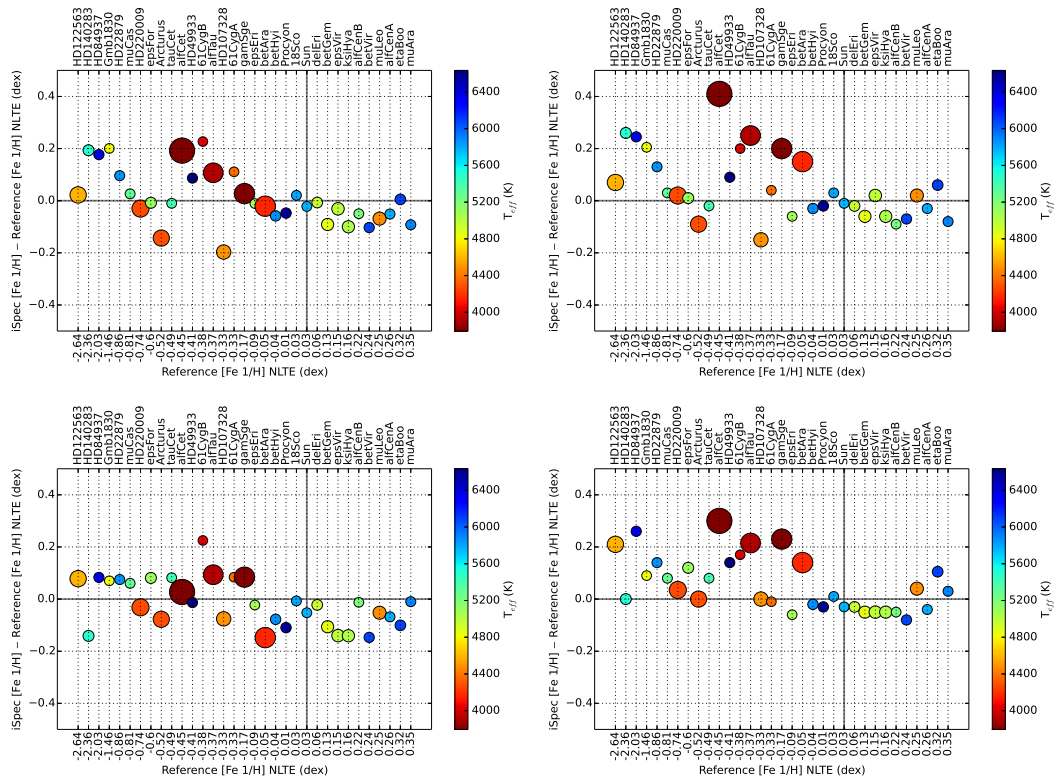


Figure 3.5 – Differences in neutral iron abundances between the reference (the Gaia FGK benchmark stars) and the derived value by iSpec, synthetic spectral fitting method (left) and equivalent width method (right) when using the atmospheric parameters found (top) and the reference values (bottom). Stars are sorted by metallicity; the color represents the temperature, and the size is linked to the surface gravity.

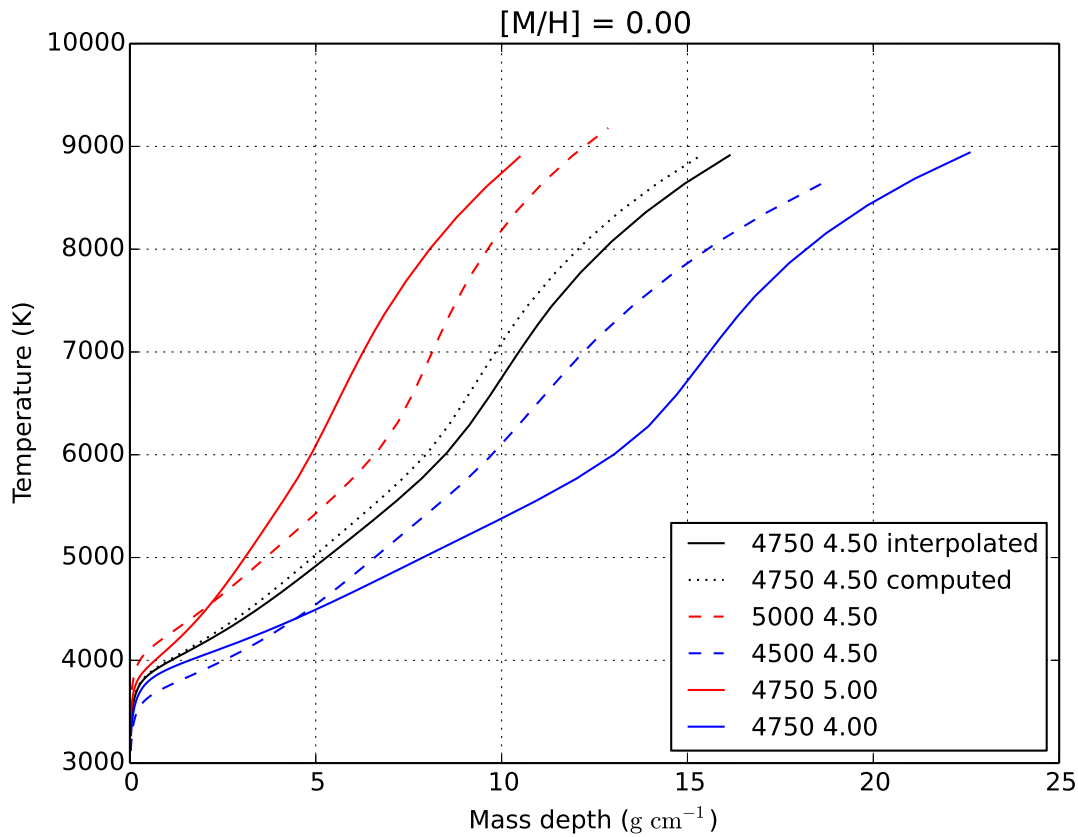


Figure 3.6 – Temperature (K) as a function of mass depth (g cm^{-1}) for a computed (dotted black) and an interpolated atmosphere (solid black) from upper and lower effective temperature models (dashed red and blue) and upper and lower surface gravity models (solid red and blue).

The models represent different stellar types (i.e., giants and dwarfs; metal-rich and poor) and they were selected not to be actually surrounded by any gap (i.e., missing model), as shown in Fig. 3.1. The test was performed for 42 model atmospheres that were the results from different combinations of the following parameters:

1. Effective temperature: 4750 and 3400 K
2. Surface gravity: 1.00, 2.00, 2.50, 3.00, 4.00 and 4.50
3. Metallicity: 1.00, 0.00, -1.00 , -2.00 , -3.00 and -4.00 .

The results show that the interpolated model atmosphere reproduces the overall shape of the pre-computed model (Fig. 3.6) with a small shift.

To understand the impact of these shifts, we generated pairs of synthetic spectra (with the interpolated and the pre-computed model) and compared their fluxes (ignoring regions near to the continuum). We found that the average flux difference is $-0.22\% \pm 2.12\%$. The spectra only differ in the central depth of the absorption lines (see Fig. 3.7). Additionally, we measured the equivalent width of a group of absorption lines and determined that the average difference is $0.10\% \pm 6.32\%$. As a reference, Blanco-Cuaresma et al. [2014b] estimated that the abundance analysis based on equivalent width methods shows a very small variation on the order of ± 0.007 dex in metallicity when equivalent widths are changed by 1% (based on the analysis of a solar spectrum).

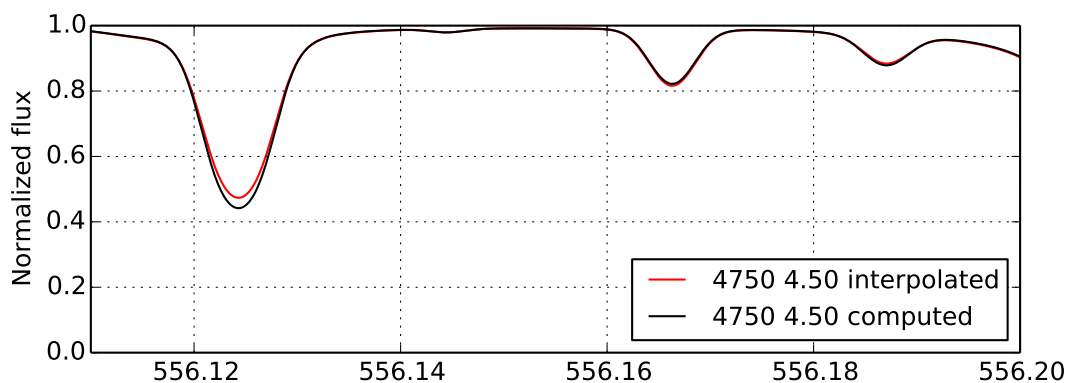


Figure 3.7 – Synthetic spectra using a computed (black) and interpolated (red) model atmosphere.

3.4.2 Minimization process

Iterations

The minimization process consists of several iterations where the free parameters are modified by a single amount to predict the next jump in the parameter space (see Sect. 3.2.4). In Table 3.8, we show the evolution of the differences compared with the reference values at each iteration and the cumulative number of spectra that have already converged toward a solution for the best configurations identified in Sections 3.3.2 and 3.3.2.

The synthetic spectral fitting technique seems to present good average results around the fifth to sixth iteration. Remarkably, the dispersion in effective temperature and surface gravity deteriorates from iteration six to ten in favor of a small improvement in the metallicity dispersion. The equivalent width method presents a more gradual evolution and the results do not stabilize until the ninth or tenth iteration.

When the number of iteration is limited to a maximum of 10, the average computation time for the synthetic spectral fitting technique is 36 minutes per spectrum, while for the equivalent width method it is about 19 minutes per spectrum⁹ (see also Sect. 3.3.2).

Correlations

Previous studies [e.g., Torres et al., 2012] found strong correlations between effective temperature, metallicity, and surface gravities when simultaneously solving for all three quantities with synthetic spectral fitting techniques, while the equivalent width methods did not show such a strong correlation.

We repeated the same analysis with our Gaia FGK benchmark stars. We rederived the effective temperatures and metallicities with surface gravities fixed to the reference value and compared them with the unconstrained results (Fig. 3.8).

The parameters are obviously correlated (see Pearson correlation coefficients in Table 3.9), but we see no strong differences that would depend on the method used for the analysis. However, the correlation is tighter for the spectral fitting technique. A change in surface gravity of 0.50 dex implies a difference in effective temperature of 129 and 157 K for the synthetic spectral fitting technique and the equivalent width method, respectively. For the metallicity, the impact is 0.10 dex for both methods.

9. Time estimated by using a computer with an Intel Xeon CPU at 3.07GHz (model X5675).

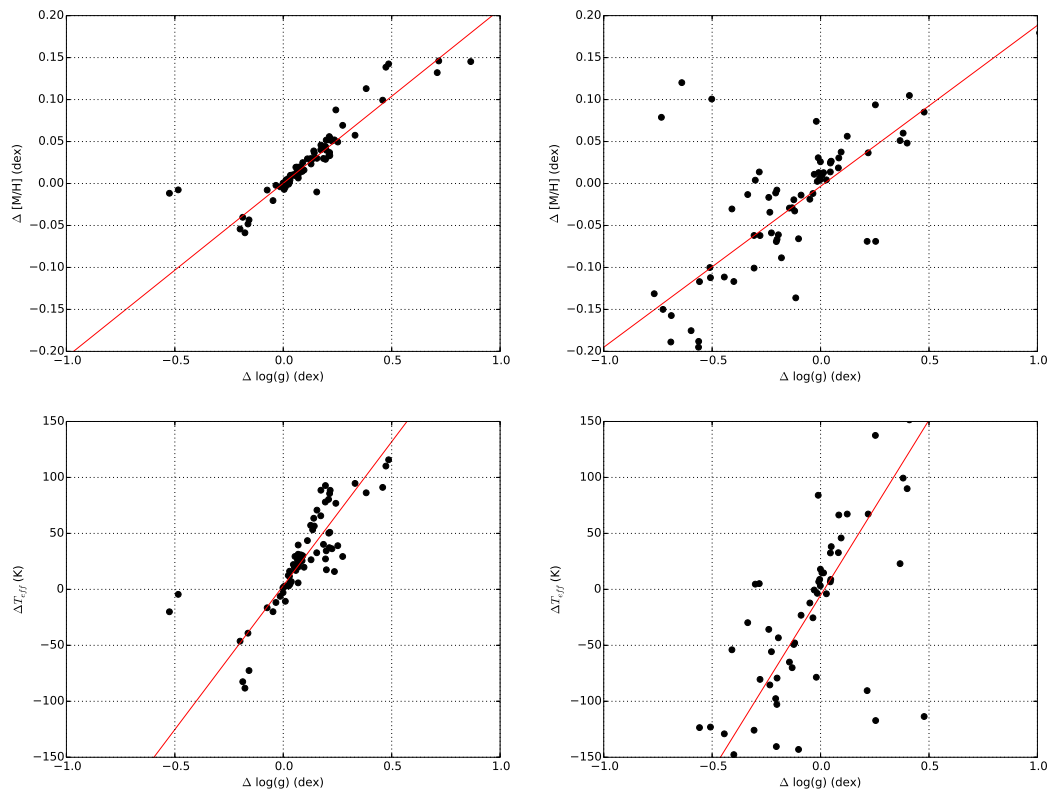


Figure 3.8 – Impact on the effective temperatures and metallicity derived from synthetic spectral fitting (left) and equivalent width method (right) when fixing the surface gravity to the reference value. A linear model was fitted (red line) and the differences correspond to the constrained minus unconstrained values.

Table 3.8 – Difference between the parameters derived from the two methods and the reference values on each iteration of the least-squares minimization process. The number of converged spectra per iteration is also included (78 in total).

Iteration	Synthetic spectral fitting							Equivalent width						
	ΔT_{eff}		$\Delta \log(g)$		$\Delta [M/H]$		Converged	ΔT_{eff}		$\Delta \log(g)$		$\Delta [M/H]$		Converged
	μ	σ	μ	σ	μ	σ		μ	σ	μ	σ	μ	σ	
1	36	530	0.30	0.87	0.03	0.36	0 (0%)	-15	560	0.22	1.01	0.20	0.43	0 (0%)
2	-52	177	0.12	0.50	0.05	0.23	0 (0%)	101	283	0.26	0.48	0.13	0.28	21 (27%)
3	-12	117	0.00	0.32	0.03	0.16	3 (4%)	146	271	0.24	0.47	0.14	0.26	38 (49%)
4	-12	124	-0.08	0.19	0.02	0.15	14 (18%)	139	267	0.23	0.47	0.13	0.26	63 (81%)
5	-14	121	-0.08	0.18	0.02	0.15	41 (53%)	140	266	0.23	0.46	0.12	0.26	67 (86%)
6	-15	120	-0.08	0.17	0.02	0.15	60 (77%)	137	259	0.22	0.45	0.12	0.26	70 (90%)
7	-16	119	-0.08	0.17	0.02	0.15	63 (81%)	133	251	0.21	0.45	0.12	0.26	71 (91%)
8	-19	120	-0.09	0.17	0.02	0.15	69 (88%)	134	244	0.20	0.45	0.12	0.26	73 (94%)
9	-22	122	-0.10	0.19	0.02	0.15	70 (90%)	136	241	0.20	0.44	0.12	0.27	76 (97%)
10	-24	124	-0.11	0.21	0.01	0.14	78 (100%)	135	241	0.20	0.44	0.12	0.27	78 (100%)

Table 3.9 – Linear model parameters ($y = mx + c$) fitted using the differences on the effective temperatures/metallicity and free or fixed surface gravity shown in Fig. 3.8. The Pearson correlation coefficients are also included.

		m	c	Pearson
Synthetic spectral fitting	T_{eff}	257	3	0.88
	[M/H]	0.21	0.00	0.90
EW	T_{eff}	313	-5	0.72
	[M/H]	0.19	0.00	0.74

It is worth noting that our analysis covers a broader parameter range: the Gaia FGK benchmark stars cover from 6600 to 3500 K in effective temperature, from 4.6 to 0.6 dex in surface gravity, and from 0.3 to -2.7 dex in metallicity, while [Torres et al. \[2012\]](#) analyzed stars between 6750 and 4800 K in effective temperature, 4.80 and 3.60 dex in surface gravity, and 0.5 and -0.4 dex in metallicity.

3.4.3 Signal-to-noise ratios and spectral resolutions

The Gaia FGK benchmark stars library consists of high-resolution and high signal-to-noise ratio spectra, but we also tested the limits of iSpec by analyzing spectra of lower quality. To do this, we generated and analyzed 34 synthetic spectra using the reference parameters of the Gaia FGK benchmark stars with different resolutions, and we added several levels of Poisson noise.

Our implementation of the synthetic spectral fitting technique seems to be more robust to noise than the equivalent width method (Table 3.10). The former derives atmospheric parameters very similar to the reference values with a signal-to-noise ratio of 25, while the latter constantly deviated, even with the highest signal levels. One possible reason is that the equivalent width method simplifies the problem by considering only the area of the absorption lines and not the whole profile. Measuring that area is quite sensitive to noise and errors in continuum placement. Then, the least-squares algorithm does not minimize the difference of N fluxes (as does the synthetic spectral fitting technique), but only three values: the two slopes to validate the ionization and excitation equilibrium, and the difference

between neutral and ionized iron abundance. This information loss may increase degeneracies between atmospheric parameters. Additionally, the tested implementation of the equivalent width method is strongly affected by the starting point in the parameter space. A incorrect initial estimate can lead to a poor solution. This also explains why the results for the spectra with a signal-to-noise ratio of 50 are poorer than those with a ratio of 40, for instance.

Regarding the spectral resolution, a lower resolution implies a higher number of blended lines. This has a higher negative impact on the equivalent width method, since abundances will be overestimated, while synthetic spectral fitting can reproduce and better match the blends even with resolutions as low as 7500 (Table 3.11).

Table 3.10 – Difference between the parameters derived from the two methods (using degraded synthetic spectra instead of observations) and the reference values for different levels of signal-to-noise ratio (S/N). The synthetic spectra had a resolution of 70,000.

S/N	Synthetic spectral fitting						Equivalent width					
	ΔT_{eff}		$\Delta \log(g)$		$\Delta [M/H]$		ΔT_{eff}		$\Delta \log(g)$		$\Delta [M/H]$	
	μ	σ	μ	σ	μ	σ	μ	σ	μ	σ	μ	σ
5	129	129	0.15	0.22	0.23	0.22	510	427	1.16	0.96	0.28	0.58
10	39	44	0.08	0.08	0.04	0.04	285	486	0.71	0.74	0.23	0.55
20	13	16	0.02	0.02	0.00	0.02	219	365	0.50	0.72	0.15	0.40
25	7	12	0.01	0.03	0.00	0.01	177	392	0.50	0.63	0.14	0.38
30	6	10	0.01	0.03	0.00	0.01	133	272	0.46	0.64	0.06	0.27
40	0	6	0.00	0.02	-0.01	0.01	149	293	0.39	0.61	0.02	0.21
50	3	5	0.00	0.02	-0.01	0.01	111	346	0.30	0.95	-0.01	0.26
100	2	5	0.00	0.01	0.00	0.01	155	261	0.37	0.59	-0.01	0.22

Table 3.11 – Difference between the parameters derived from the two methods (using synthetic spectra) and the reference values for different resolution levels. The synthetic spectra had a signal-to-noise ratio of 100. From lower to higher resolution, they approximately correspond to the surveys SDSS DR7 (R=1800-2200), Rave, Gaia RVS, GES Giraffe HR21, APOGEE, HERMES/GALAH, GES UVES and the standard resolution of the Gaia FGK benchmark stars library.

Resolution	Synthetic spectral fitting						Equivalent width					
	ΔT_{eff}		$\Delta \log(g)$		$\Delta [M/H]$		ΔT_{eff}		$\Delta \log(g)$		$\Delta [M/H]$	
	μ	σ	μ	σ	μ	σ	μ	σ	μ	σ	μ	σ
2000	56	192	0.14	0.67	-0.03	0.17	530	923	0.10	1.39	0.25	1.67
7500	2	13	0.00	0.03	0.01	0.01	629	874	-0.16	1.53	0.12	1.97
11500	4	6	0.00	0.02	0.01	0.01	769	574	0.69	1.42	0.53	0.39
16200	1	5	0.00	0.01	0.01	0.01	450	600	0.88	1.24	0.28	0.32
20000	1	3	0.00	0.01	0.00	0.00	324	440	0.82	1.10	0.25	0.34
28000	1	4	0.00	0.01	0.00	0.00	267	292	0.69	0.87	0.15	0.21
47000	1	4	0.00	0.01	0.00	0.01	218	217	0.47	0.57	0.06	0.23
70000	2	5	0.00	0.01	0.00	0.01	155	261	0.37	0.59	-0.01	0.22

3.5 Conclusions

iSpec is an integrated spectroscopic software framework with the necessary functions for determining of atmospheric parameters (i.e., effective temperature, surface gravity, metallicity) and individual chemical abundances. It relies on the widely known code SPECTRUM developed by R. O. Gray for spectral synthesis and derivation of abundances from equivalent widths.

We developed two different pipelines based on the synthetic spectral fitting technique and the equivalent width method by using iSpec. The high-resolution and high signal-to-noise spectra from the Gaia FGK benchmark star library were used to assess the pipelines. We showed the following:

1. The pipeline based on the synthetic spectral fitting technique provides more accurate and precise results.
2. The derived effective temperature, surface gravity, and metallicity parameters are correlated at a similar degree, independently of the technique used on each pipeline.
3. The pipeline based on synthetic spectral fitting technique is more effective with lower resolutions (i.e., 7500) and lower signal-to-noise ratios (i.e., 25) than the pipeline based on equivalent widths.

Additionally, we showed how the Gaia FGK Benchmark Star library can be used to assess and optimize spectroscopic pipelines. Taking advantage of this set of stars to verify and improve pipelines for spectroscopic analysis can lead to more reliable and comparable results.

Testing the chemical tagging technique with Open Clusters

Paper submitted to Astronomy and Astrophysics. The co-authors contribution was mainly focused on the compilations of spectral observations from different archives, they also proposed and carried out dedicated observing programs, and they helped with the interpretation of the results. I implemented the whole pipeline process from homogeneization to derivation of atmospheric parameters and abundances, executed the clustering algorithms and analyzed the results.

Contents

4.1	Introduction	94
4.2	Sample selection and observations	95
4.2.1	NARVAL spectra	95
4.2.2	HARPS spectra	96
4.2.3	UVES spectra	96
4.2.4	Data homogenization	96
4.3	Spectral analysis	97
4.3.1	Atmospheric parameters	97
4.3.2	Chemical abundances	98
4.3.3	Chemical outliers	100
4.4	Chemical tagging	102
4.4.1	Continuum normalization effects	102
4.4.2	Abundance and astrophysical parameter correlations	102
4.4.3	Clusters homogeneity	110
4.4.4	The role of different elements	117
4.5	Conclusions	117

4.1 Introduction

Understanding the formation and evolution of galaxies and their structure (e.g. disks) is an open issue in near-field cosmology. One approach to tackle this problem is to study our own Galaxy by unravelling the sequence of events that took place in the formation of the Galactic disk (where most star formation occurs). Unfortunately, most of the dynamical information is already lost since the disk was formed in a dissipative process and it evolved dynamically. Nevertheless, the chemical composition of the stars can potentially help us to recover the history of our Galaxy.

Stars are born in aggregates from molecular clouds [Shu et al., 1987, Meyer et al., 2000, Lada and Lada, 2003]. Hydrodynamical simulations indicate that the progenitor cloud undergoes fragmentation preventing contraction onto a single star [Jappsen et al., 2005, Tilley and Pudritz, 2004, Larson, 1995]. Hundreds to thousands of stars can be formed from one single cloud. If we assume that the progenitor cloud was chemically well-mixed [Feng and Krumholz, 2014], then we expect to observe homogeneous chemical composition in the stars formed from this cloud. With this information, we could use the method of chemical tagging to track individual stars back to their common formation sites as proposed by Freeman and Bland-Hawthorn [2002].

The viability of this approach depends on two critical issues: Do stars born together have a unique chemical signature? And, are the chemical signatures different enough to distinguish stars formed from different molecular clouds?

In this context, open clusters represent a fantastic laboratory to investigate their homogeneity and validate that their progenitor clouds were uniformly mixed. The majority of the stars formed in clusters in our Galaxy have already been dispersed into the field, but a few of them managed to stay gravitationally bound, probably, thanks to a higher formation rate and/or galactic orbits that avoided high density regions and giant molecular clouds [Friel, 1995, Finlay et al., 1995, van den Bergh and McClure, 1980]. Thus, old and intermediate-age clusters (age $> \sim 100$ Myr) are the leftovers of star forming aggregates in the Galactic disk that have managed to survive until the present day. We can be certain that their stars were born from the same molecular cloud at roughly the same period.

Additionally, since each molecular cloud has its own history of pollution by ejecta from core-collapse supernovae (i.e. Type II, Ib and Ic Supernovae where most of the α -element are produced), Type Ia supernovae (SNe Ia where most iron peak elements are created) and asymptotic giant branch stars (AGB where a s-process takes place), we expect different open clusters to have different chemical patterns.

There is some observational evidence for chemical homogeneity in open clusters. For instance, De Silva et al. [2006] present an abundance analysis of the heavy elements Zr, Ba, La, Ce, and Nd (their abundances are not thought to be modified during normal stellar evolution) for F-K dwarfs of the Hyades open cluster. They claimed that the abundances of member stars are highly uniform and they showed a scatter of the order of 0.06 dex for Zr, 0.05 dex for Ba, 0.03 dex for Ce, La, and Nd.

In a subsequent study, De Silva et al. [2007] measured the lighter elements Na, Mg, Si, Ca, Mn, Fe, Ni (apart from Zr and Ba) for 12 red giants of the old open cluster Collinder 261. They demonstrated again a high chemical homogeneity for this cluster finding a dispersion of 0.07 dex for Na, 0.05 dex for Mg and Ca, 0.06 dex for Si, 0.03 dex for Mn, 0.02 dex for Fe, and 0.04 dex for Ni. Additionally, they compared Collinder 261, the Hyades, and the HR 1614 moving group and could show that the three have unique chemical signatures.

The latter study was extended in De Silva et al. [2009], where the authors compiled abundances of 24 open clusters from the literature and showed that different clusters seem to have different chemical patterns (from average values). They observe significant dispersion for some elements, however one possible reason is systematic uncertainties among the different studies (e.g. use of different methods,

atomic data, model atmospheres).

Mitschang et al. [2013] quantified the level to which chemical tagging can distinguish between conatal stars (stars born at the same period and formation site) by developing a metric and deriving an empirical probability function based on chemical abundances for 35 clusters collected from the literature. The authors showed that achieving a high clustering detection efficiency is difficult and it depends on the level of uniqueness of conatal stars' chemical signatures.

Most of the previous studies were based on non-homogeneous determined abundances found in the literature. For instance, the use of different methods (e.g. equivalent width or synthetic spectral fitting), atomic data, model atmospheres and continuum normalization processes can lead to systematic errors. Other studies derive very accurate chemical abundances but in a non-automatic way (e.g. manual continuum and/or line fitting). Manual analysis is affected by the subjective criteria that can vary with time and is not easily feasible when a huge quantity of spectra should be analyzed. For instance, the on-going Gaia-ESO Public Spectroscopic Survey [GES; Gilmore et al., 2012] will target approximately 100,000 field and open cluster stars in the Galaxy and the GALactic Archaeology [GALAH; Anguiano et al., 2014] with HERMES [Barden et al., 2010] survey will target a million disk stars at high-resolution in a relatively short time-span.

To evaluate the potential of chemical tagging when using homogeneous and automatic analysis, we collected high-resolution spectra of open clusters' stars observed by different instruments, we implemented a completely automatic process to derive atmospheric parameters and chemical abundances, and we used machine learning algorithms to try to recover the original clusters from the homogeneously derived chemical abundances.

We describe the collected data in Sect. 4.2. The spectral analysis developed to derive the atmospheric parameters and chemical abundances is presented in Sect. 4.3. In Sect. 4.4 we explore the results of our analysis to validate the viability of the chemical tagging technique and, finally, the conclusions can be found in Sect. 4.5.

4.2 Sample selection and observations

We compiled 467 high-resolution spectra of which 101 come from the NARVAL instrument, 187 from HARPS and 179 from UVES. The initial selection criteria were: the spectral resolution is at least of 47,000 and the star is located in the field of view of a cluster. We mainly looked for clusters discussed on Paunzen et al. [2010] and Heiter et al. [2014], although we did not strictly limit the selection to these. Based on this dataset, a further selection process has been performed according to cluster membership and spectrum quality as described in Sect. 4.2.4.

4.2.1 NARVAL spectra

The NARVAL spectropolarimeter is mounted on the 2m Telescope Bernard Lyot [Aurière, 2003] located at Pic du Midi (France). The data from NARVAL were reduced with the Libre-ESpRIT pipeline [Donati et al., 1997]. These spectra were taken within a large programme proposed as part of the "Ground-based observations for Gaia" (P.I: C. Soubiran).

NARVAL spectra cover a large wavelength range ($\sim 300 - 1100$ nm), with a resolving power¹ that varies for different observation dates and along the wavelength range, typically from 75,000 around

1. The terms "resolving power" and "resolution" refer to the relation $R = \frac{\lambda}{\Delta\lambda}$, although we prefer to use the former when talking about instrumental capabilities and the latter for already observed spectra

400 nm to 85,000 around 800 nm. However, it is acceptable to initially assume a constant resolving power of $R \approx 81,000$ as we showed in Blanco-Cuaresma et al. [2014b].

4.2.2 HARPS spectra

HARPS is the ESO facility for the measurement of radial velocities with very high accuracy. It is fibre-fed by the Cassegrain focus of the 3.6m telescope in La Silla [Mayor et al., 2003]. The spectra were originally reduced by the HARPS Data Reduction Software (version 3.1). The data used in this work were taken from the public HARPS archive by selecting observed stars in the clusters' field of view.

The spectral range covered is 378 – 691 nm, but as the detector consists of a mosaic of two CCDs, one spectral order (from 530 nm to 533 nm) is lost in the gap between the two chips.

4.2.3 UVES spectra

The UVES spectrograph is hosted by unit telescope 2 of ESO's VLT [Dekker et al., 2000]. We took the spectra available from the Advanced Data Products collection of the ESO Science Archive Facility² (made available in October 2013) by selecting observed stars in clusters' field of view.

The setup used for each observation (CD#3, centered around 580 nm) provides a spectrum with two different parts which approximately cover the ranges from 476 to 580 nm (lower part) and from 582 to 683 nm (upper part).

4.2.4 Data homogenization

The wavelength range varies from one set of observations to another. We chose to limit the spectral analysis to the range between 480 and 680 nm, where all the spectra provide their best signal-to-noise ratio (S/N).

To increase the overall S/N, we co-added spectra corresponding to the same star when they were observed by the same instrument and with the same setup (i.e. same resolution). After co-addition, we discarded spectra with S/N lower than 40, which is an optimal level for determining atmospheric parameters with iSpec [Blanco-Cuaresma et al., 2014a].

All the spectra were convolved to 47,000, which is the minimum resolving power from our initial selection of spectra.

Observations were cross-correlated with a zero point template corresponding to a solar spectrum observed by NARVAL [Blanco-Cuaresma et al., 2014b]. The derived radial velocities were used to shift and align all the spectra.

We assume that cluster members share the same velocity vector with a small random dispersion, thus we discarded stars with a radial velocity higher/lower than the cluster's reference velocity ± 2 km/s (see Table 4.1), which is a reasonable limit considering the observed dispersion by previous studies such as Mermilliod et al. [2009]. We did not detect any double lined spectroscopic binary star in our dataset.

After co-addition and the second selection criteria (i.e., S/N higher than 40 and membership validation by radial velocity), the dataset is reduced to 266 spectra of which 51 come from the NARVAL

2. http://archive.eso.org/eso/eso_archive_adp.html

instrument, 101 from HARPS and 114 from UVES.

4.3 Spectral analysis

An automatic computational process was developed to derive atmospheric parameters and chemical abundances. The process is based on the integrated spectroscopic framework named iSpec [Blanco-Cuaresma et al., 2014a].

For the atmospheric parameter derivation we used the atomic data (without hyperfine structures and molecules) kindly provided by the GES line-list sub-working group prior to publication (Heiter et al., in prep.). The line-list covers our wavelength range of interest and it also provides a selection of middle and high quality lines (based on the reliability of the oscillator strength and the blend level) for iron and other elements (e.g. Na, Mg, Al, Si, Ca, Sc, Ti, V, Cr, Mn, Co, Ni, Cu, Zn, Sr, Y, Zr, Ba, Nd and Sm), which are ideal for the determination of chemical abundances.

As model atmosphere we used MARCS³ [Gustafsson et al., 2008] with the solar abundances from Grevesse et al. [2007]. It is worth noting that the model atmosphere grid is formed by a combination of plane-parallel and spherical models. The first is adequate for modeling the atmosphere of dwarf stars, while the second is more appropriate for giant stars. However, the synthesizer used by iSpec [SPECTRUM; Gray and Corbally, 1994] will interpret the spherical models as plane-parallel. The differences that may be introduced for F, G, and K giants are below 0.03 dex in terms of iron abundances as shown by Heiter and Eriksson [2006].

4.3.1 Atmospheric parameters

The determination of atmospheric parameters forms part of an iterative process, based on iSpec, where the continuum normalization also takes place. It consists of the following steps:

1. Blind normalization. At this stage we do not know the kind of star we are analyzing, thus we fit the continuum by using the default iSpec algorithm where the following general subprocesses are executed:
 - (a) Reduce the noise effects by applying a median filter with a window of 0.01 nm.
 - (b) Apply a maximum filter with a window of 1.0 nm to select those fluxes that have a larger probability to belong to the continuum.
 - (c) Fit second degree splines every 1.0 nm to the filtered points and divide the original observed spectrum by the fitted model.
2. Line fitting. For each spectrum, we fit the selected absorption lines with Gaussian profiles and we automatically discard lines that fall into one of these cases:
 - (a) Fitted Gaussian peak is too far away from the expected position (more than 0.0005 nm). Convection could produce shifts, but it is also possible that a strong close-by absorption line is dominating the region and blending considerably the original targeted line. The analysis would require manual inspection, thus we reject those lines.
 - (b) Bad fits with a root mean square bigger than 1.0 (e.g. extreme values due to a cosmic ray)
 - (c) Potentially affected by telluric lines (they are previously identified by cross-correlating with a telluric line mask).

3. <http://marcs.astro.uu.se/>

(d) Invalid fluxes (i.e. negative or inexistent due to gaps in the observation).

This verification process allows us to adapt the analysis to the peculiarities of each observation, ensuring that only the best quality regions are used.

3. Fast atmospheric parameter estimation. We use the synthetic spectral fitting technique implemented in *iSpec*, where a least-square algorithm compares the observed spectra with synthetic spectra. The compared regions correspond to the selected absorption lines from step 2 together with the wings of H- α , H- β and the Mg triplet (around 515-520 nm). The process estimates the following atmospheric parameters: effective temperature, surface gravity, metallicity, microturbulence, and macroturbulence. The rotational velocity is fixed to 2.0 km/s since it generally degenerates with the macroturbulence. To speed-up this first estimation, we limit the minimization algorithm to one iteration and we use a small pre-computed synthetic grid with key spectra (i.e. metal-rich/poor dwarf/giant). This process allows us to quickly distinguish dwarfs from giants and overall metallicities.
4. Guided normalization. The same steps described in the blind normalization stage are executed but after ignoring all the fluxes that have a value below 0.98 in their respective synthetic spectra (computed with the fast estimation of atmospheric parameters from step 3). This way, we reduce the effect of strong lines in the normalization process.
5. Line re-fitting. Step 2 is repeated with the new normalized spectra obtained from step 3.
6. Final atmospheric parameter determination: The same analysis described in step 3 is repeated but now the maximum number of iterations is increased to six, being an optimal value as shown in [Blanco-Cuaresma et al. \[2014a\]](#).

To reduce the dataset to mainly FGK stars in the main sequence and red giant branch, we discarded spectra for which we found an effective temperature higher than 6500 K/lower than 4500 K and a surface gravity higher than 4.60 dex/lower than 2.00 dex (same limits as in [Heiter et al. 2014](#)).

After this third selection criterion, 232 spectra are remaining which correspond to 189 stars. The selection covers the 32 clusters listed in [Table 4.1](#), where we included their coordinates, radial velocity, spectroscopic metallicity and age from the literature.

4.3.2 Chemical abundances

The metallicity obtained in the atmospheric parameter determination process (Sect. 4.3.1) corresponds to a global scaling factor that is applied to all the elements (taking the solar abundance as the reference point). In subsequent step, individual abundances are derived.

It has been shown that line-by-line differential analysis with a manual selection of lines can reach precision of 0.003 dex for solar twins [[Meléndez et al., 2012](#)]. In our case, all the analysis is automated and stars cover a wider parameter space, thus we cannot expect such a level of precision. Nevertheless, we developed a differential analysis where we have derived the solar absolute abundances of all the absorption line selection for 7 solar spectra included in the Gaia FGK Benchmark Stars library [[Blanco-Cuaresma et al., 2014b](#)]. The process follows these steps for each element and spectrum:

1. Derive the absolute abundances for each of the selected lines by using the synthetic spectral technique implemented in *iSpec*.
2. Calculate the relative abundances by subtracting the solar absolute abundances from the absolute abundances for each line.

Table 4.1 – List of analyzed clusters with the number of co-added spectra per instrument and other known cluster properties from the literature.

Cluster	HARPS	NARVAL	UVES	l (deg)	b (deg)	Distance (pc)	RV (km/s)	[M/H] (dex)	Age (Gyr)
Collinder350	-	1	-	26.75	14.66	280	-15.20	0.12	0.4
IC2714	8	-	4	292.40	-1.80	1240	-13.60	-0.03	0.3
IC4651	6	-	10	340.09	-7.91	890	-30.36	0.02	1.1
IC4756	-	-	3	36.38	5.24	480	-25.16	-0.01	0.7
M67	10	-	28	215.70	31.90	790	33.77	0.00	4.1
Melotte111	-	6	-	221.35	84.02	100	0.01	-0.01	0.7
Melotte20	-	1	-	146.57	-5.86	190	-2.04	-0.27	0.1
Melotte22	-	1	-	166.57	-23.52	130	5.41	-0.11	0.1
NGC1817	-	1	-	186.16	-13.10	1970	65.31	-0.16	0.4
NGC2099	-	5	-	177.64	3.09	1380	8.30	-0.09	0.4
NGC2251	-	2	-	203.58	0.11	1330	25.33	-0.03	0.3
NGC2360	8	-	4	229.81	-1.43	1890	27.69	-0.03	0.6
NGC2423	1	-	5	230.48	3.54	770	18.47	0.05	1.0
NGC2447	-	-	13	240.04	0.13	1040	22.08	-0.02	0.6
NGC2477	8	-	-	253.56	-5.84	1570	7.61	0.07	0.9
NGC2539	7	-	5	233.71	11.11	1360	29.23	-0.04	0.5
NGC2547	-	-	1	264.46	-8.60	360	14.00	-0.16	0.0
NGC2548	-	2	-	227.87	15.39	770	7.70	0.20	0.4
NGC2567	4	-	2	249.80	2.96	1680	36.71	0.05	0.3
NGC2632	2	15	1	205.92	32.48	190	34.07	0.00	0.6
NGC3114	-	-	2	283.33	-3.84	910	-1.72	-0.01	0.2
NGC3532	3	-	3	289.57	1.35	490	4.23	-0.07	0.4
NGC3680	-	-	8	286.76	16.92	940	1.28	-0.19	1.2
NGC4349	5	-	4	299.72	0.83	2180	-11.33	0.08	0.2
NGC5822	2	-	3	321.57	3.59	930	-29.31	-0.04	0.9
NGC6475	-	-	1	355.86	-4.50	300	-15.57	0.14	0.3
NGC6494	4	-	1	9.89	2.83	630	-8.08	0.12	0.3
NGC6633	1	-	3	36.01	8.33	380	-28.95	0.06	0.4
NGC6705	13	-	1	27.31	-2.78	1880	34.70	0.23	0.3
NGC6811	-	2	-	79.21	12.01	1220	7.28	-0.18	0.6
NGC6940	-	5	-	69.86	-7.15	770	7.89	-0.02	0.7
NGC752	-	7	-	137.13	-23.25	460	5.04	-0.01	1.1

Notes. Galactic coordinates and distances from [Dias et al. \[2002\]](#). Radial velocities from [Kharchenko et al. \[2005\]](#), [Carraro et al. \[2007\]](#), [Montalto et al. \[2011\]](#), [Francis and Anderson \[2012\]](#), [Hayes and Friel \[2014\]](#), [Donati et al. \[2014\]](#), [Friel et al. \[2014\]](#), and HARPS. Spectroscopic metallicities from [Heiter et al. \[2014\]](#). Indicative ages from [Dias et al. \[2002\]](#), [Paunzen and Netopil \[2006\]](#), [Pöhl and Paunzen \[2010\]](#), [Netopil and Paunzen \[2013\]](#).

3. Derive the final abundance for the spectrum by calculating the weighted average:

$$\bar{x}_w = \frac{\sum_{i=1}^n w_i x_i}{\sum_{i=1}^n w_i}, \quad (4.1)$$

where the weight is the inverse of the abundance error $w = \frac{1}{eA(X)^2}$ reported by iSpec, which is influenced by the spectral S/N and the goodness of fit.

4. The error associated to the final abundance is derived from the unbiased weighted sample dispersion:

$$\sigma_w = \frac{V_1}{V_1^2 - V_2} \sqrt{\frac{\sum_{i=1}^n w_i (x_i - \bar{x}_w)^2}{\sum_{i=1}^n w_i}}, \quad (4.2)$$

where $V_1 = \sum_{i=1}^n w_i$ and $V_2 = \sum_{i=1}^n w_i^2$.

We analyzed 211,606 lines corresponding to 9,258 element abundances, from which we discarded extreme values/errors which are clearly outliers (i.e. relative abundances bigger than 1.0 dex and smaller than -5.0 dex) and elements with only one measured line (we required at least two lines to be able to calculate the weighted sample dispersion).

The abundances that were successfully measured in all the spectra cover 17 species corresponding to 14 different elements. The list includes iron peak elements (V I, Cr I/II, Mn I, Fe I/II, Co I, Ni I), alpha elements (Mg I, Si I, Ca I, Ti I/II), odd-Z elements (Na I, Sc II) and s-process elements (Ba II, Y II).

4.3.3 Chemical outliers

Assuming that stars born together share the same chemical signature, we used the 17 abundances to identify outliers in each cluster. However, the low number of stars per cluster is a limiting factor for the detection of outliers. To overcome this limitation, firstly, we compressed the 17 dimensions (abundance values) by using the statistical procedure named Principal Component Analysis (PCA), where the abundances are converted into a set of linearly uncorrelated variables (named components) by applying an orthogonal transformation. The first principal component has the largest possible variance, and each subsequent component has the highest variance possible under the constraint that it is orthogonal to (i.e., uncorrelated with) the preceding components. [Ting et al. \[2012\]](#) illustrated the power of PCA to study and interpret stellar element abundances.

Secondly, using the two first components, we estimated and subtracted the central location in the PCA space for each independent cluster. Thus, all the clusters share the same central location (i.e. origin of coordinates in the PCA space) and outlying stars are placed farther away from there. It is important to minimize the impact of deviant values in the determination of clusters' central locations in the PCA space. Therefore, we used a robust estimator named Minimum Covariance Determinant (MCD) and the Mahalanobis distance [[Mahalanobis, 1936](#)], which can tolerate the effect of nearly 50% of contamination in the data [[Rousseeuw, 1984](#)] and for which there is a computationally fast and well-known algorithm [[Rousseeuw and Driessen, 1999](#)].

Finally, we redetermined the central location and scatter of all the stars applying again the same algorithm and assuming that all the cluster have similar dispersion. For multivariate normally distributed data, the Mahalanobis distances to the central location are approximately chi-square distributed with p degrees of freedom [χ_p^2 where $p = 2$ in our case since we use the two first principal components; [Filzmoser, 2004](#)]. We tagged as outliers those stars with a squared distance higher than the 80% quantile of the chi-squared distribution (see Fig. 4.1). It is worth noting that all the stars (2 in total) from NGC3114 were classified as outliers, they seem to be chemically too different compared to the typical dispersion of the rest of clusters.

After executing this procedure and discarding the identified outliers (see an example in Fig. 4.2), the dataset was reduced to 160 stars. The 29 discarded stars could be chemically peculiar or simply

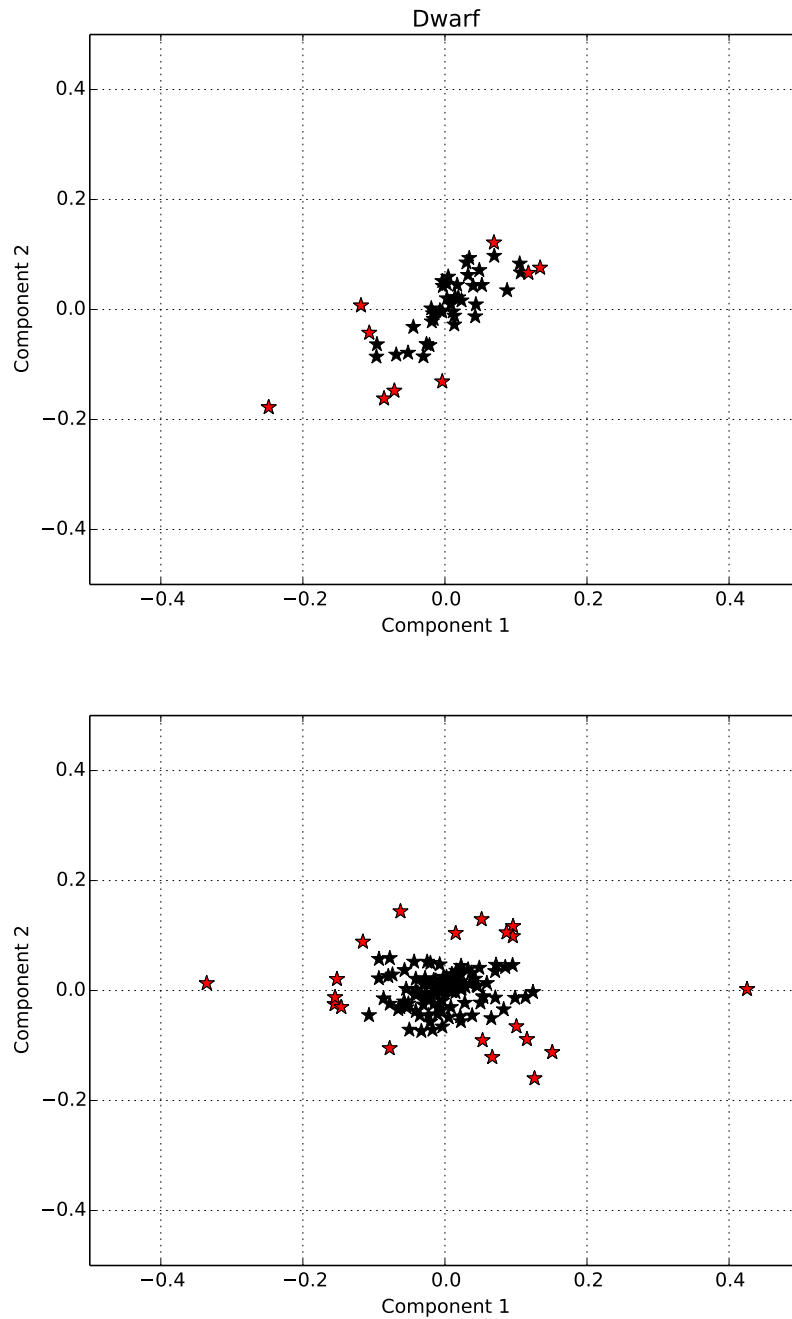


Figure 4.1 – Dwarf (left) and giant stars (right) from all clusters represented using the first two components of the PCA with the central cluster location subtracted. Stars chemically identified as outliers are shown in red.

not belong to the cluster. We decided not to perform any further detailed analysis of these stars since this would fall outside of the scope of this work. Detailed abundances per cluster and stellar type can be found in Table 4.7 and 4.8.

4.4 Chemical tagging

4.4.1 Continuum normalization effects

As pointed out in the introduction, some of the chemical studies found in the literature are based on non-homogeneous compilations of abundances, obtained from different sources and by different methods (e.g. equivalent width/synthetic spectra) and ingredients (e.g. atomic data, model atmospheres). This inhomogeneity implies systematic uncertainties that can mislead our scientific conclusions.

To illustrate the impact of those changes on the metallicity, we repeated our full analysis changing only one parameter in the continuum normalization process (see Section 4.3.1). We increased the median filter window from 0.01 to 0.04 nm, which globally lowers the continuum placement.

We used the iron abundance $[\text{Fe}/\text{H}]$ as a pertinent tracer of the metallicity, and we compared the values obtained from both slightly different normalization procedures. A small change in the normalization criteria produces a systematic average difference of -0.05 ± 0.02 dex.

When we compared both results (median filter window of 0.01 and 0.04nm) with open cluster metallicities found in the literature, we obtained the average differences of -0.05 ± 0.15 dex and 0.10 ± 0.14 dex, respectively (details in Table 4.2). The large dispersion confirms the inadequacy of mixing chemical abundances from different literature sources to draw solid scientific conclusions.

Nevertheless, among the two configurations, we preferred to continue using the median filter windows of 0.01 nm since it provides results more centered with respect to the current literature values.

For the rest of abundances, we chose to work in terms of $[\text{X}/\text{Fe}]$ ⁴ since this way we can partially cancel out the effect of different continuum placements.

4.4.2 Abundance and astrophysical parameter correlations

Previous works have already detected trends in chemical abundances with effective temperature and surface gravity for metal poor globular clusters, measuring iron abundances smaller in the turnoff stars than in the red giants of the order of 30% or 0.13 dex [Korn et al., 2007, Lind et al., 2008, Nordlander et al., 2012, Gruyters et al., 2013].

Systematic differences were also found for open clusters with metallicities closer to solar such as M67 [Önehag et al., 2014], NGC5822 or IC4756 [differences higher than 0.15 dex for Na, Si and Ti; Pace et al., 2010].

The assumption of Local Thermodynamic Equilibrium (LTE) may introduce systematic errors and abundance trends when analyzing stars covering large intervals of effective temperatures, surface gravities and metallicities. For instance, Randich et al. [2006] exposes that the Na difference between dwarfs and giants in M67 can be explained by NLTE effects that are larger for cool giants than for warm dwarfs [Mashonkina et al., 2000].

4. By definition, $[\text{X}/\text{Y}] \equiv \log_{10}(\text{N}_X/\text{N}_Y)_{\text{star}} - \log_{10}(\text{N}_X/\text{N}_Y)_{\odot}$, where N_X and N_Y are the abundances of element X and element Y respectively.

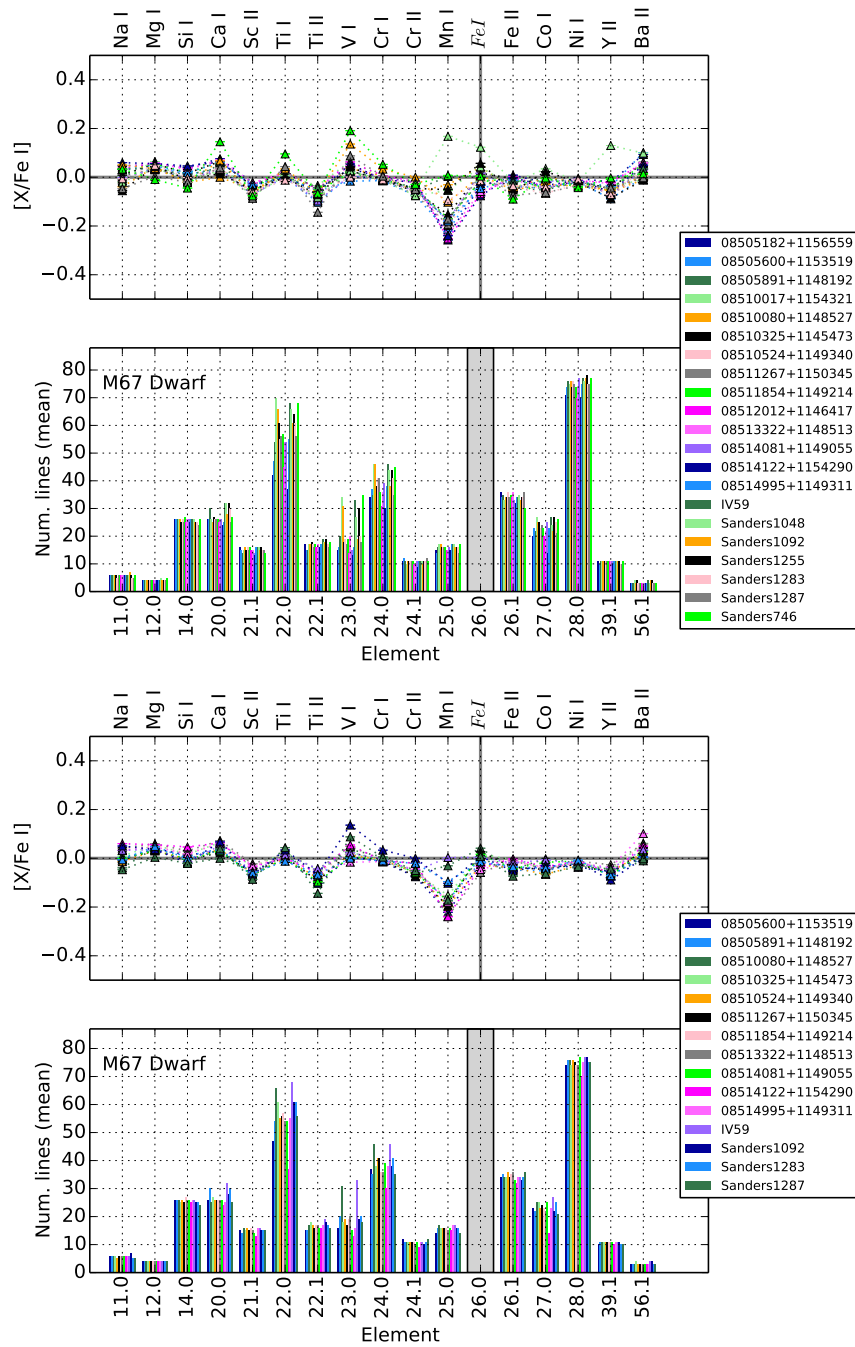


Figure 4.2 – Abundances (top) and mean number of lines used (bottom) in function of species (element code at top, atomic number and ionization state in Kurucz format at bottom where '0' is neutral and '1' is ionized) for M67 dwarfs showing all the analyzed stars (left) and after filtering outliers (right). All the abundance ratios are referenced to iron except iron itself, which is relative to hydrogen. Each color represents a star with an identification name shown in the legend.

Table 4.2 – Iron abundances from neutral lines when using two slightly different normalization processes and comparison to literature metallicities.

cluster	[Fe I/H] ₁			[Fe I/H] ₂			Δ_{Cont}	★
	\bar{x}_w	σ_w	Δ_{Lit}	\bar{x}_w	σ_w	Δ_{Lit}		
Collinder350	-0.06	-	-0.18	-0.11	-	-0.23	-0.05	1
IC2714	-0.14	0.04	-0.11	-0.16	0.04	-0.13	-0.02	7
IC4651	0.00	0.10	-0.02	-0.04	0.08	-0.06	-0.04	9
IC4756	-0.06	0.01	-0.05	-0.09	0.01	-0.08	-0.03	3
M67	-0.06	0.07	-0.06	-0.11	0.06	-0.11	-0.05	27
Melotte111	-0.06	0.03	-0.05	-0.12	0.03	-0.11	-0.06	4
Melotte20	0.12	-	0.39	0.03	-	0.30	-0.09	1
Melotte22	0.03	-	0.14	-0.08	-	0.03	-0.11	1
NGC1817	-0.17	-	-0.01	-0.23	-	-0.07	-0.06	1
NGC2099	0.05	0.02	0.14	0.04	0.03	0.13	-0.01	5
NGC2251	-0.07	0.01	-0.04	-0.10	0.00	-0.07	-0.03	2
NGC2360	-0.13	0.03	-0.10	-0.16	0.03	-0.13	-0.03	7
NGC2423	0.03	0.01	-0.02	0.00	0.01	-0.05	-0.03	2
NGC2447	-0.09	0.03	-0.07	-0.15	0.03	-0.13	-0.06	6
NGC2477	-0.04	0.02	-0.11	-0.08	0.02	-0.15	-0.04	5
NGC2539	-0.06	0.04	-0.02	-0.09	0.04	-0.05	-0.03	8
NGC2547	-0.12	-	0.04	-0.19	-	-0.03	-0.07	1
NGC2548	-0.04	0.00	-0.24	-0.09	0.00	-0.29	-0.05	2
NGC2567	-0.15	0.03	-0.20	-0.18	0.02	-0.23	-0.03	4
NGC2632	0.14	0.05	0.14	0.08	0.03	0.08	-0.06	16
NGC3114	-0.04	0.04	-0.03	-0.06	0.04	-0.05	-0.02	2
NGC3532	-0.12	0.03	-0.05	-0.15	0.03	-0.08	-0.03	3
NGC3680	-0.12	0.07	0.07	-0.16	0.05	0.03	-0.04	5
NGC4349	-0.18	0.04	-0.26	-0.21	0.03	-0.29	-0.03	4
NGC5822	-0.08	0.03	-0.04	-0.11	0.02	-0.07	-0.03	2
NGC6475	0.09	-	-0.05	0.04	-	-0.10	-0.05	1
NGC6494	-0.12	0.03	-0.24	-0.15	0.03	-0.27	-0.03	4
NGC6633	-0.05	0.02	-0.11	-0.08	0.01	-0.14	-0.03	4
NGC6705	-0.10	0.05	-0.33	-0.12	0.04	-0.35	-0.02	13
NGC6811	-0.08	0.01	0.10	-0.13	0.01	0.05	-0.05	2
NGC6940	0.03	0.01	0.05	-0.02	0.02	0.00	-0.05	3
NGC752	-0.08	0.01	-0.07	-0.12	0.01	-0.11	-0.04	7

Notes. [Fe I/H]₁ normalized with a median filter window of 0.01 nm, [Fe I/H]₂ normalized with a window of 0.04 nm, Δ_{Lit} corresponds to the difference with literature metallicities [Heiter et al., 2014, Paunzen et al., 2010, Dias et al., 2002], Δ_{Cont} represents the difference between [Fe I/H]₁ and [Fe I/H]₂. The number of stars is indicated in the last column (★).

Furthermore, we need to be aware of hyperfine structure effects [Huehnermann, 1993] caused by line splittings or line shifts due to the interaction of the electrons with the nucleus (usually smaller than the fine structure due to mutual interaction of the electrons). As mentioned in Sect. 4.3, the atomic data used in the analysis do not include hyperfine structure and some abundances (i.e. V, Mn, Co, Ba) might be affected by that [Booth and Blackwell, 1983].

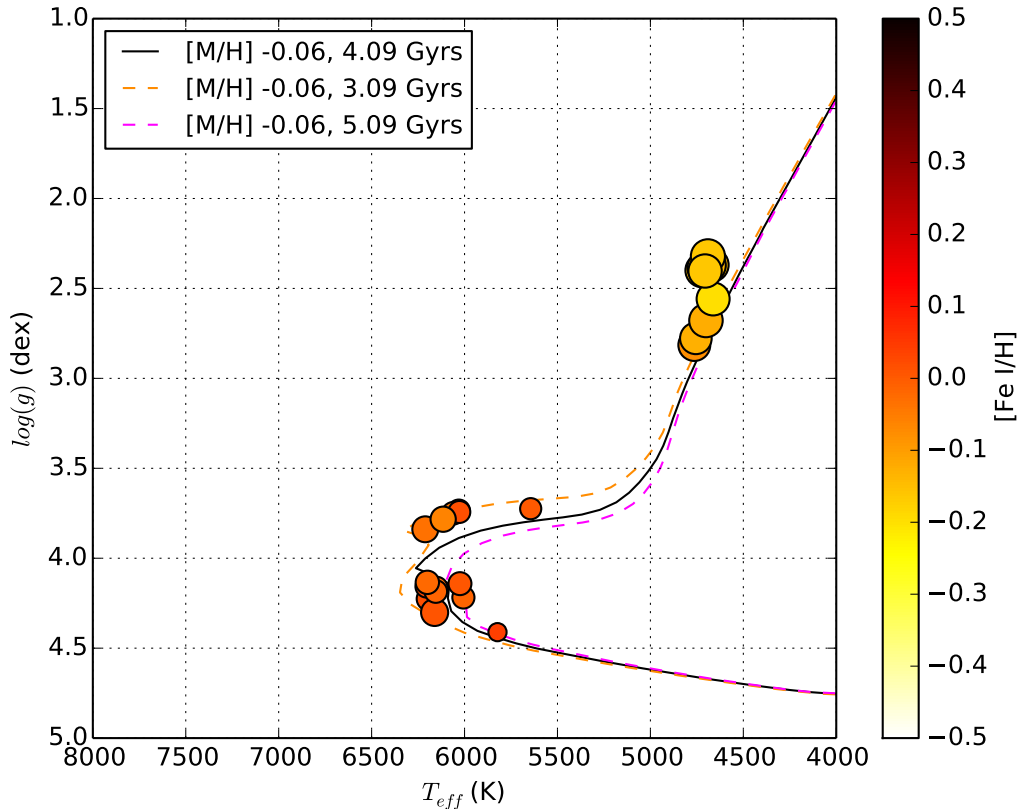


Figure 4.3 – Hertzsprung–Russell diagram for M67 with Yonsai-Yale isochrones [3 different ages; Demarque et al., 2004], color scale corresponding to the neutral iron abundance and size represents abundance dispersion.

The depletion of some elements could also be caused by the atomic diffusion (pushing heavier elements in the direction of increasing pressure and temperature) that takes place during the main sequence lifetime of the star and modifies the chemical composition of the stellar atmosphere. The effect is element-specific since radiative levitation reduces the gravitational acceleration (caused by the interaction of photons with gas particles) and acts selectively on different atoms and ions. When the star evolves toward the red giant branch, elements previously drained from the surface are mixed up again as the outer convection zone gradually reaches deeper layers.

We observe a correlation between iron abundance and effective temperature/surface gravity (see Fig. 4.3), but in the opposite sense. For instance M67 dwarfs are more metal rich (0.00 dex) than giants (-0.13 dex). As shown in Blanco-Cuaresma et al. [2014a], when deriving the effective temperature, surface gravity and metallicity at the same time from spectra, degeneracies among those parameters lead to correlations where lower metallicities are found for lower surface gravities and vice versa.

Consequently, chemical abundances derived for stars in different evolutionary stages might be affected by NLTE effects, hyperfine structure, atomic diffusion processes and correlations from atmospheric parameter determinations. The NLTE effects can be partly cancelled out only for solar dwarf by performing differential analysis (see Sect. 4.3.2), and the effects from parameter determinations can be minimized by working with $[X/Fe]$ ratios⁵ (see Fig. 4.4). Additionally, to reduce these effects in our work, we decided to divide each cluster in two subgroups formed by dwarfs and giant stars (i.e. $\log(g) \leq 3.5$ dex).

5. $[X/Fe] = [X/H] - [Fe/H]$

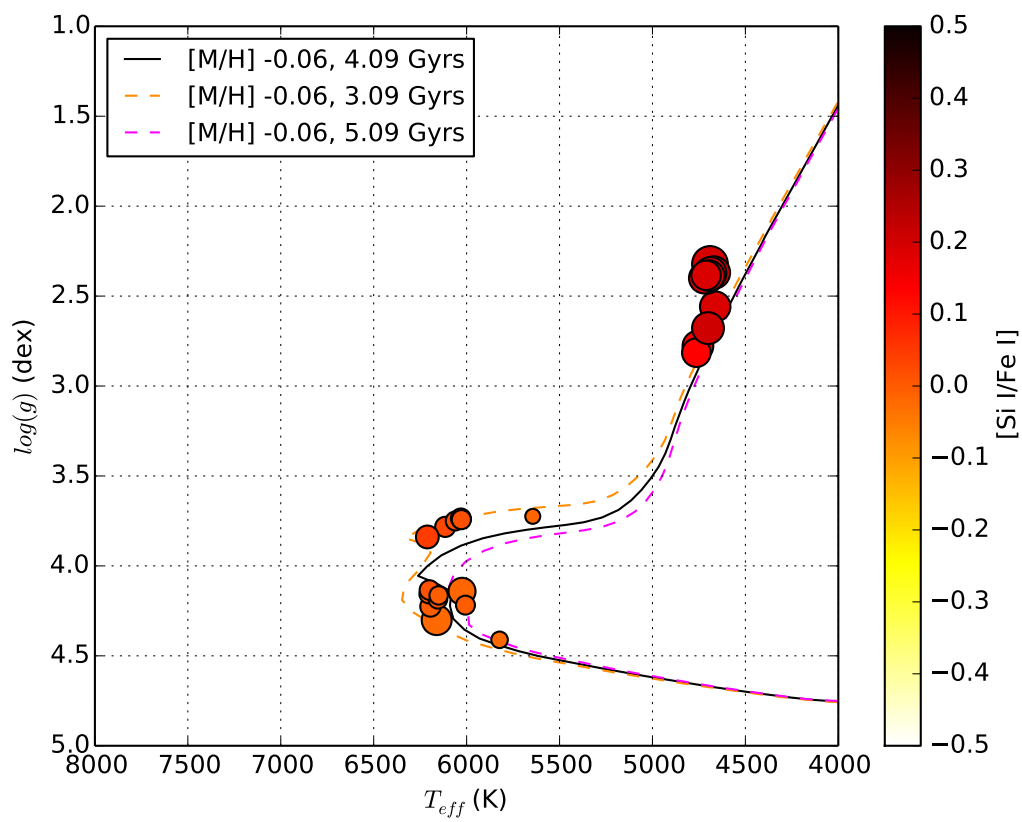


Figure 4.4 – Hertzsprung–Russell diagram for M67 with Yonsei-Yale isochrones [3 different ages; [Demarque et al., 2004](#)], color scale corresponding to the silicon abundance and size represents abundance dispersion.

It is worth noting that the outlier detection process (see Sect. 4.3.3) was executed at this subgroup level for each cluster, otherwise we would have detected a significant number of false outliers due to this stellar processes.

In Fig. 4.5 we present the chemical pattern for M67, one of the clusters with a high number of spectra in our dataset. The signature is different for each subgroup and the elemental abundance dispersion is lower when we subdivide clusters per evolutionary stages. The chemical differences for M67 and IC4651 stars in various evolutionary stages for each analyzed element are shown in Table 4.3. We observe that V I, Mn I, Co I, Mg I, Si I, and Na I are effectively enhanced for evolved stars with increases higher than 0.10 dex (we prioritize abundances for neutral elements when possible since we have more lines for them). The rest present smaller variations that in most of the cases fall inside the error margins (lower than 0.05 dex).

Table 4.3 – Chemical differences for M67 and IC4651 stars in different evolutionary stages.

		M67		IC4651	
		D	ΔG	D	ΔG
Iron peak	[Fe I/H]	0.00	-0.13	0.09	-0.19
	[Fe II/Fe]	-0.03	0.13	-0.01	0.04
	[V I/Fe]	0.02	0.13	0.05	0.12
	[Cr I/Fe]	0.00	-0.01	0.00	-0.01
	[Cr II/Fe]	-0.05	0.11	-0.02	0.05
	[Mn I/Fe]	-0.09	0.56	-0.08	0.55
	[Co I/Fe]	-0.02	0.21	-0.02	0.21
	[Ni I/Fe]	-0.02	0.05	-0.03	0.06
α elements	[Mg I/Fe]	0.04	0.11	0.00	0.13
	[Si I/Fe]	0.00	0.19	0.00	0.18
	[Ca I/Fe]	0.04	-0.01	0.04	0.02
	[Ti I/Fe]	0.01	-0.03	-0.02	0.01
	[Ti II/Fe]	-0.06	0.09	-0.09	0.09
Others	[Na I/Fe]	0.01	0.22	-0.03	0.26
	[Sc II/Fe]	-0.05	0.07	-0.09	0.11
	[Ba II/Fe]	0.02	0.03	0.01	0.03
	[Y II/Fe]	-0.06	-0.04	-0.05	-0.02

Notes. Dwarfs (D) values and differences relative to giants (G) where $G = D + \Delta G$. Iron abundances from neutral lines ([Fe I/H]) were used as a proxy for total iron abundance ([Fe/H])

An alternative approach to visually evaluate the chemical differences between subgroups is to reduce the 17 dimensions to two components using PCA as shown in Fig. 4.6. Dwarfs reside in a clearly different parameter space compared to giants, showing that the subgroups have evident distinguished chemical patterns.

Regardless of whether these abundance enhancements are real or due to systematic errors, they have important implications that we cannot ignore for the chemical tagging technique when applied to stars in very different evolutionary stages.

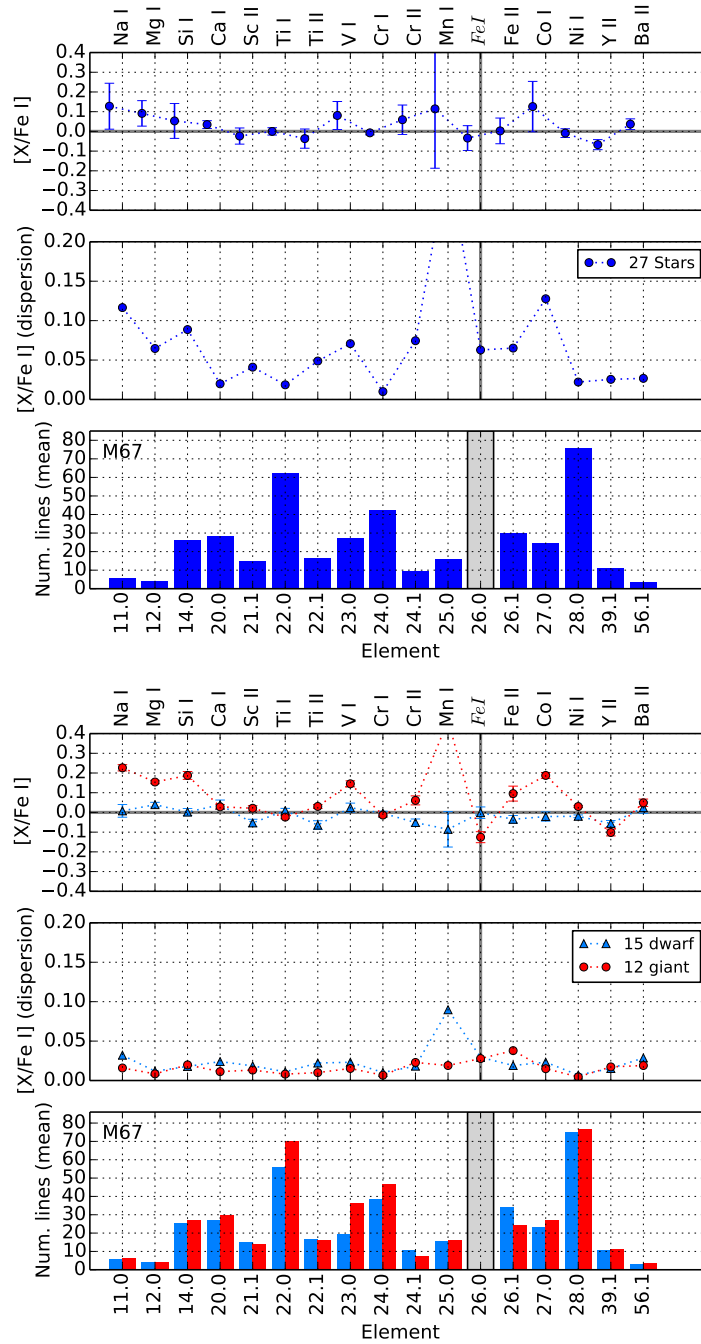


Figure 4.5 – Average chemical abundances (top), dispersion (middle) and mean number of lines (bottom) used for M67 stars (left) and divided in four stellar type groups (right). All the abundance ratios are referenced to iron except iron itself, which is relative to hydrogen.

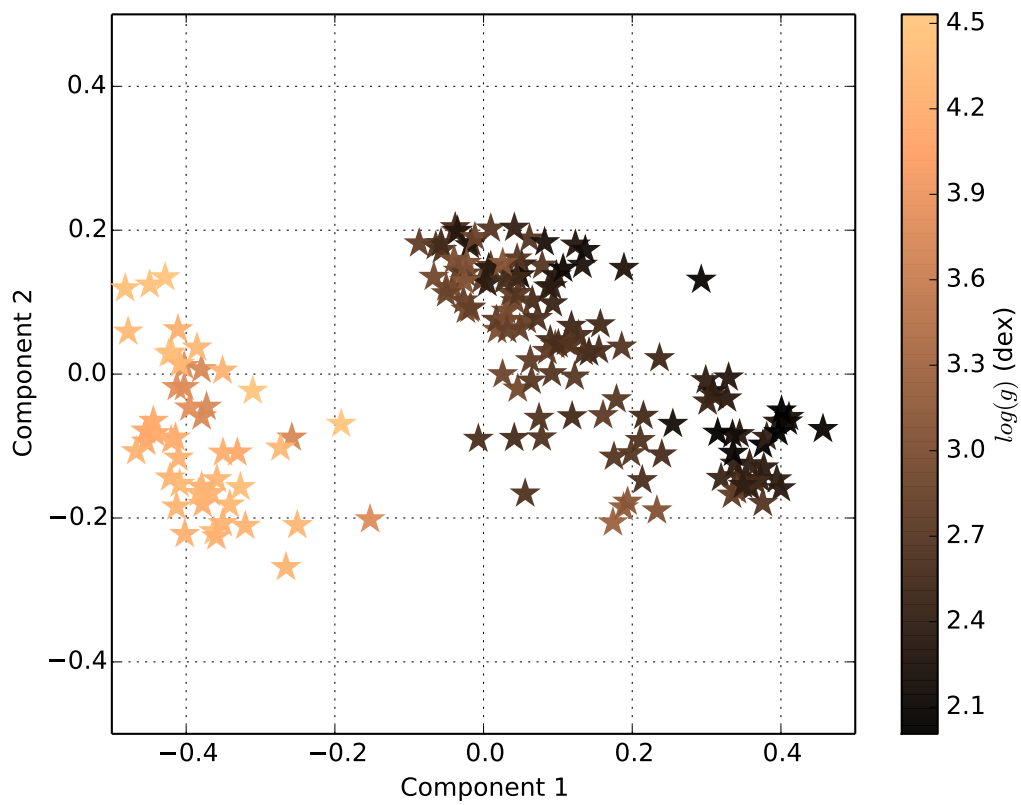


Figure 4.6 – Abundances represented by the two first principal components. The surface gravity of each star is encoded in a color scale bar.

4.4.3 Clusters homogeneity

To evaluate the viability of the chemical tagging technique, we performed a blind chemical tagging experiment designed to recover the initial stellar groups by only using the chemical abundances and the total number of clusters. We should recall that we discarded stars considered outliers based on their chemical signature, thus this should make the task easier than a real scenario with unknown stellar groups (i.e. field stars). Additionally, in this experiment we also discarded 6 clusters for which we only have one star per stellar type (i.e. dwarfs and giants).

[Mitschang et al. \[2013\]](#) already designed an algorithm and a metric to recover clusters and they tested it by using abundances collected from the literature. Even if their method seems to be very adequate for this kind of problem, we preferred to perform our analysis with well established machine learning algorithms such as K-Means [also known as Lloyd's algorithm, [Lloyd, 1982](#)], for which the benefits and drawbacks have already been widely studied.

K-Means clustering aims to partition the observations (one observation would be one star with its measured abundances) into K clusters in which each observation belongs to the cluster with the nearest mean (called centroid). Given a fixed number of clusters, K-Means clustering is reduced to an optimization problem where it finds the K centroids and assigns the observations to the nearest one, such that the squared distances are minimized.

The election of the number of clusters is usually a limitation if no a priori information is available, in our case we provided the real number of clusters. Another known drawback is that this algorithm tends to find clusters of comparable spatial extent, it often cuts incorrectly the borders in between clusters (the algorithm optimizes cluster centers, not cluster borders) and the final results might depend on the initial position of the centroids. To address the latter, we used a variation of the algorithm named K-Means++ which optimizes the position of the (initially random) centroid with a probability proportional to its squared distance from the closest observation [[Arthur and Vassilvitskii, 2007](#)].

There are other clustering algorithms publicly available, such as affinity propagation [[Frey and Dueck, 2007](#)] and DBSCAN [[Ester et al., 1996](#)], with different advantages and drawbacks. After evaluating the alternatives, we preferred to use the widely used K-Means++ because it yielded better results for this particular experiment and it does not include parameters difficult to interpret from a physical point of view.

To evaluate the goodness of the clustering, we used the following well-known metrics:

1. V-measure⁶ [[Hirschberg and Rosenberg, 2007](#)] is a harmonic mean between homogeneity and completeness:

$$v = 2 \times \frac{\text{homogeneity} \times \text{completeness}}{\text{homogeneity} + \text{completeness}}, \quad (4.3)$$

- (a) Homogeneity: A clustering result satisfies homogeneity if all of its predicted clusters contain only data points which are members of one real open cluster. Score is between 0.0 and 1.0 and the latter stands for perfectly homogeneous labeling.
 - (b) Completeness: A clustering result satisfies completeness if all the data points that are members of a given real open cluster are elements of the same predicted cluster. Score is between 0.0 and 1.0 and the latter stands for perfectly complete labeling.
2. Silhouette coefficient [[Rousseeuw, 1987](#)]: Measures the concepts of cluster cohesion (favoring models which contain tightly cohesive clusters) and cluster separation (favoring models which contain highly separated clusters). The coefficient is calculated as:

6. The 'V' stands for "validity", in the sense of the goodness of a clustering solution.

$$s = \frac{d_{\text{inter}} - d_{\text{intra}}}{\max(d_{\text{intra}}, d_{\text{inter}})} \quad (4.4)$$

where d_{intra} is the mean intra-cluster distance and d_{inter} is the mean nearest-cluster distance. Negative values (never smaller than -1) indicate that most of the stars are assigned to a wrong cluster, values close to zero indicate the existence of overlapping clusters and values close to 1.0 indicate that the stars of a given cluster are similar to each other and well-separated to other clusters.

The clustering configurations that maximizes the V-measure and the mean silhouette coefficient is the most optimal. We found the best results when the clustering algorithm is run separately in groups divided by stellar types (i.e. dwarfs and giants) and with only 2 or 3 principal components (built from the 17 abundances; see Table 4.4).

For all the configurations, the silhouette coefficient is under 0.50, indicating that the structure found is reasonable but weak. There is a non-negligible chemical overlapping among stars of different clusters.

Table 4.4 – Clustering metrics for different stellar groups and dimensions.

	D	H	C	V-Measure	Silhouette
All 25 clusters	2	0.70	0.68	0.69	0.41
	3	0.74	0.72	0.73	0.40
	4	0.76	0.72	0.74	0.35
	5	0.76	0.72	0.74	0.33
	10	0.77	0.73	0.75	0.26
	17	0.72	0.71	0.72	0.27
	17*	0.72	0.71	0.72	0.27
	Dwarfs 6 clusters	2	0.75	0.68	0.71
3		0.69	0.67	0.68	0.42
4		0.63	0.60	0.61	0.33
5		0.62	0.58	0.60	0.30
10		0.66	0.68	0.67	0.28
17		0.66	0.68	0.67	0.27
17*		0.66	0.68	0.67	0.27
Giants 24 clusters		2	0.71	0.70	0.71
	3	0.79	0.78	0.79	0.36
	4	0.77	0.77	0.77	0.32
	5	0.80	0.79	0.80	0.30
	10	0.77	0.78	0.78	0.27
	17	0.77	0.77	0.77	0.25
	17*	0.77	0.77	0.77	0.25

Notes. The number of dimension (D) refers to the number of principal components used, except those marked with * where the non-transformed abundances were used. The V-Measure is calculated from the homogeneity (H) and completeness (C) values.

The clustering analysis (using 2 principal components) groups together stars from different open clusters (see Tables 4.5, and 4.6; Fig. 4.7, and 4.8) pointing out that, for the analyzed elemental abundances, the clusters' chemical signature are not significantly different. If we focus our attention

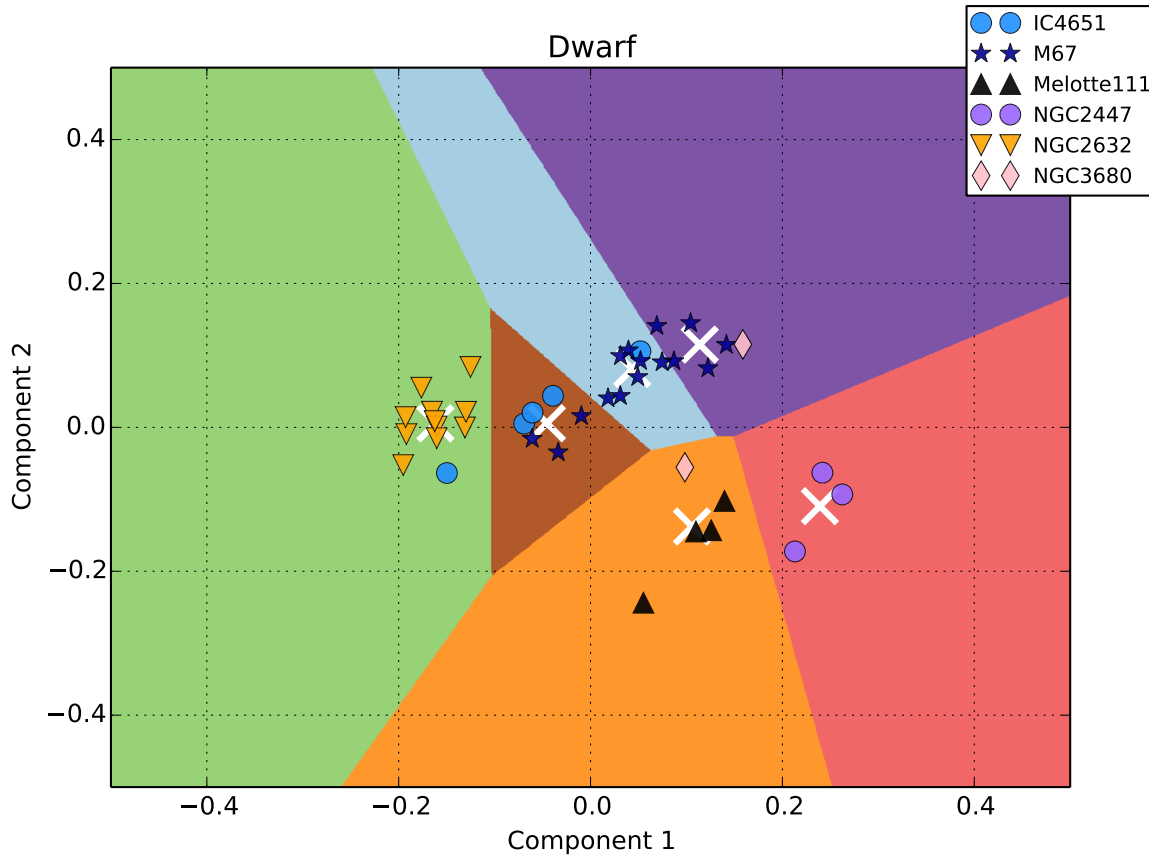


Figure 4.7 – Dwarfs represented using the first two components of PCA. Background colors correspond to the clusters found by the K-Means algorithm. Centroids are marked with white crosses.

on giants (where there is a higher number of stars), the identified groups "N. 19 G"⁷ and "N. 23 G" contain all the stars from M67 and IC4651 which are effectively very similar (see Fig. 4.9) but different from others. For instance, the group "N. 21 G" is different from M67 but at the same time it contains stars from 6 different open clusters such as NGC6494 and IC2714 which are definitely similar as seen in Fig. 4.10.

To estimate an order of magnitude of the star contamination level, we linked each group (found by the K-Means++ algorithm) to the open cluster from which it contains the most number of stars (unless the open cluster was already assigned) and we found that around 30-50% of the stars are not assigned to their expected cluster. The more open clusters are included into the analysis, the higher is the contamination percentage. Considering that it has been estimated that about 10^8 clusters were dissolved in the Galaxy [Bland-Hawthorn and Freeman, 2004], we expect a severe contamination when applying the chemical tagging technique to field stars in order to recover conatal aggregates.

For the giant case, where the number of stars is higher, there might exist a correlation between the two first principal components and the stellar ages. In Fig. 4.11 we see that the stars with a lower value in the two first components belong to younger clusters, while older stars have lower values in the first component but higher in the second one. The correlation seems to follow a semi-circular path in that visualization of the PCA space. Thus, this keeps open the possibility of finding coeval aggregates (stars born at the same period although not necessary from the same molecular cloud) by using the chemical tagging technique.

7. The identified groups are named as "N. [number] [G or D for giant or dwarf] and they are listed in Tables 4.5, and 4.6

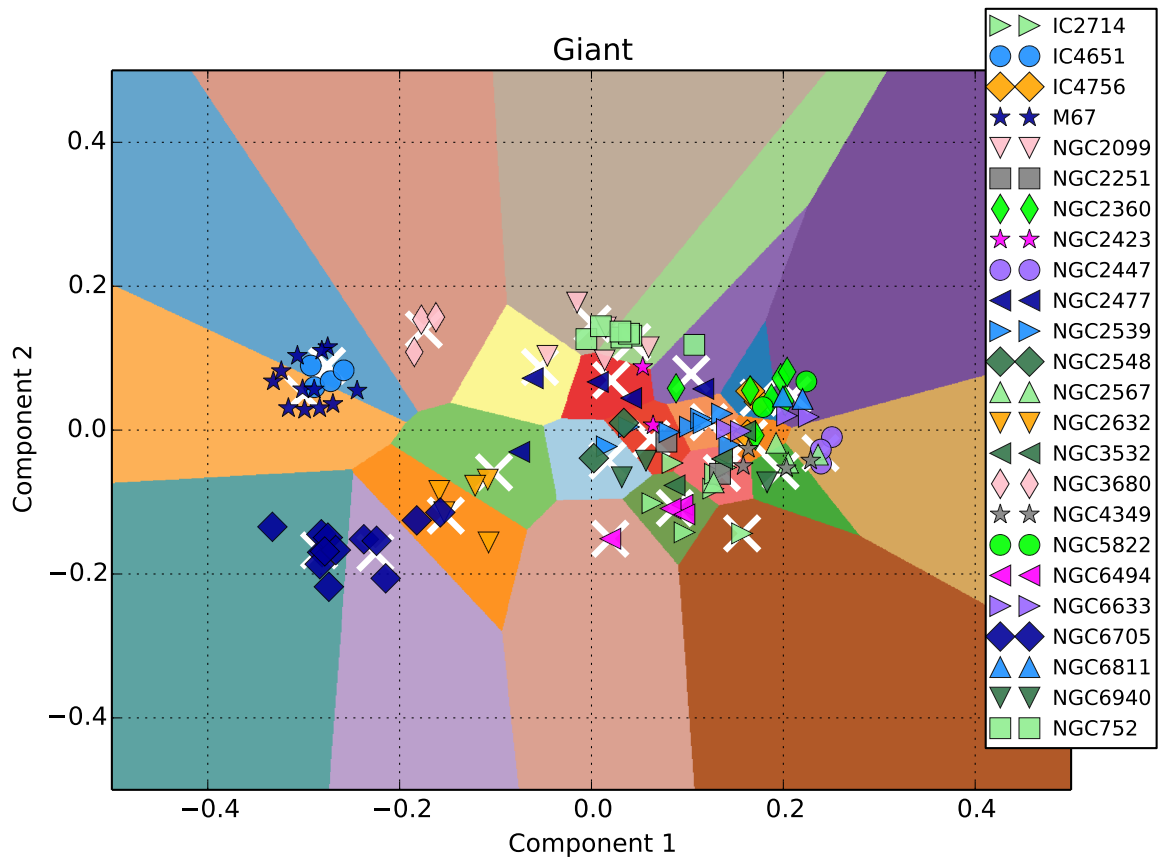


Figure 4.8 – Giants represented using the first two components of PCA. Background colors correspond to the clusters found by the K-Means algorithm. Centroids are marked with white crosses.

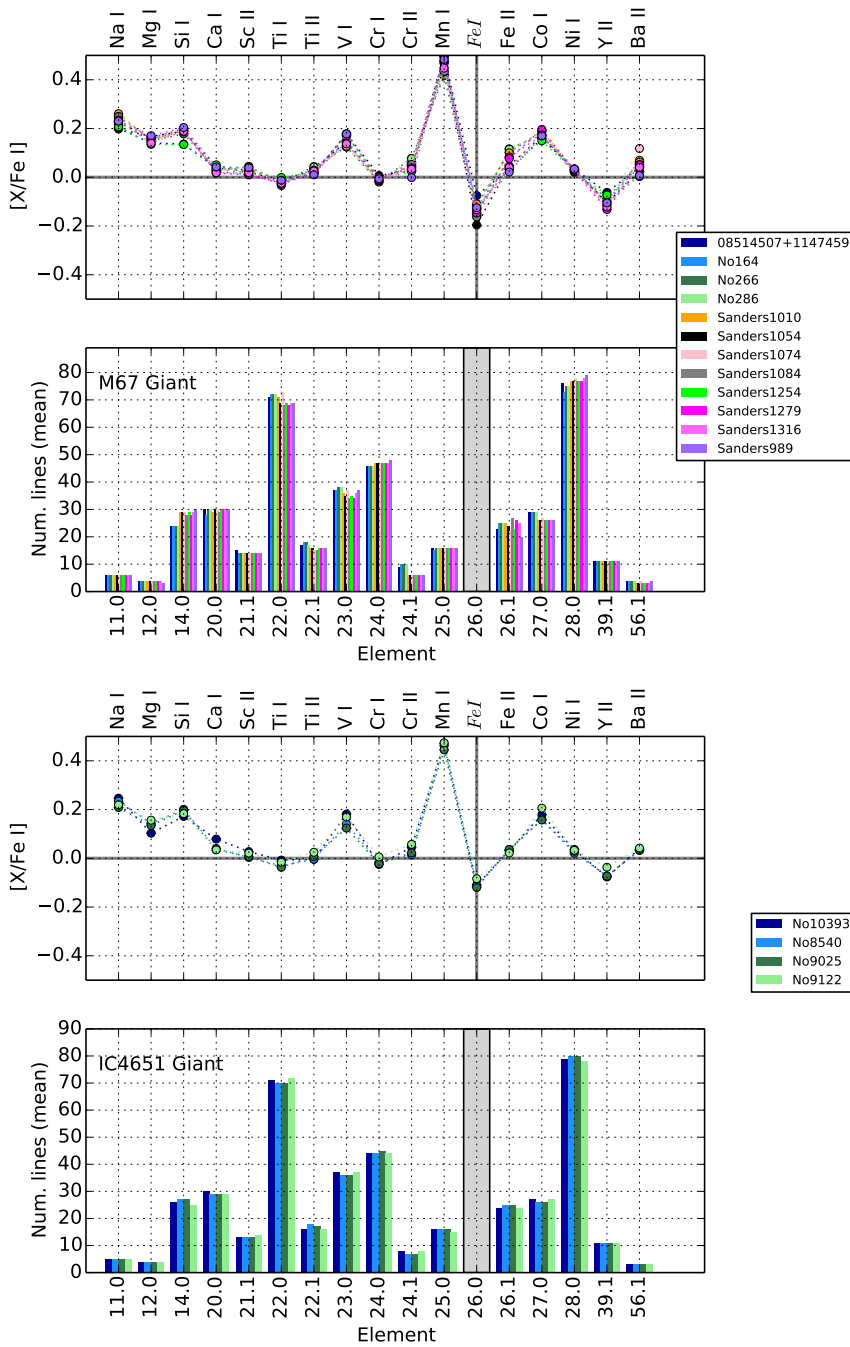


Figure 4.9 – Stellar abundances and mean number of lines used in function of species (element code at top, atomic number and ionization state in Kurucz format at bottom where '0' is neutral and '1' is ionized) for M67 and IC4651 giants. The number of neutral iron lines are not included because they outnumber significantly the rest. All the abundance ratios are referenced to iron except iron itself, which is relative to hydrogen. .

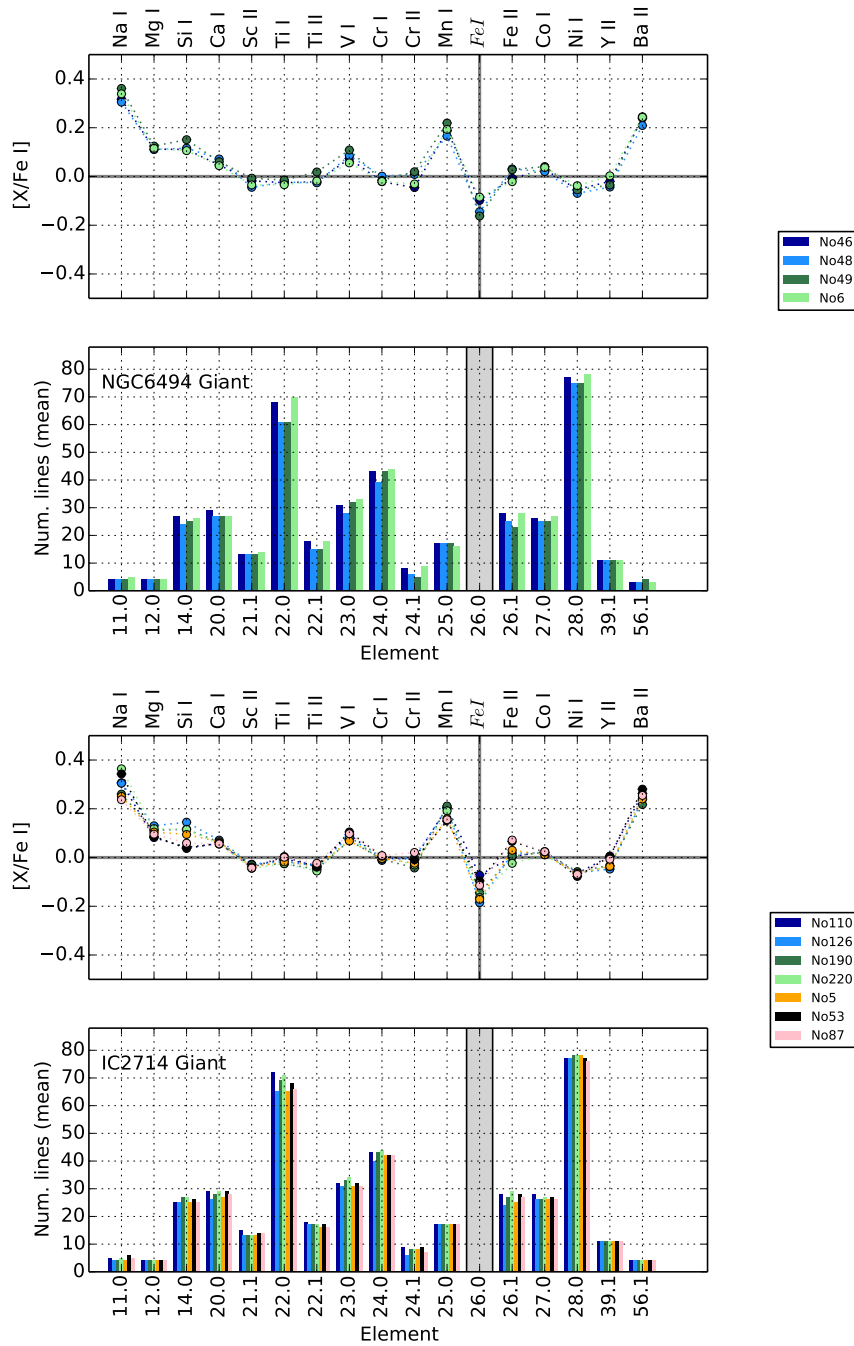


Figure 4.10 – Stellar abundances and mean number of lines used in function of species for NGC6494 and IC2714 giants. The figure format is described in the caption of the Fig. 4.9.

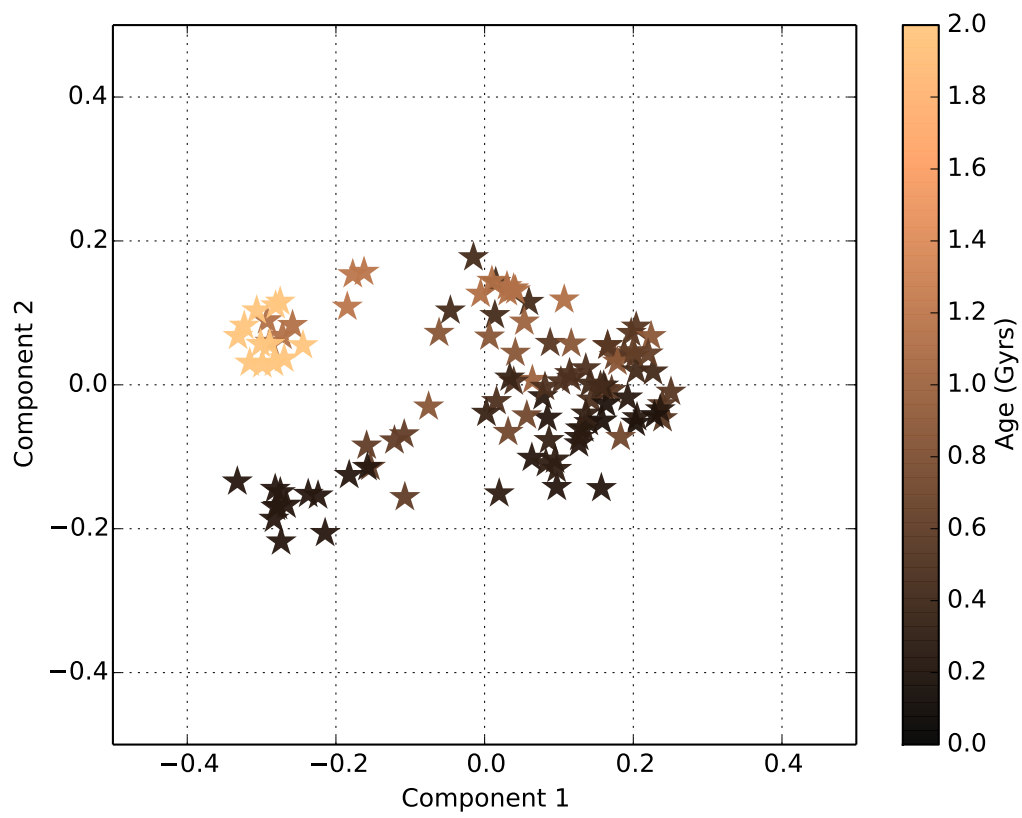


Figure 4.11 – Stars represented in the PCA space using the two first principal components. The stellar ages are encoded in a color scale bar.

Table 4.5 – Clusters found for dwarf stars and their real open clusters.

Cluster	OC	Stars	Coverage		Age (Gyrs)
			Cluster	OC	
N.01 D	IC4651	3	50%	60%	1.14
	M67	3	50%	20%	4.09
N.02 D	M67	5	83%	33%	4.09
	NGC3680	1	17%	50%	1.19
N.03 D	Melotte111	4	80%	100%	0.71
	NGC3680	1	20%	50%	1.19
N.04 D	NGC2447	3	100%	100%	0.56
N.05 D	NGC2632	11	92%	100%	0.63
	IC4651	1	8%	20%	1.14
N.06 D	M67	7	88%	47%	4.09
	IC4651	1	13%	20%	1.14

Notes. The clustering algorithm assigns numbers to each identified group as indicated in the first column. The number of stars are presented next to the real open cluster to which they belong. The coverage indicates the percentage of stars that represent when compared to the total number of stars in the identified group and in the real open cluster.

4.4.4 The role of different elements

The selection of measured abundances has also an impact on the clustering algorithms, hence on the potential of the chemical tagging technique. The best elements among those included in this study are those which can be measured with high precision (i.e. low dispersion) and show no correlation among them (e.g., alpha elements have similar trends). It is also important to have elements produced in different processes with significantly different yields.

Working with high-resolution and high S/N spectra contributes to better precisions, even though not all the elements can be easily measured for all kind of stellar types because their absorption lines can be too weak or highly blended. In this context, high quality atomic data and reliable physical models are fundamental.

A principal component analysis can help us to understand the role of the measured abundances by looking at the weights assigned to each one. Elements with similar weights have similar behaviours and they don't contribute significantly to distinguish among clusters. In Fig 4.12 we observe that the elements that contribute more to distinguish between stars are the heavier elements (Y II, Ba II), Na I and Mn I. To fully take advantage of this information, it is desirable to include a higher number of stars in future studies, specially for the dwarf subgroup, and to extend the analysis to include other elements. For instance, [Freeman and Bland-Hawthorn \[2002\]](#) argue that n decoupled elements are needed to identify 2^n unique chemical signatures and they state that n -capture elements are the best candidates (e.g. Ba and Sr). In our analysis with giant stars we are using 25 open clusters, hence we would need around 4-5 decoupled elements while we seem to have around 3-4.

4.5 Conclusions

We compiled 467 high-resolution spectra acquired with different instruments (i.e. NARVAL, HARPS, UVES) in the field of view of known open clusters, we implemented an automatic process based on

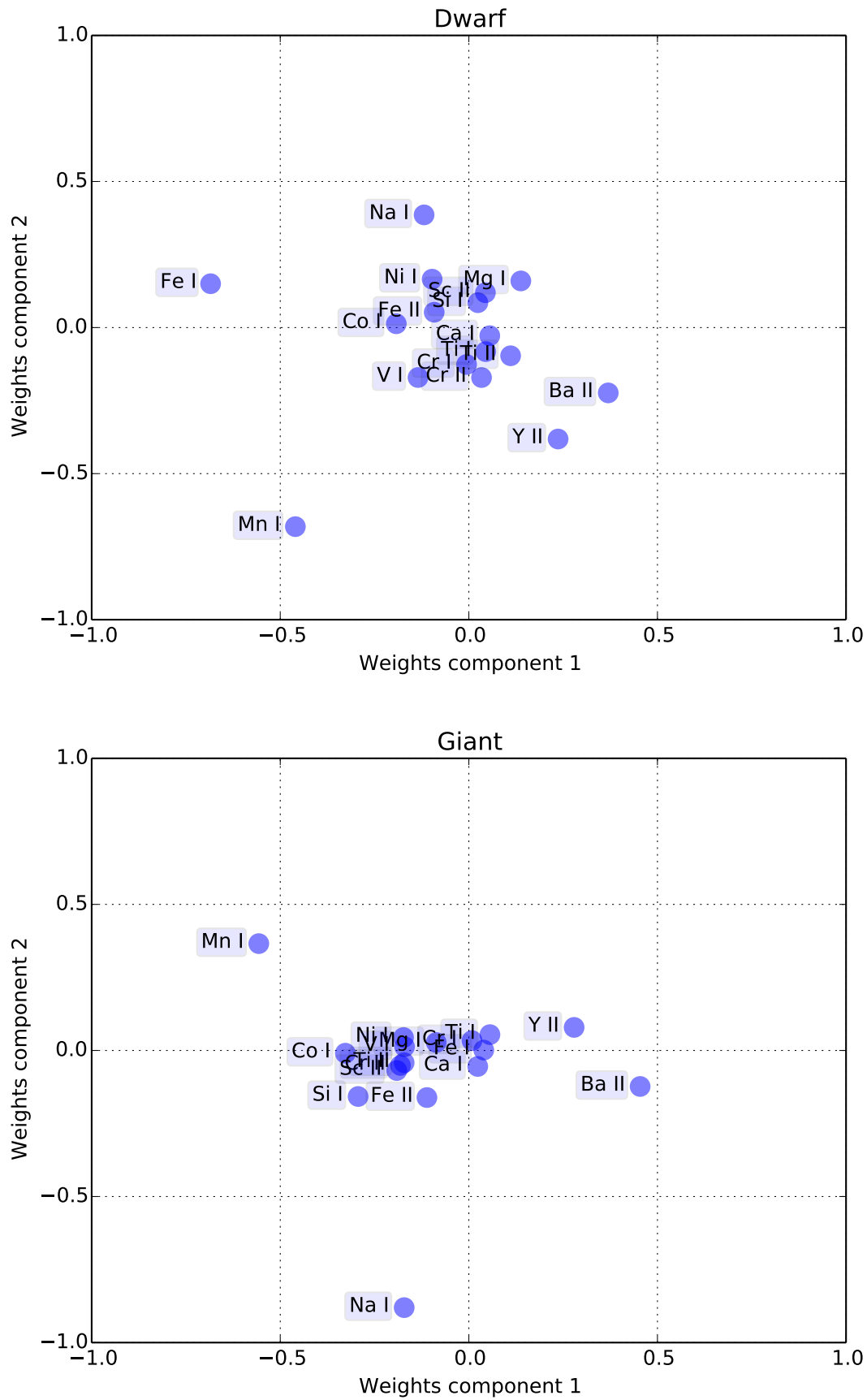


Figure 4.12 – Elements’ PCA weights per stellar subgroup.

iSpec to homogenize the observations, derive atmospheric parameters and determine chemical abundances using a differential approach. After filtering low S/N spectra, non-members by radial velocity, non-FGK and/or chemically peculiar stars, we were left with a dataset of 232 stars covering 32 open clusters with abundances for 17 species corresponding to 14 different elements.

By slightly varying our continuum normalization process, we show how inhomogeneities in the spectral analysis imply systematic uncertainties in, for instance, the derived chemical abundances. It is not recommended to use the heterogeneous literature compilations to draw scientific conclusions about extensive topics such as the chemical history of our Galaxy.

We identified distinct chemical signatures for stars in different evolutionary stages that belong to the same open cluster. The origin of these differences may be explained by NTLE effects (minimized for solar dwarfs thanks to the applied differential approach in the abundance determination), atomic diffusion, mixing processes and correlations from atmospheric parameter determinations (reduced when working in the [X/Fe] space). Regardless of whether these abundance enhancements are real or artificial, they have important implications for the chemical tagging technique when applied to stars in different evolutionary stages.

To evaluate the viability of the chemical tagging technique when analyzing a huge quantity of spectra in an automatized fashion, we performed experiments where we applied machine learning algorithms to blindly group stars based on their chemical abundances. We should note that our analysis was limited to mainly close-by clusters and it covers a narrow metallicity range. We found that the analyzed open clusters overlap in the chemical space for the 17 elemental abundances analyzed and it is not possible to completely recover conatal stars (born from the same cloud at the same time). It is worth noting that chemical outliers were already discarded and the clustering analysis was performed individually in subgroups with stars in similar evolutionary stages. Thus, in a real scenario where the chemical tagging technique would be applied to a greater number of field stars, we expect to have a high level of overlapping that would severely affect the success rate of this technique for recovering conatal aggregates.

In Mitschang et al. [2014], the authors conducted the first blind chemical tagging experiment to find stellar groups from 714 field stars. They also found that the viability of finding conatal groups was doubtful but they claimed that the technique can still identify coeval groups of stars (stars born at the same period). In our study, we observed a possible correlation between the two first principal components and the stellar ages for giant stars. The door remains open for the possibility of using the chemical tagging technique for finding coeval aggregates.

It is intuitive to conclude that increases in chemical dimensionality lead to improvements in the clustering experiments, although the difficulty in deriving abundances for some elements (e.g., weak absorption lines, fewer lines, blended regions) at a given resolution could also yield greater uncertainties and potential scatter. We showed that not all the elements have the same discriminatory power [as previous studies did, such as Mitschang et al., 2013], some tend to act in concert while others contribute significantly such as the heavy n-capture element Ba. For future analysis, it would be interesting to include other elements such as La, Nd and Eu that are formed through similar processes that produce Ba (slow and rapid n-capture processes in low mass AGB stars, Busso et al. 2001; and core-collapse supernovae, Kratz et al. 2007). It would be also necessary to explore open clusters with lower metallicities, where less line blending could make different elements accessible.

There is also room to improve automatic analysis and spectral modelling, for instance, incorporating NTLE effects, hyperfine structure and averaged 3-D model atmosphere. Time dependent 3-D hydrodynamical models [Pereira et al., 2013] are still computationally too expensive as to use them for massive analysis, thus the averaged 3-D model are a good compromise. This improvements could reduce discrepancies among stars in different evolutionary stages and achieve a higher degree of success when recovering clusters using chemical abundances [Bergemann et al., 2012, Lind et al., 2012].

Table 4.6 – Clusters found for giant stars and their real open clusters.

Cluster	OC	Stars	Coverage		Age (Gyrs)
			Cluster	OC	
N.01 G	IC2714	3	43%	43%	0.25
	NGC2251	1	14%	50%	0.27
	NGC2567	1	14%	25%	0.28
	NGC3532	1	14%	33%	0.35
	NGC4349	1	14%	25%	0.21
N.02 G	NGC3680	3	100%	100%	1.19
N.03 G	NGC6494	3	50%	75%	0.3
	IC2714	2	33%	29%	0.25
	NGC3532	1	17%	33%	0.35
N.04 G	NGC2567	1	33%	25%	0.28
	NGC4349	1	33%	25%	0.21
	NGC6940	1	33%	33%	0.72
N.05 G	NGC2632	2	67%	40%	0.63
	NGC2477	1	33%	20%	0.88
N.06 G	NGC752	4	67%	57%	1.12
	NGC2099	1	17%	20%	0.45
	NGC2423	1	17%	50%	1
N.07 G	NGC6705	8	100%	62%	0.25
N.08 G	IC2714	1	100%	14%	0.25
N.09 G	NGC2447	3	60%	100%	0.56
	NGC2567	1	20%	25%	0.28
	NGC4349	1	20%	25%	0.21
N.10 G	NGC2099	1	50%	20%	0.45
	NGC2477	1	50%	20%	0.88
N.11 G	NGC2099	2	50%	40%	0.45
	NGC752	2	50%	29%	1.12
N.12 G	IC4756	2	40%	67%	0.67
	NGC2360	2	40%	29%	0.56
	NGC5822	1	20%	50%	0.89
N.13 G	NGC2360	3	38%	43%	0.56
	NGC6633	2	25%	50%	0.43
	NGC6811	2	25%	100%	0.64
	NGC5822	1	13%	50%	0.89
N.14 G	NGC2360	1	33%	14%	0.56
	NGC2477	1	33%	20%	0.88
	NGC752	1	33%	14%	1.12
N.15 G	NGC6705	3	100%	23%	0.25
N.16 G	NGC6494	1	100%	25%	0.3
N.17 G	IC4756	1	14%	33%	0.67
	NGC2360	1	14%	14%	0.56
	NGC2539	1	14%	13%	0.49
	NGC2567	1	14%	25%	0.28
	NGC3532	1	14%	33%	0.35
	NGC4349	1	14%	25%	0.21
	NGC6633	1	14%	25%	0.43
N.18 G	NGC2632	3	60%	60%	0.63
	NGC6705	2	40%	15%	0.25
N.19 G	M67	8	89%	67%	4.09
	IC4651	1	11%	25%	1.14
N.20 G	NGC2539	4	80%	50%	0.49
	NGC6633	1	20%	25%	0.43
	NGC2539	2	29%	25%	0.49

Table 4.7 – Weighted mean abundances and dispersion per cluster and stellar subgroup.

Cluster	[Ba 2/Fe]	[Ca 1/Fe]	[Co 1/Fe]	[Cr 1/Fe]	[Cr 2/Fe]	[Fe 1/H]	[Fe 2/Fe]	[Mg 1/Fe]	[Mn 1/Fe]	[Na 1/Fe]	[Ni 1/Fe]	[Sc 2/Fe]	[Si 1/Fe]	[Ti 1/Fe]	[Ti 2/Fe]	[V 1/Fe]	[Y 2/Fe]	★	
	\bar{x}_w σ_w	\bar{x}_w σ_w	\bar{x}_w σ_w	\bar{x}_w σ_w	\bar{x}_w σ_w	\bar{x}_w σ_w	\bar{x}_w σ_w	\bar{x}_w σ_w	\bar{x}_w σ_w	\bar{x}_w σ_w	\bar{x}_w σ_w	\bar{x}_w σ_w	\bar{x}_w σ_w	\bar{x}_w σ_w	\bar{x}_w σ_w	\bar{x}_w σ_w	\bar{x}_w σ_w	\bar{x}_w σ_w	\bar{x}_w σ_w
IC2714	g	0.26 0.02	0.06 0.00	0.02 0.01	-0.01 0.02	-0.12 0.04	0.03 0.04	0.10 0.02	0.17 0.03	0.28 0.04	-0.07 0.01	-0.04 0.01	0.06 0.03	-0.01 0.01	-0.04 0.01	0.09 0.01	-0.02 0.02	7	
IC4651	d	0.01 0.02	0.04 0.03	-0.02 0.01	-0.02 0.02	0.09 0.04	-0.01 0.01	0.00 0.02	-0.08 0.08	-0.03 0.03	-0.03 0.01	-0.09 0.01	0.00 0.01	-0.02 0.02	-0.09 0.01	0.05 0.06	-0.05 0.02	5	
IC4651	g	0.04 0.00	0.06 0.03	0.19 0.02	-0.01 0.02	0.10 0.02	0.03 0.01	0.13 0.03	0.47 0.00	0.23 0.02	0.03 0.01	0.02 0.01	0.18 0.01	-0.01 0.01	0.00 0.02	0.17 0.02	-0.07 0.02	4	
IC4756	g	0.21 0.01	0.06 0.01	0.01 0.00	-0.01 0.01	-0.06 0.01	-0.01 0.03	0.08 0.01	0.17 0.01	0.18 0.03	-0.06 0.00	-0.04 0.01	0.02 0.00	0.02 0.00	-0.04 0.01	0.07 0.01	0.00 0.01	3	
M67	d	0.02 0.03	0.04 0.02	-0.02 0.02	0.00 0.01	-0.05 0.02	-0.03 0.02	0.04 0.01	-0.09 0.09	0.01 0.03	-0.02 0.01	-0.05 0.02	0.00 0.02	0.01 0.01	-0.06 0.02	0.02 0.02	-0.06 0.02	15	
M67	g	0.05 0.02	0.03 0.01	0.19 0.01	-0.01 0.01	-0.13 0.03	0.10 0.04	0.15 0.01	0.47 0.02	0.23 0.02	0.03 0.00	0.02 0.01	0.19 0.02	-0.02 0.01	0.03 0.01	0.15 0.02	-0.10 0.02	12	
Melotte 111	d	0.13 0.03	0.05 0.03	-0.06 0.02	0.00 0.02	-0.06 0.03	-0.03 0.01	-0.01 0.01	-0.06 0.07	-0.09 0.06	-0.08 0.01	-0.12 0.02	-0.02 0.02	0.02 0.03	-0.08 0.03	0.06 0.09	0.03 0.03	4	
NGC2099	g	0.11 0.03	0.06 0.02	0.08 0.01	0.09 0.02	0.05 0.10	0.05 0.03	-0.09 0.05	0.11 0.02	0.27 0.03	0.14 0.02	-0.02 0.03	-0.04 0.03	-0.01 0.04	0.02 0.08	0.08 0.03	-0.04 0.06	5	
NGC2251	g	0.25 0.00	0.08 0.01	0.03 0.02	0.01 0.03	0.02 0.04	-0.08 0.01	0.02 0.07	0.11 0.01	0.20 0.05	0.25 0.03	-0.05 0.01	-0.04 0.01	0.08 0.03	0.00 0.01	-0.03 0.01	0.08 0.04	-0.01 0.00	2
NGC2360	g	0.23 0.01	0.07 0.01	0.00 0.01	-0.01 0.01	-0.12 0.03	-0.04 0.01	0.09 0.01	0.17 0.01	0.17 0.03	-0.07 0.01	-0.04 0.01	0.03 0.02	0.01 0.00	-0.04 0.01	0.07 0.01	0.00 0.01	7	
NGC2423	g	0.16 0.00	0.04 0.01	0.04 0.00	-0.02 0.00	0.01 0.02	0.04 0.02	0.07 0.02	0.27 0.02	0.15 0.06	-0.03 0.00	-0.01 0.01	0.05 0.00	-0.02 0.00	0.00 0.01	0.07 0.00	0.02 0.00	2	
NGC2447	d	0.22 0.02	0.06 0.01	-0.07 0.00	0.02 0.01	-0.10 0.02	-0.01 0.00	0.00 0.01	-0.21 0.06	-0.11 0.01	-0.09 0.00	-0.10 0.01	-0.01 0.02	0.01 0.02	-0.07 0.02	0.05 0.02	0.04 0.04	3	
NGC2447	g	0.28 0.01	0.07 0.00	0.00 0.01	-0.02 0.00	-0.05 0.00	-0.08 0.03	-0.02 0.01	0.10 0.01	0.10 0.00	0.21 0.01	-0.06 0.00	0.03 0.01	0.02 0.01	-0.03 0.01	0.05 0.02	0.01 0.01	3	
NGC2477	g	0.16 0.03	0.07 0.00	0.05 0.03	0.01 0.02	-0.03 0.03	-0.04 0.02	0.07 0.02	0.29 0.06	0.22 0.05	-0.03 0.02	-0.03 0.02	0.10 0.03	-0.02 0.00	-0.06 0.02	0.11 0.01	-0.04 0.02	5	
NGC2539	g	0.21 0.03	0.05 0.01	0.02 0.01	-0.01 0.01	-0.05 0.04	0.00 0.02	0.07 0.01	0.22 0.02	0.22 0.03	-0.06 0.01	-0.03 0.01	0.04 0.03	-0.01 0.01	-0.04 0.01	0.07 0.01	0.00 0.01	8	
NGC2548	g	0.17 0.05	0.06 0.03	0.06 0.02	0.01 0.04	0.03 0.13	-0.04 0.00	0.01 0.05	0.10 0.01	0.25 0.04	0.28 0.07	-0.03 0.03	-0.03 0.02	0.07 0.08	-0.03 0.04	0.01 0.10	0.09 0.06	0.00 0.01	2
NGC2567	g	0.28 0.02	0.07 0.01	0.01 0.01	-0.01 0.02	-0.03 0.02	-0.15 0.03	0.02 0.03	0.09 0.03	0.11 0.02	0.22 0.04	-0.07 0.01	-0.04 0.01	0.05 0.02	0.01 0.02	-0.04 0.03	0.08 0.02	0.00 0.02	4
NGC2632	d	-0.01 0.03	0.04 0.02	-0.02 0.03	0.02 0.01	-0.04 0.04	0.16 0.03	0.02 0.01	-0.04 0.05	0.01 0.05	-0.03 0.02	-0.10 0.01	-0.01 0.02	-0.01 0.02	-0.12 0.02	0.10 0.05	-0.06 0.02	11	
NGC2632	g	0.04 0.02	0.03 0.01	0.12 0.02	-0.02 0.02	0.05 0.02	0.08 0.02	0.04 0.04	0.09 0.01	0.30 0.01	0.35 0.03	0.01 0.01	0.02 0.01	0.14 0.02	-0.04 0.01	0.01 0.02	0.11 0.01	-0.05 0.01	5
NGC3532	g	0.28 0.01	0.06 0.02	0.03 0.01	-0.01 0.03	0.02 0.06	-0.11 0.04	0.02 0.07	0.10 0.03	0.17 0.03	0.30 0.07	-0.05 0.02	-0.03 0.01	0.11 0.03	-0.01 0.02	-0.01 0.01	0.07 0.03	0.01 0.01	3
NGC3680	d	0.11 0.01	0.07 0.01	-0.06 0.01	-0.01 0.05	-0.04 0.04	-0.05 0.01	0.02 0.03	-0.18 0.07	0.00 0.09	-0.07 0.00	-0.09 0.01	-0.01 0.03	0.02 0.03	-0.08 0.02	0.12 0.03	0.01 0.03	2	
NGC3680	g	0.17 0.01	0.05 0.01	0.12 0.02	-0.01 0.01	-0.17 0.04	0.08 0.01	0.15 0.01	0.46 0.01	0.13 0.03	0.00 0.00	0.02 0.01	0.18 0.01	-0.01 0.00	0.04 0.01	0.14 0.01	0.01 0.01	3	
NGC4349	g	0.25 0.02	0.07 0.01	0.01 0.01	-0.01 0.01	-0.03 0.03	-0.16 0.04	-0.01 0.02	0.11 0.01	0.12 0.02	0.23 0.01	-0.06 0.01	-0.06 0.02	0.07 0.01	-0.01 0.01	-0.05 0.02	0.08 0.03	-0.02 0.01	4
NGC5822	g	0.28 0.02	0.06 0.00	0.02 0.01	-0.01 0.02	0.03 0.03	-0.08 0.04	0.03 0.08	0.08 0.03	0.17 0.04	0.15 0.01	-0.07 0.01	-0.04 0.03	0.02 0.00	0.01 0.02	-0.02 0.02	0.08 0.03	0.10 0.08	2
NGC6494	g	0.23 0.02	0.05 0.01	0.03 0.01	-0.02 0.01	-0.02 0.03	-0.11 0.04	-0.01 0.03	0.12 0.01	0.19 0.02	0.33 0.02	-0.05 0.01	-0.03 0.02	0.11 0.02	-0.03 0.01	-0.02 0.02	0.06 0.02	-0.02 0.02	4
NGC6633	g	0.25 0.01	0.05 0.00	0.00 0.00	-0.01 0.01	-0.03 0.01	-0.05 0.02	0.01 0.03	0.08 0.01	0.17 0.04	0.18 0.02	-0.06 0.01	-0.05 0.01	0.02 0.03	0.00 0.01	-0.04 0.01	0.06 0.01	0.01 0.01	4
NGC6705	g	0.06 0.02	0.08 0.04	0.15 0.01	-0.01 0.02	-0.09 0.05	0.03 0.05	0.12 0.03	0.29 0.06	0.40 0.06	0.00 0.02	0.05 0.02	0.19 0.02	-0.04 0.01	0.07 0.06	0.14 0.03	-0.10 0.03	13	
NGC6811	g	0.29 0.01	0.06 0.01	0.01 0.01	0.02 0.00	0.00 0.03	-0.08 0.01	0.07 0.02	0.06 0.01	0.17 0.01	0.14 0.00	-0.07 0.01	0.03 0.02	0.01 0.01	-0.05 0.01	0.08 0.00	0.04 0.04	2	
NGC6940	g	0.16 0.04	0.05 0.00	0.03 0.01	-0.01 0.00	0.03 0.01	0.00 0.05	0.08 0.01	0.22 0.03	0.30 0.01	-0.03 0.02	-0.03 0.01	0.06 0.05	-0.01 0.02	-0.04 0.01	0.08 0.01	0.05 0.08	3	
NGC752	g	0.20 0.01	0.06 0.00	0.03 0.02	-0.01 0.01	-0.02 0.02	-0.08 0.01	-0.03 0.01	0.10 0.01	0.34 0.04	0.13 0.01	-0.03 0.00	-0.03 0.01	0.08 0.01	-0.01 0.01	-0.02 0.01	0.07 0.01	-0.01 0.01	7
NGC3114	g	0.24 0.06	0.05 0.02	0.01 0.05	-0.03 0.02	-0.04 0.05	0.00 0.02	0.07 0.00	0.19 0.15	0.21 0.09	-0.05 0.03	-0.04 0.03	0.03 0.05	0.01 0.03	-0.03 0.03	0.06 0.02	0.02 0.00	2	
Col.350	g	0.32	-0.09	-0.02	-0.03	-0.06	0.07	-0.09	0.17	0.22	-0.06	-0.04	0.04	0.01	0.01	-0.09	0.01	1	
Melotte20	d	0.15	-0.05	-0.02	-0.01	-0.12	-0.01	0.00	-0.20	-0.11	-0.08	-0.11	-0.04	0.03	-0.14	-0.17	0.00	1	

Table 4.7 – Continued.

Cluster	Ba 2	Ca 1	Co 1	Cr 1	Cr 2	Fe 1	Fe 2	Mg 1	Mn 1	Na 1	Ni 1	Sc 2	Si 1	Ti 1	Ti 2	V 1	Y 2	★
	\bar{x}_w σ_w	\bar{x}_w σ_w	\bar{x}_w σ_w	\bar{x}_w σ_w	\bar{x}_w σ_w	\bar{x}_w σ_w	\bar{x}_w σ_w	\bar{x}_w σ_w	\bar{x}_w σ_w	\bar{x}_w σ_w	\bar{x}_w σ_w	\bar{x}_w σ_w	\bar{x}_w σ_w	\bar{x}_w σ_w	\bar{x}_w σ_w	\bar{x}_w σ_w	\bar{x}_w σ_w	
Melotte22 _d	0.10	0.05	-0.01	0.01	-0.02	0.03	-0.06	-0.02	-0.17	-0.03	-0.04	-0.15	0.00	0.00	-0.16	0.22	-0.01	1
NGC1817 _g	0.24	0.08	0.01	-0.01	-0.12	-0.17	-0.07	0.10	0.17	0.15	-0.06	-0.05	0.03	0.02	-0.08	0.05	-0.01	1
NGC2547 _d	0.12	0.11	-0.22	0.01	0.11	-0.12	-0.05	-0.04	-0.09	-0.01	-0.09	-0.10	0.03	0.07	-0.10	0.11	0.03	1
NGC6475 _d	0.10	0.01	-0.08	0.03	-0.02	0.09	0.00	-0.04	-0.05	-0.17	-0.08	-0.13	-0.06	0.00	-0.09	0.00	0.03	1

Notes. Subgroups correspond to dwarfs (D) and giants (G). The number of stars is indicated in the last column (★).

Table 4.8 – Weighted mean abundances and dispersion per cluster.

Cluster	[Ba 2/Fe]		[Ca 1/Fe]		[Co 1/Fe]		[Cr 1/Fe]		[Cr 2/Fe]		[Fe 1/H]		[Fe 2/Fe]		[Mg 1/Fe]		[Mn 1/Fe]		[Na 1/Fe]		[Ni 1/Fe]		[Sc 2/Fe]		[Si 1/Fe]		[Ti 1/Fe]		[Ti 2/Fe]		[V 1/Fe]		[Y 2/Fe]		★
	\bar{x}_w	σ_w	\bar{x}_w	σ_w	\bar{x}_w	σ_w	\bar{x}_w	σ_w	\bar{x}_w	σ_w	\bar{x}_w	σ_w	\bar{x}_w	σ_w	\bar{x}_w	σ_w	\bar{x}_w	σ_w	\bar{x}_w	σ_w	\bar{x}_w	σ_w	\bar{x}_w	σ_w	\bar{x}_w	σ_w	\bar{x}_w	σ_w	\bar{x}_w	σ_w	\bar{x}_w	σ_w	\bar{x}_w	σ_w	
IC2714	0.26	0.02	0.06	0	0.02	0.01	0	0.01	-0.01	0.02	-0.12	0.04	0.03	0.04	0.1	0.02	0.17	0.03	0.28	0.04	-0.07	0.01	-0.04	0.01	0.06	0.03	-0.01	0.01	-0.04	0.01	0.09	0.01	-0.02	0.02	7
IC4651	0.03	0.20	0.50	0.03	0.12	0.11	-0.01	0.02	-0.01	0.03	0.00	0.11	0.00	0.02	0.01	0.05	0.38	0.28	0.10	0.14	0.01	0.03	-0.05	0.05	0.09	0.10	-0.01	0.01	-0.04	0.05	0.16	0.05	-0.06	0.02	9
IC4756	0.21	0.10	0.60	0.01	0.01	0.00	-0.01	0.01	-0.03	0.01	-0.06	0.01	-0.01	0.03	0.08	0.01	0.17	0.01	0.18	0.03	-0.06	0.00	-0.04	0.01	0.02	0.00	0.02	0.00	-0.04	0.01	0.07	0.01	0.00	0.01	3
M67	0.04	0.30	0.30	0.02	0.13	0.13	-0.01	0.01	0.06	0.07	-0.03	0.06	0.00	0.07	0.09	0.06	0.11	0.30	0.13	0.12	-0.01	0.02	-0.02	0.04	0.05	0.09	0.00	0.02	-0.04	0.05	0.08	0.07	-0.07	0.03	27
Melotte111	0.13	0.30	0.50	0.03	-0.06	0.02	0.03	0.01	0.00	0.02	-0.06	0.03	-0.03	0.01	-0.01	0.01	-0.06	0.07	-0.09	0.06	-0.08	0.01	-0.12	0.02	-0.02	0.02	0.02	0.03	-0.08	0.03	0.60	0.09	0.03	0.03	4
NGC2099	0.11	0.30	0.60	0.02	0.08	0.01	0.09	0.02	0.05	0.10	0.05	0.03	-0.09	0.05	0.11	0.02	0.27	0.03	0.14	0.02	-0.02	0.03	-0.04	0.03	-0.01	0.04	-0.03	0.01	0.02	0.08	0.08	0.03	-0.04	0.06	5
NGC2251	0.25	0.00	0.80	0.01	0.03	0.02	0.01	0.03	0.02	0.04	-0.08	0.01	0.02	0.07	0.11	0.01	0.20	0.05	0.25	0.03	-0.05	0.01	-0.04	0.01	0.08	0.03	0.00	0.01	-0.03	0.01	0.08	0.04	-0.01	0.00	2
NGC2360	0.23	0.10	0.70	0.01	0.00	0.01	-0.01	0.01	-0.06	0.01	-0.12	0.03	-0.04	0.01	0.09	0.01	0.17	0.01	0.17	0.03	-0.07	0.01	-0.04	0.01	0.03	0.02	0.01	0.00	-0.04	0.01	0.07	0.01	0.00	0.01	7
NGC2423	0.16	0.00	0.40	0.01	0.04	0.00	-0.02	0.00	0.01	0.02	0.04	0.02	0.02	0.02	0.07	0.02	0.27	0.02	0.15	0.06	-0.03	0.00	-0.01	0.01	0.05	0.00	-0.02	0.00	0.00	0.01	0.07	0.00	0.02	0.00	2
NGC2447	0.27	0.30	0.70	0.01	-0.01	0.02	-0.02	0.02	-0.04	0.01	-0.08	0.03	-0.02	0.01	0.03	0.06	-0.06	0.19	0.20	0.09	-0.07	0.01	-0.04	0.02	-0.01	0.03	0.01	0.01	-0.04	0.03	0.05	0.01	0.01	0.02	6
NGC2477	0.16	0.30	0.70	0.00	0.05	0.03	0.01	0.02	-0.03	0.03	-0.04	0.02	-0.04	0.02	0.07	0.02	0.29	0.06	0.22	0.05	-0.03	0.02	-0.03	0.02	0.10	0.03	-0.02	0.00	-0.06	0.02	0.11	0.01	-0.04	0.02	5
NGC2539	0.21	0.30	0.50	0.01	0.02	0.01	-0.01	0.01	-0.01	0.02	-0.05	0.04	0.00	0.02	0.07	0.01	0.22	0.02	0.22	0.03	-0.06	0.01	-0.03	0.01	0.04	0.03	-0.01	0.01	-0.04	0.01	0.07	0.01	0.00	0.01	8
NGC2567	0.17	0.50	0.60	0.03	0.06	0.02	0.01	0.04	0.03	0.13	-0.04	0.00	0.01	0.05	0.10	0.01	0.25	0.04	0.28	0.07	-0.03	0.03	-0.03	0.02	0.07	0.08	-0.03	0.04	-0.01	0.10	0.09	0.06	0.00	0.01	2
NGC2632	0.28	0.20	0.70	0.01	0.01	0.01	-0.01	0.02	-0.03	0.02	-0.15	0.03	0.02	0.03	0.09	0.03	0.11	0.02	0.22	0.04	-0.07	0.01	-0.04	0.01	0.05	0.02	0.01	0.02	-0.04	0.03	0.08	0.02	0.00	0.02	4
NGC3532	0.03	0.40	0.30	0.02	0.11	0.09	-0.01	0.03	0.05	0.06	0.10	0.06	0.03	0.02	0.03	0.08	0.21	0.23	0.34	0.22	0.00	0.02	0.01	0.08	0.09	0.09	-0.04	0.02	-0.01	0.08	0.09	0.09	-0.04	0.02	16
NGC3680	0.28	0.10	0.60	0.02	0.03	0.01	-0.01	0.03	0.02	0.06	-0.11	0.04	0.02	0.07	0.10	0.03	0.17	0.03	0.30	0.07	-0.05	0.02	-0.03	0.01	0.11	0.03	-0.01	0.02	-0.01	0.01	0.07	0.03	0.01	0.01	3
NGC4349	0.15	0.30	0.50	0.01	0.12	0.02	-0.01	0.01	0.06	0.02	-0.15	0.07	0.07	0.04	0.12	0.06	0.46	0.07	0.12	0.03	-0.01	0.03	0.02	0.03	0.16	0.06	-0.01	0.01	0.03	0.04	0.14	0.01	0.01	0.02	5
NGC5822	0.25	0.20	0.70	0.01	0.01	0.01	-0.01	0.01	-0.03	0.03	-0.16	0.04	-0.01	0.02	0.11	0.01	0.12	0.02	0.23	0.01	-0.06	0.01	-0.06	0.02	0.07	0.01	-0.01	0.01	-0.05	0.02	0.08	0.03	-0.02	0.01	4
NGC6494	0.28	0.20	0.60	0.00	0.02	0.01	-0.01	0.02	0.03	0.03	-0.08	0.04	0.03	0.08	0.08	0.03	0.17	0.04	0.15	0.01	-0.07	0.01	-0.04	0.03	0.02	0.00	0.01	0.02	-0.02	0.02	0.08	0.03	0.10	0.08	2
NGC6633	0.23	0.20	0.50	0.01	0.03	0.01	-0.02	0.01	-0.02	0.03	-0.11	0.04	-0.01	0.03	0.12	0.01	0.19	0.02	0.33	0.02	-0.05	0.01	-0.03	0.02	0.11	0.02	-0.03	0.01	-0.02	0.02	0.06	0.02	-0.02	0.02	4
NGC6705	0.25	0.10	0.50	0.00	0.00	0.00	-0.01	0.01	-0.03	0.01	-0.05	0.02	0.01	0.03	0.08	0.01	0.17	0.04	0.18	0.02	-0.06	0.01	-0.05	0.01	0.02	0.03	0.00	0.01	-0.04	0.01	0.06	0.01	0.01	0.01	4
NGC6811	0.06	0.20	0.80	0.04	0.15	0.01	-0.01	0.02	0.05	0.04	-0.09	0.05	0.03	0.05	0.12	0.03	0.29	0.06	0.40	0.06	0.00	0.02	0.05	0.02	0.19	0.02	-0.04	0.01	0.07	0.06	0.14	0.03	-0.10	0.03	13
NGC6940	0.29	0.10	0.60	0.01	0.01	0.01	0.02	0.00	0.00	0.03	-0.08	0.01	0.07	0.02	0.06	0.01	0.17	0.01	0.14	0.00	-0.07	0.01	-0.04	0.01	0.03	0.02	0.01	0.01	-0.05	0.01	0.08	0.00	0.04	0.04	2
NGC752	0.16	0.40	0.50	0.00	0.03	0.01	0.00	0.01	-0.01	0.00	0.03	0.01	0.00	0.05	0.08	0.01	0.22	0.03	0.30	0.01	-0.03	0.02	-0.03	0.01	0.06	0.05	-0.01	0.02	-0.04	0.01	0.08	0.01	0.05	0.08	3
NGC3114	0.20	0.10	0.60	0.00	0.03	0.02	-0.01	0.01	-0.02	0.02	-0.08	0.01	-0.03	0.01	0.10	0.01	0.34	0.04	0.13	0.01	-0.03	0.00	-0.03	0.01	0.08	0.01	-0.01	0.01	-0.02	0.01	0.07	0.01	-0.01	0.01	7
Col.350	0.24	0.60	0.50	0.02	0.01	0.05	-0.03	0.02	-0.04	0.05	-0.04	0.06	0.00	0.02	0.07	0.00	0.19	0.15	0.21	0.09	-0.05	0.03	-0.04	0.03	0.03	0.05	0.01	0.03	-0.03	0.03	0.06	0.02	0.02	0.00	2
Melotte20	0.32	-	0.90	-	0.02	-	0.02	-	0.03	-	0.00	-	0.07	-	0.09	-	0.17	-	0.22	-	-0.06	-	-0.04	-	0.04	-	0.01	-	0.01	-	0.09	-	0.01	-	1
Melotte22	0.15	-	0.50	-	-0.02	-	-0.02	-	0.01	-	-0.03	-	0.12	-	0.00	-	-0.20	-	-0.11	-	-0.08	-	-0.11	-	-0.04	-	0.03	-	-0.14	-	0.17	-	0.00	-	1
NGC1817	0.10	-	0.50	-	-0.01	-	-0.01	-	0.01	-	-0.02	-	0.03	-	-0.02	-	-0.17	-	-0.03	-	-0.04	-	-0.15	-	0.00	-	0.00	-	-0.16	-	0.22	-	-0.01	-	1
NGC2547	0.24	-	0.80	-	0.01	-	-0.01	-	-0.01	-	-0.12	-	-0.07	-	0.10	-	0.17	-	0.15	-	-0.06	-	-0.05	-	0.03	-	0.02	-	-0.08	-	0.05	-	-0.01	-	1
NGC2548	0.12	-	0.10	-	-0.22	-	0.01	-	0.11	-	-0.12	-	-0.05	-	-0.04	-	-0.09	-	-0.01	-	-0.09	-	-0.10	-	0.03	-	0.07	-	-0.10	-	0.11	-	0.03	-	1
NGC6475	0.10	-	0.01	-	-0.08	-	0.03	-	-0.02	-	0.00	-	0.00	-	-0.04	-	-0.05	-	-0.17	-	-0.08	-	-0.13	-	-0.06	-	0.00	-	-0.09	-	0.00	-	0.03	-	1

Notes. The number of stars is indicated in the last column (★).

Chapter 5

Conclusions and perspectives

Contents

5.1	Conclusions	126
5.1.1	The spectral library	127
5.1.2	The spectroscopic framework	127
5.1.3	The chemical tagging technique	128
5.2	Perspectives	129

5.1 Conclusions

This thesis was developed under the promising opportunity that the chemical tagging technique represented to the study of our Galaxy. Most of the stars are born together from giant molecular clouds and, assuming that the gas is chemically homogeneous and well-mixed, we can expect that stars formed from a given cloude should share a unique chemical signature. Hence, the chemical tagging technique offers the possibility to identify stars that were born together but that nowadays are gravitationally unbounded and spread all over our Galaxy.

The viability of this approach depends on two critical issues: Do stars born together have an unique chemical signature? And, are the chemical signatures different enough among different stars formed from different molecular clouds?

To answer those questions we decided to study an extensive group of open clusters. They are the leftovers of star forming aggregates in the Galactic disk that have managed to survive until the present day. Since we can be certain that their birth took place from the same molecular cloud at roughly the same period, they represent the ideal resource to test the chemical tagging technique.

When using open clusters' stars, the two critical issues presented here can now be transformed into a single question: Are we able to reconstruct the original clusters by only looking at the chemical information?

There are several challenges to be addressed that make difficult the execution of such a critical test. The first one is the need for homogeneous spectral analysis. Obtaining atmospheric parameters and abundances from the literature leads unavoidably to systematic errors because each study uses its own spectral method with different continuum normalization procedures, model atmospheres and atomic data. It is not recommended to mix literature values or the conclusions will be always questioned. For instance, if the test results in an impossibility of recovering the original clusters from the chemical information, we would never be sure if the chemical tagging technique is less promising than expected or if it is just because we are using non-homogeneous derived abundances. Hence, the best approach is to compile directly the observations and perform our own homogeneous analysis, even if that represented a much bigger investment in time and work effort.

The second challenge is that to obtain meaningful conclusions about our Galaxy using the chemical tagging technique, we need to analyse an extensive number of stellar spectra in a non-subjective way. Additionally, we need to guarantee reproducibility because it is one of the main pillars of science (too often forgotten in an increasing number of current works). To achieve those requirements, the only viable approach is automation. Reducing human interaction and subjective decisions is the only path that will allow us to analyze a huge amount of stellar spectra.

At the moment that we decided to perform our own analysis in a fully automatic fashion, a third challenge arose: assessment. It is absolutely necessary to have a set of very well-known stars covering a wide range of the parameter space (i.e. effective temperature, surface gravity and metallicity) that will help us to assess the spectroscopic pipeline. We decided to use the Gaia benchmark stars, which will be also used for the calibration of the ongoing Gaia mission [Perryman et al., 2001].

To address these challenges, we created a high-resolution and high signal-to-noise Gaia FGK benchmark stars library, we developed our own spectroscopic framework, named iSpec, together with a completely automatic pipeline (fine-tuned thanks to the benchmark stars), and we finally tested the chemical tagging technique using open clusters' stars to address the question: Are we able to reconstruct the original clusters by only looking at the chemical information?

5.1.1 The spectral library

Based on the list of the 34 Gaia benchmark stars and their reference values (Heiter et al., in prep.), we searched for high-resolution spectra with high signal-to-noise ratios observed by different instruments.

An automatic computational process was developed to transform the observed spectra into a homogeneous library of the benchmark stars. Since the wavelength range varies from one set of observations to another, we chose to limit the current library to the range between 480 and 680 nm, where all the spectra provide their best S/N. Additionally, the range matches the interests of the Gaia-ESO Survey [GES, Gilmore et al., 2012] given their UVES setup on the ESO-VLT telescope.

The automatic process reduces human interactivity (i.e. subjectivity), guarantees reproducibility, and allows us to quickly generate new versions of the library to match the needs of specific spectroscopic studies (e.g. lower resolutions and/or spectral ranges) by just changing some parameters of the automatic process.

It was also necessary to validate the consistency of the library and guarantee a high quality level, thus we carefully checked the normalization and convolution treatments by implementing automatic tests. The radial velocity corrections was certified by comparing the results with the high precision measurements of HARPS pipeline. We verified the coherence of the treated spectra by comparing them with equivalent width measurements completely independent from our process. These strict tests proved the high quality level of the spectral library.

The high-resolution Gaia benchmark stars library provides a powerful tool to assess spectral analysis methods as we show in the development of our own spectroscopic pipelines based on iSpec.

5.1.2 The spectroscopic framework

There are already several tools in the market that allow us to treat spectra (e.g. ARES from Sousa et al. 2007, DAOSPEC from Stetson and Pancino 2008 or DOOp from Cantat-Gaudin et al. 2014), and derive atmospheric parameters and chemical abundances (e.g. GALA Mucciarelli et al. 2013, FAMA Magrini et al. 2013 or SME Valenti and Piskunov 1996).

At the beginning of the project, we started to derive atmospheric parameters (i.e. effective temperature, surface gravity, metallicity) and chemical abundances with SME. This tool generates synthetic spectra on the fly and minimizes the differences with the observed spectrum by executing a least-squares algorithm (i.e. synthetic spectral fitting technique). In general terms, the minimization process is implemented in IDL scripting language and the most computationally expensive calculations (i.e. spectral synthesis) are encapsulated in a binary library. IDL is a dynamical typed language for which it is necessary to acquire commercial licences¹. There is an open source effort, named GDL², to implement an IDL-compatible alternative but unfortunately it is not mature enough to run SME.

One of the pillars of science is reproducibility and the possibility to validate the results from other studies. This requirements matches perfectly the open source philosophy where anybody has access to the source code and can easily share projects with other researchers. The use of IDL was limiting us in terms of where we can execute our analysis and how many machines can we use to parallelize our analysis. Additionally, the use of a closed binary library for the spectral synthesis was keeping us from understanding its internal implementation.

We had already implemented a bunch of routines in python for the creation of the Gaia benchmark

1. At this time, there are also free virtual machine that allow only execution of IDL programmes but no programming.

2. <http://gnudatalanguage.sourceforge.net/>

stars library. Python is an open source and widely used general-purpose, high-level programming language. We decided to replace IDL with python in order to overcome the difficulties found. We still needed a spectral synthesizer and we considered several possibilities (such as Turbospectrum, Plez 2012). We finally decided to use SPECTRUM [Gray and Corbally, 1994], it is well documented, implemented in C, relatively easy to integrate with python, and it does not require any proprietary compilers.

This is how iSpec was born, we developed a richer alternative to SME that does not depend on closed code and we integrated all our routines for spectral treatment (e.g. radial velocity determination, continuum normalization). We created a complete spectroscopic framework that can be used in an automatic way from python scripts or manually with an user-friendly visual interface.

iSpec integrates several model atmospheres and atomic line lists that the user can select. Apart from the synthetic spectral fitting technique, we also implemented the equivalent width method which is based on the assumption of excitation and ionization equilibrium (as GALA or FAMA work). This big flexibility for changing almost any of the ingredients of a spectral analysis allowed us to test different pipelines by using the Gaia benchmark stars library and their reference values. For instance, to our knowledge, it is the first time that the two methods (synthetic spectral fitting and equivalent width method) were compared by covering such a wide range of parameters and using exactly the same normalization process, atomic data, model atmospheres and radiative transfer code (i.e. SPECTRUM). The main conclusions of this test are the following:

1. The pipeline based on the synthetic spectral fitting technique provides more accurate and precise results.
2. When using only spectra to derive the atmospheric parameters, the effective temperature, surface gravity and metallicity are correlated at a similar degree, independently of the technique used on each pipeline.
3. The pipeline based on synthetic spectral fitting technique is more effective with lower resolutions (i.e. 7500) and lower signal-to-noise ratios (i.e. 25), than the one based on equivalent widths.

iSpec is now an open source tool distributed at <http://www.blancocuaresma.com/s/> that can be freely used for any spectroscopic study.

5.1.3 The chemical tagging technique

Testing the chemical tagging technique is the ultimate goal of this work. We tackle the problem by designing an experiment using open clusters' stars, for which we compiled 467 high-resolution spectra observed by different instruments (i.e. NARVAL, HARPS, UVES) in the field of view of known Open Clusters.

To ensure reproducibility, we implemented an automatic process based on iSpec to homogenize the observation, derive atmospheric parameters and determine chemical abundances with a differential approach. After filtering low S/N spectra, non-members by radial velocity, non-FGK and/or chemically peculiar stars, we were left with a dataset of 232 stars covering 32 open clusters with abundances for 17 species corresponding to 14 different elements.

We observed a correlation between iron abundance and effective temperature/surface gravity where, for instance, M67 dwarfs are more metal rich (0.00 dex) than giants (-0.13 dex). As mentioned in the previous section, when deriving the effective temperature, surface gravity and metallicity at the same time from spectra, degeneracies among those parameters leads to small correlations where

lower metallicities are found for lower surface gravities and vice versa. Nevertheless, when working with $[X/Fe]$ ratios, we observed that the correlations are minimized.

After referring all the abundances to iron, we still observe differences between stars in different evolutionary stages but this time in the opposite sense (e.g. giants tend to be richer than dwarfs). Previous works have already detected trends in chemical abundances with effective temperature and surface gravity solar metal open clusters such as M67 [weaker differences; Önehag et al., 2014], NGC5822 or IC4756 [differences higher than 0.15 dex for Na, Si and Ti; Pace et al., 2010]. For instance, in our work, the abundances of V I, Mn I, Co I, Mg I, Si I, and Na I are effectively enhanced for evolved stars in M67 and IC4651 with increases higher than 0.10 dex. The rest of elements present smaller variations that in most of the cases fall inside the error margins (lower than 0.05 dex).

The depletion of some elements could be caused by the physical atomic diffusion process (pushing heavier elements in the direction of increasing pressure and temperature) that takes place during the main sequence lifetime of the star and modifies the chemical composition of the stellar atmosphere. The effect is different in function of the element since the radiative levitation process reduces the gravitational acceleration (caused by the interaction of photons with gas particles) and acting selectively on different atoms and ions. When the star evolves toward the red giant branch, elements previously drained from the surface are mixed up again as the outer convection zone gradually reaches deeper layers. In this context, giants are preferred to study the chemical history of the Galaxy since, eventually, the initial chemical composition is going to be restored (except for fragile elements such as Lithium).

Additionally, we cannot neglect that the assumption of Local Thermodynamic Equilibrium (LTE) may introduce systematic errors and abundance trends when analyzing stars covering large intervals of effective temperatures, surface gravities and metallicities. For instance, Randich et al. [2006] reported that the Na difference between dwarfs and giants in M67 can be explained by NLTE effects that are larger for cool giants than for warm dwarfs [Mashonkina et al., 2000].

Consequently, even if stars are born from the same giant molecular clouds, we can find chemical differences that depend on the evolutionary stage of the star. This represent a serious complication if we expect to apply the chemical tagging technique to any kind of star in our Galaxy. To reduce these effects in our test, we decided to divide each cluster in four subgroups with stars in different evolutionary stages.

Once we separated all the stars per evolutionary stage and filtered out those chemically peculiar cases, we executed a blind experiment designed to recover the initial stellar groups by only using the chemical abundances. We compressed the 17 abundances into two dimensions using the Principal Components Analysis, and we executed a K-Means clustering algorithm in order to form group of stars chemically similar. Even if the conditions of the experiments were extremely favorable (i.e. separation per evolutionary stage, filtered chemically peculiar stars), we were not able to recover the original cluster because of their high degree of overlapping in the chemical space. Thus, in a real scenario where the chemical tagging technique would be applied to a great number of field stars, we expect to have a high level of contamination that would severely diminish the efficiency of this technique to recover conatal aggregates (born from the same cloud at the same time).

5.2 Perspectives

The Gaia FGK benchmark stars will be used as pillars for the calibration of the parameters that will be derived for one billion stars by Gaia [Perryman et al., 2001]. Since the satellite cannot directly observe the benchmark stars due to their brightness, Gaia will implement a two-level procedure [Bailer-Jones et al., 2013]. At the second level, a much larger sample of several thousands reference stars with parameters derived from spectra and calibrated with the Gaia benchmark stars (i.e. first level). Thus,

we plan to use our spectral pipelines based on iSpec to analyse this second level reference stars and build a high-resolution library.

Regarding the chemical tagging technique, it is intuitive to conclude that increases in chemical dimensionality lead to improvements in the clustering experiments, although the difficulty in deriving abundances for some elements (e.g., weak absorption lines, fewer lines, blended regions) at a given resolution could also yield greater uncertainties and potential scatter. We proved that not all the elements have the same discriminatory power [previous studies too such as [Mitschang et al., 2013](#)], some tend to act in concert while others contribute significantly to the discrimination such as the heavy n-capture element Ba. For future analysis, it would be interesting to include other elements such as La, Nd and Eu that are formed through similar processes that produce Ba (slow and rapid n-capture processes in low mass AGB, [Busso et al. 2001](#); and core-collapse supernovae, [Kratz et al. 2007](#)).

There is also room to improve automatic analysis and spectral modelling, for instance, incorporating NTLE effects, hyperfine structure and averaged 3-D model atmosphere. Time dependent 3-D hydrodynamical models [[Pereira et al., 2013](#)] are still computationally too expensive as to use it for massive analysis, thus the averaged 3-D model are a good compromise. This improvements could reduce discrepancies among stars in different evolutionary stages and achieve a higher degree of success when recovering clusters using chemical abundances [[Bergemann et al., 2012](#), [Lind et al., 2012](#)].

The experience gain and the powerful tools created during this work will allow us to execute further spectroscopic studies such as the study of field stars from our Galaxy to identify chemical peculiarities (e.g., among different galactic structures) or the chemical analysis of stars with confirmed exoplanets. Ongoing and future spectroscopic surveys (e.g., GES and GALAH) will provide us with a huge amount of spectra that will open the door to new studies and thrilling discoveries.

Chapter 6

Conclusions et perspectives (version en français)

Contents

6.1	Conclusions	132
6.1.1	La librairie spectrale	133
6.1.2	L'analyse spectroscopique	133
6.1.3	La technique de marquage chimique	135
6.2	Perspectives	136

6.1 Conclusions

L'idée derrière la technique de marquage chimique est une idée prometteuse pour l'étude de notre galaxie. La plupart des étoiles sont nées ensemble dans des nuages moléculaires géants. Ainsi, en faisant l'hypothèse que le gaz est chimiquement homogène et bien mélangé, on peut s'attendre à ce que les étoiles formées dans un nuage donné partagent une signature chimique unique. La technique de marquage chimique offre donc la possibilité d'identifier les étoiles qui sont nées ensemble mais qui ne sont plus aujourd'hui gravitationnellement liées et se sont éparpillées dans la galaxie.

La viabilité de cette approche dépend de la réponse à deux questions fondamentales: Est-ce que les étoiles nées ensemble ont une signature chimique unique ? Et, est-ce que les signatures chimiques sont assez différentes parmi des étoiles provenant de nuages moléculaires différents ?

Pour répondre à ces questions, nous avons décidé d'étudier un grand nombre d'amas ouverts. Ces amas sont les restes de groupes d'étoiles du disque galactique qui ont réussi à survivre jusqu'à aujourd'hui. Comme nous sommes sûrs que leur naissance a eu lieu dans le même nuage moléculaire à la même époque, les étoiles qui les constituent représentent la population idéale pour tester la technique de marquage chimique.

Quand on utilise les étoiles d'amas ouverts, les deux questions fondamentales se réduisent à une seule question: Sommes-nous capables de retrouver les amas initiaux en ne regardant que l'information chimique des étoiles ?

Il y a plusieurs défis à relever qui rendent difficile un tel test critique. Le premier est le besoin d'avoir une méthode d'analyse spectrale homogène. Déterminer les paramètres atmosphériques et les abondances chimiques grâce à la littérature aboutit forcément à des erreurs systématiques. En effet, chaque étude utilise sa propre méthode spectrale, avec des procédures de normalisation du continuum différentes, des modèles d'atmosphère différents et des données atomiques différentes. Il n'est pas recommandé de mélanger les valeurs issues de la littérature, sinon les conclusions ne seraient pas robustes. Par exemple, si les résultats du test montrent qu'il est impossible de retrouver les amas initiaux à partir de l'information chimique, cela pourrait vouloir dire que l'idée de la technique de marquage chimique est moins prometteuse que nous le pensions, ou qu'il est nécessaire de déterminer les abondances de façon homogène. Ainsi, la meilleure façon de faire était de compiler directement les observations et de faire nous-même une analyse homogène, même si ça représentait un investissement beaucoup plus important en temps et un effort supplémentaire.

Le second défi est d'obtenir des conclusions sensées à propos de notre galaxie en utilisant la technique du marquage chimique. Nous devons analyser un grand nombre de spectres stellaires d'une manière non-subjective. De plus, nous devons garantir la reproductibilité car c'est un des piliers centraux de la science (trop souvent oublié dans un nombre croissants de travaux). Afin de vérifier ces conditions, la seule approche concevable est l'automatisation du processus d'analyse. Réduire l'intervention de l'homme et les décisions subjectives est le seul chemin qui nous permette d'analyser un grand nombre de spectres stellaires.

A partir du moment où nous avons décidé de créer notre propre chaîne d'analyse d'une manière totalement automatique, un troisième défi est apparu: l'évaluation de la méthode. Il est absolument nécessaire d'avoir un ensemble d'étoiles très bien connues, recouvrant une grande partie de l'espace des paramètres (i.e., température effective, gravité de surface et métallicité), pour nous aider à évaluer la chaîne de traitement spectroscopique. Nous avons décidé d'utiliser les étoiles de référence de Gaia (les "Gaia benchmark stars"), qui seront aussi utilisées pour la calibration de la mission Gaia [Perryman et al., 2001].

Pour répondre à ces défis, nous avons créé une librairie de spectres haute résolution et à grand rapport signal-sur-bruit avec les étoiles de référence de Gaia. Nous avons développé notre propre

outil d'analyse spectrale, que nous avons appelé iSpec, comprenant une chaîne de traitement totalement automatique (et vérifiée grâce aux étoiles de référence de Gaia). Finalement, nous avons testé la technique de marquage chimique en utilisant des étoiles d'amas ouverts pour répondre à la question: sommes-nous capables de retrouver les amas initiaux en ne regardant que l'information chimique ?

6.1.1 La librairie spectrale

En nous basant sur la liste de 34 étoiles de référence de Gaia et de leurs paramètres atmosphériques (Heiter et al., en prep.), nous avons cherché des spectres haute résolution et grand signal-sur-bruit obtenus par différents instruments.

Un procédé informatique automatique a été développé pour transformer les spectres observés en une librairie homogène de spectres d'étoiles de référence de Gaia. Comme la longueur d'onde varie d'un set d'observation à l'autre, nous avons choisi de limiter la librairie à la gamme entre 480 et 680 nm, là où les spectres ont un meilleur rapport signal-sur-bruit. De plus, cette gamme correspond aux intérêts du sondage Gaia-ESO, "Gaia ESO Survey" [GES, [Gilmore et al., 2012](#)] **installation d'UVES au ESO-VLT**.

Le processus automatique réduit l'intervention humaine (i.e., la subjectivité) et garantit la reproductibilité. Ceci nous permet de générer rapidement de nouvelles versions de la librairie en changeant juste quelques paramètres dans le processus automatique afin de correspondre aux besoins d'études spectroscopiques spécifiques (e.g., des résolutions plus basses et/ou des gammes de fréquences différentes).

Il était aussi nécessaire de valider la cohérence de la librairie et de garantir un niveau de qualité élevé. Ainsi, nous avons attentivement vérifié la normalisation et les procédures de convolution en réalisant des tests automatiques. La partie de la correction de la vitesse radiale a été validée en comparant nos résultats avec les mesures de haute précision de HARPS. Nous avons vérifié la cohérence des résultats du traitement des spectres en comparant nos résultats avec ceux obtenus grâce à des mesures de largeur équivalente ("equivalent width") obtenues indépendamment de notre procédé.

La librairie de spectres haute résolution des étoiles de Gaia est un outil puissant pour évaluer la robustesse des analyses spectrales. Nous le montrons dans le développement de notre propre chaîne de traitement spectroscopique basée sur iSpec.

6.1.2 L'analyse spectroscopique

Il y a déjà plusieurs outils disponibles pour analyser des spectres (e.g. ARES de [Sousa et al. 2007](#), DAOSPEC de [Stetson and Pancino 2008](#) ou DOOp de [Cantat-Gaudin et al. 2014](#)) et pour dériver les paramètres atmosphériques et les abondances chimiques (e.g. GALA [Mucciarelli et al. 2013](#), FAMA [Magrini et al. 2013](#) ou SME [Valenti and Piskunov 1996](#)).

Au début du projet, nous avons commencé à dériver les paramètres atmosphériques (i.e., la température effective, la gravité de surface et la métallicité) et les abondances chimiques avec SME. Cet outil génère au besoin des spectres synthétiques et minimise les différences avec le spectre observé en exécutant un algorithme de moindre carré (i.e., "synthetic spectral fitting technique"). Sans entrer dans les détails, le processus de minimisation a été codé en langage IDL et les calculs les plus demandants au niveau informatique (i.e., la synthèse de spectre) font partie d'une librairie binaire. IDL est un langage dynamique pour lequel il est nécessaire d'acheter une licence commerciale¹. Il y a un

1. A ce jour, il y a des machines virtuelles qui permettent l'exécution de programmes IDL mais pas de les éditer.

équivalent open-source, nommé GDL² pour programmer avec une alternative compatible avec IDL, mais malheureusement, il n'est pas assez mature pour supporter SME.

Un des piliers de la science est la reproductibilité et la possibilité de valider les résultats d'autres études. Cette nécessité correspond tout à fait à la philosophie open-source, pour laquelle n'importe qui peut avoir accès au code source et peut facilement partager des projets avec d'autres chercheurs. L'utilisation d'IDL nous limitait sous plusieurs aspects: le lieu où exécuter l'analyse et le nombre de machines disponibles pour paralléliser l'analyse. De plus, l'utilisation d'une librairie binaire d'accès limité pour la synthèse de spectre nous empêchait de comprendre sa structure interne.

Nous avons déjà développé plusieurs routines en utilisant le langage python afin de créer la librairie d'étoiles de référence de Gaia. Python est un langage de programmation de haut niveau qui est open-source et largement utilisé par la communauté. Nous avons décidé de remplacer IDL par python pour nous affranchir des difficultés exposées précédemment. Nous avons encore besoin d'un outil pour synthétiser les spectres stellaires et nous avons considéré plusieurs options (comme Turbospectrum, Plez 2012). Finalement, nous avons décidé d'utiliser SPECTRUM [Gray and Corbally, 1994]. Ce code est bien documenté, codé en C et relativement facile à intégrer avec python. De plus, il ne nécessite pas de compilateurs propriétaires.

Voici comment est né iSpec. Nous avons développé une alternative plus riche à SME qui ne dépend pas d'un code fermé, et nous avons intégré toutes nos routines pour le traitement de spectres (e.g., détermination de la vitesse radiale, normalisation du continuum). Nous avons ainsi créé une chaîne de traitement spectroscopique qui peut être utilisée de façon automatique à partir de scripts python ou manuellement à travers une interface facile d'utilisation.

iSpec contient plusieurs modèles d'atmosphère et plusieurs listes de raies que l'utilisateur peut choisir. En plus de la technique de fit de spectre synthétique, nous avons codé la méthode des largeurs équivalentes, qui est basée sur l'hypothèse d'équilibre d'excitation et d'ionisation (comme le travail de GALA ou FAMA). Cette grande flexibilité pour changer les outils de l'analyse spectrale nous permet de tester les différentes chaînes de traitement en utilisant la librairie de spectres d'étoiles de référence de Gaia. Par exemple, à notre connaissance, c'est la première fois que les deux méthodes (fit de spectre synthétique et largeur équivalente) ont été comparées en couvrant un espace des paramètres si large et en utilisant exactement le même procédé de normalisation, de données atomiques, de modèle d'atmosphère et de code de transfert radiatif (i.e., SPECTRUM). Les conclusions principales de ce test sont :

1. La chaîne de traitement reposant sur la technique de fit de spectre synthétique donne des résultats meilleurs et plus précis.
2. Quand on utilise seulement les spectres pour dériver les paramètres atmosphériques, la température effective, la gravité de surface et la métallicité sont corrélées de façon équivalente, indépendamment de la technique utilisée.
3. La chaîne de traitement reposant sur la technique de fit de spectre synthétique est plus efficace à des résolutions faibles (i.e. 7500) et des rapports signal-sur-bruit faibles (i.e. 25) que la chaîne de traitement reposant sur la méthode de largeur équivalente.

iSpec est un nouveau outil open-source disponible à l'adresse <http://www.blancocuaresma.com/s/>, qui peut être utilisé librement pour n'importe quelle étude spectroscopique.

2. <http://gnudatalanguage.sourceforge.net/>

6.1.3 La technique de marquage chimique

Le test de la technique de marquage chimique est le but ultime de ce travail. Nous abordons le problème en concevant une expérience qui utilise les étoiles d'amas ouverts. A cet effet, nous avons fait une compilation de spectres haute-résolution obtenus par différents instruments (i.e. NARVAL, HARPS, UVES) dans le champ de vue d'amas ouverts connus.

Pour nous assurer de la reproductibilité de notre méthode, nous avons développé un processus automatique basé sur iSpec afin d'homogénéiser les observations, de dériver les paramètres atmosphériques et de déterminer les abondances chimiques avec une approche différentielle. Après avoir éliminé les étoiles ayant des spectres à rapport signal-sur-bruit faible, les étoiles qui ne font pas partie de l'amas (différenciées grâce à leur vitesse radiale), les étoiles qui ne sont pas F, G ou K ou qui ont une chimie étrange, nous nous sommes retrouvé avec un total de 232 étoiles faisant partie de 32 amas ouverts avec des abondances de 17 espèces (correspondant à 14 éléments différents).

Nous avons observé une corrélation entre l'abondance en fer et la température effective/gravité de surface. Par exemple, les naines de M67 sont plus riches en métaux (0,00 dex) que les géantes (-0,13 dex). Comme nous l'avons dit dans la section précédente, quand nous dérivons les paramètres atmosphériques (température effective, gravité de surface et métallicité) à partir du spectre, les dégénérescences entre chaque paramètre produisent de faibles corrélations. Par exemple, on trouve des métallicités faibles pour des gravités de surface faible, et vice-versa.

Nous utilisons le fer comme référence pour les abondances. En faisant ceci, nous observons toujours des différences parmi les étoiles à différents stades d'évolution, mais cette fois dans le sens opposé (e.g., les géantes sont plus riches que les naines). Des travaux précédents ont déjà fait part de la détection de ces tendances des abondances chimiques avec la température effective et la gravité de surface pour des étoiles d'amas ouverts de métallicité solaire comme M67 [petites différences; [Önehag et al., 2014](#)], NGC5822 ou IC4756 [différences plus grandes que 0,15 dex pour Na, Si et Ti; [Pace et al., 2010](#)]. Par exemple, dans cette thèse, les abondances de V I, Mn I, Co I, Mg I, Si I, et Na I sont en effet accrues (augmentation de plus de 0,10 dex) pour des étoiles évoluées de M67 et IC4651. Le reste des éléments présentent des variations plus faibles, qui dans la plupart des cas sont en dessous des barres d'erreurs (plus faibles que 0,05 dex).

Le manque de certains éléments par rapport à d'autres peut être produit par la diffusion atomique (qui pousse les éléments les plus lourds vers les régions de plus forte pression et température) qui a lieu quand l'étoile est sur la séquence principale et qui modifie la composition chimique de l'atmosphère de l'étoile. L'effet est différent en fonction de l'élément. En effet, la force de radiation (produite par l'interaction des photons avec les particules de gaz) réduit l'accélération gravitationnelle et agit de façon sélective sur les différents atomes ou ions. Quand l'étoile évolue vers la branche des géantes rouges, les éléments qui avant tombaient vers le coeur de l'étoile sont à nouveau mélangés quand la zone de convection externe atteint des couches inférieures. Dans ce contexte, les géantes sont plus adaptées à l'étude de l'histoire chimique de la galaxie puisque, éventuellement, elles vont retrouver la composition chimique initiale (sauf pour des éléments fragiles comme le Lithium).

De plus, nous ne pouvons pas négliger que l'hypothèse de l'équilibre thermodynamique local (LTE) puisse introduire des erreurs systématiques et des tendances dans les abondances lors de l'analyse d'étoiles recouvrant une large gamme de températures, gravités de surface et métallicités. Par exemple, [Randich et al. \[2006\]](#) ont reporté que la différence en sodium (Na) entre les géantes et les naines de M67 peut être expliquée par des effets de non-LTE qui sont plus importants pour des géantes froides que des naines chaudes [[Mashonkina et al., 2000](#)].

Par conséquent, même si les étoiles sont nées à partir du même nuage moléculaire, nous pouvons trouver des différences du point de vue chimique. Ces différences dépendent du stade d'évolution de l'étoile. Cette observation représente une vraie complication si l'on veut appliquer la méthode de

marquage chimique à n'importe quelles étoiles de la galaxie. Pour réduire ces effets dans notre test, nous avons décidé de diviser chaque amas en quatre sous-groupes contenant des étoiles appartenant au même stade d'évolution.

Après avoir séparé toutes les étoiles selon leur stade d'évolution et enlevé les étoiles ayant une chimie non conventionnelle, nous avons effectué une expérience en aveugle pour tenter de retrouver les amas initiaux en utilisant seulement les abondances chimiques de chaque étoile. Nous avons compressé les 17 abondances en deux dimensions en utilisant la technique d'analyse en composantes principales (PCA). Nous avons ensuite utilisé un algorithme des k-moyennes ("K-Means clustering algorithm") pour former des groupes d'étoiles chimiquement similaires. Même si les conditions de l'expérience étaient extrêmement favorables (i.e., séparation des étoiles selon leur stade d'évolution, le filtrage des étoiles chimiquement étranges), nous n'avons pas été en capacité de retrouver les amas initiaux à cause du haut degré de recouvrement dans l'espace des paramètres chimiques. Ainsi, dans un scénario plus réaliste, où la technique de marquage chimique serait utilisée pour un grand nombre d'étoiles du champ, nous nous attendons à avoir un haut degré de contamination qui réduirait fortement l'efficacité de la technique pour retrouver des groupes d'étoiles nées ensemble.

6.2 Perspectives

Les étoiles FGK de référence de Gaia de notre librairie seront utilisées pour la calibration des paramètres que nous allons dériver pour le milliard d'étoiles observé par Gaia [Perryman et al., 2001]. Comme le satellite ne peut pas observer directement les étoiles de référence à cause de leur brillance, Gaia va utiliser une procédure à deux niveaux [Bailer-Jones et al., 2013]. Le premier niveau correspond aux étoiles de référence de Gaia utilisées ici. Le deuxième niveau correspondra à un échantillon beaucoup plus grand de plusieurs milliers d'étoiles de référence. Les paramètres de ces étoiles seront obtenus grâce à leurs spectres et seront calibrés avec les étoiles du premier niveau. Ainsi, nous avons pour objectif d'utiliser notre chaîne de traitement spectroscopique basée sur iSpec afin d'analyser ce second niveau d'étoiles de référence et de construire une librairie de spectres haute-résolution.

Concernant la technique de marquage chimique, il est intuitif de conclure qu'augmenter le nombre d'éléments chimiques considérés devrait améliorer l'expérience des amas. Mais, la dérivation de certains éléments à une certaine résolution peut être difficile (e.g., petites raies d'absorption, petit nombre de raies, régions de recouvrements de raies) et peut entraîner des incertitudes plus grandes et une dispersion plus grande. Nous avons montré que tous les éléments n'avaient pas le même pouvoir discriminatoire [études précédentes comme Mitschang et al., 2013]. Certains éléments agissent dans le même sens alors que certains permettent de faire vraiment une différence comme le baryum (Ba), élément lourd principalement créé par processus S. Pour des analyses futures, il serait intéressant d'inclure d'autres éléments comme le lanthanum (La), le neodymium (Nd) et l'euporium (Eu), créés eux-aussi par des processus similaires au baryum (processus de capture neutronique rapide ou lente dans les étoiles de la branche asymptotique des géantes, Busso et al. 2001; et des supernovae de type Ib, Ic et II, Kratz et al. 2007).

Il y a aussi de la marge pour améliorer l'analyse automatique et la modélisation de spectres, en incorporant par exemple les effets non-LTE, la structure hyperfine des atomes et des modèles d'atmosphère stellaire 3-D moyennés. Les modèles d'atmosphère 3-D dépendant du temps [Pereira et al., 2013] sont toujours très demandant en temps de calcul pour être utilisés pour des analyses massives. L'utilisation de modèles moyennés semble être un bon compromis. Ces améliorations pourraient réduire les différences entre les étoiles à différents stades évolutifs et permettre de meilleurs résultats pour retrouver les amas initiaux en utilisant l'information chimique [Bergemann et al., 2012, Lind et al., 2012].

L'expérience gagnée lors de cette thèse, ainsi que les puissants outils créés, nous permettront de faire d'autres études spectroscopiques. Par exemple, nous étudierons les étoiles du champ de notre galaxie pour identifier les particularités chimiques (e.g., entre les différentes structures de notre galaxie) ou nous ferons l'analyse chimique des étoiles ayant des exoplanètes confirmées. Les sondages spectroscopiques en cours et futurs (e.g., GES et GALAH) nous donneront accès à de nombreux spectres qui ouvriront la porte vers de nouvelles études et des découvertes passionnantes.

Bibliography

- C. Allende Prieto. Velocities from Cross-Correlation: A Guide for Self-Improvement. *AJ*, 134:1843–1848, November 2007. doi: 10.1086/522051.
- C. Allende Prieto, S. R. Majewski, R. Schiavon, K. Cunha, P. Frinchaboy, J. Holtzman, K. Johnston, M. Shetrone, M. Skrutskie, V. Smith, and J. Wilson. APOGEE: The Apache Point Observatory Galactic Evolution Experiment. *Astronomische Nachrichten*, 329:1018, December 2008a. doi: 10.1002/asna.200811080.
- C. Allende Prieto, T. Sivarani, T. C. Beers, Y. S. Lee, L. Koesterke, M. Shetrone, C. Sneden, D. L. Lambert, R. Wilhelm, C. M. Rockosi, D. K. Lai, B. Yanny, I. I. Ivans, J. A. Johnson, W. Aoki, C. A. L. Bailer-Jones, and P. Re Fiorentin. The SEGUE Stellar Parameter Pipeline. III. Comparison with High-Resolution Spectroscopy of SDSS/SEGUE Field Stars. *AJ*, 136:2070–2082, November 2008b. doi: 10.1088/0004-6256/136/5/2070.
- E. Anders and N. Grevesse. Abundances of the elements - Meteoritic and solar. *Geochim. Cosmochim. Acta*, 53:197–214, January 1989. doi: 10.1016/0016-7037(89)90286-X.
- B. Anguiano, K. Freeman, J. Bland-Hawthorn, G. De Silva, M. Asplund, D. Carollo, V. D’Orazi, S. Keller, S. Martell, S. Sharma, C. Sneden, L. W. de Boer, D. Zucker, and T. Zwitter. The GALAH survey. In S. Feltzing, G. Zhao, N. A. Walton, and P. Whitelock, editors, *IAU Symposium*, volume 298 of *IAU Symposium*, pages 322–325, January 2014. doi: 10.1017/S1743921313006522.
- David Arthur and Sergei Vassilvitskii. k-means++: The advantages of careful seeding. In *Proceedings of the eighteenth annual ACM-SIAM symposium on Discrete algorithms*, pages 1027–1035. Society for Industrial and Applied Mathematics, 2007.
- M. Asplund, N. Grevesse, and A. J. Sauval. The Solar Chemical Composition. In T. G. Barnes, III and F. N. Bash, editors, *Cosmic Abundances as Records of Stellar Evolution and Nucleosynthesis*, volume 336 of *Astronomical Society of the Pacific Conference Series*, page 25, September 2005.
- M. Asplund, N. Grevesse, A. J. Sauval, and P. Scott. The Chemical Composition of the Sun. *ARA&A*, 47:481–522, September 2009. doi: 10.1146/annurev.astro.46.060407.145222.
- M. Aurière. Stellar Polarimetry with NARVAL. In J. Arnaud and N. Meunier, editors, *EAS Publications Series*, volume 9 of *EAS Publications Series*, page 105, 2003.
- T. R. Ayres. StarCAT: A Catalog of Space Telescope Imaging Spectrograph Ultraviolet Echelle Spectra of Stars. *ApJS*, 187:149–171, March 2010. doi: 10.1088/0067-0049/187/1/149.

- S. Bagnulo, E. Jehin, C. Ledoux, R. Cabanac, C. Melo, R. Gilmozzi, and ESO Paranal Science Operations Team. The UVES Paranal Observatory Project: A Library of High-Resolution Spectra of Stars across the Hertzsprung-Russell Diagram. *The Messenger*, 114:10–14, 2003.
- C. A. L. Bailer-Jones, R. Andrae, B. Arcay, T. Astraatmadja, I. Bellas-Velidis, A. Berihuete, A. Bijaoui, C. Carrión, C. Dafonte, Y. Damerджи, A. Dapergolas, P. de Laverny, L. Delchambre, P. Drazinos, R. Drimmel, Y. Frémat, D. Fustes, M. García-Torres, C. Guédé, U. Heiter, A.-M. Janotto, A. Karamelas, D.-W. Kim, J. Knude, I. Kolka, E. Kontizas, M. Kontizas, A. J. Korn, A. C. Lanzafame, Y. Lebreton, H. Lindstrøm, C. Liu, E. Livanou, A. Lobel, M. Manteiga, C. Martayan, C. Ordenovic, B. Pichon, A. Recio-Blanco, B. Rocca-Volmerange, L. M. Sarro, K. Smith, R. Sordo, C. Soubiran, J. Surdej, F. Thévenin, P. Tsalmantza, A. Vallenari, and J. Zorec. The Gaia astrophysical parameters inference system (Apsis). Pre-launch description. *A&A*, 559:A74, November 2013. doi: 10.1051/0004-6361/201322344.
- P. Ballester, A. Modigliani, O. Boitquin, S. Cristiani, R. Hanuschik, A. Kaufer, and S. Wolf. The UVES Data Reduction Pipeline. *The Messenger*, 101:31–36, 2000.
- A. Baranne, D. Queloz, M. Mayor, G. Adrianzyk, G. Knispel, D. Kohler, D. Lacroix, J.-P. Meunier, G. Rimbaud, and A. Vin. ELODIE: A spectrograph for accurate radial velocity measurements. *A&AS*, 119:373–390, October 1996.
- S. C. Barden, D. J. Jones, S. I. Barnes, J. Heijmans, A. Heng, G. Knight, D. R. Orr, G. A. Smith, V. Churilov, J. Brzeski, L. G. Waller, K. Shortridge, A. J. Horton, D. Mayfield, R. Haynes, D. M. Haynes, D. Whittard, M. Goodwin, S. Smedley, I. Saunders, P. R. Gillingham, E. Penny, T. J. Farrell, M. Vuong, R. Heald, S. Lee, R. Muller, K. Freeman, J. Bland-Hawthorn, D. F. Zucker, and G. de Silva. HERMES: revisions in the design for a high-resolution multi-element spectrograph for the AAT. In *Society of Photo-Optical Instrumentation Engineers (SPIE) Conference Series*, volume 7735 of *Society of Photo-Optical Instrumentation Engineers (SPIE) Conference Series*, July 2010. doi: 10.1117/12.856103.
- M. Bergemann, K. Lind, R. Collet, Z. Magic, and M. Asplund. Non-LTE line formation of Fe in late-type stars - I. Standard stars with 1D and <3D> model atmospheres. *MNRAS*, 427:27–49, November 2012. doi: 10.1111/j.1365-2966.2012.21687.x.
- J. L. Bertaux, R. Lallement, S. Ferron, C. Boone, and R. Bodichon. TAPAS, a web-based service of atmospheric transmission computation for astronomy. *ArXiv e-prints*, November 2013.
- J. L. Bertaux, R. Lallement, S. Ferron, C. Boone, and R. Bodichon. TAPAS, a web-based service of atmospheric transmission computation for astronomy. *A&A*, 564:A46, April 2014. doi: 10.1051/0004-6361/201322383.
- G. Bertelli, L. Girardi, P. Marigo, and E. Nasi. Scaled solar tracks and isochrones in a large region of the Z-Y plane. I. From the ZAMS to the TP-AGB end for 0.15-2.5 M stars. *A&A*, 484:815–830, June 2008. doi: 10.1051/0004-6361:20079165.
- G. Bertelli, E. Nasi, L. Girardi, and P. Marigo. Scaled solar tracks and isochrones in a large region of the Z-Y plane. II. From 2.5 to 20 M \odot stars. *A&A*, 508:355–369, December 2009. doi: 10.1051/0004-6361/200912093.
- S. Blanco-Cuaresma, C. Soubiran, P. Jofré, and U. Heiter. iSpec: An integrated software framework for the analysis of stellar spectra. *ArXiv e-prints*, December 2013.
- S. Blanco-Cuaresma, C. Soubiran, U. Heiter, and P. Jofré. Determining stellar atmospheric parameters and chemical abundances of FGK stars with iSpec. *ArXiv e-prints*, July 2014a.

- S. Blanco-Cuaresma, C. Soubiran, P. Jofré, and U. Heiter. The Gaia FGK benchmark stars. High resolution spectral library. *A&A*, 566:A98, June 2014b. doi: 10.1051/0004-6361/201323153.
- J. Bland-Hawthorn and K. C. Freeman. Galaxy Genesis - Unravelling the Epoch of Dissipation in the Early Disk. *PASA*, 21:110–120, 2004. doi: 10.1071/AS04030.
- C. Bonatto, L. O. Kerber, E. Bica, and B. X. Santiago. Probing disk properties with open clusters. *A&A*, 446:121–135, January 2006. doi: 10.1051/0004-6361:20053573.
- A. J. Booth and D. E. Blackwell. The effect of hyperfine structure on stellar abundance analysis. *MNRAS*, 204:777–781, August 1983.
- A. G. A. Brown. Open Clusters and OB Associations: a Review. In *Revista Mexicana de Astronomía y Astrofísica Conference Series*, volume 11 of *Revista Mexicana de Astronomía y Astrofísica Conference Series*, page 89, July 2001.
- M. Busso, R. Gallino, D. L. Lambert, C. Travaglio, and V. V. Smith. Nucleosynthesis and Mixing on the Asymptotic Giant Branch. III. Predicted and Observed s-Process Abundances. *ApJ*, 557: 802–821, August 2001. doi: 10.1086/322258.
- T. Cantat-Gaudin, P. Donati, E. Pancino, A. Bragaglia, A. Vallenari, E. D. Friel, R. Sordo, H. R. Jacobson, and L. Magrini. DOOp, an automated wrapper for DAOSPEC. *A&A*, 562:A10, February 2014. doi: 10.1051/0004-6361/201322533.
- D. Carollo, T. C. Beers, Y. S. Lee, M. Chiba, J. E. Norris, R. Wilhelm, T. Sivarani, B. Marsteller, J. A. Munn, C. A. L. Bailer-Jones, P. R. Fiorentin, and D. G. York. Two stellar components in the halo of the Milky Way. *Nature*, 450:1020–1025, December 2007. doi: 10.1038/nature06460.
- G. Carraro, D. Geisler, S. Villanova, P. M. Frinchaboy, and S. R. Majewski. Old open clusters in the outer Galactic disk. *A&A*, 476:217–227, December 2007. doi: 10.1051/0004-6361:20078113.
- C.-K. Chang, C.-M. Ko, and T.-H. Peng. Information on the Milky Way from the Two Micron All Sky Survey Whole Sky Star Count: The Structure Parameters. *ApJ*, 740:34, October 2011. doi: 10.1088/0004-637X/740/1/34.
- G. M. De Silva, C. Sneden, D. B. Paulson, M. Asplund, J. Bland-Hawthorn, M. S. Bessell, and K. C. Freeman. Chemical Homogeneity in the Hyades. *AJ*, 131:455–460, January 2006. doi: 10.1086/497968.
- G. M. De Silva, K. C. Freeman, M. Asplund, J. Bland-Hawthorn, M. S. Bessell, and R. Collet. Chemical Homogeneity in Collinder 261 and Implications for Chemical Tagging. *AJ*, 133:1161–1175, March 2007. doi: 10.1086/511182.
- G. M. De Silva, K. C. Freeman, and J. Bland-Hawthorn. Reconstructing Fossil Sub-structures of the Galactic Disk: Clues from Abundance Patterns of Old Open Clusters and Moving Groups. *PASA*, 26:11–16, April 2009. doi: 10.1071/AS08019.
- H. Dekker, S. D’Odorico, A. Kaufer, B. Delabre, and H. Kotzlowski. Design, construction, and performance of UVES, the echelle spectrograph for the UT2 Kueyen Telescope at the ESO Paranal Observatory. In M. Iye and A. F. Moorwood, editors, *Society of Photo-Optical Instrumentation Engineers (SPIE) Conference Series*, volume 4008 of *Society of Photo-Optical Instrumentation Engineers (SPIE) Conference Series*, pages 534–545, 2000.

- N. Delmotte, M. Dolensky, P. Padovani, J. Retzlaff, C. Rit e, P. Rosati, R. Slijkhuis, A. Wicenec, P. Fernique, and A. Micol. ESO Science Archive Interfaces. In C. Gabriel, C. Arviset, D. Ponz, and S. Enrique, editors, *Astronomical Data Analysis Software and Systems XV*, volume 351 of *Astronomical Society of the Pacific Conference Series*, page 690, July 2006.
- P. Demarque, J.-H. Woo, Y.-C. Kim, and S. K. Yi. Y^2 Isochrones with an Improved Core Overshoot Treatment. *ApJS*, 155:667–674, December 2004. doi: 10.1086/424966.
- W. S. Dias and J. R. D. L epine. Direct Determination of the Spiral Pattern Rotation Speed of the Galaxy. *ApJ*, 629:825–831, August 2005. doi: 10.1086/431456.
- W. S. Dias, B. S. Alessi, A. Moitinho, and J. R. D. L epine. New catalogue of optically visible open clusters and candidates. *A&A*, 389:871–873, July 2002. doi: 10.1051/0004-6361:20020668.
- J.-F. Donati. ESPaDOnS: An Echelle SpectroPolarimetric Device for the Observation of Stars at CFHT. In J. Trujillo-Bueno and J. Sanchez Almeida, editors, *Astronomical Society of the Pacific Conference Series*, volume 307 of *Astronomical Society of the Pacific Conference Series*, page 41, 2003.
- J.-F. Donati, M. Semel, B. D. Carter, D. E. Rees, and A. Collier Cameron. Spectropolarimetric observations of active stars. *MNRAS*, 291:658, 1997.
- P. Donati, T. Cantat Gaudin, A. Bragaglia, E. Friel, L. Magrini, R. Smiljanic, A. Vallenari, M. Tosi, R. Sordo, G. Tautvai sien e, S. Blanco-Cuaresma, M. T. Costado, D. Geisler, A. Klutsch, N. Mowlavi, C. Mu oz, I. San Roman, S. Zaggia, G. Gilmore, S. Randich, T. Bensby, E. Flaccomio, S. E. Koposov, A. J. Korn, E. Pancino, A. Recio-Blanco, E. Franciosini, P. de Laverny, J. Lewis, L. Morbidelli, L. Prisinzano, G. Sacco, C. C. Worley, A. Hourihane, P. Jofr e, C. Lardo, and E. Maiorca. The Gaia-ESO Survey: Reevaluation of the parameters of the open cluster Trumpler 20 using photometry and spectroscopy. *A&A*, 561:A94, January 2014. doi: 10.1051/0004-6361/201322911.
- O. J. Eggen, D. Lynden-Bell, and A. R. Sandage. Evidence from the motions of old stars that the Galaxy collapsed. *ApJ*, 136:748, November 1962. doi: 10.1086/147433.
- P. Englmaier, M. Pohl, and N. Bissantz. The Milky Way spiral arm pattern. 3D distribution of molecular gas. *Memorie della Societa Astronomica Italiana Supplementi*, 18:199, 2011.
- Martin Ester, Hans-Peter Kriegel, J rg Sander, and Xiaowei Xu. A density-based algorithm for discovering clusters in large spatial databases with noise. In *KDD*, volume 96, pages 226–231, 1996.
- S. Feltzing and M. Chiba. Elemental abundances in the Milky Way stellar disk(s), bulge, and halo. *New A Rev.*, 57:80–99, September 2013. doi: 10.1016/j.newar.2013.06.001.
- Y. Feng and M. R. Krumholz. Early turbulent mixing as the origin of chemical homogeneity in open star clusters. *ArXiv e-prints*, August 2014.
- Peter Filzmoser. A multivariate outlier detection method. In *Proceedings of the Seventh International Conference on Computer Data Analysis and Modeling*, volume 1, pages 18–22. Minsk: Belarusian State University, 2004.
- J. Finlay, A. Noriega-Crespo, E. D. Friel, and K. M. Cudworth. Galactic orbits and the survival of old open clusters. In *American Astronomical Society Meeting Abstracts*, volume 27 of *Bulletin of the American Astronomical Society*, page #107.02, December 1995.
- C. Francis and E. Anderson. XHIP-II: Clusters and associations. *Astronomy Letters*, 38:681–693, November 2012. doi: 10.1134/S1063773712110023.

- K. Freeman and J. Bland-Hawthorn. The New Galaxy: Signatures of Its Formation. *ARA&A*, 40: 487–537, 2002. doi: 10.1146/annurev.astro.40.060401.093840.
- K. C. Freeman. The HERMES Project: Reconstructing Galaxy Formation. In D. L. Block, K. C. Freeman, and I. Puerari, editors, *Galaxies and their Masks*, page 319, 2010. doi: 10.1007/978-1-4419-7317-7_27.
- Brendan J Frey and Delbert Dueck. Clustering by passing messages between data points. *science*, 315 (5814):972–976, 2007.
- E. D. Friel. The Old Open Clusters Of The Milky Way. *ARA&A*, 33:381–414, 1995. doi: 10.1146/annurev.aa.33.090195.002121.
- E. D. Friel, P. Donati, A. Bragaglia, H. R. Jacobson, L. Magrini, L. Prisinzano, S. Randich, M. Tosi, T. Cantat-Gaudin, A. Vallenari, R. Smiljanic, G. Carraro, R. Sordo, E. Maiorca, G. Tautvaišienė, P. Sestito, S. Zaggia, F. M. Jiménez-Esteban, G. Gilmore, R. D. Jeffries, E. Alfaro, T. Bensby, S. E. Koposov, A. J. Korn, E. Pancino, A. Recio-Blanco, E. Franciosini, V. Hill, R. J. Jackson, P. de Laverny, L. Morbidelli, G. G. Sacco, C. C. Worley, A. Hourihane, M. T. Costado, P. Jofré, and K. Lind. Gaia-ESO Survey: Properties of the intermediate age open cluster NGC 4815. *A&A*, 563: A117, March 2014. doi: 10.1051/0004-6361/201323215.
- G. Gilmore and P. Hewett. A new limit on the nature of the galactic missing mass. *Nature*, 306:669, December 1983. doi: 10.1038/306669a0.
- G. Gilmore, S. Randich, M. Asplund, J. Binney, P. Bonifacio, J. Drew, S. Feltzing, A. Ferguson, R. Jeffries, G. Micela, I. Negueruela, T. Prusti, H.-W. Rix, A. Vallenari, E. Alfaro, C. Allende-Prieto, C. Babusiaux, T. Bensby, R. Blomme, A. Bragaglia, E. Flaccomio, P. François, M. Irwin, S. Koposov, A. Korn, A. Lanzafame, E. Pancino, E. Paunzen, A. Recio-Blanco, G. Sacco, R. Smiljanic, S. Van Eck, and N. Walton. The Gaia-ESO Public Spectroscopic Survey. *The Messenger*, 147:25–31, March 2012.
- R. O. Gray and C. J. Corbally. The calibration of MK spectral classes using spectral synthesis. 1: The effective temperature calibration of dwarf stars. *AJ*, 107:742–746, February 1994. doi: 10.1086/116893.
- E. W. Greisen and M. R. Calabretta. Representations of world coordinates in FITS. *A&A*, 395:1061–1075, December 2002. doi: 10.1051/0004-6361:20021326.
- E. W. Greisen, M. R. Calabretta, F. G. Valdes, and S. L. Allen. Representations of spectral coordinates in FITS. *A&A*, 446:747–771, February 2006. doi: 10.1051/0004-6361:20053818.
- N. Grevesse and A. J. Sauval. Standard Solar Composition. *Space Sci. Rev.*, 85:161–174, May 1998. doi: 10.1023/A:1005161325181.
- N. Grevesse, M. Asplund, and A. J. Sauval. The Solar Chemical Composition. *Space Sci. Rev.*, 130: 105–114, June 2007. doi: 10.1007/s11214-007-9173-7.
- P. Grosbol, R. H. Harten, E. W. Greisen, and D. C. Wells. Generalized extensions and blocking factors for FITS. *A&AS*, 73:359–364, June 1988.
- P. Gruyters, A. J. Korn, O. Richard, F. Grundahl, R. Collet, L. I. Mashonkina, Y. Osorio, and P. S. Barklem. Atomic diffusion and mixing in old stars. IV. Weak abundance trends in the globular cluster NGC 6752. *A&A*, 555:A31, July 2013. doi: 10.1051/0004-6361/201220821.

- B. Gustafsson, B. Edvardsson, K. Eriksson, U. G. Jørgensen, Å. Nordlund, and B. Plez. A grid of MARCS model atmospheres for late-type stars. I. Methods and general properties. *A&A*, 486: 951–970, 2008. doi: 10.1051/0004-6361:200809724.
- C. R. Hayes and E. D. Friel. Radial Velocities of Three Poorly Studied Clusters and the Kinematics of Open Clusters. *AJ*, 147:69, April 2014. doi: 10.1088/0004-6256/147/4/69.
- U. Heiter and K. Eriksson. Geometry of giant star model atmospheres: a consistency test. *A&A*, 452: 1039–1048, June 2006. doi: 10.1051/0004-6361:20064925.
- U. Heiter, C. Soubiran, M. Netopil, and E. Paunzen. On the metallicity of open clusters. II. Spectroscopy. *A&A*, 561:A93, January 2014. doi: 10.1051/0004-6361/201322559.
- Serif Hekimoglu, R. Cuneyt Erenoglu, and Jan Kalina. Outlier detection by means of robust regression estimators for use in engineering science. *Journal of Zhejiang University SCIENCE A*, 10(6):909–921, June 2009. ISSN 1673-565X, 1862-1775. doi: 10.1631/jzus.A0820140. URL <http://link.springer.com/article/10.1631/jzus.A0820140>.
- K. Hinkle and L. Wallace. The Spectrum of Arcturus from the Infrared through the Ultraviolet. In T. G. Barnes, III and F. N. Bash, editors, *Cosmic Abundances as Records of Stellar Evolution and Nucleosynthesis*, volume 336 of *Astronomical Society of the Pacific Conference Series*, page 321, September 2005.
- K. Hinkle, L. Wallace, J. Valenti, and D. Harmer. *Visible and Near Infrared Atlas of the Arcturus Spectrum 3727-9300 Å*. 2000.
- Julia Bell Hirschberg and Andrew Rosenberg. V-measure: A conditional entropy-based external cluster evaluation. *Proceedings of EMNLP*, 2007.
- H. Huehnermann. Hyperfine structure in stellar spectral lines: a little nothing, a help, or a troublemaker? *Physica Scripta Volume T*, 47:70–74, 1993. doi: 10.1088/0031-8949/1993/T47/010.
- A.-K. Jappsen, R. S. Klessen, R. B. Larson, Y. Li, and M.-M. Mac Low. The stellar mass spectrum from non-isothermal gravoturbulent fragmentation. *A&A*, 435:611–623, May 2005. doi: 10.1051/0004-6361:20042178.
- P. Jofré, B. Panter, C. J. Hansen, and A. Weiss. Stellar atmosphere parameters with MA χ , a Massive compression of χ^2 for spectral fitting. *A&A*, 517:A57, July 2010. doi: 10.1051/0004-6361/201014013.
- P. Jofré, U. Heiter, S. Blanco-Cuaresma, and C. Soubiran. Gaia FGK Benchmark Stars and their reference parameters. *ArXiv e-prints 1312.2943*, December 2013.
- P. Jofré, U. Heiter, C. Soubiran, S. Blanco-Cuaresma, E. Pancino, M. Bergemann, T. Cantat-Gaudin, J. I. Gonzalez Hernandez, V. Hill, C. Lardo, P. de Laverny, K. Lind, L. Magrini, T. Masseron, D. Montes, A. Mucciarelli, T. Nordlander, A. Recio-Blanco, J. Sobeck, R. Sordo, S. G. Sousa, H. Tabernero, A. Vallenari, S. Van Eck, and C. C. Worley. FGK Benchmark Stars A new metallicity scale. *ArXiv e-prints*, September 2013.
- P. Jofré, U. Heiter, C. Soubiran, S. Blanco-Cuaresma, C. C. Worley, E. Pancino, T. Cantat-Gaudin, L. Magrini, M. Bergemann, J. I. González Hernández, V. Hill, C. Lardo, P. de Laverny, K. Lind, T. Masseron, D. Montes, A. Mucciarelli, T. Nordlander, A. Recio Blanco, J. Sobeck, R. Sordo, S. G. Sousa, H. Tabernero, A. Vallenari, and S. Van Eck. Gaia FGK benchmark stars: Metallicity. *A&A*, 564:A133, April 2014. doi: 10.1051/0004-6361/201322440.

- M. Jurić, Ž. Ivezić, A. Brooks, R. H. Lupton, D. Schlegel, D. Finkbeiner, N. Padmanabhan, N. Bond, B. Sesar, C. M. Rockosi, G. R. Knapp, J. E. Gunn, T. Sumi, D. P. Schneider, J. C. Barentine, H. J. Brewington, J. Brinkmann, M. Fukugita, M. Harvanek, S. J. Kleinman, J. Krzesinski, D. Long, E. H. Neilsen, Jr., A. Nitta, S. A. Snedden, and D. G. York. The Milky Way Tomography with SDSS. I. Stellar Number Density Distribution. *ApJ*, 673:864–914, February 2008. doi: 10.1086/523619.
- D. Katz, C. Soubiran, R. Cayrel, M. Adda, and R. Cautain. On-line determination of stellar atmospheric parameters T_{eff} , $\log g$, $[\text{Fe}/\text{H}]$ from ELODIE echelle spectra. I. The method. *A&A*, 338:151–160, October 1998.
- N. V. Kharchenko, A. E. Piskunov, S. Röser, E. Schilbach, and R.-D. Scholz. Astrophysical parameters of Galactic open clusters. *A&A*, 438:1163–1173, August 2005. doi: 10.1051/0004-6361/20042523.
- E. N. Kirby. Grids of ATLAS9 Model Atmospheres and MOOG Synthetic Spectra. *PASP*, 123:531–535, May 2011. doi: 10.1086/660019.
- M. Koleva, P. Prugniel, A. Bouchard, and Y. Wu. ULYSS: a full spectrum fitting package. *A&A*, 501:1269–1279, July 2009. doi: 10.1051/0004-6361/200811467.
- A. J. Korn, F. Grundahl, O. Richard, L. Mashonkina, P. S. Barklem, R. Collet, B. Gustafsson, and N. Piskunov. Atomic Diffusion and Mixing in Old Stars. I. Very Large Telescope FLAMES-UVES Observations of Stars in NGC 6397. *ApJ*, 671:402–419, December 2007. doi: 10.1086/523098.
- K.-L. Kratz, K. Farouqi, B. Pfeiffer, J. W. Truran, C. Sneden, and J. J. Cowan. Explorations of the r-Processes: Comparisons between Calculations and Observations of Low-Metallicity Stars. *ApJ*, 662:39–52, June 2007. doi: 10.1086/517495.
- F. Kupka, M.-L. Dubernet, and VAMDC Collaboration. Vamdc as a Resource for Atomic and Molecular Data and the New Release of Vald. *Baltic Astronomy*, 20:503–510, 2011.
- R. Kurucz and B. Bell. Atomic Line Data. *Atomic Line Data (R.L. Kurucz and B. Bell) Kurucz CD-ROM No. 23. Cambridge, Mass.: Smithsonian Astrophysical Observatory, 1995.*, 23, 1995.
- R. L. Kurucz. ATLAS12, SYNTHE, ATLAS9, WIDTH9, et cetera. *Memorie della Societa Astronomica Italiana Supplementi*, 8:14, 2005.
- R. L. Kurucz, I. Furenlid, J. Brault, and L. Testerman. *Solar flux atlas from 296 to 1300 nm*. 1984.
- C. J. Lada and E. A. Lada. Embedded Clusters in Molecular Clouds. *ARA&A*, 41:57–115, 2003. doi: 10.1146/annurev.astro.41.011802.094844.
- R. B. Larson. Star formation in groups. *MNRAS*, 272:213–220, January 1995.
- J.-W. Lee. A Chemical Abundance Study of three RHB and two RGB stars in NGC637 (M69). In S. Kurtz, editor, *Revista Mexicana de Astronomia y Astrofisica Conference Series*, volume 28 of *Revista Mexicana de Astronomia y Astrofisica Conference Series*, pages 120–124, June 2007.
- Y. S. Lee, T. C. Beers, T. Sivarani, C. Allende Prieto, L. Koesterke, R. Wilhelm, P. Re Fiorentin, C. A. L. Bailer-Jones, J. E. Norris, C. M. Rockosi, B. Yanny, H. J. Newberg, K. R. Covey, H.-T. Zhang, and A.-L. Luo. The SEGUE Stellar Parameter Pipeline. I. Description and Comparison of Individual Methods. *AJ*, 136:2022–2049, November 2008. doi: 10.1088/0004-6256/136/5/2022.
- K. Lind, A. J. Korn, P. S. Barklem, and F. Grundahl. Atomic diffusion and mixing in old stars. II. Observations of stars in the globular cluster NGC 6397 with VLT/FLAMES-GIRAFFE. *A&A*, 490:777–786, November 2008. doi: 10.1051/0004-6361/200810051.

- K. Lind, M. Bergemann, and M. Asplund. Non-LTE line formation of Fe in late-type stars - II. 1D spectroscopic stellar parameters. *MNRAS*, 427:50–60, November 2012. doi: 10.1111/j.1365-2966.2012.21686.x.
- S. Lloyd. Least squares quantization in pcm. *Information Theory, IEEE Transactions on*, 28(2):129–137, Mar 1982. ISSN 0018-9448. doi: 10.1109/TIT.1982.1056489.
- R. E. Luck and U. Heiter. Dwarfs in the Local Region. *AJ*, 131:3069–3092, June 2006. doi: 10.1086/504080.
- R. E. Luck and U. Heiter. Giants in the Local Region. *AJ*, 133:2464–2486, June 2007. doi: 10.1086/513194.
- L. Magrini, S. Randich, E. Friel, L. Spina, H. Jacobson, T. Cantat-Gaudin, P. Donati, R. Baglioni, E. Maiorca, A. Bragaglia, R. Sordo, and A. Vallenari. FAMA: An automatic code for stellar parameter and abundance determination. *A&A*, 558:A38, October 2013. doi: 10.1051/0004-6361/201321844.
- Prasanta Chandra Mahalanobis. On the generalized distance in statistics. *Proceedings of the National Institute of Sciences (Calcutta)*, 2:49–55, 1936.
- C. B. Markwardt. Non-linear Least-squares Fitting in IDL with MPFIT. In D. A. Bohlender, D. Durand, and P. Dowler, editors, *Astronomical Data Analysis Software and Systems XVIII*, volume 411 of *Astronomical Society of the Pacific Conference Series*, page 251, September 2009.
- L. I. Mashonkina, V. V. Shimanskiĭ, and N. A. Sakhbullin. Non-LTE Effects in Na I Spectral Lines in Stellar Atmospheres. *Astronomy Reports*, 44:790–803, December 2000. doi: 10.1134/1.1327637.
- M. Mayor, F. Pepe, D. Queloz, F. Bouchy, G. Rupprecht, G. Lo Curto, G. Avila, W. Benz, J.-L. Bertaux, X. Bonfils, T. Dall, H. Dekker, B. Delabre, W. Eckert, M. Fleury, A. Gilliotte, D. Gojak, J. C. Guzman, D. Kohler, J.-L. Lizon, A. Longinotti, C. Lovis, D. Megevand, L. Pasquini, J. Reyes, J.-P. Sivan, D. Sosnowska, R. Soto, S. Udry, A. van Kesteren, L. Weber, and U. Weilenmann. Setting New Standards with HARPS. *The Messenger*, 114:20–24, 2003.
- C. F. McKee and E. C. Ostriker. Theory of Star Formation. *ARA&A*, 45:565–687, September 2007. doi: 10.1146/annurev.astro.45.051806.110602.
- J. Meléndez, M. Bergemann, J. G. Cohen, M. Endl, A. I. Karakas, I. Ramírez, W. D. Cochran, D. Yong, P. J. MacQueen, C. Kobayashi, and M. Asplund. The remarkable solar twin HIP 56948: a prime target in the quest for other Earths. *A&A*, 543:A29, July 2012. doi: 10.1051/0004-6361/201117222.
- J.-C. Mermilliod, M. Mayor, and S. Udry. Catalogues of radial and rotational velocities of 1253 F-K dwarfs in 13 nearby open clusters. *A&A*, 498:949–960, May 2009. doi: 10.1051/0004-6361/200810244.
- S. Mészáros and C. Allende Prieto. On the interpolation of model atmospheres and high-resolution synthetic stellar spectra. *MNRAS*, 430:3285–3291, April 2013. doi: 10.1093/mnras/stt130.
- S. Mészáros, C. Allende Prieto, B. Edvardsson, F. Castelli, A. E. García Pérez, B. Gustafsson, S. R. Majewski, B. Plez, R. Schiavon, M. Shetrone, and A. de Vicente. New ATLAS9 and MARCS Model Atmosphere Grids for the Apache Point Observatory Galactic Evolution Experiment (APOGEE). *AJ*, 144:120, October 2012. doi: 10.1088/0004-6256/144/4/120.
- M. R. Meyer, F. C. Adams, L. A. Hillenbrand, J. M. Carpenter, and R. B. Larson. The Stellar Initial Mass Function: Constraints from Young Clusters, and Theoretical Perspectives. *Protostars and Planets IV*, page 121, May 2000.

- D. Minniti. Field Stars and Clusters of the Galactic Bulge: Implications for Galaxy Formation. *ApJ*, 459:175, March 1996. doi: 10.1086/176879.
- D. Minniti and M. Zoccali. The Galactic bulge: a review. In M. Bureau, E. Athanassoula, and B. Barbuy, editors, *IAU Symposium*, volume 245 of *IAU Symposium*, pages 323–332, July 2008. doi: 10.1017/S1743921308018048.
- A. W. Mutschang, G. De Silva, S. Sharma, and D. B. Zucker. Quantifying chemical tagging: towards robust group finding in the Galaxy. *MNRAS*, 428:2321–2332, January 2013. doi: 10.1093/mnras/sts194.
- A. W. Mutschang, G. De Silva, D. B. Zucker, B. Anguiano, T. Bensby, and S. Feltzing. Quantitative chemical tagging, stellar ages and the chemo-dynamical evolution of the Galactic disc. *MNRAS*, 438:2753–2764, March 2014. doi: 10.1093/mnras/stt2320.
- P. J. Mohr, B. N. Taylor, and D. B. Newell. CODATA recommended values of the fundamental physical constants: 2010. *Reviews of Modern Physics*, 84:1527–1605, October 2012. doi: 10.1103/RevModPhys.84.1527.
- P. Molaro and S. Monai. Solar atlas revised. *A&A*, 544:A125, August 2012. doi: 10.1051/0004-6361/201118675.
- M. Montalto, S. Villanova, J. Koppenhoefer, G. Piotto, S. Desidera, F. de Marchi, E. Poretti, L. R. Bedin, and I. Saviane. VLT multi-epoch radial velocity survey toward <ASTROBJ>NGC 6253</ASTROBJ>. Analysis of three transiting planetary candidates. *A&A*, 535:A39, November 2011. doi: 10.1051/0004-6361/200913582.
- J. Moultaqa, S. Ilovaisky, P. Prugniel, and C. Soubiran. ELODIE-SOPHIE: Spectroscopic archive. In F. Combes, D. Barret, T. Contini, F. Meynadier, and L. Pagani, editors, *SF2A-2004: Semaine de l’Astrophysique Francaise*, page 547, December 2004.
- A. Mucciarelli, E. Pancino, L. Lovisi, F. R. Ferraro, and E. Lapenna. GALA: An Automatic Tool for the Abundance Analysis of Stellar Spectra. *ApJ*, 766:78, April 2013. doi: 10.1088/0004-637X/766/2/78.
- U. Munari and R. Sordo. Available libraries of observed spectra. *Memorie della Societa Astronomica Italiana Supplementi*, 8:170, 2005.
- J. F. Navarro, C. S. Frenk, and S. D. M. White. The Structure of Cold Dark Matter Halos. *ApJ*, 462:563, May 1996. doi: 10.1086/177173.
- M. Netopil and E. Paunzen. Towards a photometric metallicity scale for open clusters. *A&A*, 557:A10, September 2013. doi: 10.1051/0004-6361/201321829.
- T. Nordlander, A. J. Korn, O. Richard, and K. Lind. Atomic Diffusion and Mixing in Old Stars. III. Analysis of NGC 6397 Stars under New Constraints. *ApJ*, 753:48, July 2012. doi: 10.1088/0004-637X/753/1/48.
- A. Önehag, B. Gustafsson, and A. Korn. Abundances and possible diffusion of elements in M 67 stars. *A&A*, 562:A102, February 2014. doi: 10.1051/0004-6361/201322663.
- G. Pace, J. Danziger, G. Carraro, J. Melendez, P. François, F. Matteucci, and N. C. Santos. Abundances and physical parameters for stars in the open clusters NGC 5822 and IC 4756. *A&A*, 515:A28, June 2010. doi: 10.1051/0004-6361/200913029.

- E. Paunzen and M. Netopil. On the current status of open-cluster parameters. *MNRAS*, 371:1641–1647, October 2006. doi: 10.1111/j.1365-2966.2006.10783.x.
- E. Paunzen, U. Heiter, M. Netopil, and C. Soubiran. On the metallicity of open clusters. I. Photometry. *A&A*, 517:A32, July 2010. doi: 10.1051/0004-6361/201014131.
- F. Pepe, M. Mayor, F. Galland, D. Naef, D. Queloz, N. C. Santos, S. Udry, and M. Burnet. The CORALIE survey for southern extra-solar planets VII. Two short-period Saturnian companions to <ASTROBJ>HD 108147</ASTROBJ> and <ASTROBJ>HD 168746</ASTROBJ>. *A&A*, 388: 632–638, June 2002. doi: 10.1051/0004-6361:20020433.
- S. M. Percival, M. Salaris, S. Cassisi, and A. Pietrinferni. A Large Stellar Evolution Database for Population Synthesis Studies. IV. Integrated Properties and Spectra. *ApJ*, 690:427–439, January 2009. doi: 10.1088/0004-637X/690/1/427.
- T. M. D. Pereira, M. Asplund, R. Collet, I. Thaler, R. Trampedach, and J. Leenaarts. How realistic are solar model atmospheres? *A&A*, 554:A118, June 2013. doi: 10.1051/0004-6361/201321227.
- M. A. C. Perryman, K. S. de Boer, G. Gilmore, E. Høg, M. G. Lattanzi, L. Lindegren, X. Luri, F. Mignard, O. Pace, and P. T. de Zeeuw. GAIA: Composition, formation and evolution of the Galaxy. *A&A*, 369:339–363, April 2001. doi: 10.1051/0004-6361:20010085.
- P. Petit, T. Louge, S. Théado, F. Paletou, N. Manset, J. Morin, S. C. Marsden, and S. V. Jeffers. PolarBase: A Database of High-Resolution Spectropolarimetric Stellar Observations. *PASP*, 126: 469–475, May 2014. doi: 10.1086/676976.
- A. E. Piskunov, N. V. Kharchenko, S. Röser, E. Schilbach, and R.-D. Scholz. Revisiting the population of Galactic open clusters. *A&A*, 445:545–565, January 2006. doi: 10.1051/0004-6361:20053764.
- B. Plez. Turbospectrum: Code for spectral synthesis, May 2012. Astrophysics Source Code Library.
- H. Pöhl and E. Paunzen. A statistical method to determine open cluster metallicities. *A&A*, 514:A81, May 2010. doi: 10.1051/0004-6361/200810855.
- H. Posbic, D. Katz, E. Caffau, P. Bonifacio, A. Gómez, L. Sbordone, and F. Arenou. SPADES: a stellar parameters determination software. *A&A*, 544:A154, August 2012. doi: 10.1051/0004-6361/201219417.
- P. Prugniel and C. Soubiran. A database of high and medium-resolution stellar spectra. *A&A*, 369: 1048–1057, April 2001. doi: 10.1051/0004-6361:20010163.
- Y. Ralchenko. NIST atomic spectra database. *Memorie della Societa Astronomica Italiana Supplementi*, 8:96, 2005.
- I. Ramírez and C. Allende Prieto. Fundamental Parameters and Chemical Composition of Arcturus. *ApJ*, 743:135, December 2011. doi: 10.1088/0004-637X/743/2/135.
- I. Ramírez, J. Meléndez, and M. Asplund. Accurate abundance patterns of solar twins and analogs. Does the anomalous solar chemical composition come from planet formation? *A&A*, 508:L17–L20, December 2009. doi: 10.1051/0004-6361/200913038.
- S. Randich, P. Sestito, F. Primas, R. Pallavicini, and L. Pasquini. Element abundances of unevolved stars in the open cluster M 67. *A&A*, 450:557–567, May 2006. doi: 10.1051/0004-6361:20054291.
- S. Randich, G. Gilmore, and Gaia-ESO Consortium. The Gaia-ESO Large Public Spectroscopic Survey. *The Messenger*, 154:47–49, December 2013.

- A. Recio-Blanco, A. Bijaoui, and P. de Laverny. Automated derivation of stellar atmospheric parameters and chemical abundances: the MATISSE algorithm. *MNRAS*, 370:141–150, July 2006. doi: 10.1111/j.1365-2966.2006.10455.x.
- Peter J Rousseeuw. Least median of squares regression. *Journal of the American statistical association*, 79(388):871–880, 1984.
- Peter J Rousseeuw. Silhouettes: a graphical aid to the interpretation and validation of cluster analysis. *Journal of computational and applied mathematics*, 20:53–65, 1987.
- Peter J Rousseeuw and Katrien Van Driessen. A fast algorithm for the minimum covariance determinant estimator. *Technometrics*, 41(3):212–223, 1999.
- P. Sánchez-Blázquez, R. F. Peletier, J. Jiménez-Vicente, N. Cardiel, A. J. Cenarro, J. Falcón-Barroso, J. Gorgas, S. Selam, and A. Vazdekis. Medium-resolution Isaac Newton Telescope library of empirical spectra. *MNRAS*, 371:703–718, September 2006. doi: 10.1111/j.1365-2966.2006.10699.x.
- L. Searle and R. Zinn. Compositions of halo clusters and the formation of the galactic halo. *ApJ*, 225:357–379, October 1978. doi: 10.1086/156499.
- F. H. Shu, F. C. Adams, and S. Lizano. Star formation in molecular clouds - Observation and theory. *ARA&A*, 25:23–81, 1987. doi: 10.1146/annurev.aa.25.090187.000323.
- C. Sneden, J. Bean, I. Ivans, S. Lucatello, and J. Sobeck. MOOG: LTE line analysis and spectrum synthesis, February 2012. Astrophysics Source Code Library.
- S. G. Sousa, N. C. Santos, G. Israelian, M. Mayor, and M. J. P. F. G. Monteiro. A new code for automatic determination of equivalent widths: Automatic Routine for line Equivalent widths in stellar Spectra (ARES). *A&A*, 469:783–791, July 2007. doi: 10.1051/0004-6361:20077288.
- S. G. Sousa, N. C. Santos, V. Adibekyan, E. Delgado-Mena, H. M. Tabernero, J. I. González Hernández, D. Montes, R. Smiljanic, A. J. Korn, M. Bergemann, C. Soubiran, and S. Mikolaitis. A new procedure for defining a homogenous line-list for solar-type stars. *A&A*, 561:A21, January 2014. doi: 10.1051/0004-6361/201322290.
- M. Steinmetz, T. Zwitter, A. Siebert, F. G. Watson, K. C. Freeman, U. Munari, R. Campbell, M. Williams, G. M. Seabroke, R. F. G. Wyse, Q. A. Parker, O. Bienaymé, S. Roeser, B. K. Gibson, G. Gilmore, E. K. Grebel, A. Helmi, J. F. Navarro, D. Burton, C. J. P. Cass, J. A. Dawe, K. Fiegert, M. Hartley, K. S. Russell, W. Saunders, H. Enke, J. Bailin, J. Binney, J. Bland-Hawthorn, C. Boeche, W. Dehnen, D. J. Eisenstein, N. W. Evans, M. Fiorucci, J. P. Fulbright, O. Gerhard, U. Jauregi, A. Kelz, L. Mijović, I. Minchev, G. Parmentier, J. Peñarrubia, A. C. Quillen, M. A. Read, G. Ruchti, R.-D. Scholz, A. Siviero, M. C. Smith, R. Sordo, L. Veltz, S. Vidrih, R. von Berlepsch, B. J. Boyle, and E. Schilbach. The Radial Velocity Experiment (RAVE): First Data Release. *AJ*, 132:1645–1668, October 2006. doi: 10.1086/506564.
- P. B. Stetson and E. Pancino. DAOSPEC: An Automatic Code for Measuring Equivalent Widths in High-Resolution Stellar Spectra. *PASP*, 120:1332–1354, December 2008. doi: 10.1086/596126.
- P. Stumpff. Two Self-Consistent FORTRAN Subroutines for the Computation of the Earth’s Motion. *aaps*, 41:1, June 1980.
- H. M. Tabernero, D. Montes, and J. I. González Hernández. Chemically tagging the Hyades Supercluster. A homogeneous sample of F6-K4 kinematically selected northern stars. *A&A*, 547:A13, November 2012. doi: 10.1051/0004-6361/201117506.

- F. Thévenin, P. Kervella, B. Pichon, P. Morel, E. di Folco, and Y. Lebreton. VLT/VINCI diameter constraints on the evolutionary status of δ Eri, ξ Hya, η Boo. *A&A*, 436:253–262, June 2005. doi: 10.1051/0004-6361:20042075.
- D. A. Tilley and R. E. Pudritz. The formation of star clusters - I. Three-dimensional simulations of hydrodynamic turbulence. *MNRAS*, 353:769–788, September 2004. doi: 10.1111/j.1365-2966.2004.08077.x.
- Y.-S. Ting, K. C. Freeman, C. Kobayashi, G. M. De Silva, and J. Bland-Hawthorn. Principal component analysis on chemical abundances spaces. *MNRAS*, 421:1231–1255, April 2012. doi: 10.1111/j.1365-2966.2011.20387.x.
- G. Torres, D. A. Fischer, A. Sozzetti, L. A. Buchhave, J. N. Winn, M. J. Holman, and J. A. Carter. Improved Spectroscopic Parameters for Transiting Planet Hosts. *ApJ*, 757:161, October 2012. doi: 10.1088/0004-637X/757/2/161.
- F. Valdes, R. Gupta, J. A. Rose, H. P. Singh, and D. J. Bell. The Indo-US Library of Coudé Feed Stellar Spectra. *ApJS*, 152:251–259, June 2004. doi: 10.1086/386343.
- J. A. Valenti and N. Piskunov. Spectroscopy made easy: A new tool for fitting observations with synthetic spectra. *A&AS*, 118:595–603, September 1996.
- S. van den Bergh and R. D. McClure. Galactic distribution of the oldest open clusters. *A&A*, 88:360–362, August 1980.
- R. P. van der Marel, G. Besla, T. J. Cox, S. T. Sohn, and J. Anderson. The M31 Velocity Vector. III. Future Milky Way M31-M33 Orbital Evolution, Merging, and Fate of the Sun. *ApJ*, 753:9, July 2012. doi: 10.1088/0004-637X/753/1/9.
- A. Vazdekis, E. Ricciardelli, A. J. Cenarro, J. G. Rivero-González, L. A. Díaz-García, and J. Falcón-Barroso. MIUSCAT: extended MILES spectral coverage - I. Stellar population synthesis models. *MNRAS*, 424:157–171, July 2012. doi: 10.1111/j.1365-2966.2012.21179.x.
- Y. Wu, A.-L. Luo, H.-N. Li, J.-R. Shi, P. Prugniel, Y.-C. Liang, Y.-H. Zhao, J.-N. Zhang, Z.-R. Bai, P. Wei, W.-X. Dong, H.-T. Zhang, and J.-J. Chen. Automatic determination of stellar atmospheric parameters and construction of stellar spectral templates of the Guoshoujing Telescope (LAMOST). *Research in Astronomy and Astrophysics*, 11:924–946, August 2011. doi: 10.1088/1674-4527/11/8/006.
- R. F. G. Wyse. Kinematical & Chemical Characteristics of the Thin and Thick Disks. In J. Andersen, Nordströara, B. m, and J. Bland-Hawthorn, editors, *IAU Symposium*, volume 254 of *IAU Symposium*, pages 179–190, March 2009. doi: 10.1017/S1743921308027579.
- S. K. Yi, Y.-C. Kim, and P. Demarque. The Y^2 Stellar Evolutionary Tracks. *ApJS*, 144:259–261, February 2003. doi: 10.1086/345101.
- D. G. York, J. Adelman, J. E. Anderson, Jr., S. F. Anderson, J. Annis, N. A. Bahcall, J. A. Bakken, R. Barkhouser, S. Bastian, E. Berman, W. N. Boroski, S. Bracker, C. Briegel, J. W. Briggs, J. Brinkmann, R. Brunner, S. Burles, L. Carey, M. A. Carr, F. J. Castander, B. Chen, P. L. Colestock, A. J. Connolly, J. H. Crocker, I. Csabai, P. C. Czarapata, J. E. Davis, M. Doi, T. Dombeck, D. Eisenstein, N. Ellman, B. R. Elms, M. L. Evans, X. Fan, G. R. Federwitz, L. Fiscelli, S. Friedman, J. A. Frieman, M. Fukugita, B. Gillespie, J. E. Gunn, V. K. Gurbani, E. de Haas, M. Haldeman, F. H. Harris, J. Hayes, T. M. Heckman, G. S. Hennessy, R. B. Hindsley, S. Holm, D. J. Holmgren, C.-h. Huang, C. Hull, D. Husby, S.-I. Ichikawa, T. Ichikawa, Ž. Ivezić, S. Kent, R. S. J. Kim, E. Kinney, M. Klaene, A. N. Kleinman, S. Kleinman, G. R. Knapp, J. Korienek, R. G. Kron, P. Z.

- Kunszt, D. Q. Lamb, B. Lee, R. F. Leger, S. Limmongkol, C. Lindenmeyer, D. C. Long, C. Loomis, J. Loveday, R. Lucinio, R. H. Lupton, B. MacKinnon, E. J. Mannery, P. M. Mantsch, B. Margon, P. McGehee, T. A. McKay, A. Meiksin, A. Merelli, D. G. Monet, J. A. Munn, V. K. Narayanan, T. Nash, E. Neilsen, R. Neswold, H. J. Newberg, R. C. Nichol, T. Nicinski, M. Nonino, N. Okada, S. Okamura, J. P. Ostriker, R. Owen, A. G. Pauls, J. Peoples, R. L. Peterson, D. Petravick, J. R. Pier, A. Pope, R. Pordes, A. Prosapio, R. Rechenmacher, T. R. Quinn, G. T. Richards, M. W. Richmond, C. H. Rivetta, C. M. Rockosi, K. Ruthmansdorfer, D. Sandford, D. J. Schlegel, D. P. Schneider, M. Sekiguchi, G. Sergey, K. Shimasaku, W. A. Siegmund, S. Smee, J. A. Smith, S. Snedden, R. Stone, C. Stoughton, M. A. Strauss, C. Stubbs, M. SubbaRao, A. S. Szalay, I. Szapudi, G. P. Szokoly, A. R. Thakar, C. Tremonti, D. L. Tucker, A. Uomoto, D. Vanden Berk, M. S. Vogeley, P. Waddell, S.-i. Wang, M. Watanabe, D. H. Weinberg, B. Yanny, N. Yasuda, and SDSS Collaboration. The Sloan Digital Sky Survey: Technical Summary. *AJ*, 120:1579–1587, September 2000. doi: 10.1086/301513.
- F. Zhang, L. Li, and Z. Han. Evolutionary population synthesis for binary stellar population at high spectral resolution: integrated spectral energy distributions and absorption-feature indices. *MNRAS*, 364:503–514, December 2005. doi: 10.1111/j.1365-2966.2005.09563.x.
- G. Zhao, Y.-Q. Chen, J.-R. Shi, Y.-C. Liang, J.-L. Hou, L. Chen, H.-W. Zhang, and A.-G. Li. Stellar Abundance and Galactic Chemical Evolution through LAMOST Spectroscopic Survey. *CJAA*, 6: 265–280, June 2006. doi: 10.1088/1009-9271/6/3/01.
- M. Zoccali, D. Minniti, B. Barbuy, V. Hill, A. Lecureur, A. Renzini, Y. Mamony, A. Gómez, and S. Ortolani. Chemical abundances in the Galactic Bulge: evidence for a fast enrichment. In *Revista Mexicana de Astronomía y Astrofísica Conference Series*, volume 26 of *Revista Mexicana de Astronomía y Astrofísica Conference Series*, pages 88–89, June 2006.
- S. Zucker. Cross-correlation and maximum-likelihood analysis: a new approach to combining cross-correlation functions. *MNRAS*, 342:1291–1298, July 2003. doi: 10.1046/j.1365-8711.2003.06633.x.

Appendix **A**

iSpec User's manual

A.1 Introduction

iSpec is an open source framework for spectral analysis [Blanco-Cuaresma et al., 2013]. It is suitable for the creation of spectral libraries such as the Gaia FGK Benchmark Stars library [?] and the determination of astrophysical parameters such as effective temperature, surface gravity, metallicity and individual abundances. iSpec works in conjunction with “SPECTRUM: a Stellar Spectral Synthesis Program” [Gray and Corbally, 1994] for the generation of synthetic spectra and the derivation of abundances from equivalent widths.

The framework can be used from python scripts in an automatic way by using its API, but it also includes a visual interface that is SAMP ready and it can interoperate with other astronomical applications such as TOPCAT¹, VOSpec² and splat³ facilitating an indirect way to access the Virtual Observatory⁴.

iSpec can be downloaded from <http://www.blancocuaresma.com/s/>. It is distributed under the terms of the GNU Affero General Public License⁵ (open source license), except the SPECTRUM code which is also included in the framework thanks to R. O. Gray. The latest SPECTRUM version can also be obtained from <http://www.appstate.edu/~grayro/spectrum/spectrum.html>.

This document presents the installation steps for the iSpec framework, together with a general overview of the functionalities that can be accessed through the visual interface and from python scripts.

A.2 Installation

A.2.1 Virtual Machine

The fastest way to experiment with iSpec on any platform (Mac, Windows, Linux and Solaris) is to use a ready-to-use the virtual machine with iSpec and all its dependencies already included (i.e. python packages and compilers). To run it, the only necessary step is to install the software for running virtual machines called VirtualBox (free software):

-
1. <http://www.star.bris.ac.uk/~mbt/topcat/>
 2. <http://www.sciops.esa.int/index.php?project=ESAVO&page=vospec>
 3. <http://star-www.dur.ac.uk/~pdraper/splat/splat.html>
 4. <http://www.ivoa.net/>
 5. <https://www.gnu.org/licenses/agpl-3.0.html>



Figure A.1 – Oracle VirtualBox website, download section (2014/03/31).

1. Go to the "Download" section of <http://www.virtualbox.org>, download the VirtualBox package for your platform and install it. A reboot might be necessary.
2. Download the "VirtualBox Extension Pack" too (platform independent), executed it and it will be automatically integrated into your installation of VirtualBox.

Once installed, the iSpec virtual machine can be decompressed and recognized by VirtualBox by opening "iSpec_Xubuntu.vbox":

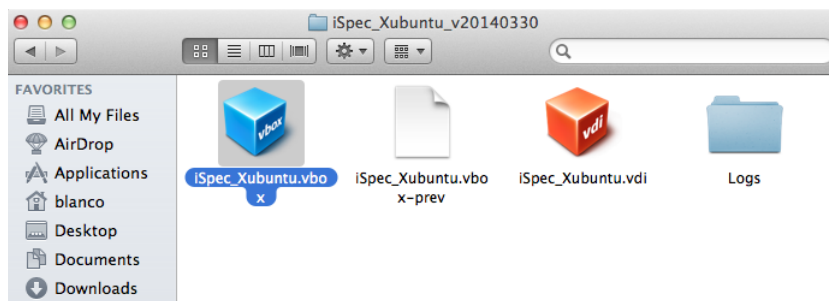


Figure A.2 – Open "iSpec_Xubuntu.vbox" with VirtualBox to add it to the list of virtual machines.

The new virtual machine will be listed in VirtualBox, now it can be run by selecting it and clicking "Start":

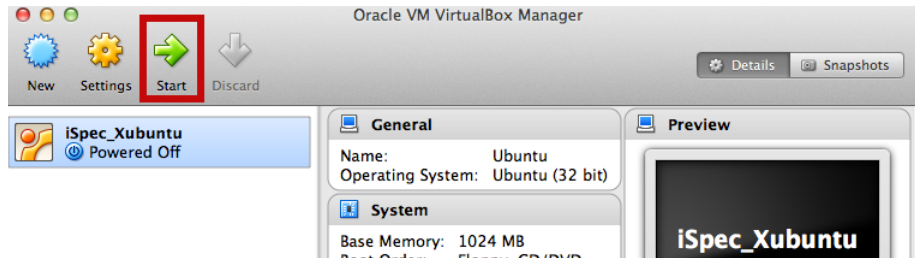


Figure A.3 – Start the virtual machine.

By default, the virtual machine will show the Xubuntu Desktop with two icons that allow to execute iSpec (normal execution and test). Double clicking the test will launch iSpec with the example spectra:

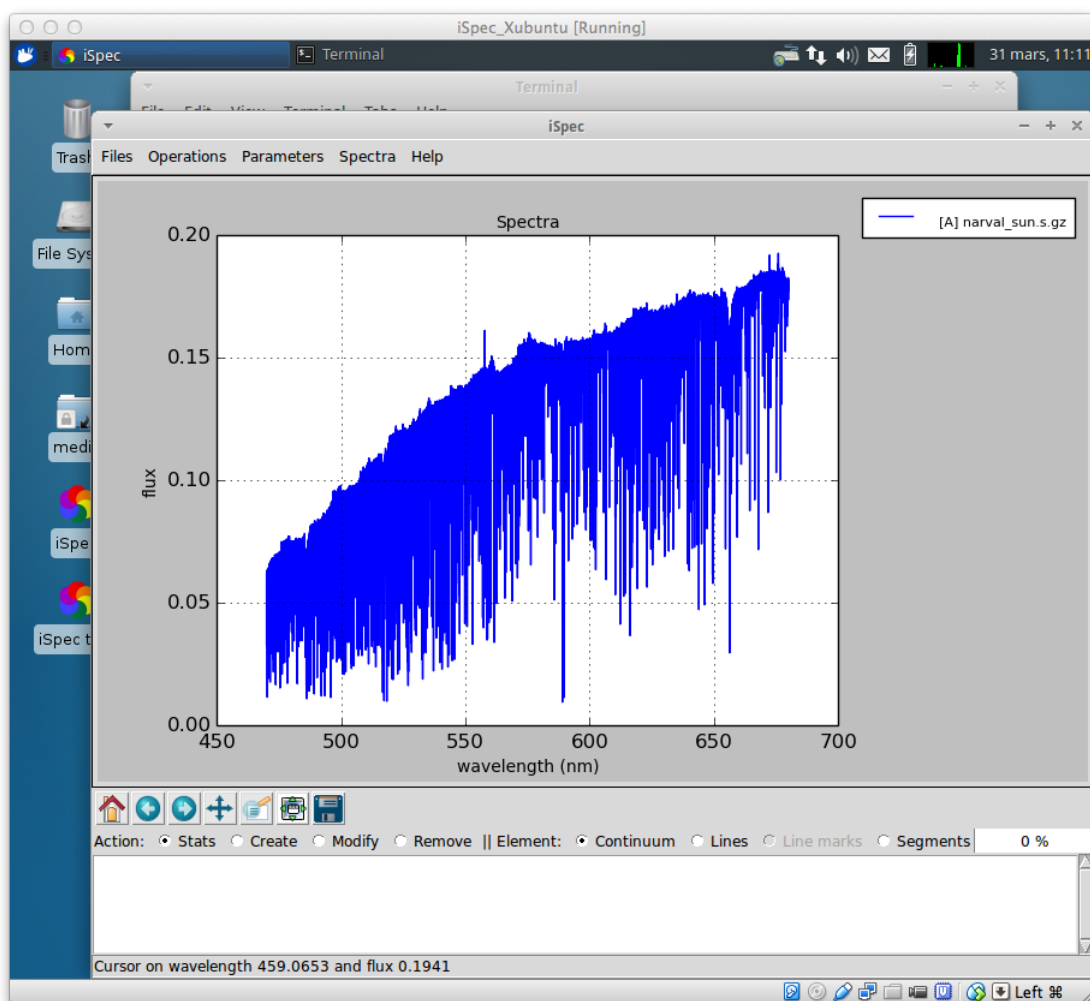


Figure A.4 – Virtual machine running iSpec with a solar spectrum.

iSpec is installed on “/home/virtual/shared/iSpec” in the virtual machine (check section A.2.2 for more details about the contents) and the application can also be executed from the terminal by invoking “iSpec” in any directory.

It is also possible to share a folder from your real computer to the virtual one, thus files can be easily accessed from it. To activate that option, go to “Settings - Shared folders” and add a shared folder by clicking on the plus sign. It is important to mark the “Auto-mount” option to have an easier

access from the virtual machine:

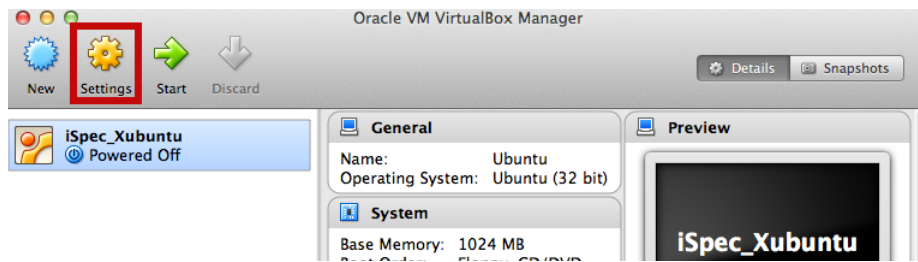


Figure A.5 – Access to the virtual machine settings.

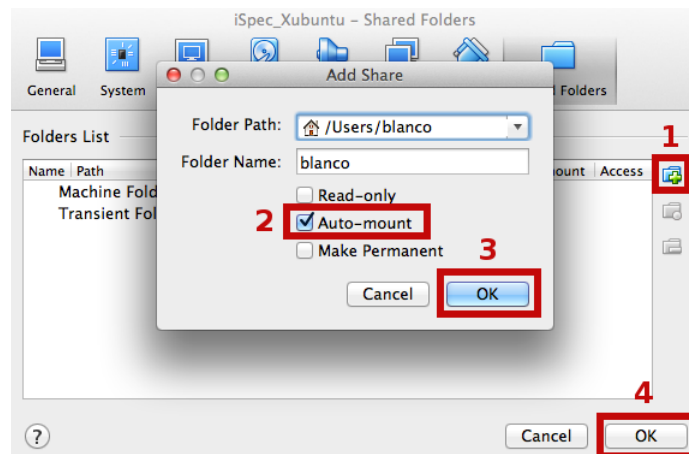


Figure A.6 – Add a shared folder between the real and virtual machine.

The shared folder can be accessed from the virtual machine by double clicking the folder “media” on the Desktop:

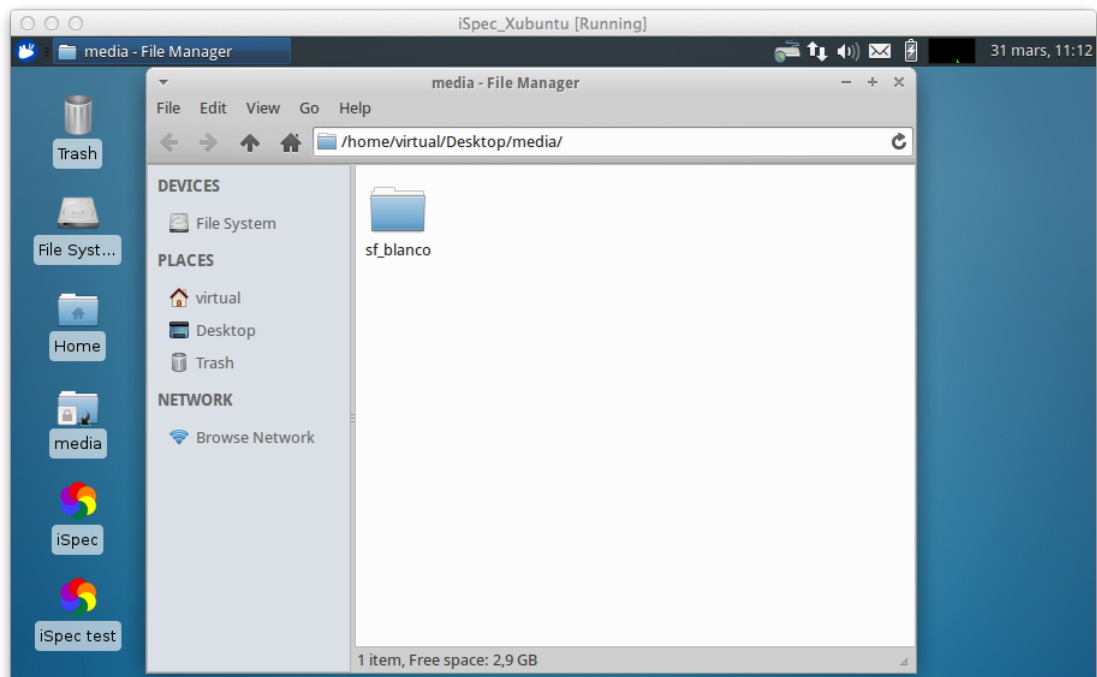


Figure A.7 – Access to a shared folder from the virtual machine.

A.2.2 GNU/Linux systems

Python distribution

On debian based GNU/Linux distributions such as Ubuntu or Linux Mint, the following packages should be installed by using the visual package manager (i.e. Ubuntu Software Center⁶ or Synaptic⁷) or from a terminal by executing “apt-get install *package_name*”⁸:

- python (2.7.5 or higher but not 3.x branch)
- python-numpy (1.8 or higher)
- python-scipy (0.13.3 or higher)
- python-astropy (0.3 or higher)
- python-matplotlib (1.3.1 or higher)
- python-statsmodel (0.5 or higher)
- python-pip (1.4.1 or higher)
- cython (0.20.1 or higher)
- gfortran (0.20.1 or higher)

Additionally, several extra packages should be installed by using the python package installer PIP from a terminal:

Listing A.1 – Extra packages installation

```
1 | pip install pymodelfit
2 | pip install sampy
```

iSpec Framework

Once the system is ready for execution of python applications, it is possible to proceed with iSpec installation by decompressing the editor’s file “iSpec_v20140331.tar.gz” (the version number may vary with time):

Listing A.2 – iSpec installation

```
1 | tar -zxvf iSpec_v20140331.tar.gz
2 | cd iSpec_v20140331
```

[OPTIONAL] In case we want to have the functionality of generating synthetic spectrum and determining astrophysical parameters, an additional step should be executed in order to compile the needed libraries:

Listing A.3 – Compilation of “SPECTRUM: a Stellar Spectral Synthesis Program” [Gray and Corbally, 1994]

```
1 | bash compile.sh
```

6. <http://www.ubuntu.com/ubuntu/features/ubuntu-software-centre>

7. <http://wiki.debian.org/Synaptic>

8. Administrator rights will be needed.

Finally, it is possible to test iSpec by double clicking “test.command” (or executing “./test.command” in a terminal) and selecting a star by entering its number:

```

blanco@macpblanco.obs.u-bordeaux1.fr: ~ -- bash -- 80x24
Last login: Fri Sep 21 14:12:09 on ttys002
blanco@macpblanco:~$ /Users/blanco/Downloads/sve/test.command ; exit;
-----
Resolving power per instrument
-----
Narval    ~70,000 - 90,000
ESPaDOnS ~68,000 - 81,000
HARPS     ~115,000
-----
Wavelength range = 480 - 680 nm
-----
1) Procyon (Metal Rich Dwarf) - Teff 6545 logg 3.99 [M/H] -0.02 - HARPS
2) Sun (Metal Rich Dwarf) - Teff 5777 logg 4.44 [M/H] 0.00 - Narval
3) Mu Cas A (Metal Poor Dwarf) - Teff 5308 logg 4.41 [M/H] -0.89 - Narval
4) Arcturus (Metal Poor Giant) - Teff 4247 logg 1.59 [M/H] -0.54 - Narval
5) Mu Leo (Metal Rich Giant) - Teff 4433 logg 2.50 [M/H] 0.29 - ESPaDOnS
.....
6) All of them simultaneously (1 to 5)
7) Sun with example region masks
8) Exit
-----
Enter the spectra number you want to use :
7

```

Figure A.8 – Test execution script which allows to view 5 different stars.

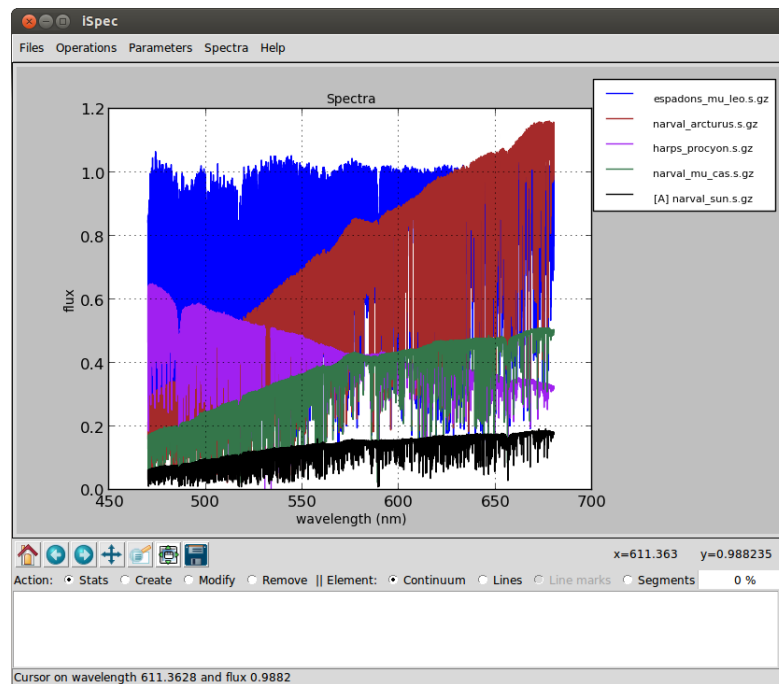


Figure A.9 – iSpec showing several spectra.

The iSpec compressed file contains the program and some additional data in the “input/” directory:

- Observed spectra for 5 very well-known stars: Procyon, Sun, μ Cas A, Arcturus, μ Leo (input/spectra/example/ directory)
 - Filenames:
 - * *NARVAL_*.s.gz*: NARVAL [Aurière, 2003] spectra (resolving power \sim 70,000 - 90,000)

- * *ESPaDOnS_*.s.gz*: ESPaDOnS [Donati, 2003] spectra (resolving power $\sim 68,000 - 81,000$)
- * *HARPS_*.s.gz*: HARPS [Mayor et al., 2003] spectra (resolving power $\sim 115,000$)
- Characteristics:
 - * Not normalized
 - * Radial velocity not corrected
 - * Barycentric correction applied
 - * Resolution depends on the instrument
 - * Wavelength range from ~ 480 to ~ 680 nm
- ELODIE [Moultaka et al., 2004] spectra for binarity tests (input/spectra/binaries/ directory, see section A.3.12):
 - Filenames:
 - * *elodie_hd005516A_spectroscopic_binary.s.gz*
 - * *elodie_hd085503_single_star.s.gz*
 - Characteristics:
 - * Not normalized
 - * Resolution $\sim 42,000$
 - * Wavelength range from ~ 400 to ~ 680 nm
- Regions (input/regions/ directory):
 - Example of continuum regions
 - Line masks for Fe I/II
 - Line masks for the wings of H-Alpha, H-Beta and Magnesium triplet.
 - Segments for the previous lines

Star	Type	Teff (K)	Log g (dex)	[M/H]	Radial Vel. (km/s)
Procyon	Metal Rich Dwarf	6545	3.99	-0.02	-3.2
Sun	Metal Rich Dwarf	5777	4.44	0.00	0.00
μ Cas A	Metal Poor Dwarf	5308	4.41	-0.89	-96.06
Arcturus	Metal Poor Giant	4247	1.59	-0.54	-5.18
μ Leo	Metal Rich Giant	4433	2.50	0.29	14.25

Table A.1 – Astrophysical parameters for the 5 very well-known stars included

A.2.3 MacOSX systems

Python distribution

One of the easiest ways to install a Python distribution on MacOSX with most of the needed libraries for the iSpec (i.e. matplotlib⁹) is by using MacPorts¹⁰

9. <http://matplotlib.sourceforge.net/>

10. <http://www.macports.org/>

However, it is important to know that the installation can take time (1 hour or more depending on the computer) because, depending on your operating system version, it might compile all the python libraries from source code. On the other hand, MacPorts is completely open source without limiting licenses and it can be used to install other free software apart from python.

1. It should be taken into account that MacPorts requires X11 application for Mac OS X¹¹, Xcode and the Command Line Tools¹².
2. Download the MacPorts binary version¹³ that correspond to the Mac OS X version, install it by double clicking and following the instructions (all options should be left by default).



Figure A.10 – MacPorts installation

3. [OPTIONAL] After the installation, if the user's default shell is bash, edit the file "\$HOME/.bash_profile" and verify that the installer has added the following lines (PATH variable includes the MacPorts directories):

Listing A.4 – .bash_profile

```
1 | export PATH=/opt/local/bin:/opt/local/sbin:$PATH
```

4. Close all the terminals and open a new one. If the user's default shell is bash, you can instead execute "source \$HOME/.bash_profile" in order to load the new configuration.
5. Update the local ports tree with the ports repository:

Listing A.5 – Update MacPorts

```
1 | sudo port selfupdate
```

6. Install python framework and several required extra libraries (it can take several hours because it compiles everything from the sources):

Listing A.6 – Python installation

```
1 | sudo -s # Execute everything with administrative privileges (root)
2 | port selfupdate
3 | port install python27
4 | port select --set python python27
5 | port install py27-readline
```

11. <http://guide.macports.org/chunked/installing.html#installing.x11>
 12. <http://guide.macports.org/chunked/installing.xcode.html>
 13. <http://www.macports.org/install.php>

```

6 | port install py27-tkinter
7 | port install py27-numpy
8 | port install py27-scipy
9 | port install py27-matplotlib
10 | port install py27-astropy
11 | port install py27-cython
12 | port select --set cython cython27
13 | port install py27-statsmodels
14 | port install py27-pip
15 | ln -sf /opt/local/bin/pip-2.7 /opt/local/bin/pip
16 | pip install pymodelfit
17 | pip install sampy
18 | exit # Stop having administrative privileges (root)

```

The user password may be required to gain administrative rights for some commands.

iSpec framework

Check section [A.2.2](#) for specific instructions about the installation of iSpec.

A.3 Interactive usage

A.3.1 Input and output files

iSpec can read/write spectra and region definition for:

- Continuum regions: spectrum regions where there is only continuum (no absorption/emission lines)
- Line masks: Individual absorption lines where the mask covers from base point to base point and specifies where is the peak.
- Segments: Group of continuum regions and line masks.

The user is responsible for not creating incoherent overlapping regions (the program does not perform this kind of validations). It is highly recommended to work with **nanometer units** (instead of armstrongs) since some operations in iSpec expect this. The corresponding files should respect the format exposed in this section.

Spectra

Spectra should be in plain text files with **tab** character as column delimiter. Three columns should exist: wavelength, flux and error (although in case the error is unknown, it can be set all to zero). The first line should contain the header names 'waveobs', 'flux' and 'err' such as in the following example:

Listing A.7 – Fragment of a spectrum file

```

1 | waveobs      flux      err
2 | 370.00000000 1.26095742505 1.53596736433
3 | 370.001897436 1.22468868618 1.55692475754
4 | 370.003794872 1.18323884263 1.47304952231
5 | 370.005692308 1.16766911881 1.49393329036

```

For all the iSpec operation, the error propagation is taken into account. To save space, the file can be compressed in gzip format.

iSpec can read FITS with the format following the standards of the IAU¹⁴ [Greisen and Calabretta, 2002, Greisen et al., 2006] where the spectral coordinates (wavelengths) are specified in the header via CRVAL1 and CDELTA1 keywords. The fluxes and errors should be stored, respectively, in the primary data unit and in an image extension [Grosbol et al., 1988] as 1D arrays. In the same way, the spectrum can be saved in FITS format if “.fits” extension is specified in the file name.

Continuum

Continuum region files should be plain text files with **tab** character as column delimiter. Two columns should exist: 'wave_base' and 'wave_top' (the first line should contain those header names). They indicate the beginning and end of each region (one per line). For instance:

Listing A.8 – Fragment of a continuum region file

1	wave_base	wave_top
2	480.6000	480.6100
3	481.1570	481.1670
4	491.2240	491.2260
5	492.5800	492.5990

Additionally, “wave base” should be always lower than “wave top” or iSpec will not be able to process the file.

Lines

Line region files should be plain text files with **tab** character as column delimiter. Four columns should exist: 'wave_peak', 'wave_base', 'wave_top' and 'note' (the first line should contain those header names). They indicate the peak of the line, beginning and end of each region (one per line) and a note (it can be any string comment). For example:

Listing A.9 – Fragment of a line regions file

1	wave_peak	wave_base	wave_top	note
2	480.8148	480.7970	480.8330	Fe 1
3	496.2572	496.2400	496.2820	Fe 1
4	499.2785	499.2610	499.2950	
5	505.8498	505.8348	505.8660	Fe 1

The note can be blank but the previous **tab** character should exist anyway.

Regarding the wavelengths, “wave base” should be always lower than “wave top” and “wave peak” should be in between or iSpec will not be able to process the file.

Segments

Segment region files should be plain text files with **tab** character as column delimiter. Two columns should exist: 'wave_base' and 'wave_top' (the first line should contain those header names). They indicate the beginning and end of each region (one per line). For instance:

14. International Astronomical Union

Listing A.10 – Fragment of a segments file

```

1 | wave_base      wave_top
2 | 480.6000      480.6100
3 | 481.1570      481.1670
4 | 491.2240      491.2260
5 | 492.5800      492.5990

```

The values in the column “wave base” should be always lower than “wave top” or iSpec will not be able to process the file.

A.3.2 Execution

The editor can be initiated by double clicking “iSpec.command” or executing in a terminal located in iSpec’s directory:

Listing A.11 – Command line execution

```

1 | ./iSpec.command

```

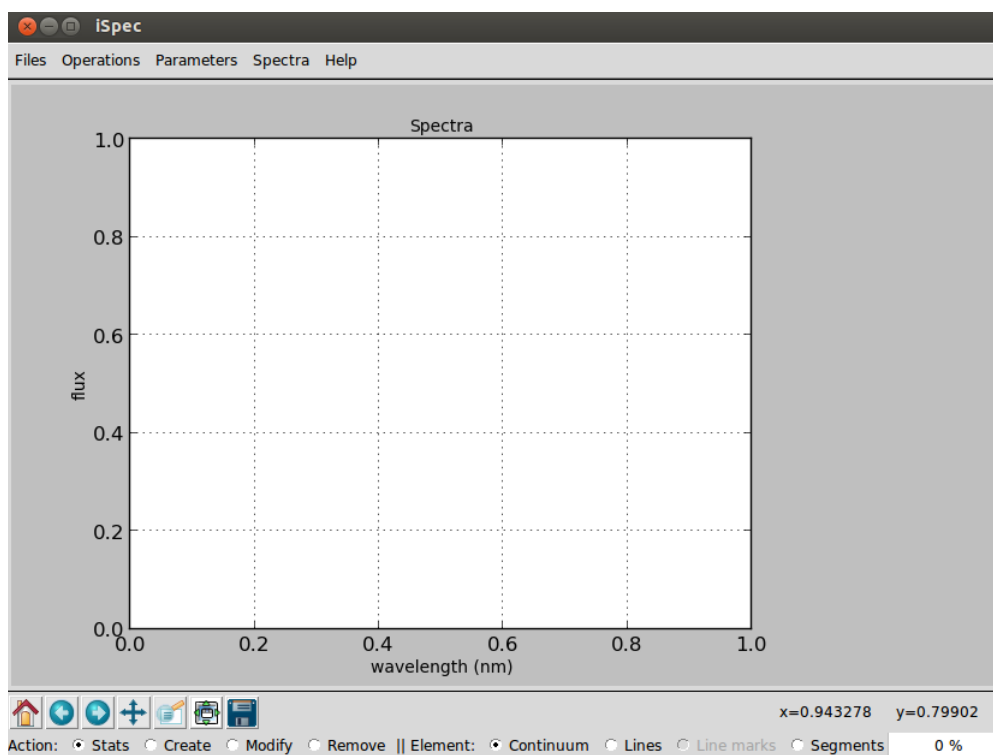


Figure A.11 – Empty editor.

Once initiated, it is possible to load spectra or region files through the “File” menu. Alternatively, they can also be specified from command line like for example:

Listing A.12 – Command line execution with all the possible arguments

```

1 | ./iSpec.command --continuum=input/LUMBA/UVES_MRD_sun_cmask.txt --lines=
   | input/LUMBA/UVES_MRD_sun_Fe-linelist.txt --segments=input/LUMBA/
   | UVES_MRD_sun_segments.txt input/LUMBA/UVES_MRD_sun_official.s.gz

```

A.3.3 Basic interaction

Opening, selecting and closing spectra files

iSpec can open multiple spectra files simultaneously with the format specified on section A.3.1 through the menu “File - Open spectra”. At every moment, only one spectrum is active and its marked with a “[A]” symbol in the legend box.

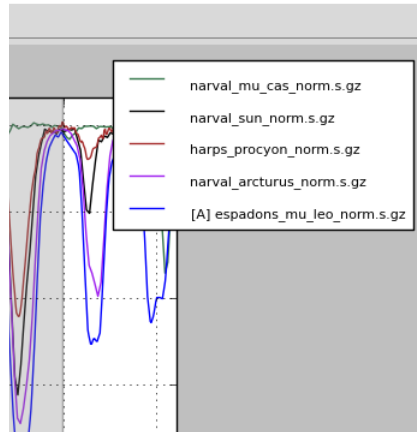


Figure A.12 – Multiple spectra: the active one is marked with an “[A]” in the legend.

Operations such as continuum fitting or radial velocity determination are performed using only the active spectrum. This can be changed through the menu “Spectra - Name of the spectrum” or directly closed through “Spectra - Close spectrum”. In case the spectrum has been modified and not saved, iSpec will ask for confirmation before closing it.

Additionally, the errors associated to each spectrum's point can be plotted by activating “Spectra - Show errors in plot”. This will plot two discontinuous lines above and below the spectrum representing the flux \pm the errors.

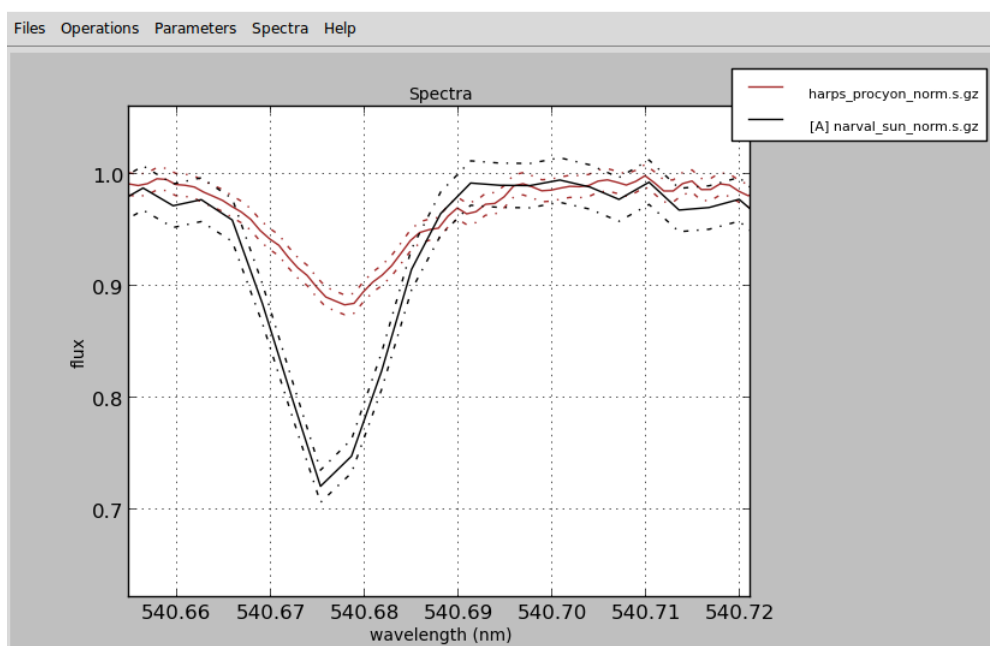


Figure A.13 – Show errors in plot.

Opening and closing region files

Any kind of region files (continuum, line masks or segments) with the format specified on section [A.3.1](#) can be opened by iSpec through the menu “File”.

Once loaded, they can also be completely removed from the plot through the menu “Operations - Clear - Continuum/Line masks/Segments”. In case some regions have been modified and not saved, iSpec will ask for confirmation before clearing them.

Saving images, spectra and regions

Through the “File” menu it is possible to save a PNG image of the current plot, the active spectrum or the definition of the different regions. It is worth noting that in the title of the editor’s window will appear “*segments”, “*lines”, “*continuum” or “*name_of_spectrum” to indicate that some of these elements have been modified but not saved.

Visualization

iSpec provides zoom capabilities by activating the zoom mode. Once done, left clicking and dragging defines the zone to be augmented. The home icon reverts the zoom and the back/forward arrows permits going back to the previous zoomed region.



Figure A.14 – From left to right: Home button, back/forward arrows, Pan mode and Zoom mode.

On the other hand, it is possible to move the current visualization zone by selecting the Pan mode, left clicking and dragging the mouse. Additionally, in this mode it is possible also to zoom in/out by right clicking and dragging the mouse.

While Zoom or Pan modes are active, no actions (stats, create, modify, remove) can be performed on any element (see section [A.3.4](#)).

A.3.4 Regions

As exposed in section [A.3.1](#), there are three different types of regions:

- Continuum: they can be used for fitting the star’s continuum instead of using the whole spectrum (see [A.3.5](#)). Continuum region candidates can also be automatically identified by using the functionality described in section [A.3.7](#).
- Line masks: its goal is to isolate lines of interest and they are used for gaussian fitting (see section [A.3.27](#)) and astrophysical parameters/abundance determination (see section [A.3.27](#))
- Segments: regions that generally include one or more line masks and one or more continuum regions.

For creating, modifying or removing regions, an action and an element should be selected in iSpec:

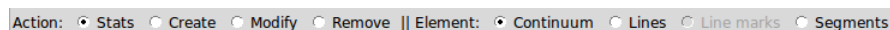


Figure A.15 – Actions and elements.

The possibilities with each combination are explained in the following table (it is worth noting that the mouse position in wavelength/flux can be found in the status bar of the editor's window):

	Stats	Create	Modify	Remove
Continuum Lines Segments	Left click on a region and its statistical information will be visible in the bottom part of the window.	Left click on an empty space and a new region will appear. If it is a line region, it will ask for an optional note.	Left click and drag modifies the left edge. Right click and drag modifies the right edge.	Left click to remove the region.
Line marks	-	Left click on a line region to add a note.	Left click on a line region to modify the peak mark. Right click on a line region to add/modify a note.	Left click on a line region to remove the note.

Table A.2 – Combination of actions and elements

It is important to remark that Zoom/Pan mode should be disabled in order to be able to execute the above actions. On the other hand, the user is responsible for not creating incoherent overlapping regions (the program does not perform this kind of validations).

A.3.5 Continuum fitting

The continuum of the star can be fitted by going to the menu “Operations - Fit continuum”.

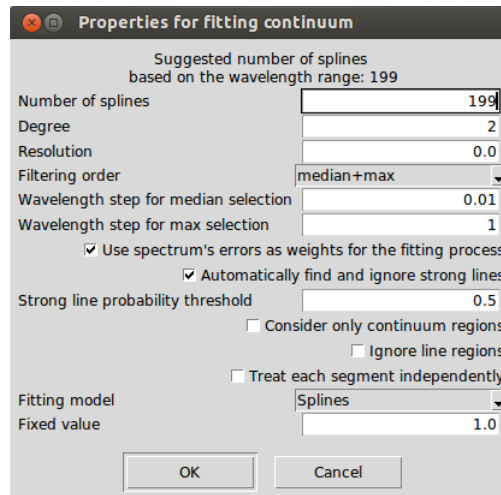


Figure A.16 – Properties for the fitting of the continuum.

The process applies a median filter and a maximum filters (recommended sense, but the inverse order can be chosen too) with windows of given sizes specified by the user. It is frequently useful to fine tune those values depending on the spectral type and signal-to-noise ratio because it will affect the continuum placement. The steps are visually shown in Fig. A.17 and the details are better described in ?.

The spectral resolution can be specified to optimize the computation, but it is completely optional (it can be set to zero). If the spectrum contains errors, they can be propagated thus they will be used as weights during the fitting process. Regarding absorption lines, iSpec implements a probabilistic mechanism to automatically detect them which can also be adjusted.

The process can consider only the defined continuum regions and/or ignore line regions if the corresponding options are selected, if not it will use the whole spectra. Additionally, it can treat each region independently fitting the continuum without considering the rest of the regions.

Once the spectra is filtered, a model will be fitted which can be: several splines (recommended degree is 2) or one polynomial model. The suggested number of splines/degree for the polynomial is shown on the top of the window (by default, it depends on the wavelength range and it proposes 1 spline every 1 nm).

There is a third fitting model named “fixed value” which is useful when the spectrum is already normalized and it is not necessary to re-normalize.

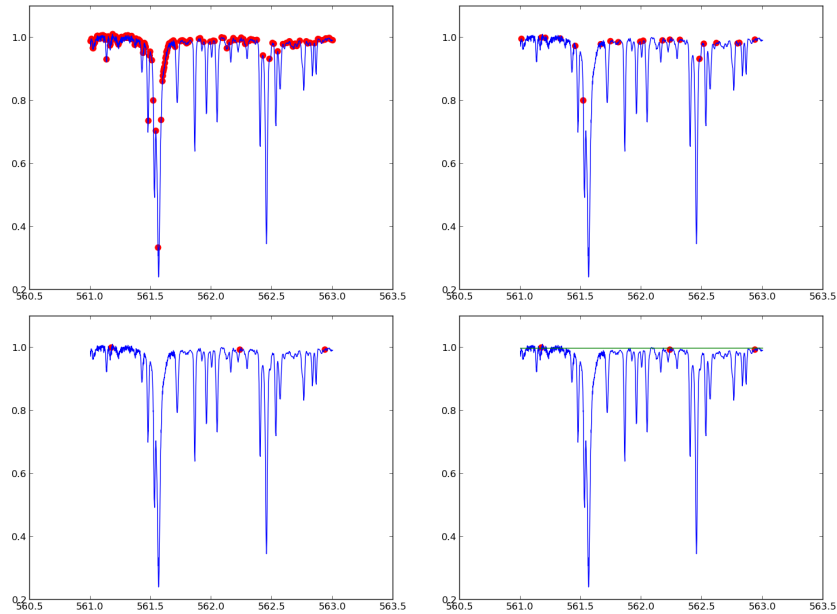


Figure A.17 – Continuum fitting algorithm.

Once the continuum fit is executed, related information can be visualized if the “Stats” action is selected and a region is clicked. On the other hand, the fitted continuum can be removed by using the function “Operations - Clear - Fitted continuum”.

A.3.6 Line fitting

For all the line masks, a Gaussian fit can be done by using the “Operations - Fit lines” menu option. It requires a previously fitted continuum and the velocities respect to atomic/telluric lines. This fields will be automatically filled if the velocity determination process has been executed previously.

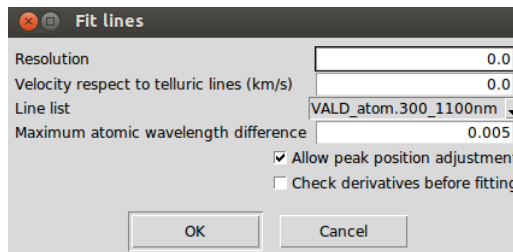


Figure A.18 – Properties for fitting lines.

Fitted lines will be cross-matched with an atomic line list (chosen by the user) and if the difference between the theoretical and measured wavelength peak is smaller than a given limit, the information will be linked to line region. The user can choose also to freely fit the measured wavelength peak, instead of using the line mark linked to each line region. iSpec can also do an additional verification, calculating second derivatives from the observed data to improve the absorption lines' limits (although generally it is not needed).

Additionally, iSpec will cross-match the lines with a telluric line list to identify the element that produces each absorption line (it will be written in the line note) and if it may be affected by a telluric line (indicated with a * symbol in the line note). It is worth noting that if a region can not be fitted, it will be removed.

The information related to the fit and the cross-match can be visualized if the “Stats” action is selected and a line region is clicked.

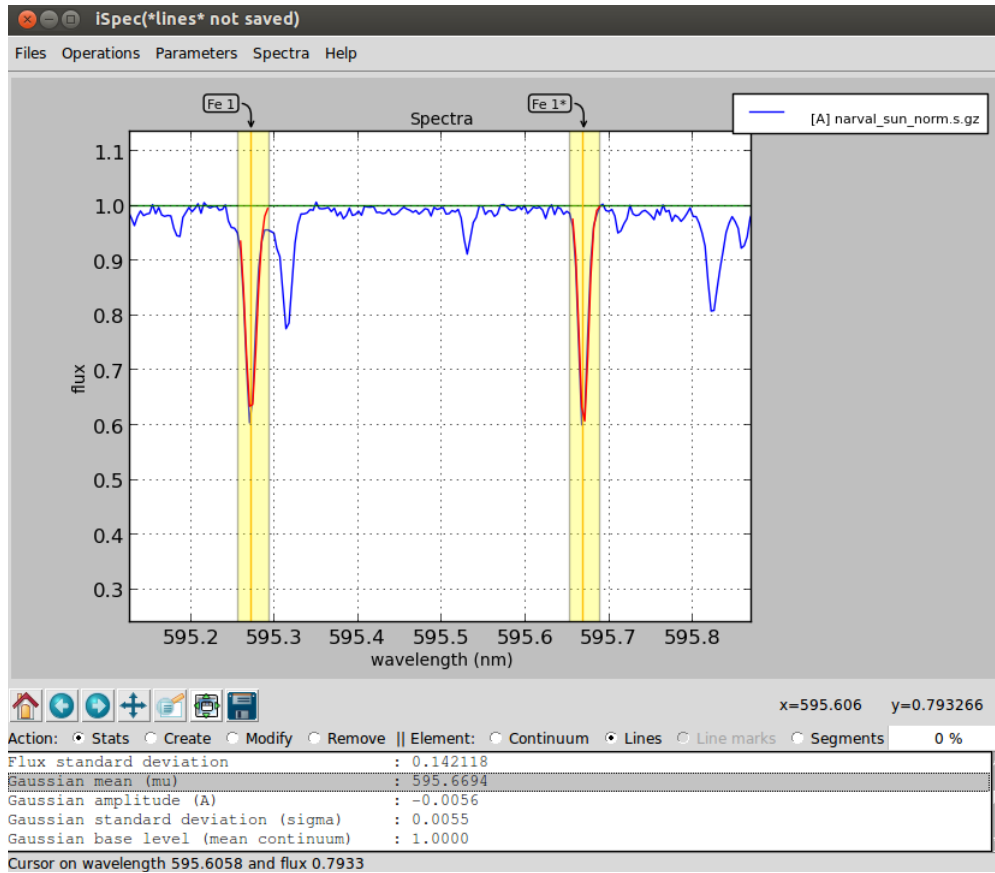


Figure A.19 – Continuum and lines fitted.

Finally, the fitted lines can be removed by using the function “Operations - Clear - Fitted lines”.

A.3.7 Automatic continuum regions

It is possible to find continuum regions automatically by analyzing the spectra slice by slice. The slice is selected as continuum if the following conditions are met:

- The region is at least as big as the size specified by the user.
- The standard deviation specified by the user is less than a given maximum.
- The median flux is above or below the continuum fit but not more than a given percentage.

Depending on the spectrum type, the slice size and the standard deviation can be adjusted to find better results.

This functionality is located in the “Operations - Find continuum regions” menu and can be applied over the whole spectra or only inside the defined segments. In both cases, it needs a previously fitted continuum. After the computation, it removes the current continuum regions (if there are any) and draws the ones that the process has found.

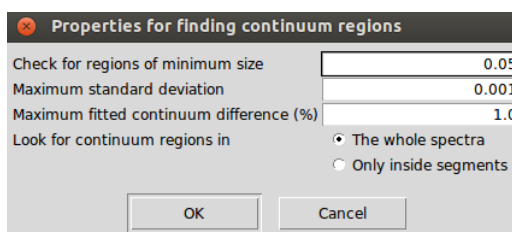


Figure A.20 – Properties for the automatic mechanism of finding continuum regions.

A.3.8 Automatic line masks

iSpec can find line regions automatically by applying the following steps:

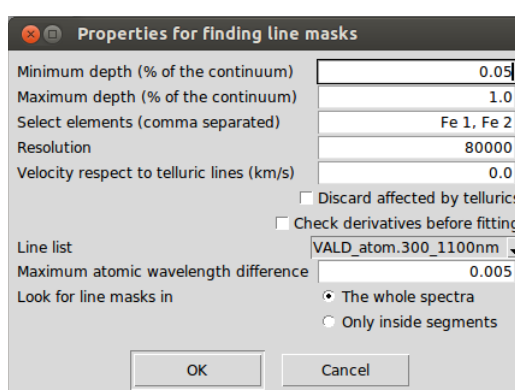


Figure A.21 – Properties for the automatic mechanism of finding line masks.

- Search local maximum and minimum points of a spectrum that has been smooth by using two times the resolution
- Select those line candidates that have a minimum depth (1.0 represents 100% of depth with respect to the continuum)
- Fit the line candidates with a Gaussian model and discard those with bad fit
- Cross-match the remaining lines with an atomic line list considering the velocity specified by the user
- Select the lines that correspond to the elements specified by the user (comma separated or blank to avoid this filter)
- Cross-match again with a telluric line list considering the velocity specified by the user
- Discard lines that may be affected by telluric lines if the user has indicated so

This functionality is located in the “Operations - Find line masks” menu and can be applied over the whole spectra or only inside the defined segments. In both cases, it needs a previously fitted continuum. After the computation, it removes the current line regions (if there are any) and draws the ones that the process has found.

A.3.9 Adjust line masks

Line masks automatically found or manually defined for a given type of stars may not fit well enough the shape of the line. iSpec can adjust automatically previous defined line masks to match a better beginning/end of the masks to the particular form of the active spectrum.

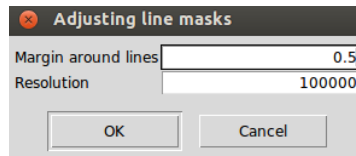


Figure A.22 – Properties for the automatic mechanism of finding line masks.

To do so, iSpec will check where is the optimal limit of the line by looking at a window of a given margin (in nanometers) around the line center. The algorithm will search for the local maximum in each side of the line that is closer to the line center.

A.3.10 Create segments around line masks

The user that has a group of line masks already defined could be interested in creating segments around them, for instance, in order to compute synthetic spectra. iSpec can do that automatically, the user should specify how many nanometers he wants around each line masks and iSpec will group those lines that are close enough under the same segment.

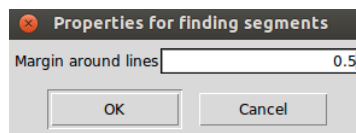


Figure A.23 – Properties for the automatic mechanism of finding line masks.

A.3.11 Barycentric velocity calculation

iSpec incorporates an option for calculating the earth's velocity towards the earth ("Parameters - Calculate barycentric velocity" menu, algorithm based on Stumpff 1980 [Stumpff, 1980]) so that the spectra can be corrected and transformed to the solar barycentric reference frame ("Operations - Correct - Barycentric velocity" menu). For the determination it is necessary to know the date/time of the observation and the star's coordinates (RA: Right Ascension in hours, DEC: Declination in degrees) in epoch J2000.0.

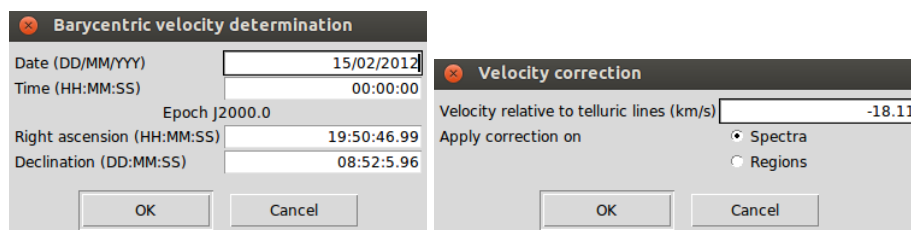


Figure A.24 – Barycentric velocity determination and correction.

A.3.12 Velocity determination and correction

The velocity profile can be determined relative to three different references:

- Atomic data: Useful for determining the radial velocity of a star, considering that the barycentric velocity due to the earth orbit has been already corrected.
- Telluric lines: It can be used to identify the position of the telluric lines (thus these regions can be ignored) or to evaluate if a given spectrum has already been corrected by the barycentric velocity (if not, the output velocity will be zero). Additionally, in this process iSpec can estimate the resolving power of the instrument as described in section A.3.17
- Template: Any loaded spectrum or an internal synthetic one can be used for determining the relative radial velocity.

The figure shows three dialog boxes for velocity determination. The top-left dialog is titled 'Velocity profile relative to atomic lines' and has fields for Velocity lower limit (km/s) set to -200, Velocity upper limit (km/s) set to 200, Velocity steps (km/s) set to 1.0, Fitting model set to '2nd order polynomial + a', a checkbox for 'CCF in Fourier space', Mask list set to 'Atlas.Sun.372_926nm', Mask size (km/s) set to 2.0, and Minimum depth set to 0.1. The top-right dialog is titled 'Velocity profile relative to telluric lines' and has fields for Velocity lower limit (km/s) set to -100, Velocity upper limit (km/s) set to 100, Velocity steps (km/s) set to 0.5, Fitting model set to '2nd order polynomial + a', a checkbox for 'CCF in Fourier space', Mask size (km/s) set to 2.0, and Minimum depth set to 0.01. The bottom dialog is titled 'Velocity profile relative to template' and has fields for Velocity lower limit (km/s) set to -200, Velocity upper limit (km/s) set to 200, Velocity steps (km/s) set to 1.0, Fitting model set to '2nd order polynomial + a', a checkbox for 'CCF in Fourier space', and Cross-correlate with set to '[Internal template]'. Each dialog has 'OK' and 'Cancel' buttons.

Figure A.25 – Velocity determination by using atomic/telluric lines or a template.

The generation of the velocity profile is done by an implementation of the cross-match correlation algorithm [Pepe et al., 2002] which sum up the spectrum's fluxes (f) multiplied by a template function 'p':

$$C(v) = \sum_{lines} \sum_{pix} p(pix, v) \cdot flux(pix) \quad (A.1)$$

1. Calculate $C(v)$ where $p(pix, v)$ is varied from a lower to an upper velocity in fixed steps.
2. Normalize $C(v)$

The 'p' function represents the fraction of the line of a template spectrum (which depends on the spectral type of the star) that falls on a given pixel at a given velocity.

The cross-correlation can be computed in Fourier space, taking advantage of the correlation theorem [Allende Prieto, 2007] although when the spectrum has a large wavelength the computation can take more time compare to the normal cross-correlation.

iSpec includes an internal template (it can be found in the directory “input/spectra/synthetic/”) which corresponds to a synthetic spectrum of a star with $T_{\text{eff}} 5777.0$, gravity ($\log g$) 4.44 and metallicity 0.02 (solar type) which has been generated by using SPECTRUM[Gray and Corbally, 1994], atomic data extracted from the VALD database[Kupka et al., 2011] (350 to 11000 nm) and MARCS model atmospheres. In case that another ground-base observed spectrum is used as template, it is recommended to clean the regions that may be affected by telluric lines as explained in the section A.3.23.

In the case of selecting the option of using atomic lines, a mask is used instead of a template which means that the ‘p’ function has values only on the peak of the line and the value corresponds to the depth of the line. The possible masks line lists are:

- Narval Sun: lines and depths detected from observed asteroids by the NARVAL spectrograph with a wavelength range from 370 to 1048 nm.
- Solar and Arcturus atlas: lines and depths detected in the solar and arcturus atlas with a wavelength range from 372 to 926 nm.
- HARPS/SOPHIE A0, F0, G2, K0, K5, M5: mask specially prepared to be used by HARPS/SOPHIE with a wavelength range from around 375 to 680 nm.
- Synthetic Sun: lines and depths detected from a synthetic spectrum generated with SPECTRUM, VALD linelist and MARCS model atmosphere with a wavelength range from 350 to 1100 nm.
- VALD: mask based on a line list extracted from the VALD database[Kupka et al., 2011] with a wavelength range from 300 to 1100 nm. The depth of each line correspond to a star with $T_{\text{eff}} 5770.0$ and gravity ($\log g$) 4.40 (solar type).

For the telluric lines, the mask has been generated from the analysis of a synthetic spectra of the typical telluric lines obtained from TAPAS [Bertaux et al., 2013] (an on-line service that provides simulated atmospheric transmission spectra for specific observing conditions).

Internally, for the cross-correlation process, iSpec creates a mask from the given line list with a user defined size. If one or more mask lines fall into one range, the max depth is assigned as the mask value (otherwise it will be zero).

Afterwards, it re-samples the mask uniformly in terms of velocity by using the specified velocity step (recommended to be half of the mask size). This implies that the distance between the elements in the mask is variable in wavelength but constant in velocity (depends on the mask size specified by the user).

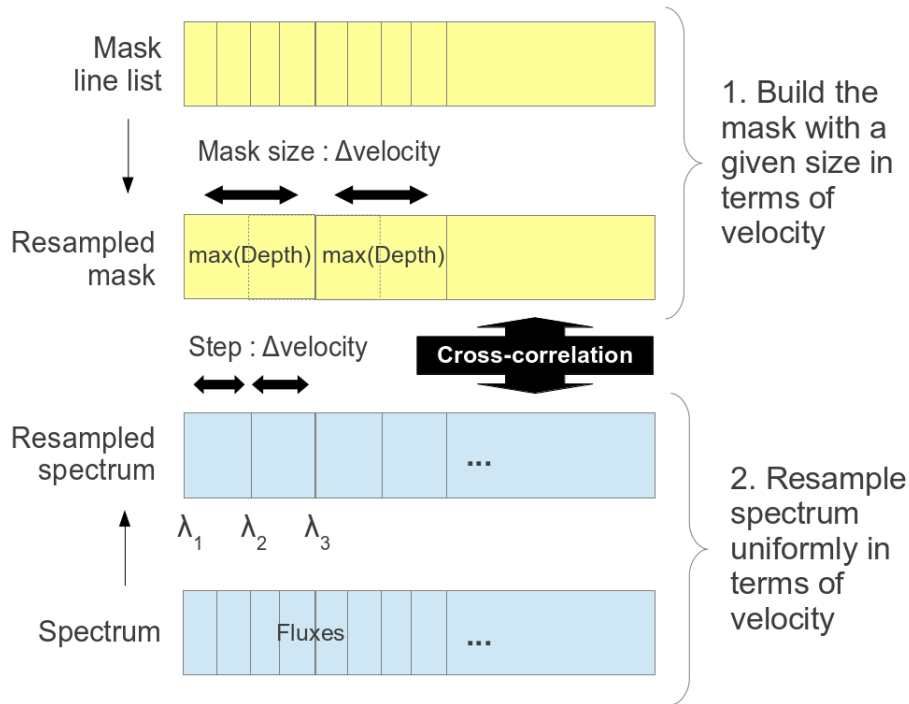


Figure A.26 – Mask for cross-correlation. iSpec permits to choose the mask size in velocity and the minimum depth.

The following formula is used for determining the wavelength ranges:

$$\lambda_{i+1} = \lambda_i + \lambda_i \left(1 - \sqrt{\frac{1 - \frac{\text{velocity}}{c}}{1 + \frac{\text{velocity}}{c}}} \right) \quad (\text{A.2})$$

After the mask construction, the spectrum is re-sampled to have the same points as the mask and the cross-correlation algorithm can be easily applied by shifting the mask values to the left/right (each shift represents a constant increment/decrement in velocity). This approach allows to reduce the computation time needed for calculating the velocity respect to the atomic/telluric mask.

The results are presented in a new window where the velocity profile is shown. The mean velocity is calculated by fitting a second order polynomial near the peak and additionally a Gaussian/Voigt is fitted (with fixed mean velocity) to determine other complementary parameters:

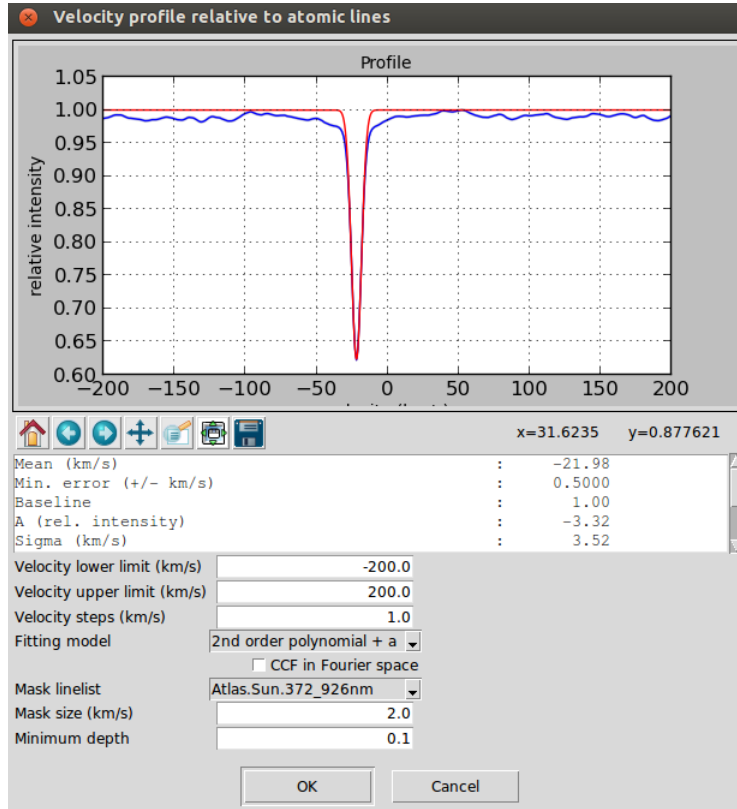


Figure A.27 – Velocity profile.

The error in the radial velocity is calculated following [Zucker \[2003\]](#):

$$\sigma_v^2 = - \left[N \frac{C''(v)}{C(v)} \frac{C^2(v)}{1 - C^2(v)} \right]^{-1}, \quad (\text{A.3})$$

where N is the number of bins in the spectrum, C is the cross-correlation function and C'' is its second derivative.

Finally, the spectrum and the regions can be shifted considering the determined velocity (or indicating a custom one) by using the option "Operations - Correct velocity...". The following formula is applied:

$$\lambda_{corrected} = \lambda \sqrt{\frac{1 - \frac{velocity}{c}}{1 - \frac{velocity}{c}}} \quad (\text{A.4})$$

where c is the speed of light in vacuum and λ the original wavelengths.

A.3.13 Spectroscopic binaries identification

The velocity determination function relative to atomic data (section [A.3.12](#)) can be used to identify spectroscopic binaries. In those cases, the resulting profile would have two different peaks:

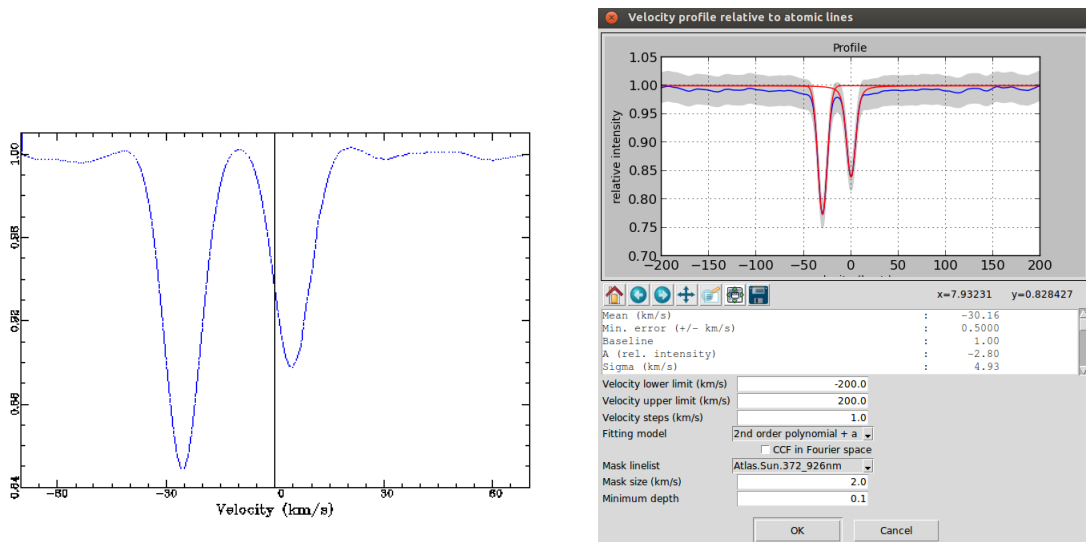


Figure A.28 – Cross-match correlation determined by ELODIE and iSpec for HD005516A spectroscopic binary

iSpec incorporates (into the “input/spectra/binaries/” directory) the spectrum of HD005516A observed with ELODIE [Moultaka et al., 2004]

- Date 4.10.1996 / RA 00 57 12.40 / DEC +23 25 03.54
- ELODIE:
 - RV component 1: -25.49 km/s
 - RV component 2: 4.72 km/s
- iSpec results with parameters by default:
 - Barycentric vel: 5.15 km/s
 - RV component 1: -30.16 km/s
 - RV component 2: -0.04 km/s
 - RV corrected component 1: -25.01 km/s
 - RV corrected component 2: 5.11 km/s

iSpec will try to automatically detect outliers peaks in the velocity profile in order to detect spectroscopic binaries and fit more than one Gaussian/Voigt.

A.3.14 Signal-to-Noise Ratio (SNR) estimation

iSpec provides two slightly different approaches to estimate the spectrum's SNR:

- From errors: The SNR is calculated by using the flux divided by the reported errors in the spectrum. This is the best way to calculate the SNR if the errors are present.
- From fluxes: The whole spectrum is checked, resampling to ensure homogeneous steps and taking 10 by 10 measures (although this value can be modified by the user), calculating the SNR (equation A.5) for each one and finally selecting the mean SNR as the global SNR.

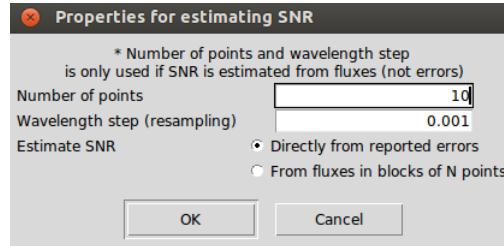


Figure A.29 – Properties for the global SNR estimation.

The Signal-to-Noise Ratio (SNR) can be defined as the ratio of mean to standard deviation of a measurement:

$$SNR = \frac{\mu}{\sigma} \quad (\text{A.5})$$

where μ is the mean value and σ the standard deviation.

A.3.15 Errors estimation

Given a SNR, iSpec can estimate the errors associated to each flux measurement. This functionality is found in “Operations - Estimate errors based on SNR”.

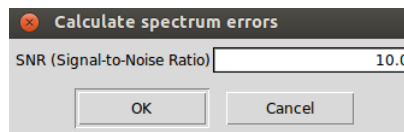


Figure A.30 – Properties for the global SNR estimation.

A.3.16 Add noise

Poisson/Gaussian noise can be artificially added by using the function “Operations - Add noise to spectrum fluxes”.

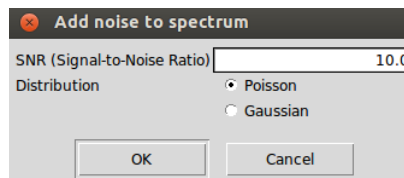


Figure A.31 – Add Poisson noise given a SNR.

A.3.17 Resolving power estimation

iSpec can try to estimate the resolving power of the instrument that has observed the spectrum based on the FWHM of the telluric lines. This estimation can be found in the velocity determination function relative to telluric lines (section A.3.12) and it is obtained by the following equation:

$$R = \frac{c}{(FWHM_{telluric} - FWHM_{theoretical})} \quad (\text{A.6})$$

where c is the speed of light in the vacuum (km/s), $FWHM_{telluric}$ (km/s) correspond to the telluric lines observed in the spectrum and $FWHM_{theoretical}$ (km/s) to the theoretical telluric lines.

The resolving power is also estimated when iSpec determines the velocity profile relative to the atomic data, however this is a bad estimator since it uses directly the FWHM measured and there are several factors that contribute to the broadening of the absorption lines (i.e. star's rotation).

A.3.18 Resolution degradation

The active spectrum resolution can be degraded to a lower one by selecting the menu “Operations - Degrade resolution” and selecting the original and target resolution. If the user has previously generated a velocity profile function (sections A.3.12 and A.3.17), the current resolution has been already estimated and it will be shown in the degradation dialog (although the user can modify it).

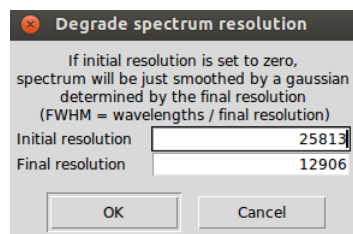


Figure A.32 – Resolution degradation properties

For each flux value, the process will:

1. Define a window based on the FWHM size which depends on the original and target resolution
2. Build a gaussian using the sigma value and the wavelength values of the spectra window
3. Convolve the spectra window with the gaussian and save the convolved value

In case that the user specifies an initial resolution of zero, the spectrum will be just smoothed by a gaussian with variable FWHM determined by each wavelength and the final resolution:

$$FWHM = \frac{wavelength}{final_resolution} \quad (\text{A.7})$$

A.3.19 Continuum normalization

The continuum normalization operation can be found in “Operations - Continuum normalization” and it divides all the fluxes of the active spectrum by the fitted continuum.

Errors in continuum placement will be propagated in this operation if the continuum was fitted taken into account the errors from the spectrum.

A.3.20 Wavelength range reduction

The current active spectrum can be cut by selecting “Operations - Wavelength range reduction” and specifying a base and top wavelength or using directly the defined segments/line regions. The user can also choose to replace the removed flux by zeros.

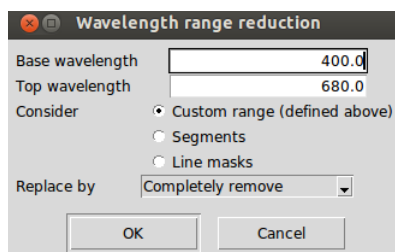


Figure A.33 – Wavelength range reduction properties

A.3.21 Apply mathematical expression

The wavelength, fluxes and error values of the active spectrum can be modified by applying a mathematical expression which can contain any combination of the following functions:

- $\sin(x)$ Trigonometric sine, element-wise.
- $\cos(x)$ Cosine elementwise.
- $\tan(x)$ Compute tangent element-wise.
- $\arcsin(x)$ Inverse sine, element-wise.
- $\arccos(x)$ Trigonometric inverse cosine, element-wise.
- $\arctan(x)$ Trigonometric inverse tangent, element-wise.
- $\arctan2(x1, x2)$ Element-wise arc tangent of $x1/x2$ choosing the quadrant correctly
- $\sinh(x)$ Hyperbolic sine, element-wise.
- $\cosh(x)$ Hyperbolic cosine, element-wise.
- $\tanh(x)$ Compute hyperbolic tangent element-wise.
- $\operatorname{arcsinh}(x)$ Inverse hyperbolic sine elementwise.
- $\operatorname{arccosh}(x)$ Inverse hyperbolic cosine, elementwise.
- $\operatorname{arctanh}(x)$ Inverse hyperbolic tangent elementwise.
- $\operatorname{round}(a[, \text{decimals}, \text{out}])$ Evenly round to the given number of decimals.
- $\operatorname{floor}(x)$ Return the floor of the input, element-wise.
- $\operatorname{ceil}(x)$ Return the ceiling of the input, element-wise.
- $\exp(x)$ Calculate the exponential of all elements in the input array.
- $\log(x)$ Natural logarithm, element-wise.

- $\log_{10}(x)$ Return the base 10 logarithm of the input array, element-wise.
- $\log_2(x)$ Base-2 logarithm of x .
- $\text{sqrt}(x)$ Return the positive square-root of an array, element-wise.
- $\text{absolute}(x)$ Compute the absolute values elementwise.
- $\text{add}(x1, x2)$ Add arguments element-wise.
- $\text{multiply}(x1, x2)$ Multiply arguments element-wise.
- $\text{divide}(x1, x2)$ Divide arguments element-wise.
- $\text{power}(x1, x2)$ First array elements raised to powers from second array, element-wise.
- $\text{subtract}(x1, x2)$ Subtract arguments, element-wise.
- $\text{mod}(x1, x2)$ Return element-wise remainder of division.

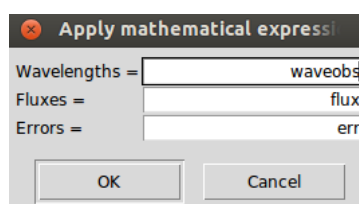


Figure A.34 – Apply a mathematical expression to the active spectrum

The functionality can be found in “Operations - Apply mathematical expression” and the current values can be referred as “waveobs”, “flux” and “err“. Some examples of the utility of this functionality:

- Convert the wavelengths from Armstrong to nanometers by dividing the wavelengths by 10: $\text{Waves} = \text{waveobs} / 10$.
- Change the scale of the fluxes: $\text{Fluxes} = \text{power}(\text{flux}, 2)$
- Modify the errors by using a percentage relative to the flux: $\text{Errors} = \text{flux} * 0.05$
- Assign a constant value to the error values: $\text{Errors} = \text{err} * 0.0 + 1.0$

The result of the mathematical operation should always be an array with the same number of elements as the original spectrum.

A.3.22 Fluxes and errors cleaning

In order to filter out bad measurements, the current active spectrum can be cleaned by selecting “Operations - Clean fluxes and errors” and specifying a base and top flux and error.

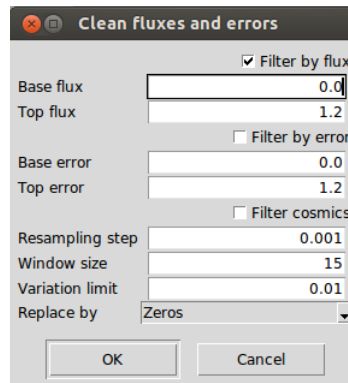


Figure A.35 – Filter out all the measurements that are not in these range limits.

Additionally, the cleaning can be done by considering the mean and standard deviation of a limited region (between a top and base flux level). This option can be useful to remove cosmics residuals although it should be used carefully since it would remove also emission lines.

Finally, the user can chose to completely remove the fluxes or replace them by the continuum instead of zeros.

A.3.23 Clean telluric regions

Through the menu “Operations - Clean telluric regions”, one can clean the regions of the spectrum that may be affected by telluric lines. For that purpose it is needed: the radial velocity of the spectrum, the minimum depth of the telluric lines to consider (previously measured by iSpec from a synthetic model) and the region around those lines to be cleaned (in km/s). The user can chose to completely remove the fluxes or replace them by the continuum instead of zeros.

By default a margin of 30 km/s is suggested, since it represents the typical maximum velocity ranges where the telluric lines may be. For instance, considering a fictitious star that has zero radial velocity respect to the sun, when it is observed from earth a radial velocity might be measured due to the rotation of the earth around the sun. This radial velocity respect to the each will typically be between -30 and +30 km/s for this fictitious star depending on the region of the sky that it is observed.

This functionality is mainly useful when the spectrum is going to be used as a template for measuring the radial velocity of another spectrum (see section A.3.12). Cleaning all this fluxes from the template reduces the impact of potential telluric lines in the spectrum to be measured.

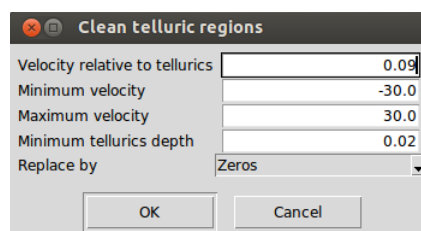


Figure A.36 – Filter out all the measurements potentially affected by telluric lines.

A.3.24 Spectrum resampling

By selecting “Operations - Resample spectrum”, the current active spectrum can be uniformly resampled from a given wavelength range/increment by linear or spline interpolation.

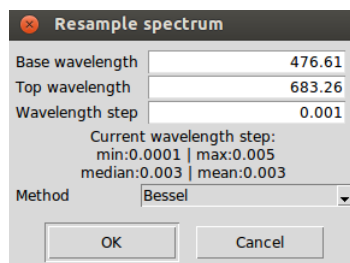


Figure A.37 – Properties for spectrum resampling. Some basic statistics of the active spectrum are printed next to the wavelength step field in order to have a point of reference.

The interpolation method can be linear, bessell (4 points are considered at each interpolated point, the result tends to be smoother than the linear interpolation) or spline (it might help to smooth the spectrum).

A.3.25 Spectra combination

All the open spectra can be combine through “Edit - Combine all spectra” by finding the mean/median, subtracting (active spectrum minus the rest), co-adding or dividing (active spectrum divided by the rest) the flux values. It is recommended that before doing so, all the spectra should be corrected for its radial/barycentric velocity and they should have the same resolution.

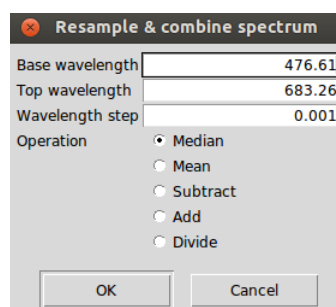


Figure A.38 – Spectra combination properties

The process does the following operations:

1. It builds a common wavelength coordinates which will depend on the ranges and wavelength step specified by the user
2. It homogenizes all the spectra by interpolating the flux at each point of the common wavelength coordinates. It is worth noting that the visualized spectra is not replaced by the homogenized version, they are only used internally by the combine function.
3. The homogenized spectra is combined and the result is displayed.

A.3.26 Interoperability with other SAMP applications

iSpec is a SAMP ready application and therefore it can send/receive spectra to/from other astronomical programs (i.e. TOPCAT ¹⁵, VOSpec ¹⁶, splat ¹⁷) running in the same machine.

To enable the interoperability option, it is necessary to run a SAMP hub in the system. The easiest way to do so is to install and run TOPCAT (it starts automatically a SAMP hub).

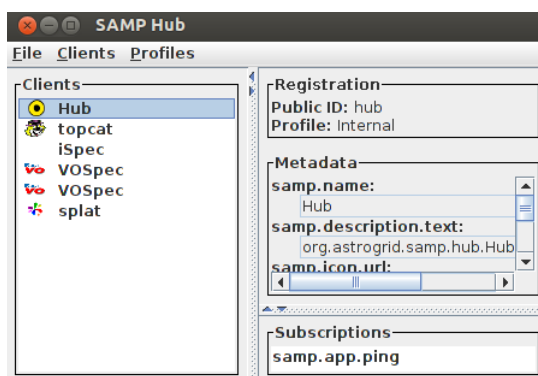


Figure A.39 – TOPCAT SAMP hub with different programs already connected

From the menu “Edit - Send spectrum to...”, the current active spectrum can be sent to any external program connected to the SAMP hub that supports spectra or data tables.

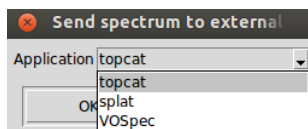


Figure A.40 – iSpec “Send spectrum to...” option

15. <http://www.star.bris.ac.uk/~mbt/topcat/>

16. <http://www.sciops.esa.int/index.php?project=ESAV0&page=vospec>

17. <http://star-www.dur.ac.uk/~pdraper/splat/splat.html>

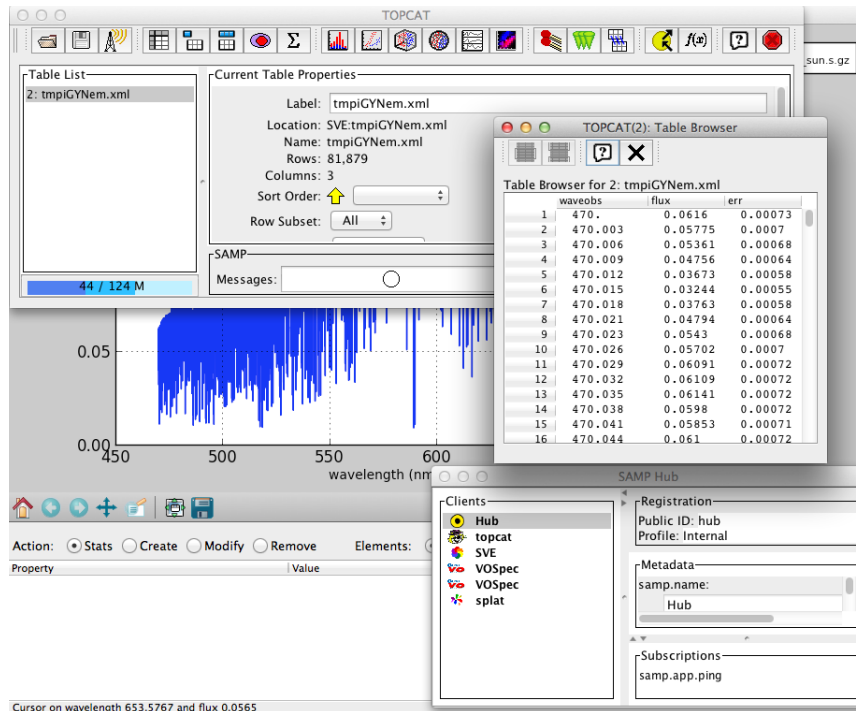


Figure A.41 – TOPCAT with data sent from iSpec

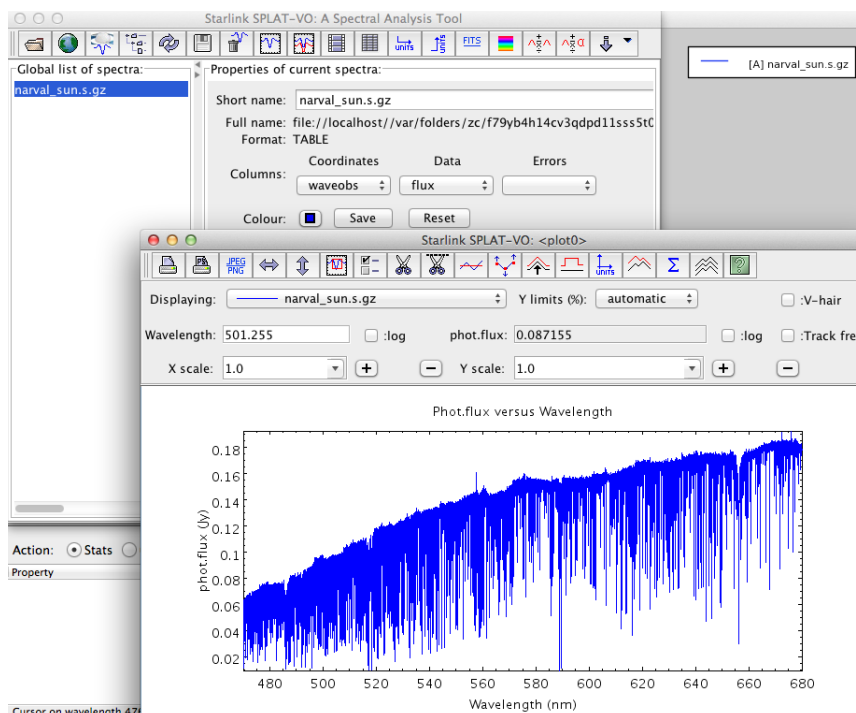


Figure A.42 – Splat with data sent from iSpec

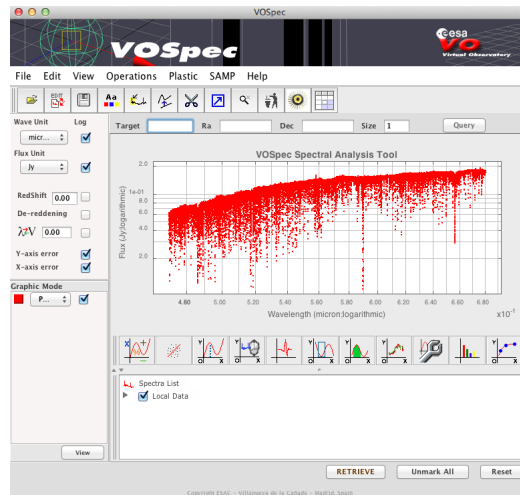


Figure A.43 – VOSpec with data sent from iSpec

It is also possible to send spectra from external programs to iSpec, in this case it is required that the data is structured in three columns in the following order: wavelengths, fluxes and errors. It is highly recommended to name the columns with the following labels: waveobs, flux, err.

By using this functionality, iSpec can receive data from the Virtual Observatory ¹⁸ in an indirect way through external programs such as TOPCAT, VOSpec and splat.

A.3.27 Spectral synthesis and parameter determination

In case that the optional functionality of synthetic spectrum generation has been activated (compiled), it is going to be possible to use “SPECTRUM: a Stellar Spectral Synthesis Program” [Gray and Corbally, 1994] to generate synthetic spectrum, determine astrophysical parameters and calculate chemical element abundances.

Synthetic spectrum generation

Through “Spectra - Synthesize spectrum”, iSpec can generate synthetic spectrum. The user can specify the different parameters and select a line list among different options:

- VALD: line list extracted from the VALD database [Kupka et al., 2011] (February 2012) with a wavelength range from 300 to 11000 nm.
- GES linelist: they are used in the Gaia ESO Survey (GES). It covers the wavelength range from 475 685 nm.
- Kurucz linelist covering from 300 to 1100 nm.
- NIST linelist covering from 300 to 1100 nm.
- SPECTRUM linelist (300nm - 1100nm) [Gray and Corbally, 1994] (February 2012), which contains atomic and molecular lines obtained mainly from the NIST Atomic Spectra Database [Ralchenko, 2005] and Kurucz line lists. Its wavelength range covers from 300 to 11000 nm.

18. <http://www.ivoa.net/>

On the other hand, the solar abundance can be chosen too from different authors and publications:

- Asplund 2005/2009
- Grevese 1998/2007
- Anders 1989

Additionally, iSpec incorporates several different grids of model atmospheres:

- MARCS GES/APOGEE¹⁹ models [Gustafsson et al., 2008] (plane-parallel + spherical²⁰)
 - Effective temperature (Teff): [2500, 2600, 2700, 2800, 2900, 3000, 3100, 3200, 3300, 3400, 3500, 3600, 3700, 3800, 3900, 4000, 4250, 4500, 4750, 5000, 5250, 5500, 5750, 6000, 6250, 6500, 6750, 7000, 7250, 7500, 7750, 8000] K
 - Gravity (Logg): [0.0, 0.5, 1.0, 1.5, 2.0, 2.5, 3.0, 3.5, 4.0, 4.5, 5.0] dex
 - Metallicity ([M/H]): [-5.00 , -4.00 , -3.00 , -2.50, -2.00 , -1.50, -1.00 , -0.70, -0.50, -0.20, 0.00 , 0.20, 0.50, 0.70, 1.00] dex
 - Standard abundance composition, 30% of all models

[Fe/H]	[α /Fe]	[C/Fe]	[N/Fe]	[O/Fe]
+1.00 to 0.00	0.00	0.00	0.00	0.00
-0.25	+0.10	0.00	0.00	+0.10
-0.50	+0.20	0.00	0.00	+0.20
-0.75	+0.30	0.00	0.00	+0.30
-1.00 to -5.00	+0.40	0.00	0.00	+0.40

Table A.3 – MARCS Standard abundance composition

- The MARCS “.mod” files have been transformed to the format needed by SPECTRUM (Kurucz format):
 1. RHOX: mass depth
 2. T: temperature (K)
 3. P: gas pressure (Pgas)
 4. Electron density (1/cc): $XNE = \frac{Pe(MARCS)}{1.380658e^{-16*T}}$
 5. ABROSS: Rosseland mean absorption coefficient (KappaRoss)
 6. ACCRAD: Radiation pressure (Prad)
 7. VTURB: Microturbulent velocity in meters/second
- ATLAS9 Kurucz/CastelliApogee/Kirby²¹ models [Kurucz, 2005] (plane-parallel)
 - Effective temperature (Teff): [3500, 3750, 4000, 4250, 4500, 4750, 5000, 5250, 5500, 5750, 6000, 6250, 6500, 6750, 7000, 7250, 7500, 7750, 8000, 8250, 8500, 8750] K

19. <http://marcs.astro.uu.se/>

20. SPECTRUM is a plane-parallel synthesizer but some tests has shown that the MARCS spherical models can be used with reasonable results. Additionally, the transition from MARCS plane parallel to spherical is smooth enough to avoid major impacts

21. <http://kurucz.harvard.edu/grids.html>

- Gravity (Logg):[0.0, 0.5, 1.0, 1.5, 2.0, 2.5, 3.0, 3.5, 4.0, 4.5, 5.0] dex
- Metallicity ([M/H]): [-5.00, -4.50, -4.00, -3.50, -3.00, -2.50, -2.00, -1.50, -1.00, -0.50, -0.30, -0.20, -0.10, 0.00, 0.10, 0.20, 0.30, 0.50, 1.00] dex
- Standard abundances (no enhanced).

Apart from the astrophysical parameters, the model atmospheres and line lists, iSpec asks for other parameters like the rotational velocity ($V \sin(i)$), micro/macroturbulence, resolution and wavelength range/steps.

Parameter	Value
Model atmosphere	MARCS.GES
Solar abundances	Grevesse.2007
Line list	GES_atom.475_685nm
Effective temperature (K)	5777.0
Surface gravity (log g)	4.44
Metallicity [Fe/H]	0.0
Microturbulence velocity (km/s)	1.0
Macroturbulence velocity (km/s)	0.0
Rotation ($v \sin(i)$) (km/s)	2.0
Limb darkening coefficient	0.0
Resolution	300000
Wavelength min (nm)	470.0
Wavelength max (nm)	680.0
Wavelength step (nm)	0.001
Generate spectrum for	<input checked="" type="radio"/> Custom range (defined above) <input type="radio"/> Segments <input type="radio"/> Line masks

Figure A.44 – Properties for synthetic spectrum generation

It is recommended not to use too narrow wavelength ranges and wavelength steps not smaller of 0.01 (being 0.001 the optimum value).

Parameters determination

iSpec can be used to determine astrophysical parameters by comparing an observed spectrum with synthetic ones generated on the fly (in a similar way as the Spectroscopy Made Easy (SME) tool [Valenti and Piskunov, 1996] works). A least square algorithm tries to minimize the solution in order to converge towards the most similar synthetic spectrum.

To do so, iSpec should have one active spectrum with one or more segments and one or more line masks defined. The synthetic spectrum will be generated only within the segments and only the measurements that fall into the line masks will be used for comparison and minimization. In “Parameters - Determine astrophysical parameters” it is possible to specify what parameters should be free and what are their initial values.

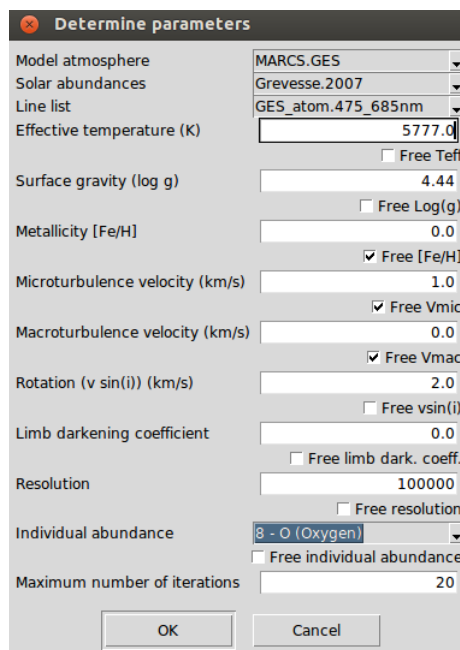


Figure A.45 – Properties for determining astrophysical parameters

The linelist, solar abundances and model atmospheres are the same as for the synthetic generation option (see section A.3.27). The results are shown directly in the terminal.

```

Generating: 6271.52 4.09 0.43 1.76 13.52 2.00 0.00 70000 1.00
Generating: 6171.52 4.19 0.43 1.76 13.52 2.00 0.00 70000 1.00
Generating: 6171.52 4.09 0.48 1.76 13.52 2.00 0.00 70000 1.00
Generating: 6171.52 4.09 0.43 2.26 13.52 2.00 0.00 70000 1.00
Cache: 6171.52 4.09 0.43 1.76 15.52 2.00 0.00 70000 1.00
Generating: 6174.09 4.08 0.43 1.76 13.52 2.00 0.00 70000 1.00
Iter      7  CHI-SQUARE = 15.23354606  DOF = 12795
teff = 6174.089416
logg = 4.084982924
MH = 0.4253733734
Vmic = 1.759699773
Vmac = 13.51913615
Vsinl = 2
limb_darkening_coeff = 0
R = 70000
continuum_correction = 1
Generating: 6176.25 4.08 0.42 1.76 13.51 2.00 0.00 70000 1.00
Generating: 6175.42 4.08 0.42 1.76 13.52 2.00 0.00 70000 1.00
Cache: 6174.09 4.08 0.43 1.76 13.52 2.00 0.00 70000 1.00
Cache: 6174.09 4.08 0.43 1.76 13.52 2.00 0.00 70000 1.00

Line      wave_peak  wave_base  wave_top  chisq(tanh)  rchisq(tanh)  chisq  rchisq  rms
Line      480.29    480.27    480.32    0.05         0.0011        0.05   0.0011  0.0314
Line      480.81    480.80    480.83    0.05         0.0026        0.05   0.0026  0.0451
Line      517.30    517.29    517.33    0.03         0.0008        0.03   0.0008  0.0259
Line      517.42    517.41    517.43    0.01         0.0009        0.01   0.0010  0.0228
Line      518.30    518.29    518.32    0.02         0.0007        0.02   0.0007  0.0253
Line      518.40    518.39    518.40    0.02         0.0039        0.02   0.0039  0.0442
Line      518.44    518.43    518.44    0.04         0.0074        0.04   0.0074  0.0636
Line      518.54    518.51    518.55    0.01         0.0003        0.01   0.0003  0.0160

Solution:      teff      logg      MH      vmic      vmac      vsinl      limb      R
Errors:        6174.09  4.08     0.43   1.76     13.52    2.00     0.00    70000
                245.50  0.38     0.16   0.44     1.68     0.00     0.00     0

Calculation time:      0:0:53:4

Stats:      DOF      niter      nsynthesis  chisq(tanh)  rchisq(tanh)  chisq  rchisq  rms
Return code: 2          12795      7           45           15.23         0.0012    16.31  0.0013  0.0357
    
```

Figure A.46 – Output with the determined astrophysical parameters.

Abundance determination

Abundance determination can be done by synthetic spectra fitting as exposed in section A.3.27, but alternatively iSpec can measure equivalent widths and use “SPECTRUM: a Stellar Spectral Synthesis

Program” [Gray and Corbally, 1994] to derive the chemical element abundances when the temperature, gravity, metallicity and microturbulence is already known.

Abundances determination

Model atmosphere: MARCS

Effective temperature (K): 5777.0

Gravity (log g): 4.44

Metallicity [M/H]: 0.02

Microturbulence velocity (km/s): 2.0

Cancel OK

Figure A.47 – Properties for the chemical abundance determination

The following steps are needed for the determination of abundances:

- Load a spectrum and the line masks to be used in the analysis
- Fit the continuum (see section)
- Fit the lines (see section):
 - A gaussian/voigt profile will be fitted to determine the equivalent width, central wavelength, etc.
 - By using the fitted paramters, a cross-match process with the internal atomic data will be performed to determine the elements and other fundamental information for each line
- Determine abundances with fitted lines: It is necessary to know the astrophysical parameters of the star (Teff, log(g), metallicity and microturbulence).

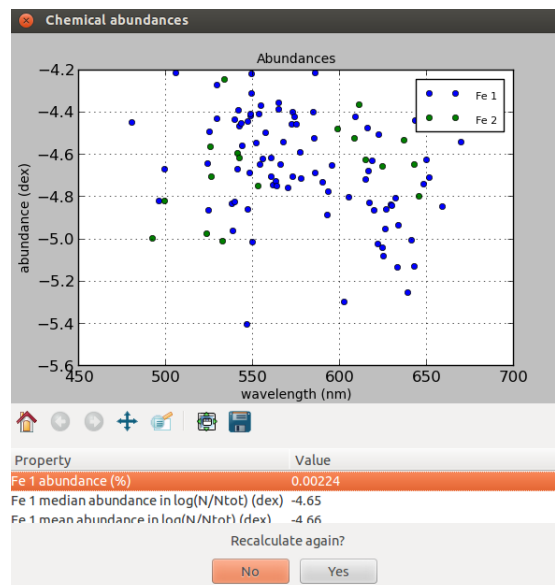


Figure A.48 – Chemical abundance determination

A.4 Automatic usage

The iSpec's functions described in this document, and some additional ones that cannot be accessed through the visual interface, can be called from a python script. An example script (named "example.py") is included into the iSpec distribution files. The example includes a list of functions for different generally useful actions:

- `read_write_spectrum()`
- `convert_air_to_vacuum()`
- `plot()`
- `cut_spectrum_from_range()`
- `cut_spectrum_from_segments()`
- `determine_radial_velocity_with_mask()`
- `determine_radial_velocity_with_template()`
- `correct_radial_velocity()`
- `determine_tellurics_shift_with_mask()`
- `determine_tellurics_shift_with_template()`
- `degrade_resolution()`
- `smooth_spectrum()`
- `resample_spectrum()`
- `coadd_spectra()`
- `merge_spectra()`
- `normalize_spectrum_using_continuum_regions()`
- `normalize_spectrum_in_segments()`
- `normalize_whole_spectrum_strategy2()`
- `normalize_whole_spectrum_strategy1()`
- `normalize_whole_spectrum_strategy1_ignoring_prefixed_strong_lines()`
- `filter_cosmic_rays()`
- `find_continuum_regions()`
- `find_continuum_regions_in_segments()`
- `find_linemasks()`
- `fit_lines_and_determine_ew()`
- `calculate_barycentric_velocity()`
- `estimate_snr_from_flux()`

- `estimate_snr_from_err()`
- `estimate_errors_from_snr()`
- `clean_spectrum()`
- `clean_telluric_regions()`
- `adjust_line_masks()`
- `create_segments_around_linemasks()`
- `synthesize_spectrum()`
- `add_noise_to_spectrum()`
- `generate_new_random_realizations_from_spectrum()`
- `precompute_synthetic_grid()`
- `determine_astrophysical_parameters_using_synth_spectra()`
- `determine_astrophysical_parameters_using_synth_spectra_and_precomputed_grid()`
- `determine_abundances_using_synth_spectra()`
- `determine_astrophysical_parameters_from_ew()`
- `determine_abundances_from_ew()`
- `calculate_theoretical_ew_and_depth()`
- `paralelize_code()`
- `estimate_vmic_from_empirical_relation()`
- `estimate_vmac_from_empirical_relation()`
- `generate_and_plot_YY_isochrone()`

The easiest way to use the script is to duplicate it, and erase all the functions except the ones that fit the user's needs. The variable "ispec_dir" (inside the script) should point to the right directory where iSpec is installed, and the script can be executing by writting on a terminal "python example.py".

A.5 Bug reporting

Bugs can be reported to the author by providing all the information needed to reproduce it:

1. Python script or detailed step list if the bug is related to the visual interface
2. Data used
3. Output printed on the terminal